

CRAS 2017

7th Joint Joint Workshop on New Technologies
for Computer/Robot Assisted Surgery



September 14-15, 2017 - Montpellier, France

Proceedings 2017



www.cras-eu.org

7th Joint Workshop on New Technologies for Computer/Robot Assisted Surgery

© Université de Montpellier – Laboratoire d’Informatique, de Robotique et de Microélectronique de Montpellier (LIRMM) - 161 rue Ada, Montpellier, 34090.

Tous droits réservés. Toute reproduction, partielle ou totale, sous quelque forme que ce soit, est interdite sans l'autorisation préalable de l'éditeur.

All rights reserved. No part of the publication may be reproduced in any form by print, photoprint, microfilm or any other means without written permission from the publisher.

ISBN 9789073802988

EAN 9789073802988

Joining Efforts – Progressing Faster

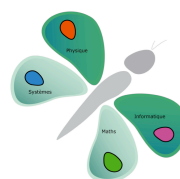
Robotic surgery is one of the most appealing fields of modern robotics. With over 3 decades history, more than 3.800 systems installed worldwide and over 600.000 robot-assisted interventions conducted per year, the field of robotic surgery is considered well established. Despite these impressive figures and increasing popularity in research labs all over the world, the list of technological advances that made it into the operating room (OR) during this last decade is fairly limited. Long expected techniques such as 3D reconstruction, motion compensation, virtual guidance, haptic feedback, under study in many labs all over the planet did not make their appearance into the market yet.

CRAS seeks to give a clear view on the status and recent trends of assistive surgical robotic technologies. It aims to support and propose concrete measures to accelerate research and innovation in this field. CRAS originates from efforts to collaborate among European groups to achieve a critical mass in surgical robotics. As such the workshop continue on discussions started at ERF in Lyon and at ICRA in Karlsruhe, and previous meetings at Verona and Genoa. More in particular CRAS attempts to identify the steps necessary to stimulate cooperation between research and industry, across national borders and different surgical robotic projects to take advantage of the growing attention and support for research and exploitation in this interesting and growing field.

Editors: Salih Abdelaziz, Yassine Haddab, Philippe Poignet, Emmanuel Vander Poorten, Leonardo De Mattos and Paolo Fiorini

Organizers: Salih Abdelaziz, Virginie Fèche, Elisabeth Greverie, Yassine Haddab, Martine Hornby, Philippe Poignet and Nabil Zemiti

This workshop was made possible through the united efforts of the following sponsor:



CRAS Steering Committee

Leonardo De Mattos, Paolo Fiorini, Benoit Herman, Arianna Menciassi, Philippe Poignet and Emmanuel Vander Poorten

CRAS Committee

Salih Abdelaziz (LIRMM)	Giancarlo Ferrigno (POLIMI)	Benoit Herman (UCLouvain)	Philippe Poignet (LIRMM)	Selene Tognarelli (SSSA)
Kaspar Althoefer (Queen Mary)	Fanny Ficuciello (Univ. Napoli)	Chao Liu (LIRMM)	Angelika Peer (Univ. of the West of England)	E. Vander Poorten (KU Leuven)
Alicia Casals (IBEC)	Paolo Fiorini (Univ. Verona)	Leonardo Mattos (IIT)	Ferdinando Rodriguez Y Baena (ICL)	Tom Vercauteren (UCL)
Gastone Ciuti (SSSA)	Stamatia Giannarou (ICL)	Arianna Menciassi (SSSA, Pisa)	Benoit Rosa (ICube, Strasbourg)	Valentina Vitiello (UCL)
Brian Davies (ICL, IIT)	Edward Grant (NCSU)	Sarthak Misra (Univ. of Twente)	Ulrich Seibold (DLR)	Helge Wurdemann (UCL)
Elena De Momi (POLIMI)	Yassine Haddab (LIRMM)	Guillaume Morel (ISIR, Paris)	Bruno Siciliano (Univ. Napoli)	Nabil Zemiti (LIRMM)
Nikhil Deshpande (IIT)	Tamas Haidegger (Obuda Univ.)	George Mylonas (ICL)	Danail Stoyanov (UCL)	

Program Overview

	Thursday 14 September		Friday 15 September
8:00	Registration	8:00	
9:00	<i>Workshop start</i>	9:00	<i>Start day 2</i>
9:15	Keynote Guang Zhong Yang Imperial College London	9:15	Keynote Jocelyne Troccaz University of Grenoble
10:00	Session 1 Novel Robotic Hardware (1)	10:00	Session 4 Image processing and algorithms (1)
10:40	Haption presentation Coffee break	11:00	<i>Coffee break</i>
11:00	Session 2 Novel Robotic Hardware (2)	11:30	Session 5 Image processing and algorithms (2)
12:00	Keynote Misra Sarthak University of Twente	12:30	<i>Lunch break</i>
12:45	<i>Lunch break</i>	14:00	Session 6 Sensing and classification
14:15	Session 3 Training and Safety	16:00	Poster session 2 <i>Coffee break</i>
15:15	Poster session 1 <i>Coffee break</i>	16:45	CRAS Evaluation and Awards
16:00	Towards the bus	17:30	CRAS future strategy Open discussions
16:15	Bus departure	18:30	<i>End of workshop</i>
17:30	Clamouse cave or St-Guilhem-le-désert visit		
20:00	Social dinner		
23:00	Bus back to Montpellier		

Detailed Program

Thursday, September 14

- 8:00-9:00 **Registration**
- 9:00-9:15 **Workshop start** - Word of welcome by **Philippe Poignet**
- 9:15-10:00 **Keynote** - **Guang Zhong Yang** - Imperial College London
Title: **Human Robot Symbiosis**

10:00- 10:45 Session 1 - *Novel Robotic Hardware (1)*

Session chairs: **Leonardo De Mattos and Benoit Rosa**

- 10:00-10:20 *Zorn, F. Nageotte, P. Zanne and M. de Mathelin*
STRAS: A Robotic Platform for Intraluminal Surgery Successfully Tested In-vivo
- 10:20-10:40 *Z. Cheng, B. Davies, D. Caldwell and L. Mattos*
A Smart Handheld Device for Over-Puncture Prevention in Peripheral Intravenous Catheterization
- 10:40-10:45 *Q. Parent*
Haption products presentation
- 10:45-11:00 **Coffee break**

11:00- 12:00 Session 2 - *Novel Robotic Hardware (2)*

Session chairs: **Elena De Momi and Chao Liu**

- 11:00-11:20 *M. Chauhan, N. Deshpande and L. Mattos*
Design of a Robotic Microsurgical Forceps for Transoral Laser Microsurgery
- 11:20-11:40 *F. Bianchi, E. Trallori, D. Camboni, C. M. Oddo, A. Menciassi, G. Ciuti and P. Dario*
Tactile Tool for Tissue Palpation in Colonoscopy
- 11:40-12:00 *A. Gerales, A. Jacassi, P. Fiorini and L. Mattos*
Design of a MEMS Varifocal Mirror for Focusing High-Power Lasers in Minimally Invasive Surgical Procedures
- 12:00-12:45 **Keynote** - **Misra Sarthak** - University of Twente
Title: **Tracking and Control of Tendon-Driven and Magnetically-Actuated Instruments**
- 12:45-14:15 **Lunch**

14:15- 15:15 Session 3 – *Training and Safety*

Session chairs: **Paolo Fiorini and Florent Nageotte**

- 14:15-14:35 *M. Pinzi, S. Galvan and F. R. Y Baena*
Adaptive Fractal Trees Parametrisation for Neurosurgery Applications
- 14:35-14:55 *M. J. Stockton, E. Grant and T. Henderson*
Using Rule Induction to Analyze Intrauterine Pressure and Oxytocin Data for Surgical Interventions in Labour
- 14:55-15:15 *J. Anso, O. Scheidegger, W. Wimmer, K. Gavaghan, M. Caversaccio and S. Weber*
Intraoperative Neuromonitoring for Robotic Surgery – Case Experiences during Robotic Cochlear Implantation

15:15- 16:00 Poster session 1 + Coffee break

J. Shen, N. Zemiti, O. Caravaca, A. Simon, J-L. Dillenseger and P. Poignet, Augmented Reality Visualization Based On 3D Ultrasonography

C. Julliard, F. Despinoy, N. Zemiti, P. Jannin and P. Poignet, Automatic Technical Surgical Skill Scoring from Motion Data

D. Dall'Alba, D. Naftalovich, G. De Rossi, J. Burdick and P. Fiorini, Foot pedal interface for intra-operative annotation of surgical phases and skill in robotic surgery

A. Acemoglu, D. Pucci and L. Mattos, System Identification and Feed-Forward Control of a Magnetic Laser Scanner

E. Mazomenos, F. Vasconcelos, J. Smelt, M. Jahangiri, A. Smith, B. Martin, S. Wright and D. Stoyanov, Objectively Assessing Performance in Transoesophageal Echocardiography from Image Comparison and Alignment

N. Lepoutre, L. Meylheuc, G. I. Bara, L. Barbé and B. Bayle, Robot-Assisted Bone Cement Injection

D. Camboni, R. Calì, J. O. Alcaide, C. M. Oddo, M. C. Carrozza, A. Menciassi, G. Ciuti and P. Dario, Tactile Robotic Endoscopic Capsule for Safe Closed-loop Force Control

P. Cabras, F. Nageotte, P. Zanne and C. Doignon, Precise estimation of the Position of Continuum Instruments in Robotic Endoscopic Surgery using LWR

G. Borghesan, M. Ourak, E. Lankenau, R. Neffin, P. Koch, K. Willekens, P. Stalmans, D. Reynaerts and E. Vander Poorten, Probabilistic Principal Component Analysis and Particle Filtering for real-time retina detection from a single fiber OCT

N. Enayati, A. Mariani, E. Pellegrini, T. Chupin, G. Ferrigno and E. De Momi, A Framework for Assisted Teleoperation with Augmented Reality

16:00-16:15	The participants are asked to go to the bus
16:15-17:30	Bus departure
17:30-20:00	Visit of the Clamouse cave or Saint-Guilhem-le-désert
20:00-23:00	Social dinner
23:00-00:00	Bus back to town

Friday, September 15

9:00-9:15 Start of the 2nd day - Word of welcome

9:15-10:00 **Keynote – Jocelyne Troccaz** - University of Grenoble
Recent advances in Computer Assisted Medical Interventions (CAMI LabEx activities)

10:00- 11:00 Session 4 – Image processing and algorithms (1)

Session chairs: **Edward Grant and Nikhil Deshpande**

10:00-10:20 *S. Hecker, T. Probst, A. Chhatkuli, K. K. Maninis, M. Havlena, E. Vander Poorten and L. Van Gool*
Online Reconstruction of Retinal 3D Maps from Stereo in Close-to-Realtime for Eye Surgery

10:20-10:40 *M. Ferro, G. A. Fontanelli, F. Ficuciello, B. Siciliano and M. Vendittelli*
Vision-based suturing needle tracking with Extended Kalman Filter

10:40-11:00 *P. Brandao, E. Mazomenos, A. Raw, M. Janatka and D. Stoyanov*
Widening Siamese neural networks for stereo matching in colonoscopy

11:00-11:30 **Coffee break**

11:30- 12:30 Session 5 – Image processing and algorithms (2)

Session chairs: **Yassine Haddab and Salih Abdelaziz**

11:30-11:50 *T. Eelbode, P. T. Tran, J. Vander Sloten and E. Vander Poorten*
Multi-region segmentation of IVUS images for endovascular procedures

11:50-12:10 *K-K. Maninis, A. Chhatkuli, J. Pont-Tuset, S. Hecker, T. Probst, M. Ourak, E. Vander Poorten and L. V. Gool*
Deeply Learned 2D Tool Pose Estimation for Robot-to-Camera Registration

12:10-12:30 *B. Rosa, G. Fagogenis, M. Mencattelli, J. Ha and P. Dupont*
Robotic stabilization of cardiac catheter-tissue contact using endoscopic imaging

12:30-14:00 **Lunch**

14:00- 16:00 Session 6 – Sensing and classification

Session chairs: **Emmanuel Vander Poorten and Nabil Zemiti**

14:00-14:20 *M. Selvaggio, G. A. Fontanelli, F. Ficuciello, L. Villani and B. Siciliano*
Task Classification of Robotic Surgical Reconstructive Procedures using Force Measurements

14:20-14:40 *S. Moccia, S. Wirkert, H. Kenngott, A. Vemuri, M. Apitz, B. Mayer, E. De Momi, L. S. Mattos and L. Maier-Hein*
Confidence-based abdominal tissue classification in laparoscopy

14:40-15:00 *G. A. Fontanelli, F. Ficuciello, L. Villani and B. Siciliano*
A Novel Force Sensor Integrated into the da Vinci Trocar for Minimally Invasive Robotic Surgery

15:00-15:20 *P. Gawenda, Y. Noh, J. Frasz, S. Han, S. Wang, R. Housden and K. Rhode*
Contact force sensor for flexible manipulators for MIS

15:20-15:40 *L. Schoevaerds, L. Esteveny, A. Gijbels, J. Smits, M. Ourak, G. Borghesan, D. Reynaerts and E. Vander Poorten*
Development of a new bio-impedance sensor to detect retinal vessel punctures for retinal vein occlusion treatment

15:40-16:00

J. Smits, M. Ourak, A. Gijbels, G. Borghesan, L. Esteveny, L. Schoevaerds, K. Willekens, P. Stalmans, E. Lankenau, H. Schulz-Hildebrandt, D. Reynaerts, E. Vander Poorten and G. Hüttmann
Combined Force and Distance Sensing for Robot-Assisted Vitreo-Retinal Surgery

16:00- 16:45 Poster session 2 + Coffee break

F. Visentin, B. M. Maris and P. Fiorini, Breast Tissue Parameter Estimation Using Finite Element Analysis

D. Naftalovich, D. Dall'Alba, G. De Rossi, P. Fiorini and J. Burdick, Foot pedal interface supplement for intra-operative camera control during microsurgery using the da Vinci Research Kit

M. Del Pistoia, M. Ciantelli, R. T. Scaramuzzo, C. Tuoni, D. Panizza, I. Baldoli, S. Tognarelli, C. Laschi, F. Vangi, E. Sigali, P. Ghirri, A. Menciassi and A. Cuttano, A multidisciplinary medical-engineering teamwork for high fidelity simulation in Neonatology

M. De Piccoli and P. Fiorini, A Shape Similarity Metric for Brain Fibers Classification

Aida Cavallo, Margherita Brancadoro, Selene Tognarelli and Arianna Menciassi, Soft-magnetic retractor for Minimally Invasive Surgery

B. Rosa, Simultaneous hand-eye registration and instrument tracking initialization for continuum robots

M. Ourak, G. Borghesan, L. Esteveny, S. Hecker, T. Probst, A. Chhatkuli, K. K. Maninis, E. Lankenau, H. Schulz-Hildebrandt, D. Reynaerts and E. B. Vander Poorten, Toward Global Calibration of a Robot-Assisted Vitreo-Retinal Surgery based on OCT C-Scan Image Registration

G. Dwyer, J. Byard, F. Vasconcelos, T. Vercauteren, S. Ourselin and D. Stoyanov, Robot Assisted Needle Control and Visualisation

S. Wang, A. Zar, R. Gandecha, D. Singh, J. Housden and K. Rhode, Towards the use of a robotic 3-D trans-esophageal ultrasound system for monitoring cardiac interventions: study of the workflow

T. Vandebroek, M. Ourak, C. Gruijthuijsen, L. Esteveny, A. Javaux, C. Pimsamut, D. Reynaerts, S. Ourselin, D. Stoyanov, T. Vercauteren, J. Deprest and E. Vander Poorten, Rendering Flexible Endoscopy Manageable through In-Hand Automation

C. D'Ettorre, M. Janatka, F. Vasconcelos, E. De Momi and D. Stoyanov, Towards automatic needle grasping for robotic surgical suturing

Y. T. Creamy Lam, Y. Noh, S. Luo, S. Han, M. Howard and K. Rhode, Modular tactile sensing array for localising a tumor for palpation instruments

16:45-17:30

CRAS Evaluation & Award

17:30-18:30

CRAS future and strategy + Open Discussions

18:30

End of workshop

Keynote speech

Guang-Zhong Yang, Professor, Hamlyn Centre for Robotic Surgery, Imperial College London

Title: Human Robot Symbiosis



Professor Guang-Zhong Yang is director and co-founder of the Hamlyn Centre for Robotic Surgery. Professor Yang is also the Chairman of the UK-RAS Network (<http://ukras.org>). The mission of the UK-RAS Network is to provide academic leadership in RAS, expand collaboration with industry and integrate and coordinate activities of the EPSRC funded RAS capital facilities, Centres for Doctoral Training (CDTs) and partner universities across the UK. Professor Yang's main research interests are in medical imaging, sensing and robotics. He is a Fellow of the Royal Academy of Engineering, fellow of IEEE, IET, AIMBE, IAMBE, MICCAI, CGI and a recipient of the Royal Society Research Merit Award and listed in The Times Eureka 'Top 100' in British Science. Professor Yang is

the founding editor of Science Robotics (<http://robotics.sciencemag.org/>) – a journal of the Science family dedicated to the latest advances in robotics and how it enables or underpins new scientific discoveries. He was awarded a CBE in the Queen's 2017 New Year Honour for his contribution to biomedical engineering.

Keynote speech

Sarthak Misra, Assistant professor, Surgical Robotics Laboratory, University of Twente, Netherlands

Title: Tracking and Control of Tendon-Driven and Magnetically-Actuated Instruments



Sarthak Misra joined the University of Twente (UT) in 2009. He is currently an Associate Professor in the Department of Biomechanical Engineering within the Faculty of Engineering Technology. He directs the Surgical Robotics Laboratory, and is affiliated with MIRA - Institute for Biomedical Technology and Technical Medicine. He is also affiliated with the Department of Biomedical Engineering, University of Groningen and University Medical Center Groningen (UMCG). Sarthak obtained his doctoral degree in the Department of Mechanical Engineering at the Johns Hopkins University, Baltimore, USA. Prior to commencing his studies at Johns Hopkins, he worked for three years as a dynamics and controls analyst at MacDonald Dettwiler and Associates on the International Space Station Program. Sarthak received his Master of

Engineering degree in Mechanical Engineering from McGill University, Montreal, Canada. He is the recipient of the European Research Council (ERC) Starting grant, Netherlands Organization for Scientific Research (NWO) VENI and VIDI awards, Link Foundation fellowship, McGill Major fellowship, and NASA Space Flight Awareness award. He is the co-chair of the IEEE Robotics and Automation Society Technical Committee on Surgical Robotics, and area co-chair of the IFAC Technical Committee on Biological and Medical Systems. Sarthak's broad research interests are primarily in the area of applied mechanics at both macro and micro scales. He is interested in the modeling and control of electro-mechanical systems with applications to medical robotics.

Keynote speech

Jocelyne Troccaz, CNRS Research director, TIMC Laboratory, University of Grenoble-Alpes, France

Title: Recent advances in Computer Assisted Medical Interventions (CAMI LabEx activities)



Jocelyne Troccaz received a Ph.D. in Computer Science from the “Institut National Polytechnique de Grenoble” in 1986 and has been a teaching assistant from 1984 to 1988 in the “University Grenoble Alpes”. She is a CNRS researcher since 1988 and holds a position of Research Director since 1998.

Until 1990, her activity was in the field of automatic robot programming for industrial and spatial robotics. She moved to Medical Robotics in 1990. Her research activity in the TIMC laboratory is about medical robotics and medical imaging. She is also or has been responsible for different clinical research projects (urology, radiotherapy, cardiac surgery, orthopedics, etc.) in collaboration with Grenoble University Hospital and La Pitié Salpêtrière Paris Hospital. Therefore, a major part of her activity is about image-guided robotics and more generally image-guided diagnostic or therapeutic systems.

She is fellow member of the MICCAI society (2010) and senior member of IEEE. In 2014, she received the “French Academy of Surgery” award and was elected as a member of the “French Academy of Surgery”. In 2015, she received the “Silver Medal” from CNRS. In 2016, she was nominated to receive the highest French decoration (Légion d’Honneur).

From 1996 to 2013, she has been Director of the « Computer Assisted Medical Interventions » research group (about 40 people) of the TIMC laboratory. From 2006 to 2015, she was the Deputy Director of the laboratory (about 250 people). She coordinates the French Medical Robotic Network and the French Research Network about Computer Assisted Medical Interventions.

Sessions 1 & 2

Novel Robotic Hardware

STRAS: A Robotic Platform for Intraluminal Surgery successfully tested In-vivo

L. Zorn¹, F. Nageotte¹, P. Zanne¹, M. de Mathelin¹

¹ICube laboratory, University of Strasbourg, CNRS, France (Nageotte@unistra.fr)

INTRODUCTION*

Intraluminal surgery is an attracting technique for surgical procedures in the digestive tract since it avoids any visible scar for the patient. However, it is a very demanding technique for surgeons when realized with manual instruments. On the one hand conventional instruments used with standard endoscopes lack distal mobilities. In the other hand, surgical platforms such as the Anubiscope® from Karl Storz, are difficult to control from the proximal side and require at least two skilled physicians who must collaborate in a very limited workspace [1].

As a consequence only very skilled surgeons and endoscopists are currently able to perform advanced treatments, such as Endoscopic Submucosal Dissection (ESD) with the available manual instruments. This unfortunately limits the availability of interesting treatments for many patients.

In this context, robotics could provide solutions, since teleoperation can allow a single user to control many Degrees of Freedom (DoFs). However, MASTER [2] from the Nanyang University of Singapore is, at the current time, the only surgical flexible robotic platform having reached the level of clinical trials. In this article we present the concepts and the preclinical use of the second version of a modular robotic system called STRAS, which solves manipulation difficulties of intraluminal procedures.

MATERIALS AND METHODS

A. STRAS (v2) robotic system

The ICube laboratory has developed a robotic system, based on the Anubiscope®, a totally flexible platform from Karl Storz. The robot is called STRAS (Single-port and Transluminal Robotic Assistant for Surgeons) and the second version (v2) consists of a slave robot and a specific master console. The slave system provides two instruments, each having 3 independent DoFs (bending, translation and rotation) and with two possible kinds of effectors (grasper / electrical knife). The instruments can be inserted inside the channels of an endoscope equipped with a distal passive system used for deviating the instruments from its main axis, thus providing triangulation. The endoscope can be bended along two orthogonal axes, bringing with him the instruments in the channels, similar to an active overtube. All motions are provided through elementary motorized modules (see Fig.1): (a) An endoscope

module controlling distal bending of the endoscope, (b) Translation / Rotation modules ensuring translation and rotation of the instruments in the channels of the endoscope, (c) instrument modules providing distal bending and graspers actuation of the instruments, and (d) a cradle, which supports both endoscope and instruments and provide them with forward / backward motion and rotation. All modules are mounted onto a mobile cart (e). Additional details can be found in [3].

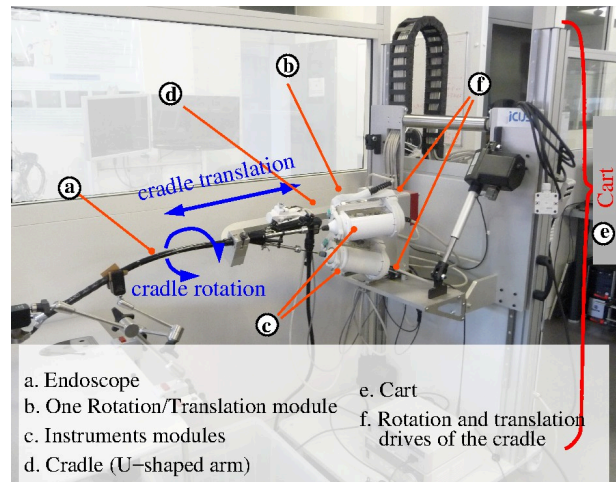


Fig. 1 View of the modular slave system

All 10 DoFs can be teleoperated by using two master interfaces, which have been specifically developed for the slave system (see Fig. 2). These interfaces are passive and provide a kinematic chain similar to that of the instruments. Especially, the kinematic singularities are identical between master and slave. Therefore, the user moves the master handle as if he held the tip of the instrument. This consequently provides very intuitive position control of the instruments. The endoscope and cradle motions can also be controlled by the surgeon in on / off modes by using two switches located on the top of the handles. Moreover, the endoscope module is equipped with an on-board joystick (see Fig. 2), which allows controlling the motorized bendings while manually holding the endoscope.

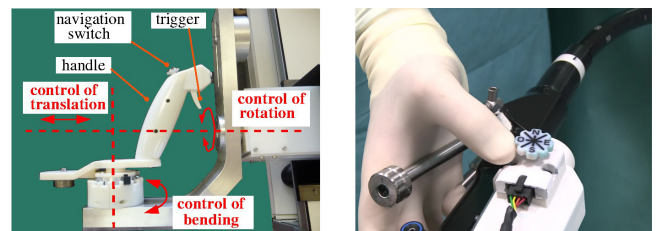


Fig. 2 Means for controlling STRAS. Left: one of the master interface and its controlled DoFs. Right: The on-board joystick attached to the endoscope module

* This work was supported by French state funds managed by the ANR within the Investissements d'Avenir program under the ANR-11-LABX-0004 (Labex CAMI). Authors thank IRCAD (Strasbourg, France) and Karl Storz (Tuttlingen, Germany) for their valuable help.

B. Use of STRAS

The modularity of the slave system allows to first perform the navigation of the endoscope manually, before attaching the different components onto the cart for the surgical procedure. The typical workflow to use STRAS v2 for intraluminal procedures can be described as follows.

1. System set-up and calibration: The master console and the slave cart are prepositioned in the operating room. They are plugged and powered on. The "STRAS" application is launched at the master console and the robot performs self-calibration.

2. Insertion of endoscope: The endoscope is navigated manually towards the operating site, by using the on-board joystick to orientate the head of the endoscope and with the visual feedback provided by the endoscopic camera. The endoscope is thus brought to the operating site.

3. Securing endoscope onto the cradle: The cart is approached, and its position is adjusted to allow clamping the endoscope's handle. This stage requires the intervention of an assistant.

4. Insertion of instruments: The flexible shafts of the instruments are manually inserted inside the channels and the motors' housings are installed onto the cart.

5. Teleoperation: The surgeon has control of all DoFs. If necessary, an assistant can use manual instruments inserted inside the central channel of the endoscope. The modularity of the slave system allows to retrieve and exchange instruments during the procedures.

C. Preclinical trials

The objectives of the preclinical trials were to show the feasibility of surgery with STRAS, and to compare the performance of use with respect to conventional endoscopes and with respect to the manual Anubiscope platform. For this purpose, a pilot surgeon (A. Legner, fellow at IHU Strasbourg, novice in flexible endoscopy) was recruited to perform ESD in the colon of pigs.

STRAS was used with a grasper as left effector and an electric knife as right effector. The following medical protocol was used:

1. Marking of the lesion contours using the electrical instrument.
2. Injection of a glycerol solution in the submucosa using an injection needle introduced in the central channel of the endoscope. The needle is guided from the master console but the insertion in the tissue is performed manually.
3. Dissection of the submucosa. This is the main surgical task realized in teleoperation.
4. Retrieval of the specimen.

RESULTS

12 ESD could be successfully realized with STRAS. Durations of the procedures ranged from 17 min. to 147 min. depending on the configuration and the size of the lesion.

System	# of skilled users	# of perforations	Dissection speed (mm ² /min)
Conventional endoscope	2	8/16	35.9±18.9
Manual Anubiscope	2	0/9	24.9±5.0
STRAS	1	1/12	64.4±34.9

Table 1: Comparisons of ESD results for the uses of conventional endoscopes, the manual Anubiscope and STRAS

For comparison purposes, we refer to [4], where ESD were performed in similar conditions 1) by an expert endoscopist with a conventional endoscope, and 2) by a fellow with the Anubiscope manual platform.

Table 1 shows comparisons of the uses of the three systems. Statistical analyses using Fisher exact test and Welch's t-test show that the perforation rate is significantly lower with STRAS than with conventional instruments ($p = 0.04$), and slightly higher (but not significantly, $p \sim 1$) than with the Anubiscope. Dissection velocity is significantly higher with STRAS than with the Anubiscope ($p=0.01$) and higher (not significantly, $p=0.06$) than with conventional instruments.

CONCLUSION AND DISCUSSION

The feasibility of using STRAS for ESD has been demonstrated. The comparison of dissection times and perforation rates with manual systems shows a real interest of the robotic system. STRAS has also important assets with respect to MASTER. All DoFs are teleoperated, allowing a single skilled user to perform the complete surgical task. Moreover, the instruments can be retrieved during the procedure without moving the endoscope, thus avoiding the need of an overtube. For reaching clinical transfer, some efforts have still to be carried out in order to make the system totally compliant with the sterility constraints of the operating room.

REFERENCES

- [1] Perretta, S. et al. "The ANUBISCOPE flexible platform ready for prime time: description of the first clinical case". *Surgical endoscopy*, 27: 2630.
- [2] Phee, S. et al. "Robot-assisted endoscopic submucosal dissection is effective in treating patients with early-stage gastric neoplasia," *Clinical Gastroenterology and Hepatology*, vol. 10, no. 10, pp. 1117–1121, October 2012.
- [3] Zorn, L. et al. "A Novel Telemanipulated Robotic Assistant for Surgical Endoscopy: Preclinical Application to ESD". *IEEE TBME*, 2017.
- [4] Diana, M et al. "Endoluminal surgical triangulation: overcoming challenges of colonic endoscopic submucosal dissections using a novel flexible endoscopic surgical platform: feasibility study in a porcine model". *Surgical Endoscopy*, 27:4130-4135.

A smart handheld device for over-puncture prevention in peripheral intravenous catheterization

Zhuoqi Cheng¹, Brian Davies^{1,2}, Darwin Caldwell¹, Leonardo S. Mattos¹

¹*Istituto Italiano di Tecnologia, Genova, Italy,*

²*Imperial College London, London, U.K.*

zhuoqi.cheng@iit.it

INTRODUCTION

Peripheral IntraVenous Catheterization (PIVC) is a very common procedure for medicinal infusion and blood sampling, with over 2.7 million PIVCs take place in the United States daily. Unfortunately, this operation suffers from very low success rates, especially for children younger than 2 years old, because their veins are very small and fragile. The overall success rate is reported to be around 60% [1].

One of the most difficult tasks during pediatric PIVC is to detect venipuncture and immediately stop the insertion. The traditional unassisted PIVC relies on the practitioner's haptic sensing of a small decrease in insertion force to detect the venipuncture. But this force signal was studied and found to be noisy [2]. Also, it is difficult for the practitioner to stop pushing the catheter forwards immediately due to physiological limitations and motion inertia. Consequently, over-puncture is a common reason for failure in pediatric PIVC.

Whilst several fully autonomous robots [2, 3] have been proposed for improving the PIVC procedure, handheld devices which can deal with specific tasks in PIVC are better at overcoming concerns about safety, cost and device complexity. This has motivated our previous design: SAID [4]. In this study, instead of using a motor to control the catheter insertion, a latch based disengage mechanism is integrated into the new device to provide a security guarantee by stopping the catheter advancement immediately after venipuncture. Here we show this is feasible and effective in preventing over-puncture, indicating that a simple yet smart handheld device can potentially have significant impact in these difficult procedures.

DEVICE DESIGN

Fig. 1(A) shows the configuration of the device, which integrates a venipuncture detection system based on an electrical impedance sensing (the same as [4, 5]) and a latch disengage mechanism. In order to measure the impedance of the contacting tissue at the needle tip, a Concentric Electrode Needle, CEN, is used. A central controller reads the electrical impedance measurement from an electrical impedance converter (AD5933). If the impedance measurement is found within the range of blood ($\approx 1.8 \text{ k}\Omega$), the controller commands the actuator to open the latch immediately and lights up an LED on the holding case. The Safe Travel Distance, STD, which represents the distance that the needle can travel within

the vein was studied and found to be 1.6 mm [4]. Assuming the maximum penetration-event speed is 3 mm/s [2], the response time of the device should be less than $1.6/3 = 530 \text{ ms}$. After the latch is open, there are 2 axial forces acting on the shaft that carries the catheter if the casing is still moved forwards. One is the tissue-catheter friction f_t which is about 1 N [3]. The other is the friction between the casing and the shaft f_d . To ensure the catheter is not moved by the casing after the latch is open, f_d should be smaller than f_t .

As shown in Fig. 1(B), the device is comprised of a carrier block, a main body and a pair of casings. The casings are attached to the main body for user grasping. Two parallel shafts are used to connect the carrier block to the main body, and allow it to slide only along the insertion direction. When the latch is closed, it locks the shaft collar on Shaft 2 so that the carrier block is fixed to the main body. The carrier block can slide backwards when the latch is open. We set 10 mm as the reserved distance d_r denoting the distance that allows the user to push the device forwards with the catheter fixed in placed after the disengage mechanism is activated. In order to have fast actuation and simple control, a solenoid (8M100262, Mecalectro) is selected as the actuator which can satisfy the design requirement of the disengage mechanism: provide $>1.75 \text{ N}$ and 2.3 mm stroke to open the latch.

In addition, an adaptor is designed for connecting the cannula and the CEN, and locking them to the carrier block. The casings are made as a 30 mm diameter cylinder with the LED placed on top. A prototype was made as shown in Figure. 1(C). In addition, this device can be easily covered by a sterile drape for clinical use.

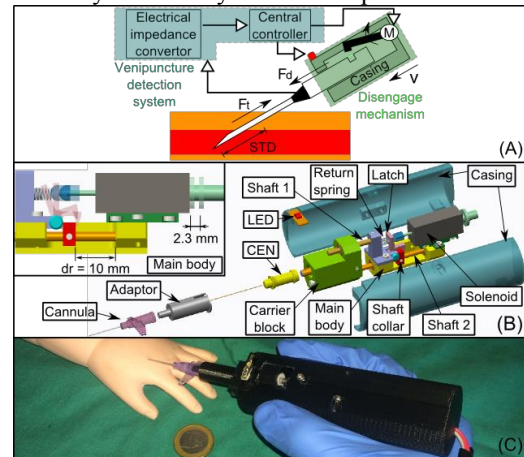


Figure. 1. (A) system configuration of the device; (B) 3D modeling of the device; and (C) the prototype of the device.

DEVICE CHARACTERIZATION

Response time: Activation of the disengage mechanism should be fast after the catheter enters the vein. Here, the response time of the mechanism was measured. The device was fixed on a platform and a laser range sensor was used to measure the displacement of the solenoid plunger. Then the solenoid was activated and the displacement of the plunger was recorded. The measurement was repeated 5 times and the time from the solenoid open status to the close status, representing the mechanical response time of the latch, was extracted. An average of 69.6 ms was found. Considering an extra 21.6 ms for the electrical impedance detection [4, 5], the total response time for the whole system is 91.2 ms, which is comparatively small given the required response time 530 ms.

Sliding friction: The friction f_d between the main body and the shaft within the reserved distance d_r was measured. For this, an ATI Nano17 force sensor was connected between the device's casing and a linear motion stage. The device's latch was open and the carrier block was fixed to a stationary platform, allowing the casing to move axially when driven by the motion stage. Various tilt angles (15° , 30° , 45° , 60° , 75° and 90°) were tested to evaluate potential effects of gravity. The motion stage drove the casing to move 10 mm (d_r) along the axial direction in a constant speed of 1mm/s. The friction f_d was found to be 0.19 N in average with $STD = 0.05$ N among different insertion angles. This value is much smaller than f_t (1 N) and thus satisfies the design requirements.

PRE-CLINICAL ASSESSMENT OF THE DEVICE

A series of experiments were designed and conducted to assess the proposed device in a realistic pediatric PIVC scenario with a baby arm phantom (M95, Kyoto Kagaku Co.). A 0.5% saline solution which has similar electrical impedance characteristic to real blood was circulated inside the phantom by a pump. A VeinFinder (BVF-260, Bestman Instrument Ltd., China) was used to offer trans-illumination and increase the contrast of the vein with its surrounding material so that the chances of missing the vein during insertion could be minimized. Five subjects who had no previous experience on PIVC were invited to participate to the experiment, which started with a 5 minutes video tutorial providing fundamental knowledge of PIVC. Then the subjects were asked to read an introduction document about the device. After that, each subject performed 10 attempts to catheterize the baby arm phantom with the device. During the catheterization operation, the subjects needed to pick up the device, find a proper vein site, and insert the catheter with an appropriate insertion angle. After the device detected the venous entry and activated the disengage mechanism, the subject was required to lower the insertion angle and advanced the catheter 1-2 mm. This is because the venipuncture detection occurs when the needle tip enters the vein but there is a small distance between the needle tip and the cannula tip. Subsequently, the subject pushed the cannula off the CEN and into the vein and then removed the device.

RESULTS

Catheterization success was established by observing saline solution flowing out through the cannula. If that did not happen, the trial was considered a failure, and the most likely reason for that was assessed.

In total, 50 trials were collected, and an overall success rate of 78% was achieved. Also, 2 out of 5 subjects (40%) achieved successful insertions in their first attempts. For all trials, the device could successfully detect venipuncture and activate the disengage mechanism. The 11 failed insertions were all caused by the subsequent advancement needed after venipuncture: 3 insertions (6%) were too deep and punctured through the vein, and the other 8 insertions (16%) were too shallow so the catheter did not enter the vein.

DISCUSSION AND CONCLUSION

This study presented a new handheld smart device integrating a latch-based disengage mechanism and an electrical impedance venipuncture detection system to enhance the insertion depth control during PIVC. This design can also be applied in related tasks such as needle biopsies or other needle-based treatments.

The characterization results demonstrate the device has fast response and low sliding friction, satisfying its design requirements to efficiently stop the catheter insertion immediately after the venipuncture irrespective of the user's unintentional hand advance.

Also, pre-clinical assessment of the device was conducted with 5 naïve subjects. A considerably high PIVC success rate of 78% was found. For all trials, the device could successfully detect venous entry and activate the disengage mechanism. The failed catheterizations were assessed as caused by the subsequent manual advancement needed for compensating the needle-cannula gap after the venipuncture. Future work will improve the mechanism design to automatically advance the catheter and eliminate this problematic need.

REFERENCES

- [1] Myers, Lucas A., Grace M. Arteaga, Logan J. Kolb, Christine M. Lohse, and Christopher S. Russi. "Prehospital peripheral intravenous vascular access success rates in children." *Prehospital Emergency Care*; 2013.
- [2] Reuben Brewer. "Improving peripheral iv catheterization through robotics: From simple assistive devices to a fully-autonomous system." Thesis (Ph.D.), Stanford University; 2015.
- [3] Zivanovic Aleksandar, Brian Davies. "A robotic system for blood sampling." *IEEE Transactions on Information Technology in Biomedicine*; 2000.
- [4] Zhuoqi Cheng, Brian Davies, Darwin Caldwell, Leonardo Mattos. "SAID: a Semi-Autonomous Intravenous access Device for pediatric PIVC." Hamlyn symposium; 2017.
- [5] Zhuoqi Cheng, Brian Davies, Darwin Caldwell, Leonardo S. Mattos. "A Novel Venipuncture Detection System Based on Electrical Impedance Measurement." *CRAS*; 2016.

Design of a Robotic Microsurgical Forceps for Transoral Laser Microsurgery

M. Chauhan, N. Deshpande, and L. S. Mattos

Department of Advanced Robotics, Istituto Italiano di Tecnologia, Genova, Italy
nikhil.deshpande@iit.it

INTRODUCTION

Transoral Laser Microsurgery (TLM) deals with the non-invasive treatment of malignancies in the laryngeal region. A CO₂ surgical laser serves as the resection tool while microsurgical forceps are used for tissue manipulation and tensioning. The configuration, dimensions, and constraints of the setup are seen in Fig. 1 and discussed in [1]. Traditionally, the forceps are manually handled for manipulating (grasping, stretching, orienting, removing) tissues and operated through the same small space as the laser beam itself. The limitations of the tool designs, i.e., single degree-of-freedom (DOF, open/close), long, thin, rigid shaft (length~200mm, thickness~2-2.5mm), and pre-curved design, undoubtedly makes their usage cumbersome, non-ergonomic and subject to hand tremors. The lack of any intraoperative tactile feedback further aggravates the functional challenges for the surgeons in accessing and treating different parts of the vocal folds [1].

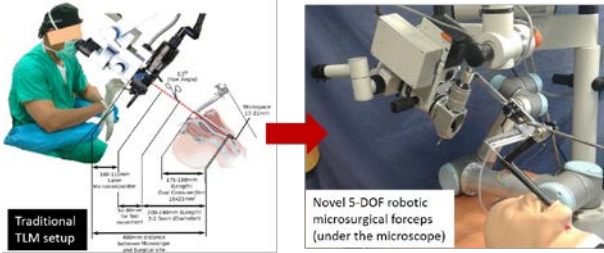


Figure 1. The proposed novel 5-DOF robotic forceps

For best surgical results, it would be beneficial to improve the functionality and the reach of these tools by adding the capability of robotic control with additional DOFs and force feedback. The enhanced reachability would enable accessibility at the surgical site for proper grasping of the tissue. This article extends the benefits of robot-assisted technologies to TLM and presents the design and development of a novel, 5-DOF, robotic microsurgical forceps with capability of tissue gripping force feedback. The device provides a more comfortable tool-handling interface with gesture scaling capabilities, improved accuracy, and enhanced surgical site perception. Preliminary trials with expert surgeons resulted in positive evaluation of the device.

MATERIALS AND METHODS

A. Motorized Microsurgical Forceps (MMF): The constraints of the TLM procedure served as the design specifications for the device [1]. Based on the specifications, a motorized microsurgical forceps was designed, having two DOFs, composed of three modules:

(1) Tool shaft: A modified version of the traditional microsurgical tool shaft (outer shaft ϕ 2mm; inner translating wire, *itw* ϕ 1mm), this module has an adaptation introduced at the proximal end for its connection to the *tool shaft holder* module. The adaptation, made up of short hollow tube with M3 internal threading, acts as a docking interface (DI) (Refer Fig. 2). The translation of the *itw* (\approx 3mm) provides the open-close DOF of the tool jaws.

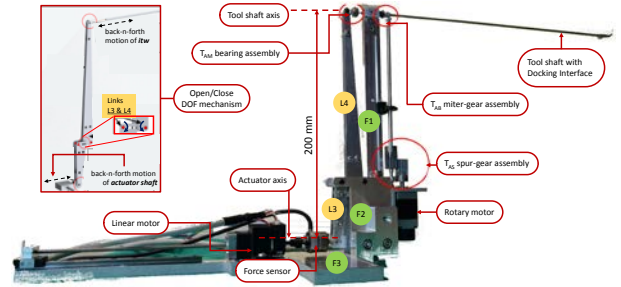


Figure 2. The 2-DOF MMF device prototype

(2) Tool shaft holder (TH): This module connects the *tool shaft* with *tool actuation mechanism* (TM) module. The design comprises of three sub-frames F1, F2, and F3 (Refer Fig. 2). The *tool shaft* attaches to F1 keeping an offset of 200mm from the actuator axis (TM module), and the cross-section of F1 is designed to be 5mm.

(3) Tool actuation mechanism (TM): This module is responsible for introducing the two motorized DOFs for the device and is made up of two components:

(i) Open/Close DOF mechanism: is responsible for the linear translation of the *itw* through a five-linkage mechanism, supported by the frames of the TH (Refer Fig. 2). An inverse relationship (between links L3 & L4) transmits the motion from the actuator to the tool shaft *itw*. A linear actuator (Nanotec L2818 with 30N force feed) drives the open/close. Additionally, a force sensor (ATI Nano17) is located with its measurement axis coincident with the actuator axis allowing the sensing of the tissue gripping force.

(ii) Rotational DOF: The tool shaft rotation is implemented through the coordinated action of three components: (i) Spur gear assembly (T_{AS}); (ii) Miter Gear assembly (T_{AB}); and (iii) Rotation adaptation in actuation mechanism (T_{AM}) (Refer Fig. 2). A rotary actuator (Nanotec SC2018 with 1.8 N-cm torque) drives the T_{AB} through the T_{AS} . T_{AB} , with an outer ϕ of 8 mm, converts the rotation of the T_{AS} to the axial rotation required for the *tool shaft*. The T_{AM} includes a small bearing, which allows the simultaneous rotation of the tool shaft and the open/close of the MMF jaws.

B. Integration with robotic manipulator & teleoperation master: The MMF is integrated with the UR5 6-DOF serial manipulator for precise global positioning of the forceps at the surgical site. Combined with the rotation and open/close DOFs of the forceps device, this results in a 5-DOF robotic slave device (3-DOF UR5 + 1-DOF open/close + 1-DOF rotation). The master teleoperation interface is the Force Dimension Omega.7. The interface is equipped with an active gripper, the 7th DOF, which is used for the gripping force feedback (Refer Fig. 3). The haptic control loop for rendering of the force feedback runs at 500 Hz.

The teleoperation of the integrated 5-DOF robotic forceps is implemented in two parts:

(i) For the Cartesian positioning in 3-DOF, the end-effector velocity of the *Omega.7* is mapped to the joint velocities of the robot through the equation:

$$\dot{q}_r = J^{-1} \cdot v_h \cdot \gamma$$

where, \dot{q}_r is the robot joint velocity vector, J^{-1} is the inverse robot Jacobian and v_h is the 3-DOF end-effector velocity of teleoperation master. The scaling factor ($\gamma = 0.2$) is suitably tuned for gesture scaling and accuracy.

(ii) The rotation and open/close DOFs of the device are implemented with position control. The *yaw*-DOF of the master commands the rotation DOF of the MMF, while the gripper DOF of the master commands its open/close DOF. The same master gripper DOF is used to render the tissue gripping force measured by the ATI Nano 17 through the MMF jaws. The following equation is used:

$$\begin{bmatrix} q_{mmf}^{rot} \\ q_{mmf}^{grip} \\ f_{grip} \end{bmatrix} = \begin{bmatrix} \alpha_1 & 0 & 0 \\ 0 & \alpha_2 & 0 \\ 0 & 0 & \alpha_3 \end{bmatrix} \begin{bmatrix} q_h^{yaw} \\ q_h^{grip} \\ f_{sensor} \end{bmatrix}$$

q is the angular position and f is the force. The mapping constants $\alpha_1 = 2$; $\alpha_2 = 3$; $\alpha_3 = 4$ are arrived at empirically.

C. For performance analysis, user trials were conducted with 10 non-medical subjects (avg. age=28.2 years; 8 Males, 2 Females). The trial involved a pick-n-place teleoperation of 4 different shapes (triangle, rectangle, semi-circle, and circular ring), lifting from one cavity and placing in another. The shapes were made with phantom tissue using bi-component polyurethane elastomer. Preliminary trials were also conducted with expert surgeons using ex-vivo pig larynxes.

RESULTS

A. Positioning Accuracy: The integrated system was tested by moving the master interface in free-space over a period of 120 seconds, and recording the position of the slave device. The overall error in the 3-axis positioning of the slave device was **0.3901 mm** (RMSE) with a standard deviation of **0.3829 mm**, showing that the slave device was able to track the gestures of the master interface very well.

B. Gripping Force Feedback: Fig. 4 shows the difference in the object gripping forces. The average tissue gripping force applied when the force feedback rendering is on is statistically significantly less than when the feedback

rendering is turned off, according to Student's t-test ($p=0.0486$).

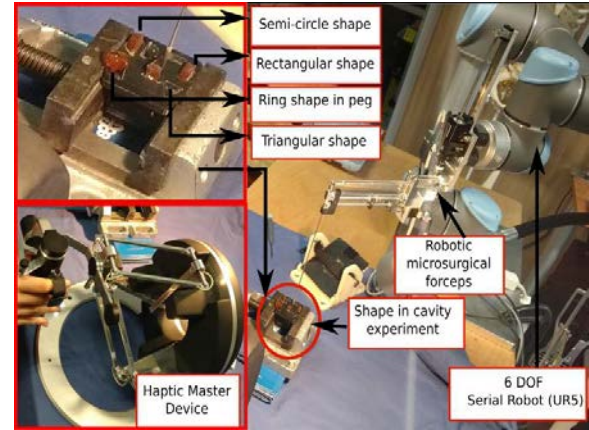


Figure 3. The integrated 5-DOF device with master and experimental setup.

C. Preliminary trials with surgeons: Informal feedback was received from the surgeons: (i) strong appreciation of tool-tip rotation helping the surgeons to reach different areas of the larynx with ease along with the grip-n-turn of the vocal tissue for improved exposure. (ii) strong appreciation of force feedback for regulating forces applied on tissues. (iii) device partially occluded the vision through surgical microscope implying the need for further reduction in size as well as some required training in controlling the new device with a teleoperation master.

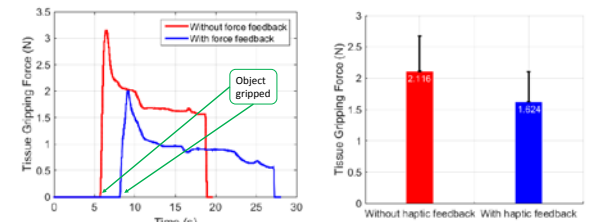


Figure 4. Gripping force variation without & with feedback

CONCLUSION AND DISCUSSION

This paper presented a novel design of a 5-DOF robotic microsurgeon forceps tool for intraoperative use in TLM, integrated with a teleoperation haptic master and a force sensor for tissue gripping force feedback.

The complete design & functional analysis and force feedback performance are being investigated for a journal paper. In future works, the gripping force shall be further investigated for isolating different components like stretching, twisting, etc. At this stage, the force sensor value is low-pass filtered to suppress the noise from the moving mechanisms in the system. As a result of this, the limits of stability and transparency of the robotic teleoperation shall be established for intuitive behaviour.

REFERENCES

- [1] Chauhan M. et al. "Design and control of a novel robotic microsurgeon forceps for Transoral Laser

Microsurgery." Proc. IEEE AIM 2017, July 3-7,
2017, Munich, Germany.

Tactile tool for tissue palpation in colonoscopy

F. Bianchi, E. Trallori, D. Camboni, C. M. Oddo, A. Mencassi, G. Ciuti, P. Dario

The Biorobotics Institute, Sant'Anna School of Advanced Studies, Pisa, Italy.

federico.bianchi@santannapisa.it

INTRODUCTION

Colorectal cancer (CRC) is a major medical threat with more than 600 thousand people dead annually worldwide and 215 thousand death in Europe [1]. Moreover, it is the second cause of cancer death in the United States [2], second most common cancer for European women and third for European men [1]. Early detection of CRC is a key-factor to survival and the survival rate at 5 years decreases with the progress of the pathology stage. For this reason, regular screening is strongly recommended for people over 50 [3]. In recent years, new imaging methods have been adopted, supporting conventional white light (WL) inspection in the clinical practice. These imaging-based methods use specific wavelengths that are strongly absorbed by haemoglobin to view blood vessels [4]. These methods have been very successful in current clinical practice; however, many comparative studies have demonstrated that these methods are not more efficient than the WL (attested around 70%), as reported by N. Gilani *et al.* [5]. Many research teams have focused their studies on developing tactile-based diagnostic methods to improve detection sensitivity of tumour tissue. Force and tactile feedback are commonly used in the medical practice. Manual palpation helps the clinician to identify abnormalities in part of body manually accessible, such as: breast, thyroid, abdomen, rectum and prostate. Instead, other parts of the body, not easily accessible, are examined through echography diagnostic techniques, based on the changes of the reflection of ultrasound waves according to the different density (acoustical impedance) of the body tissues. In this paper, the authors present an innovative tool, equipped with three optical fibres having each one a fibre Bragg grating sensor (FBG), able to be inserted in a colonoscopic standard operating channel with the aim to help clinicians with remote palpation of the inner colonic wall.

MATERIALS AND METHODS

A. Clinical Evidences

Generally, cancerous tissue is more rigid than normal tissue, so evaluation of tissue elasticity can be helpful for the clinician to establish a more accurate diagnosis. Kawano *et al.* [6] measured the elastic modulus (EM) of colorectal tissue in *ex-vivo* conditions. Results of this study demonstrated how the EM of colorectal cancer tissue is significantly higher than the normal colorectal tissue (0.936 kPa for normal tissue and 7.51 kPa for cancer tissue), and it progressively increases in accordance with the cancer pathological stage.

B. Fibre Bragg Gratings Force Sensors

Following a technology analysis, optical fibre force sensors were chosen for their intrinsic advantages, *i.e.*: *i)* chemically inert *ii)* small size; *iii)* easy to be miniaturized and produced at significant low cost; *iv)* no electromagnetic interference (EMI); and *v)* MRI compatibility. Moreover, since optical fibre sensors employ reflection change of light signal, they are intrinsically safe in terms of electrical short circuit, current leakage, and signal interference with surgical equipment.

C. Tool Design

Three FBG sensors [Draw Tower Grating (DTG®)'s] in reduced cladding fibres, selected for its high sensitivity] were embedded longitudinally along the instrument body with 120° intervals; each one is placed in the centre of a lightened part closest as possible to the instrument tip in order to maximize the stress along a preferential direction, as shown in Figure. 1. This design allows to determine the magnitude and direction of three orthogonal force components (F_x , F_y and F_z) and to estimate the force along the tool axis.

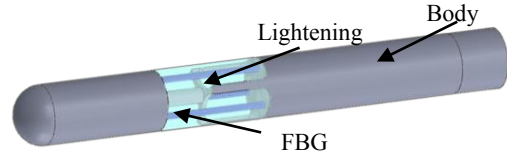


Figure. 1. CAD model of the 3-DOFs force sensing.

The body of the tool will be developed with a material with an intrinsic elasticity comparable with the rigidity of the optical fiber; so, in the simulation phase it was chosen the Aluminum 7075 as the material for the body and the external diameter and total length were chosen to fit into the operative channel of standard endoscopes. Three optical fibres were inserted along the tool axis. To guarantee the integrity of the optical fibers and to optimize the distribution of the stress on them, the optical fibers are embedded in a soft silicone material and enclosed in the lightened part.

D. FEM Simulations

In order to evaluate the outputs of the fibres, the tool has been simulated in different conditions, *i.e.*: *i)* the tissue has been modelled as an isotropic material [6], the tool was fixed on lateral sides; *ii)* the tool is constrained to move along its own axis; *iii)* the force is constant and it is applied along the axis of the tool; *iv)* the points of strain calculation are equidistant, 0.1mm from each other, in central position relative to the fibre from the start of the sensitive area; *v)* the contact angle (pitch angle) between the normal to the tissue plane and the plane of the tissue

varies between 0° to 80° ; and v_i) the roll angle of the fibres varies between 0° to 120° .

RESULTS

The shift in Bragg wavelength of the FBG sensors is linearly dependent on local strain and temperature change:

$$\Delta\lambda_i = k_\varepsilon \varepsilon_i + k_{\Delta T} \Delta T \quad (1)$$

where $\Delta\lambda$ indicate the shift in Bragg wavelength, ε the local strain, ΔT the temperature change, k_ε and $k_{\Delta T}$ strain and temperature coefficients, respectively. In (1) the dependence on ΔT can be deleted by measuring the strain at no load condition and assuming that the temperature fluctuation during the procedure is negligible.

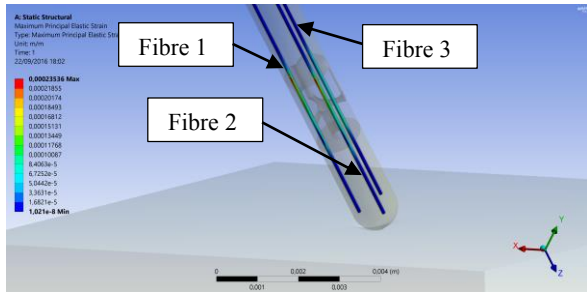


Figure 2. FEM simulation analysis of the normal strain generated along the fibres under 70mN axial force load.

Figure 2 shows the fibres configuration in the tool and the distribution of the strain detected by each fibre described by the following law:

$$\varepsilon_i = \frac{Fd_i}{EI} r \quad (2)$$

where ε is the strain detected by FBG sensor, F the force applied at the tool tip, d the distance between the tool tip and the FBG sensor, E the Young's modulus of the body, I the moment of inertia, and r the distance between the FBG sensor and the neutral axis.

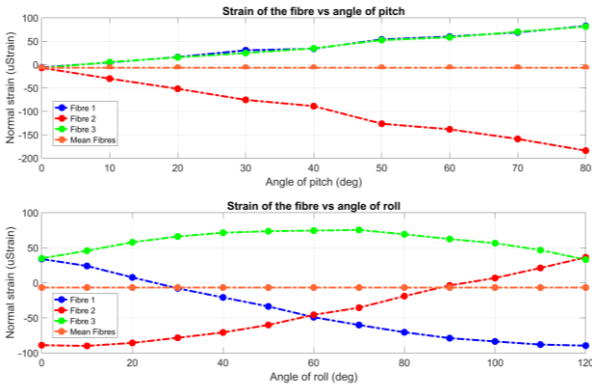


Figure 3. Comparison between the normal strain detected by each fibre and the mean strain under 70mN axial force load.

Figure 3 shows how the mean of normal strain detected by each fibre is constant and independent on roll and pitch angles, as represented with the orange lines:

$$\varepsilon_{mean} = \frac{1}{3} \sum_{i=1}^3 \varepsilon_i \quad (3)$$

Figure 4 reports the calibration curves of the sensor at different angles of pitch (from 0° to 80°).

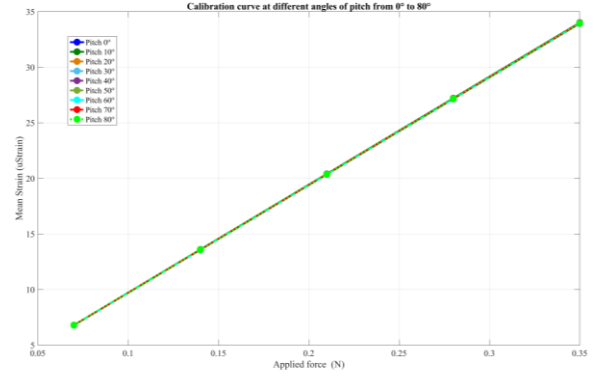


Figure 4. Calibration curve of the tool at different angles of pitch from 0° to 80° at roll angle of 40° .

The force-strain relationship is linear in the range we explored, *i.e.* 70 mN up to 280 mN.

DISCUSSION AND CONCLUSION

This work presents the design of a novel device based on a FBG sensors for palpation of colonic wall during colonoscopy procedures. These simulations demonstrate the capabilities of the tool to measure the contact force. The results obtained will be validated in the next future in extensive experimental session with a dedicated test bench. In future steps, it is envisaged to develop a modular tool, starting from the repetition of the tool presented in this paper, to also evaluate texture properties in active tactile exploration (with unknown sliding velocity) as well as tissue elasticity.

AKNOWLEDGMENTS

The work described in this paper was supported by the European Commission within the framework of EndoVESPA European project - H2020-ICT-24-2015 (GA: 688592). The authors thank all the collaborators of the EndoVESPA EU project (www.endovespa.eu).

REFERENCES

- [1] UEG. Colorectal Cancer (CRC) in Europe. Available: <https://www.ueg.eu/press/crceurope/>
- [2] S. D. Crockett, et al., "Sessile Serrated Adenomas: An Evidence-Based Guide to Management," Clin Gastroenterol Hepatol, vol. 13, pp. 11-26.e1, 2015.
- [3] S. Winawer, et al., "Colorectal cancer screening and surveillance: clinical guidelines and rationale-Update based on new evidence," Gastroenterology, vol. 124, pp. 544-560, 2003.
- [4] T. D. Wang, et al., "Optical biopsy: a new frontier in endoscopic detection and diagnosis," Clin Gastroenterol Hepatol, vol. 2, pp. 744-53, Sep 2004.
- [5] N. Gilani, et al., "Polyp detection rates using magnification with narrow band imaging and white light," World J Gastrointest Endosc, vol. 7, pp. 555-562, 2015.
- [6] S. Kawano, et al., "Assessment of elasticity of colorectal cancer tissue, clinical utility, pathological and phenotypical relevance," Cancer Sci, vol. 106, pp. 1232-9, Sep 2015.

Design of a MEMS Varifocal Mirror for Focusing High-Power Lasers in Minimally Invasive Surgical Procedures

A.A. Geraldes^{1,2}, A. Jacassi¹, P. Fiorini², L.S. Mattos¹

¹*Istituto Italiano di Tecnologia, Italy*

²*University of Verona, Italy*
andre.geraldes@iit.it

INTRODUCTION

Today many surgical interventions make use of laser tools. In otolaryngology, Laser Phonomicrosurgery is the state-of-the-art procedure for treating vocal cord tumors because the precision of laser cutting allows preserving more healthy tissue, while excising the tumor [1]. Additionally, the infrared lasers used in these procedures cauterize small blood vessels while cutting tissue, which reduces bleeding, significantly improving the quality and safety of the procedure.

However, one of the main limitations of laser tools is the laser delivery to the targeted site, since some areas of the head and neck are difficult to be properly exposed for direct visualization. In order to overcome that, flexible fiber delivery systems have been developed, allowing laser tools to be integrated in endoscopic and minimally invasive systems [2]. This has improved the access to the surgical site, expanding the applicability of lasers to all kinds of procedures.

In order to ensure the precision of the cut, it is essential that the laser spot remains focused at the target tissue. This becomes challenging when the target is moving or the surface to be ablated is non-planar. At the same time, adjustable focusing systems based on moving lenses are too large and bulky to be incorporated in fiber laser tools. For this reason, fiber laser systems typically have no focusing optics and require the fiber to be in direct contact with the tissue, which often leads to thermal damage to surrounding tissues and, consequently, reduced surgical quality.

In order to solve this problem, a varifocal mirror could be used. Varifocal mirrors are deformable mirrors, whose focal length can be dynamically controlled, without the need of mechanical displacement. Over the last decade, many MEMS varifocal mirrors have been developed for imaging applications, such as OCT and confocal laser microscopy [3]. Using electrostatic actuation, these mirrors can be made very compact and provide fast actuation. Nevertheless, this approach has never been used with surgical lasers, since the laser damage threshold of the existing mirrors is not compatible with high-power lasers.

In this work, we propose a new MEMS varifocal mirror design for focusing a surgical laser. In order to withstand the high power of the laser, we design the mirror with increased dimensions to provide better heat

dissipation. To achieve large deflection of the mirror and provide high optical power, we propose bending the mirror with hydraulic actuation instead of electrostatic. The next sections present the design and fabrication of such mirror and the preliminary evaluation of the first obtained prototypes.

MATERIALS AND METHODS

Fig. 1 shows a schematic representation of the proposed focusing system using a MEMS varifocal mirror. In this system, the laser delivered by the optical fiber is collimated with a biconvex lens and directed to the varifocal mirror using a fixed mirror. The varifocal mirror consists on a circular reflective membrane on top of a liquid chamber connected to an actuation channel. When pressure is applied to the liquid chamber, the membrane surface deforms, changing the focal length of the reflected beam. The magnitude of the obtained deflection is determined by the applied pressure and the membrane parameters, such as diameter, thickness and elasticity.

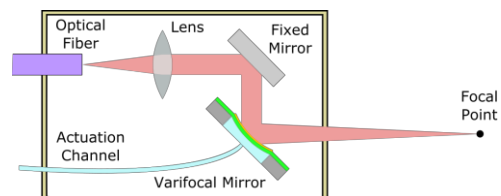


Figure 1. Schematic diagram of the focusing system using the varifocal mirror with hydraulic actuation.

To build this mirror, we performed microfabrication using a clean room facility. The adopted design consisted of a silicon wafer with a silicon nitride membrane, coated with gold to provide high reflectivity. Fig. 2 shows a diagram of the entire fabrication process.

The fabrication of the mirror was composed mainly of two stages: the creation of the circular membrane and the deposition of the gold layer. To build the membrane, we started with silicon wafers of 525 μm of thickness, coated with 500 nm of LPCVD super low stress silicon nitride on both sides and sputtered a layer of chromium on the bottom nitride. Then a circular window was patterned in the chromium using optical lithography, to allow etching a hole in the silicon substrate. The silicon was etched with deep reactive ion etching (DRIE) and wet etching with a solution of TMAH and IPA. The wet etching operation is necessary, because the DRIE can also etch the silicon nitride layer, which forces us to

interrupt the process before all the Si is etched. To apply the gold coating, we evaporated gold on top of a circular window patterned with photolithography and performed a lift-off operation. The performance of the lift-off was improved by creating an undercut in the photoresist, using a layer of sacrificial material (LOR 7B).

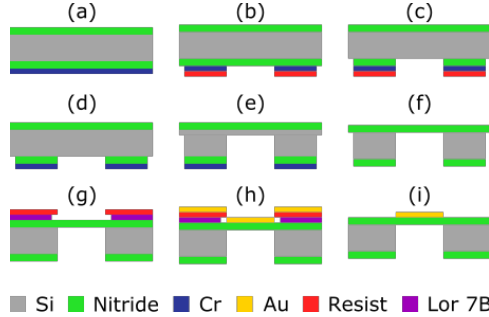


Figure 2. Fabrication process of the varifocal mirror. (a) Sputter the Cr layer. (b) Pattern and etch a circular window in the Cr using photoresist. (c) RIE the bottom nitride layer. (d) Strip the resist. (e) DRIE a circular hole in the Si bulk. (f) Etch the remaining Cr and Si with chromium etchant and TMAH+IPA solution respectively. (g) Pattern a circular window of photoresist and LOR 7B on the top nitride layer. (h) Evaporate the gold layer. (i) Lift-off the resist with the excess gold.

RESULTS

Initially the proposed mirror design was evaluated using finite element simulation with ANSYS. The investigated properties were the heat dissipation on the mirror surface and the curvature of the mirror generated by the hydraulic pressure. Table 1 presents an example of the simulated results. In the thermal simulation, a laser of 5W was used, assuming a reflectivity of 99% for the mirror. The cooling mechanism assumed for the mirror was only convection to stagnant air. In the mechanical simulation, the applied pressure to the liquid chamber was -300 Pa.

Table 1. Results of the thermal and mechanical FEM simulations.

Steady-state Thermal simulation	
Temperature at mirror's center	140.46 °C
Temperature at mirror's border	67.54 °C
Mechanical simulation	
Mirror deflection	2.98 μ m
Corresponding optical power	47.73 diopters
Maximum stress at the membrane	9.67 MPa

Using the fabrication method described above, we built a set of initial prototypes. Each prototype was 10 mm wide and had a membrane of 1 mm in diameter. Even though a larger membrane would be more suitable for high-power laser, since it allows reducing the laser damage over the mirror by spreading the power on a larger area, we started with this design to evaluate the quality of the fabrication process. Fig. 3 shows an image of the bottom view of the mirror obtained with a scanning electron microscope, where the circular chamber etched in the Si substrate can be seen. The

image shows the obtained interface between the membrane and the bulk was circular, even though the walls of the chamber suffered some anisotropic etching.

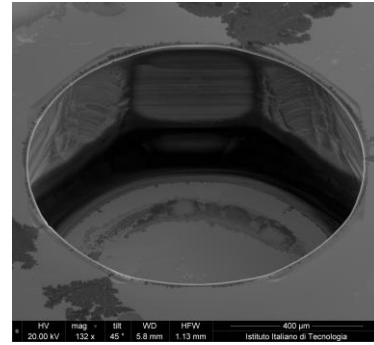


Figure 3. Scanning electron micrograph of the fabricated mirror (bottom view)

In order to evaluate the performance of the fabricated prototypes, an experimental setup was built using a CellTram vario microinjection system (Eppendorf, Germany) and a Shack-Hartmann wavefront sensor (ThorLabs, US). To connect the liquid chamber of the mirror to the microinjection system, a custom metallic holder was manufactured. This setup is currently being used to characterize the mirror. Qualitative experiments have confirmed the mirror's ability to deflect both in concave and convex shape.

CONCLUSION AND DISCUSSION

In this work, we proposed a MEMS varifocal mirror with hydraulic actuation for focusing a surgical laser. A preliminary prototype has been fabricated and is currently under evaluation. Simulated results show it can provide an optical power range above 40 diopters, which is enough to move the focal point from 15 to 35 mm, without reaching the yield stress of the membrane. The estimated maximum temperature reached by the mirror under 5W laser irradiation is around 140°C, which should not damage the membrane. This will be verified experimentally in the near future, especially in view of refining the microfabrication process and the system modeling, which currently does not account for internal stresses in the mirror membrane nor imperfections created by the fabrication process.

REFERENCES

- [1] Mattos L., Deshpande N., Barresi G., Guastini L., Peretti G., A Novel Computerized Surgeon-Machine Interface for Robot-Assisted Laser Phonomicrosurgery, *The Laryngoscope*, 124:1887–1894, August 2014.
- [2] Jacobson A.S., Woo P., Shapshay S.M., Emerging technology: Flexible CO₂ laser WaveGuide, *Otolaryngol-Head & Neck Surg*, 135:469-470, 2006.
- [3] T. Sasaki and K. Hane, Varifocal Micromirror Integrated With Comb-Drive Scanner on Silicon-on-Insulator Wafer, *Journal of Microelectromechanical Systems*, 21:971-980, August 2012.

Session 3

Training and Safety

Adaptive Fractal Trees Parametrisation for Neurosurgery Applications

Marlene Pinzi¹, Stefano Galvan¹, Ferdinando Rodriguez y Baena¹

¹ *Mechatronics in Medicine Laboratory, Mechanical Engineering Department, Imperial College, London, UK*

INTRODUCTION

Minimally invasive neurosurgery represents a major trend in contemporary neurosurgery, aiming to minimise patient trauma, and thus the risk of complications and recovery time. Steerable needles are a promising technology in this medical field because of their capability to reach a target following a curvilinear trajectory, avoiding main anatomical brain structures such as blood vessels. They could provide a step change in the delivery of diagnostic sensors and therapies to the brain via flexible surgical access, with a possible focus on cancer therapy. In this context, the EDEN 2020 catheter [1] is an example of a biologically inspired, nonholonomic steerable needle, which is expected to improve minimally invasive treatment in neurosurgery. Steerable needles have the potential to update the needle insertion trajectory in real-time considering the tissue deformation and any shift that may occur during surgery. However, the design of real-time path planning algorithms capable of online updates is challenging. A common issue in most existing path planning approaches, is that the algorithm performs the search sequentially, relying on a single CPU, a fact that imposes a considerable lower bound on computation time and cost. A “parallelizable” path planner, such as the Adaptive Fractal Tree (AFT) [2] is required in order to cope with the catheter nonholonomic constraints and enable successful real-time path computations in complex surgery. The AFT is an innovative algorithm characterised by the expansion of a self-similar (fractal) structure through the search space. Each branch of the tree is associated to a GPU thread and runs in parallel on the graphic card, thus optimising the use of computational resources. AFT parameters can be modified, leading to a change in the fractal pattern and, therefore, in the amount and in the characteristics of the generated paths. In this paper, we propose a quantitative study of the relationship between existing parameter values and AFT performance in terms of a cost function based on the steerable needle’s expected use. Therefore, an automatic parameters tuning process is designed to identify optimal values for each, according to patient-specific characteristics, with the aim to improve trajectory generation.

MATERIALS AND METHODS

The topological structure of the tree resembles the recursive nature associated to the motion of nonholonomic needles. At each step, all possible future motions depend on the current pose, a process that reverses recursively from the target to the insertion point

via all tree levels. The basic tree structure with this fractal geometry features five possible motion directions: straight, up, down, right and left, represented by a straight line in the first case and arcs for all remaining cases, the curvature value of which can be chosen based on the needle’s constraints. The search space between the straight line and the maximum curvature arcs can be explored by adding further arcs featuring lower curvature. For instance, if there are two arcs for each direction, the amount of possible motion directions, which is labelled as the tree density parameter (ρ), increases from five to nine. The tree’s basic structure can be shaped according to any given scenario by tuning a set of fundamental parameters associated with trajectory generation and the needle design parameters. These

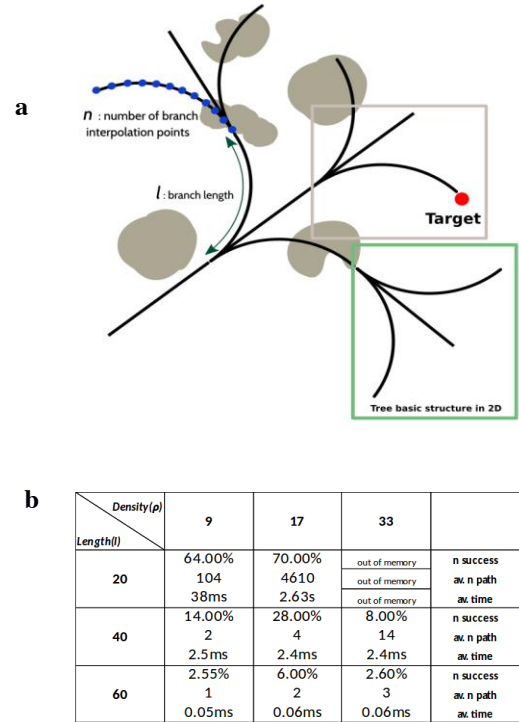


Figure. 1. The figure (a) shows the geometry of the tree in 2D with a focus on the basic structure of the fractal geometry (within the green window). On the bottom (b) a table showing for each combination of length (l), and density (ρ) the percentage of success on 196 trials; the average number of paths found and the average computation time.

include the branch length (l), density of the tree (ρ) and branch interpolation constant (n). The choice of parameter value is partly limited by the computational cost constraints associated to a given hardware, but is also influenced by the number and complexity of the

obstacles within the search space and the maximum length of the needle.

Here, we aim to understand the relationship between the first two parameters, l and ρ , and algorithm performance, as other parameters are a function of these. In our simulations, l is assigned one of the following arbitrarily values: 20, 40 or 60 mm. This set was chosen in order to measure the AFT's behaviour for clearly different cases. Next, the interpolation constant n is calculated by performing an obstacle collision check at each interpolated point. In order to set its value, blood vessels are segmented from the patient's MRI image volume via, e.g. thresholding, and the minimum vessel radius is used to identify the resolution required. Then, the GPU memory needed is computed from the number of tree segments, using the worst-case scenario of a path with length equal to the maximum reachable needle length. Knowing the exponential law governing tree growth and branch length set up beforehand, it is possible to compute the required number of tree levels, and thus the total number of segments necessary to reach the desired extension. Ultimately, the density of the AFT is set to one of these values: 9, 17 or 33. In turn, these define the number of branches forming the basic fractal structure. Of particular importance is the understanding of the relationship between ρ , the computational cost and the AFT outcome in order to reach a good trade-off. The initial tree space orientation is also considered as a variable. The tree can be oriented towards any point along a circumference around the target, which lies on the plane perpendicular to the line subtended between insertion and target points. This further variability increases the number of cases. In a first study, we executed a total of 1764 simulations on a standard PC workstation with a NVIDIA TITAN X Maxwell (with 3072 CUDA cores, a 1GHz base-clock and 12 GB of memory) varying parameter values as discussed above. Each path is evaluated by a cost function:

$$CF = \frac{1}{3} * \sum_{i=1}^{nseg-1} |C_{i+1} - C_i| + \frac{1}{3} * \sum_{i=1}^{nseg} |C_i| + \frac{1}{3} * path_length$$

Where “nseg” represents the number of segments composing the path. The cost function considers the preferential path characteristics, where the first term of the equation is the gradient of curvature which is calculated as the sum of the difference of curvatures (C_{i+1} and C_i) between consecutives branches constituting the path. It measures the smoothness of the trajectory in terms of absence of inflection points and curvature variability. This feature is preferred because it facilitates the control of the needle movement. The second term refers to the sum of the segments curvature (C_i), which reflects the linearity of the path. Trajectories presenting moderate curvature, away from the maximum constraint of the needle, are favoured. “path_length” is minimised to favour short paths, with the effect of reducing potential for tissue damage during needle insertion. From the entire set of collision-free generated paths, only those that reach the target to within 1mm are selected to be

classified according to CF and the best path is the one which minimises the cost function value.

RESULTS

From a preliminary analysis of the simulations it is possible to identify strong relationships between AFT parameters and the generated trajectory (Figure. 1b). When l decreases, the complexity of the path, related to the first two terms of CF, and the computation cost increase. However, a considerably larger number of paths is found, confirming that it is easier to find a way within a dense network of obstacles when the trajectory is composed by segments of minimum length. For instance, setting $\rho = 9$ with $l = 40mm$ and $l = 20mm$ respectively, the average amount of paths, calculated on 196 trials, increases from 2 (averaging 28 successful trials) to 104 (averaging 126 successful trials) while the computation time increases from 2.5 ms to 38 ms, respectively. The number of paths within the tolerance, found for each set of parameters, is considered as a safety index for the patient and the surgeon to be maximised. In fact, in case the chosen path needs to be updated, the probability of success in generating a new candidate is higher. Considering the density parameter ρ , its influence on the amount of paths generated increases as l decreases, with a considerable rise in computation time, from 38 ms ($\rho = 9, l = 20mm$) to 2.63 s ($\rho = 17, l = 20mm$). Ultimately, the results show that a smaller branch length and a higher density guarantees greater robustness on finding a path for each initial tree growth orientation. However, as the AFT runs on the GPU, a compromise is required to deal with the limited memory resources.

CONCLUSION AND DISCUSSION

The relationship between parameter values and AFT performance in terms of a cost function highlights the need for automatic parameter tuning, which should be case specific. Appropriate parametrisation would maximise the probability of finding a collision free path from the insertion point to the target. The parametrisation also enables the user to favour those trajectories which respect steerable needle constraints and minimise the risk for the patient. Future studies will focus on a more in depth analysis of the relationship between obstacle map features and algorithm performance, with the aim to improve efficiency and robustness.

REFERENCES

- [1] Frasson, L., Et al (2010). STING: a soft-tissue intervention and neurosurgical guide to access deep brain lesions through curved trajectories. *Journal of Engineering in Medicine*, 224(6), 775–88.
- [2] Liu, F., Et al (2016). Fast and Adaptive Fractal Tree-Based Path Planning for Programmable Bevel Tip Steerable Needles. *IEEE Robotics and Automation Letters*, 1(2), 601–608.

Using Rule Induction to Analyze Intrauterine Pressure and Oxytocin Data for Surgical Interventions in Labour

M.J. Stockton¹, E. Grant², T.C. Henderson³

¹*Department of Marketing and Communications, Longwood University*

²*Joint BME Department, UNC-Chapel Hill & North Carolina State University*

³*School of Computing, University of Utah*

egrant@ncsu.edu

INTRODUCTION

Uterine activity analysis is of major importance in the management of labour in childbirth. It has been shown that insufficient or excessive activity can delay progress and lead to many serious problems for both the mother in labour and the foetus, e.g., the decision to perform a Caesarean section [1]. Quite often, oxytocin, a drug that stimulates contractions, is used [2]. The aim of this project was to investigate the effectiveness of using an artificial intelligence technique known as *rule induction* in the control of oxytocin administration [3]. A doctor or midwife controls the rate of administration of oxytocin, by intuitively increasing or decreasing the infusion rate. The number of contractions the patient has and the strength of these contractions are monitored by examining the patient, or feeling the stomach, and decisions are based on this. Occasional checks of cervical dilation are noted as an indication of how far labour has progressed. So, a goal of the reported research is the provision of a computer-assisted system to advise medical practitioners whether to increase or decrease the infusion rate. Or, to have a credible guide that explains why a classification was made, including a percentage of certainty. Commonly, sensor data is gathered in the domain by using a tacodynamometer, or by measuring the intrauterine pressure in the amniotic fluid behind the foetal head. However, the tacodynamometer data is very noisy due to relative motion between the sensor, the mother, and the tissue. Alternatively, intrauterine pressure measurements require the pressure sensor to be placed internally, which involves the puncturing of the foetal membrane, an action that can itself stimulate contractions. And, one labour can differ greatly from another. Numerous approaches have been proposed for deriving objective evaluations of intrauterine pressure, from recorded waveforms gathered over time, including Steer et al. [4]. Steer et al. proposed an *activity unit*, a product of peak pressure and duration of contraction. When the *activity unit* is summed over time, i.e., frequency, the activity unit approximates to a measure of area.

Rule Induction is important in the field of machine learning. Rule based inductive learning is a technique that derives classification rules from a training set of examples that are the input to the system. The training set consists of a set of attributes and the desired outputs, known as classes. The attributes, paired with the

particular class, represent the output expected by an ideal system. The system should give expected outputs on newly presented inputs if a good, comprehensive training set was used. During the learning process the rules are continuously modified under strictly defined conditions to reduce the outputs between the actual outputs produced by the rules and the desired output.

Clark and Niblett developed CN2 [5] in 1986. CN2 was designed with the aim of inducing short, simple comprehensible rules in domains where problems of poor description language and/or noise may be present. The induced rules are in a form similar to production rules. An important feature of the search for such rules is the relaxing of the requirement of complete consistency of rules within the training data during their generation, in order to minimize the problems of noise in the description language. This has the benefit of allowing induction to be halted in regions of the search space where there is little training data to guide the system, where further search is as often damaging as beneficial, similar to pruning of trees, as is done by NewID.

NewID is an ancestor of Quinlan's ID3 (Iterative Ditchotomiser) [6] and the algorithm is very similar. It expresses its induced knowledge in terms of a decision tree. A decision tree is a conventional tree with nodes and arcs. Internal nodes (or decision nodes) are named with the attributes and the arcs are labelled with the possible values of the attributes. Each leaf node specifies a decision. Any object is associated with a unique leaf of the tree. This association is accomplished by a procedure that begins at the root node and traces a path to a leaf by following the arcs that correspond to the attribute values of the object being classified.

MATERIALS AND METHODS

The data used in this project came from Phillips [7], see Fig.1 and 2. Cartiographs from four patients were digitized. The digitized data was used to develop a program to extract the features of intrauterine pressure, that subsequently became the attributes for classifying the signals. Care was taken to mark the points where labour progresses adequately or inadequately. Data related to oxytocin infusion rates was recorded simultaneously with intrauterine pressure. This action provided accurate classification verification, because the

rate of infusion at any point during labour indicates a medical practitioner's decision on contractile activity.

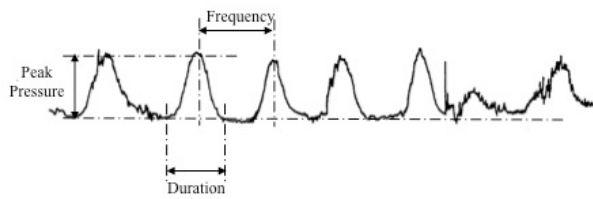


Fig.1. First Stage Intrauterine Pressure

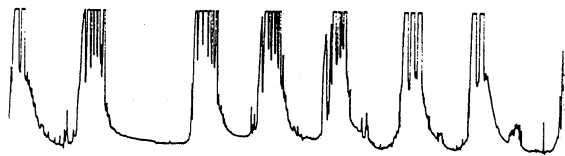


Fig.2. Second Stage Intrauterine Pressure

Fig.1 represents the first stage of intrauterine pressure measure, it shows peak contraction, duration and frequency. Fig.2 shows a high frequency component superimposed onto the contraction peaks, this is the effect of *bearing down*. The resulting pressure is beyond the range of the recorder.

The extraction software developed to calculate values from input data was tested at procedure and system level and was shown to calculate the features satisfactorily. But, the software may tend to overestimate the activity where there are increases in pressure due to patient movement and other noise. An end of contraction is noted if the pressure drops within a threshold of the baseline pressure value, therefore the area may be overestimated when there is a long period of pressure just above the threshold that is not a contraction. One possible solution to this problem may be to incorporate a procedure to measure the gradient of the line and if the gradient becomes low enough, i.e., it "levels out" enough, then the contraction can be seen as ended.

RESULTS

The extracted features from intrauterine pressure signals, used as attributes in the learning process were: (1) peak pressure of every contraction, (2) the number of peaks per contraction, (3) duration of every contraction, and (4) the area under the intrauterine pressure curve calculated over the duration of each contraction. Intrauterine pressures from two labours were used to generate the attribute and example file. Part of an attribute, example, classification file is shown in Table 1. Table 2 shows rule trees generated for data set one, starting with the current contraction only. Rule trees are then generated using attributes from the current contraction plus current contraction – n (n = 1, 2, etc.).

Peak Pressure	Number of Peaks	Duration of Contraction	Area Under Curve	Classification
73.15	3	85.00	2876.6	c
135.85	1	70.00	4220.25	a
66.55	1	80.00	2941.25	a

Table 1

Format of Attributes	Total Number of Nodes	Internal Nodes	Leaf Nodes
Current Only	47	23	24
Current & 1 Previous	37	18	19
Current & 2 Previous	35	17	18
Current & 3 Previous	35	17	18
Current & 4 Previous	33	16	17

Table 2

CONCLUSION AND DISCUSSION

With the assistance of Dr. Fiona Fairlie [8] a set of attributes was identified in data files of intrauterine pressure and oxytocin simultaneously recorded during labour. An attribute extraction program to automatically extract these features was then produced. Experiments were conducted using the rule induction algorithms NewID and CN2. From these experiments NewID, with its tree pruned with a 4% threshold, produced an acceptable set of rules. This tree classified the oxytocin level, given new data, at an average overall accuracy level of 73.8%. In addition the rule tree generated had a comparatively low complexity level of 58 nodes. The results from automatically induced rules showed a higher correspondence to 'actual' values than those derived using Steer's [4] method for controlling oxytocin levels. It was concluded that Steer's approach is too rigid for this kind of domain. Learning from examples may hold the answer for an optimal system for controlling oxytocin level, decreasing cesarean sections, and shortening labour. The main problem encountered in all induced rules was that of predicting a decrease in oxytocin. NewID's unpruned, highly complex tree could achieve the best average accuracy level of 41.9%, hence two or three decreases in oxytocin will be wrongly predicted in a single labour.

REFERENCES

- [1] Shu-Qin Wei, Zhong-Cheng Luo, Hui-Ping Qi, Hairong Xu, Fraser, W.D., "High-dose vs low-dose oxytocin for labour augmentation: a systematic review," In: American Journal of Obstetrics & Gynecology, October 2010, pp 296-304.
- [2] Guidelines for the use of Oxytocin in Labour, Report: University College London Hospitals, June 2010, 7 pages.
- [3] Creaney, M.J. (1991) "The use of rule induction in the analysis of intrauterine pressure signals." MSc, University of Strathclyde.
- [4] Steer, P.J. et al (1975) "Uterine activity in induced labour." Br J. Obstet. Gynaecol. vol 82, pp 433-441.
- [5] Clark, P. and Boswell, R. (1991) "Rule induction with CN2: some recent improvements." EWSL-91.
- [6] Meta-Learning in Decision Tree Induction, Author: Krzysztof Grabczewski, Pub: Springer, ISBN: 978-3-319-00959-5, 2014.
- [7] Philips, G.F. (1986) "The contractile activity of the human uterus during labour." PhD, University of Strathclyde.
- [8] Fairlie et al (1988) "An analysis of uterine activity in spontaneous labour using a microcomputer." Br. J. Obstet. Gynecol. Vol 95, pp 57-64.

Intraoperative Neuromonitoring for Robotic Surgery – Case Experiences during Robotic Cochlear Implantation

J. Ansó¹, O. Scheidegger², W. Wimmer¹⁻³, K. Gavaghan¹, M. Caversaccio³, S. Weber¹

¹ARTORG Center for Biomedical Engineering, University of Bern, Switzerland

²Department of Neurology, ENMG-Station, Inselspital, University of Bern, Switzerland

³Department of ENT Head and Neck Surgery, Inselspital, University of Bern, Switzerland
juan.anso@artorg.unibe.ch

INTRODUCTION

Surgical robots are becoming part of operation room experience in different fields (e.g. spine, neuro) [1], [2]. Typically, surgical robots are able to achieve precision, accuracy and/or dexterity tasks which are close to impossible to human capabilities. In some surgical applications robots are used to remove tissue in the vicinity of delicate nerves, e.g. during robotic cochlear implantation (RCI), where a drill passes at submillimeter distance from the facial nerve (FN) [3]. In order to increase the safety of RCI, a navigated neuromonitoring (NM) approach has been developed and integrated in the first RCI system and clinical work flow. The NM method has been established based on pre-clinical (in-vivo) validations reported previously in [4]. The approach relies on multipolar minimum stimulation intensity via a probe that fits in the RCI drilled tunnel. Our aim is to develop a robust safety mechanism that can be used during robotic drilling near a delicate nerve structure, and assess *safe* versus *unsafe* distance margins based on NM. Herein this work, the first clinical experiences (n = 4 subjects) using integrated neuromonitoring during RCI is presented. It is hypothesized that the NM system enables a sensitive and specific (> 95%) drill-to-FN proximity assessment at submillimeter distances.

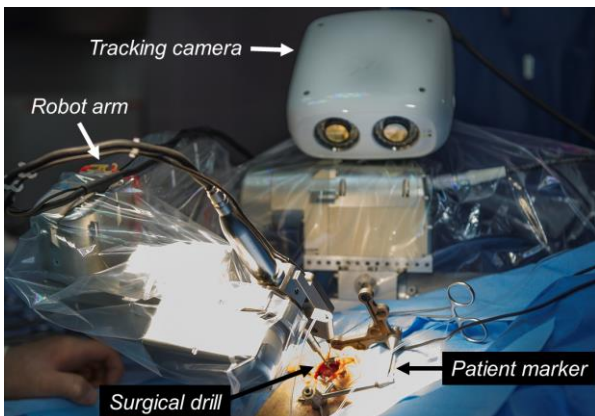


Figure 1. Robotic Cochlear Implantation system during first-in man RCI operation (University Hospital Bern, July 2016).

MATERIALS AND METHODS

Neuromonitoring system

The neuromonitoring system is composed of: 1) Electromyography (EMG) system (ISIS, inomed): EMG

measuring needles (orbicularis oris and oculi) and EMG ground needle (Fig. 2). 2) Stimulation system: positive control surface electrodes; and multipolar stimulating probe with one cathode C and four anode A_i combinations (C-A₁, C-A₂, C-A₃ and C-A₄).

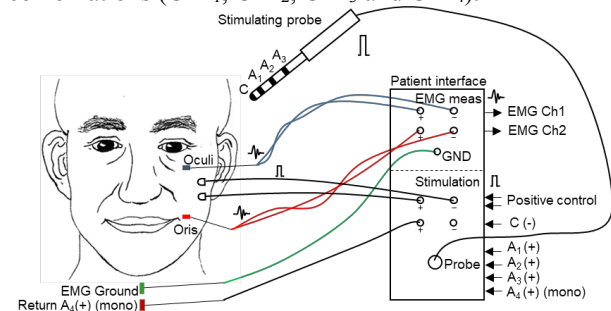


Figure 2. Patient to neuromonitoring system interface with the stimulating probe, the EMG measuring electrodes, the positive control surface electrodes, the EMG ground and stimulation return electrode (A₄ monopolar).

Neuromonitoring approach

The RCI-NM approach consists on the combination of: 1) Positive control: assess sensitivity of the NM system during the procedure. 2) Free-running EMG: continuously monitors nerve activity during the procedure. 3) *Safe* vs. *Unsafe* assessment: determines distance margins from the trajectory to the facial nerve during the critical segment (drill-to-FN distance < 2 mm).

Image-Guided Robotic Drilling

After approval of the local ethics commission (IRB Bern, Switzerland, KEK-BE Nr.156/13) a first RCI clinical trial is undergoing at the university hospital of Bern [5]. The RCI procedure starts with implantation of four fiducial screws (2.2mm × 5mm, M-5243.05, Medartis) in the mastoid of the patient. Thereafter a computer tomography scan is acquired (SOMATOM, Siemens) and a trajectory planned to the entrance of the cochlea. Then, via utilization of a non-invasive head-rest, the patient's head is fixed to the operation bed. The electromyogram (EMG) measuring electrodes are located in the facial muscles (orbicularis oris and oculi). The surface stimulating electrodes are positioned on the superficial branch of the FN (*positive control*). The positive control is executed and a minimum EMG amplitude level of 200 μV needs to be verified. Positive confirmation of the positive control leads to draping of

the patients' surgical site. Then, a reference marker (Fig. 1) is fixed in the patient's mastoid to enable tracking of head movements during the robotic drilling operation. After physical registration of the mastoid to the preoperative plan via the implanted fiducial screws, RCI drilling is initiated up to 3 mm before the FN (1000 RPM, 0.5 mm/s, 2 mm pecking steps, Ø 1.8 mm). At this level, a radiologic safety confirmation of the drilled axis is achieved via intraoperative CT imagery (xCAT, Xoran). Thereafter, a temperature minimization drilling protocol (0.5 mm pecking steps) is initiated towards the critical drilling segment (drill-to-FN distances < 2mm).

Facial nerve distance assessment from NM

Drill-to-FN distance based on NM measurements is determined at five consecutive measurement points equally spaced ($AD = 0.5$ mm) through the facial recess (Fig. 3). The first NM point P_1 is defined 1.2 mm in front of the FN center, and the last NM point P_5 at 0.9 mm passed the FN center. At each point, monophasic stimulating pulses (0.2 to 2.5 mA, 250 μ s) are applied per each of the stimulating channels of the probe (Fig. 3).

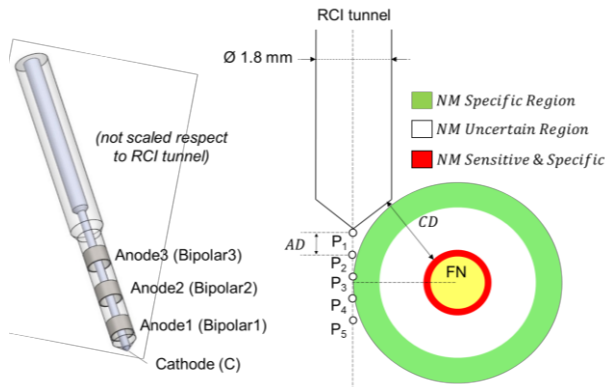


Figure 3. (Left) Neuromonitoring probe with cathode at the tip and the three ring anodes (B1, B2 and B3). (Right) Discretized NM measuring points. The *safe* (green), *unsafe* (red) and uncertain (while) regions based on NM approach are depicted.

The minimum stimulating intensity that elicits an EMG response above threshold (> 100 μ V) is defined as stimulus threshold (ST). From previous in-vivo experimental studies [4], the stimulus threshold capable of discriminating *safe* and *unsafe* drill-to-FN proximity ranges below 0.6 mm was 0.3 mA. Consequently, bipolar (B_{1-2}) stimulus thresholds equal or above 0.35 mA are used as indication of sufficient drill-to-FN distance greater than 0.4 mm (*safe passage*). On the other hand, bipolar stimulus thresholds below 0.35 (B_1) indicate an *unsafe* (< 0.1 mm), or an uncertain (B_{1-2}) drill-to-FN distance margin (0.1- 0.4 mm), as defined in [3]. To ensure minimization of false negatives and/or false positives (e.g. EMG measuring artifacts), the NM system allows the surgeon to verify the suggested stimulus thresholds via a manual stimulation module. Finally, if the NM assessment confirms sufficient safety margin ($ST > 0.3$ mA), robotic drilling is finalized up to the entrance of the cochlea and CI electrode insertion is carried out.

Data analysis

Drill-to-FN distance assessment was determined from postoperative CT images co-registered to the preoperatively determined (plan) facial nerves. For each measurement point, the Euclidian distance from the drill to the FN surface was defined as closest distance (CD). A sensitivity and specificity analysis was done assessing the stimulus thresholds and postoperative minimum distance from the drill tunnel to the facial nerve (CD_{min}).

RESULTS

The RCI approach has been applied in $n = 4$ subjects. In all cases, the NM approach was able to determine drill-to-FN proximity ranges above 0.7 mm (Table 1). From these results, 100% sensitivity/specificity to discriminate drill-to-FN distance above 0.6 mm was determined.

Table 1 Stimulus threshold and distance data ($n = 4$ subjects)

Subject	Min. stimulus threshold (mA)				FN-NM distance (mm)	CD_{min} (mm)
	B1	B2	B3	Mo.		
1	NR	NR	NM	2	> 0.7	0.82
2	NR	2.5	2.5	1.5	> 0.7	0.67
3	NR	NR	NM	2	> 0.7	0.78
4	1.25	0.5	0.5	0.4	> 0.7	0.61

NR: no EMG response; NM: not measured ($Z > 22$ K Ω)

CONCLUSION AND DISCUSSION

The proposed NM approach was capable of determining *safe* drill-to-FN proximity ranges during the first RCI cases. The results were consistent with in-vivo (sheep) experimental data at drill-to-facial nerve distance ranges above 0.6 mm [4]. However, the robustness of the NM approach at the critical FN distance range (< 0.3 mm) remains undetermined. To enable determination of the NM algorithm at the critical distance range, a prospective in-vivo validation is currently under preparation.

REFERENCES

- [1] Davies B, A review of robotics in surgery. *Proc. Inst. Mech. Eng. H.* 2000; 214(1):129–40.
- [2] Bertelsen A, Melo J, Sánchez E et al. A review of surgical robots for spinal interventions. *Int. J. Med. Robot.* 2013; 9(4):407–22.
- [3] Weber S, Gavaghan K, Wimmer W et al. Instrument flight to the inner ear. *Science Robot.* 2017; 2(4).
- [4] Ansó J, Dür C, Gavaghan K et al. A Neuromonitoring Approach to Facial Nerve Preservation During Image-guided Robotic Cochlear Implantation. *Otol Neurotol.* 2016; 37(1):89–98.
- [5] Caversaccio M, Gavaghan K, Wimmer W et al. Robotic cochlear implantation: surgical procedure and first clinical experience. *Acta Otolaryngol.* 2017 Apr; 137(4):447–454.

Sessions 4 & 5

Image Processing and Algorithms

Online Reconstruction of Retinal 3D Map from Stereo in Close-to-Realtime for Eye Surgery

S. Hecker¹, T. Probst¹, A. Chhatkuli¹, K. K. Maninis¹, M. Havlena¹

E. Vander Poorten², L. Van Gool^{1,2}

¹*Computer Vision Lab, ETH Zürich, Switzerland*

²*KU Leuven, Belgium*
heckers@vision.ee.ethz.ch

INTRODUCTION

3D reconstruction has become an important tool in many camera-assisted medical interventions. As such, one of the goals of the EU funded project *EurEyeCase* is to use reconstructed 3D maps of the retina to help the surgeon during retinal interventions. To that end, a stereo microscope is used to view a small fraction of the retina at each instant. In this paper, we investigate how the reconstructed point clouds from each stereo image pair can be fused to generate a more consistent global retinal model. A global 3D model of the retina would help the surgeon to accurately localize the tools with respect to the retinal surface. We build upon previous work of stereo microscopic calibration and retinal 3D reconstruction [1] while implementing them in a framework compatible with real-time applications. We use a coarse to fine surface registration algorithm based on 2D image features, transformation estimation using singular value decomposition (SVD) and an Iterative Closest Point (ICP) method to align each new point cloud surface to the global retinal 3D model. Fusion is achieved by filtering aligned incoming depth maps using a voxel grid. In contrast to [1], the approach can be implemented online with close to real-time performance. We also remark several encountered challenges in achieving such a task and the solutions we used to tackle them. Finally we present our results on a sequence of recorded images of a surgery performed on an open sky porcine eye.

MATERIALS AND METHODS

The *EurEyeCase* camera setup consists of a surgical stereo microscope that can be moved freely to capture different views of the retinal surface. The camera setup and its functionality are described in the related previous work [1]. We follow the same methodology to pre-calibrate the stereo camera using checkerboard images [4]. We fix certain distortion coefficients to zero and principal point to the middle of the images for obtaining better stability in focal length. The low depth of field as well as non-conventional optical arrangement further requires that certain parameters of the camera intrinsics are fixed to have better stability in focal length. This is followed by the relative stereo extrinsic calibration. We fix both the camera intrinsics and relative extrinsics of the stereo to calibrated values when reconstructing the retina. On the one hand, the

reconstructed point clouds for each image pair in the sequence thus obtained are generally noisy and cannot be directly fused. This is particularly true for high focal length stereo reconstruction such as the ones done in this work. On the other hand, fusing them offline using surface reconstruction methods may not be relevant to the surgical application. Nonetheless, through incremental fusion of incoming point clouds, we are able to filter out noise and obtain a consistent global model of the retina without resorting to offline methods. Figure 1 shows the pipeline of the work.

Stereo Matching and Point Cloud Generation

Given a pair of stereo images, we first rectify both images using the intrinsic and extrinsic camera parameters obtained during calibration. We perform stereo matching on the GPU using the Constant Space Belief Propagation algorithm [3], due to its global optimality and speed. Reprojecting the depth map into 3D space gives a dense point cloud. A brightness-based filter is applied to remove reconstruction at points where there are specular reflections. Such reflections cause false stereo matches introducing artifacts in the point cloud that would limit the performance of the subsequent alignment process.

Motion Estimation and Point Cloud Registration

We adopt a coarse to fine registration technique based on the premise that consecutive frames often contain significant translation in the observed model, taking into account the noisy nature of the computed point cloud; thus, limiting the use of traditional registration techniques such as ICP. Directly running ICP on two such point clouds fails to give a satisfactory fusion results due to bad local minima. Instead, we first compute a rough estimate of the relative 3D motion: We find feature point correspondences for consecutive frames and triangulate these to obtain two corresponding 3D point sets, one for each view. We use the GPU implementation of SURF [2] to that end. The least-square estimation of the 3D transformation (R, t) between the two point sets is then computed using SVD. Using this estimate as an initialization for the ICP algorithm, we can refine our registration and obtain an optimal alignment.

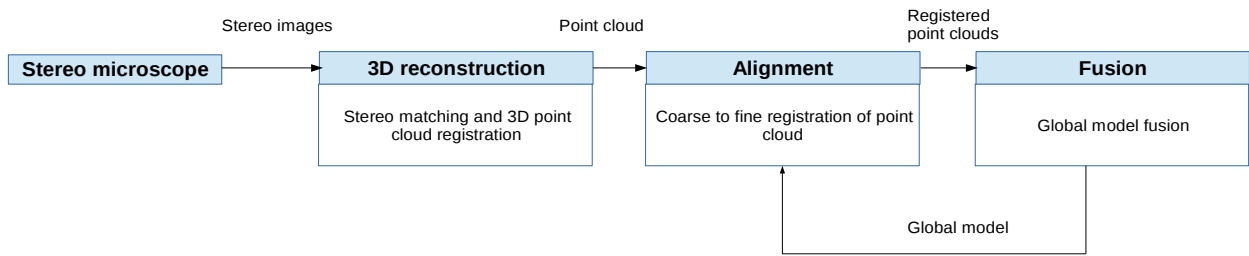


Figure 1. Our workflow for reconstructing a global retinal 3D model during an eye surgery using a stereo microscope.

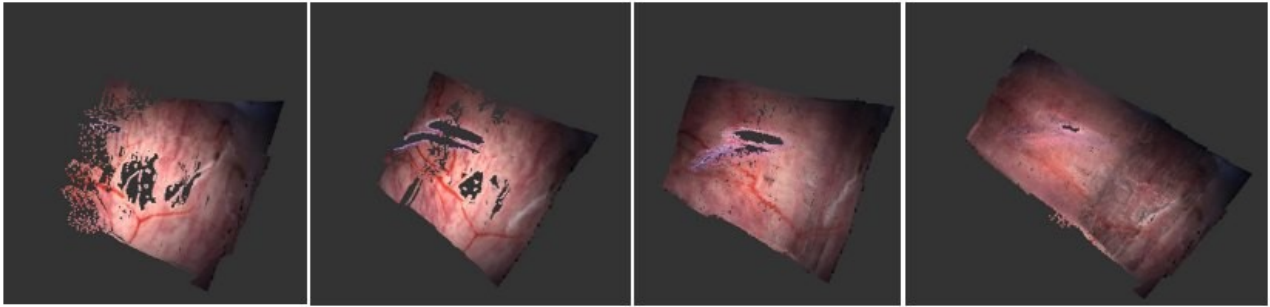


Figure 2. Fusion of point clouds in the stereo sequence. The left rendering is a noisy point cloud obtained from a single stereo pair reconstruction. Point clouds are added from left to right to generate more complete surface reconstruction. Note that holes in point clouds are progressively filled because of complementary data.

Point Cloud Fusion

Incoming point clouds, once aligned, are robustly fused together using a voxel grid filter, which averages out noise and results in a global model of the reconstructed retina. To minimize error during alignment, our ICP implementation aligns to the global fused model.

RESULTS

Our experiments are based on a recorded sequence of an open sky pig eye surgery. We run our methods on downsampled 640 x 480 pixel images. We show the rendered results of our workflow in Figure 2. The fusion process is shown progressively from left to the right with the renderings. The results show that the quality of the point cloud from each stereo image has holes and noise due to filtering of the depth image and removal of specular reflections. The fusion process helps to recover some of these missed surface regions while integrating them into the same 3D model. The whole pipeline can be run at about 1 Hz with a GPU implementation of ICP. It is possible to further improve the pipelines speed by parallelizing additional components on the GPU.

DISCUSSIONS AND CONCLUSIONS

We investigated the reconstruction and online fusion of retinal eye surface using a stereo microscope. The fused 3D map obtained for the retinal surface shows that a good model can be obtained for the retinal surface in this setup without going for an offline reconstruction method. The key contribution here was the coarse to fine strategy for aligning point clouds and showing that dense reconstruction is possible in a retinal image without an offline global refinement step.

However several challenges still remain. The first being the calibration of the stereo microscope. In future work a different calibration setup will be used to calibrate the stereo camera using a robot controlled tool and tracking the points in images.

ACKNOWLEDGEMENTS

Research funded by the EU's Horizon 2020 programme under grant agreement No 645331 – EurEyeCase.

REFERENCES

- [1] Havlena M., Maninis K. K., Bouget D., Vander Poorten E., Van Gool L. "3D Reconstruction of the Retinal Surface for Robot-Assisted Eye Surgery", In CRAS 2016.
- [2] Bay H., Tuytelaars T., Van Gool L. "SURF: Speeded Up Robust Features", In ECCV 2006.
- [3] Yang Q., Wang L., Ahuja N. "A Constant-Space Belief Propagation Algorithm for Stereo Matching", In CVPR 2010.
- [4] Zhang Z. "Flexible Camera Calibration By Viewing a Plane From Unknown Orientations" IEEE Trans. Pattern Recog. Machine Int., 22(11):1330-1334, 2000.
- [5] Besl P. J., McKay N. D. "Method for registration of 3-D shapes", In SPIE 1992.
- [6] Low K-L. "Linear least-squares optimization for point-to-plane ICP surface registration", Technical Report, University of North Carolina, 2004.

Vision-based suturing needle tracking with Extended Kalman Filter

M. Ferro^{1*}, G. A. Fontanelli^{2*}, F. Ficuciello², B. Siciliano² and M. Vendittelli³

¹*Dipartimento di Ingegneria Informatica, Automatica e Gestionale, Sapienza Università di Roma*

²*Dipartimento di Ingegneria Elettrica e delle Tecnologie dell'Informazione, Università di Napoli Federico II*

³*Dipartimento di Ingegneria dell'Informazione, Elettronica e Telecomunicazioni, Sapienza Università di Roma*

INTRODUCTION

After the last two decades of lively activity, research in Minimally Invasive Robotic Surgery (MIRS) is focusing on enhancing the degree of autonomy for procedures that are still executed by surgeons, through the introduction of autonomous robot operation modes. These procedures include suturing that, as repetitive and tiring task, usually increases the operation time, costs and complications risks. Automatic suturing presents many challenges related to both perception and manipulation. Left alone the interaction with soft tissues, an automatic suturing procedure has to deal with the difficulty of perception in an unstructured and highly noisy environment for needle and thread detection and tracking. The circular shape of the suturing needle encouraged the development of a family of *model-based* approaches for detection and tracking. Authors in [2] present a RANSAC-based method for needle detection, where 3D needle pose reconstruction is achieved with the use of a stereo camera. However, the method does not run in real time and cannot be used for tracking. In [8], the 3D needle pose is adaptively reconstructed by relying on the observations of needle tip and junction, but tracking is not faced. Finally, [7] presents a method for a colored-needle tracking that involves a partial needle pose reconstruction and the use of markers. However, none of these works takes advantage of the kinematics information available from the robot, that are typically high-frequency and can ease the needle detection and tracking problem.

In this work we propose an approach to needle detection and tracking based on Kalman filtering to combine visual information from a monocular camera with the robot kinematics. Beside providing a fast and reliable needle pose estimation, the proposed method is robust with respect to scene variations as in case of partially needle occlusion or of needle re-grasping operation, as well as external disturbances perturbing the needle pose. In addition, the covariance matrices can be adapted taking into account the particular task that is being performed.

MATERIALS AND METHODS

This work proposes the use of an Extended Kalman Filter (EKF) [5] for the estimation of the needle pose \mathcal{F}_n in Fig. 1a, expressed in the base frame \mathcal{F}_b with origin at

the Remote Center of Motion (RCM) of the manipulator holding the needle.

In particular, the filter provides an estimate of the needle pose $\zeta = [\mathbf{p}_n, \mathbf{q}_n]^T$, being \mathbf{p}_n the true needle position, represented by the coordinates of the circle supporting the needle shape, and \mathbf{q}_n its quaternion-based true orientation in \mathcal{F}_b . The prediction step provides a preliminary estimation of the needle pose through the linear and angular velocities of the gripper provided by the manipulator kinematics. Then, a vision-based 3D pose reconstruction is used in the filter correction step.

Extended Kalman Filter

Determined from robot kinematics the linear and angular velocities $[\mathbf{v}_g, \boldsymbol{\omega}_g]^T$ of the gripper in \mathcal{F}_b , we consider the following continuous-time process dynamics for the state vector ζ

$$\begin{aligned}\dot{\mathbf{p}}_n &= \mathbf{v}_g + [\boldsymbol{\omega}_{g \times}] \mathbf{r}_{gn} + \mathbf{w}_p \\ \dot{\mathbf{q}}_n &= \frac{1}{2} \boldsymbol{\Omega}({}^n\boldsymbol{\omega}_g) \mathbf{q}_n + \mathbf{w}_q\end{aligned}\quad (1)$$

where $[\ast_{\times}]$ denotes the skew-symmetric operator, $\mathbf{r}_{gn} = \mathbf{p}_n - \mathbf{p}_g$ is the relative position of the needle with respect to the gripper, expressed in \mathcal{F}_b , ${}^n\boldsymbol{\omega}_g$ is the angular gripper velocity expressed in \mathcal{F}_n , and $\mathbf{w} = [\mathbf{w}_p, \mathbf{w}_q]^T \sim \mathcal{N}(0, \mathbf{W})$ is the process noise. Details on the form of $\boldsymbol{\Omega}$ can be found in [6]. On the other hand, the measurement model of the filter employs the visual-based pose measurements extracted from the monocular camera: first, a detection algorithm computes the ellipse-shaped projection of the needle on the image plane. Then, the 3D pose is reconstructed from the size and projective reasonings ([3]). So, The measurement model is

$$\mathbf{y} = \zeta + \mathbf{m} \quad (2)$$

where $\mathbf{m} \sim \mathcal{N}(0, \mathbf{M})$ is the measurement noise. The error-state vector is defined as

$$\tilde{\zeta} = [\tilde{\mathbf{p}} \quad \delta\tilde{\boldsymbol{\theta}}]^T \quad (3)$$

where $\tilde{\mathbf{p}} = \mathbf{p} - \hat{\mathbf{p}}$ is the position error and $\delta\tilde{\boldsymbol{\theta}}$ is the 3×1 small-angle approximation vector of the quaternion orientation error $\delta\tilde{\mathbf{q}} = \mathbf{q} \otimes \hat{\mathbf{q}}^{-1}$, defined to avoid numerical instability issues related to the unit norm constraint on the quaternion vector. Expressing the process dynamics (1) and the measurement model (2) with \mathbf{f} and \mathbf{h} , respectively, the corresponding jacobian matrices, \mathbf{F} and \mathbf{H} , are constant with respect to (3)

$$\mathbf{F} = \begin{bmatrix} [\boldsymbol{\omega}_{g \times}] & \mathbf{0}_3 \\ \mathbf{0}_3 & [{}^n\boldsymbol{\omega}_{g \times}] \end{bmatrix}, \quad \mathbf{H} = \mathbf{I}_6. \quad (4)$$

*Joint first authorship.

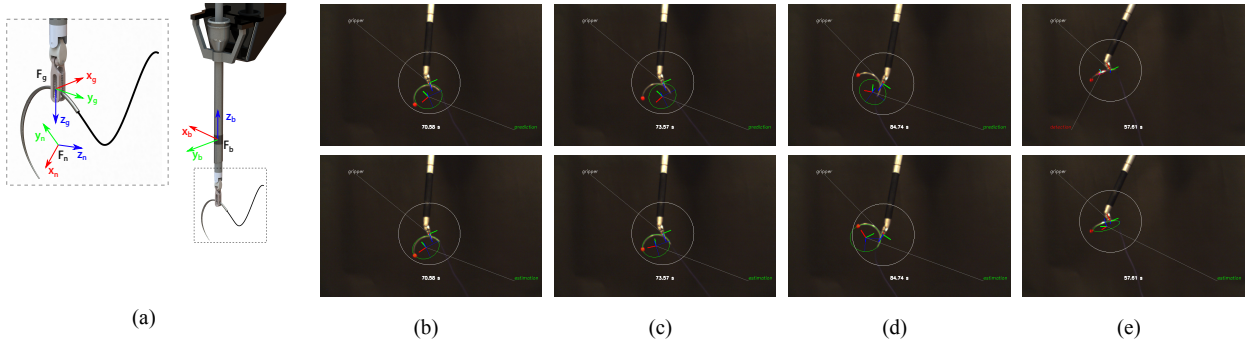


Fig. 1: (1a): Frames of interest in our discussion. (1b)-(1c)-(1d): Prediction failure scenario compared with the vision-based corrected estimation. (1e): Detection failure scenario compared with the estimation. The white circle represents the image area in which the needle is assumed to be found, based on its radius and the depth of the gripper with respect to the camera.

Then, the EKF state estimate is readily computed.

RESULTS

To evaluate the robustness of needle pose estimation with respect to perturbations due to the needle-tissues interactions, we use the simplified experimental setup shown in Fig. 1. Typical vision-related challenges (e.g., shadows, sparkling metal surfaces, small-sized objects) are not considered to focus on the geometric part of the pose reconstruction. So, an RGB segmentation procedure and a least-square fitting are sufficient to extract the projection of the needle on the image plane [4]. In addition, the needle tip has been colored to ease the detection of the projective point required for the 3D pose reconstruction.

The target experimental system is a da Vinci Research Kit robot (DVRK) [1]. Fig. 1 shows some preliminary results to prove the advantages in employing both robot kinematics and visual information for the needle pose estimation. During grasping, the needle is assumed as a rigid body attached to the gripper, and its pose can be predicted through robot kinematics, provided an initial estimate. However, since the needle-gripper transformation is not rigid, external disturbances (e.g., contact with tissues, slippages) can alter its pose, as shown in Fig (1b)-(1c)-(1d), where the needle pose has been explicitly changed. Robot kinematics can not cope with these disturbances, the prediction fails and propagates the error on the next iterations (top). The vision-based correction of our filter allows to detect the needle movements due to disturbances, and adjust the estimation accordingly (bottom). On the other hand, Fig (1e) shows a scenario where the vision-based detection fails, because the projected ellipse of the circular needle is degenerate on the image plane of the camera (top). However, kinematics information provided by the robot allows to maintain a stable estimation of the needle, even when this is not clearly visible. The figures are extracted from the videos that can be found at the link <http://www.diag.uniroma1.it/~labrob/research/ekfNeedleTracking.html>.

CONCLUSION AND DISCUSSION

In this work we propose an EKF-based approach to estimate the pose of the suturing needle during robot-assisted laparoscopic procedures. The filter fuses the kinematic information from the robot proprioceptive sensors with the visual information provided by a monocular endoscopic camera. The use of robot kinematics allows to restrict the region of interest in processing the image, thus speeding up computations, and renders the estimation robust with respect to visual occlusions. On the other hand, visual information allows to catch possible unmodeled motions of the needle, e.g., slippage or movements due to the interaction with tissues. Future work include development of robust image processing algorithms for the detection of the needle in realistic experimental setups. In vitro and ex-vivo experiments are planned to validate the approach in increasingly challenging conditions.

REFERENCES

- [1] da Vinci research kit (DVRK) wiki web page.
- [2] J. Chang. Robust needle recognition using Artificial Neural Network (ANN) and Random Sample Consensus (RANSAC). *Applied Imagery Pattern Recognition Workshop (AIPR), 2012 IEEE*, pages 1–3, 2012.
- [3] D. L. De Ipina, P. R. S. Mendonca, and A. Hopper. TRIP: A low-cost vision-based location system for ubiquitous computing. *Personal and Ubiquitous Computing*, 6(3):206–219, 2002.
- [4] A. Fitzgibbon, M. Pilu, and R. B. Fisher. Direct least square fitting of ellipses. *IEEE Transactions on Pattern Analysis and Machine Intelligence*, 21(5):476–480, 1999.
- [5] S. Thrun, W. Burgard, and D. Fox. *Probabilistic Robotics (Intelligent Robotics and Autonomous Agents)*. The MIT Press, 2005.
- [6] N. Trawny and S. I. Roumeliotis. Indirect Kalman Filter for 3D Attitude Estimation A Tutorial for Quaternion Algebra Indirect Kalman Filter for 3D Attitude Estimation A Tutorial for Quaternion Algebra 1 Elements of Quaternion Algebra 1.1 Quaternion Definitions. 2005.
- [7] F. Wengert, L. Bossard, C. Baur, G. Székely, and P. C. Cattin. Endoscopic navigation for minimally invasive suturing. *Computer aided surgery : official journal of the International Society for Computer Aided Surgery*, 13(5):299–310, 2008.
- [8] F. Zhong, D. Navarro-alarcon, Z. Wang, Y.-h. Liu, T. Zhang, H. M. Yip, and H. Wang. Adaptive 3D Pose Computation of Suturing Needle Using Constraints From Static Monocular Image Feedback. In *2016 IEEE/RSJ International Conference on Intelligent Robots and Systems (IROS)*, pages 5521–5526, 2016.

Widening Siamese Neural Networks for Stereo Matching in Colonoscopy

P. Brandao¹, E. Mazomenos¹, A. Rau¹, M. Janatka¹, D. Stoyanov¹

¹Centre for Medical Imaging, University College London
patrick.brandao.15@ucl.ac.uk

INTRODUCTION

Colorectal cancer is the third most common cancer worldwide [1] and, although the fourth deadliest form of cancer, early diagnosis can increase the survival rate significantly. As the quality of colonoscopy diagnosis highly depends on the proficiency of the operator, computer-aided systems have been researched aiming to improve the detection rate of polyps during the procedure. While segmentation algorithms have improved the accuracy of polyp detection on observed surfaces, 3D reconstruction of the colon has the potential to unveil unscanned areas and to provide instructions to the operator guiding the colonoscopy in a manner that guarantees the observation of the entire inner surface of the colon.

3D reconstruction from stereo images has been actively researched for many decades. Recent work has focused on improving stereo matching cost functions which describe the correspondence between two pixels algebraically. However, the performance of stereo algorithms depends on the choice of the cost-function, which might not be ideal for different environment conditions. Despite the progress in the field, accurately finding stereo correspondences in colonoscopy/surgery images is still very challenging because of occlusions, reflective surfaces, repetitive patterns, and textureless or low detail regions-.

Recent research has aimed to discard hand-crafted cost-functions and hand-selected parameters entirely. First approaches proposed to train Convolutional Neural Nets (CNNs) to compare two input images and output a similarity measure [2] or to directly output a depth map [3].

We apply similar Deep Learning methods but with small considerations for colonoscopy. We aim to improve the 3D reconstruction of the colon so we can provide better diagnostic information in clinical settings.

MATERIALS AND METHODS

We construct our stereo matching network with a two branch Siamese architecture by layering 7 blocks of 3×3 2D convolutions with 64 neurons, batch normalization and a Rectified Linear Unit (ReLU). The parameters in both branches are shared. The last layers are added without batch normalization and ReLU operations.

Endoscopic procedures present challenges for stereo matching due to the lack of discriminative features in the environment. We address this issue by incorporating pooling operations within our model, which allows a much wider global receptive field [4]. We use two max-pooling layers stacked between every other pair of convolution blocks, widening the global receptive field

from 15 to 28 pixels. This allows the CNN to extract more visual cues and helps more accurate matching, especially in textureless regions or areas of aperture problems. We compensate the loss of detail from down-sampling by using transpose convolution (deconvolution) layers. We implement the same amount of 2 strided 3×3 deconvolutions as the number of max-poolings before computing any correlation metric. An illustration of our architecture is presented in Figure 1.

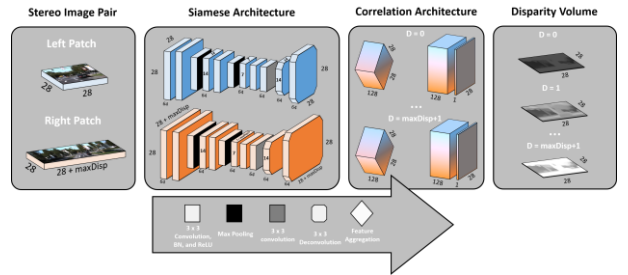


Figure 1 - Representation of our 7-layered stereo matching CNN.

We use an inner product layer as a correlation metric between feature vectors extracted from the Siamese branches like Luo et al. [3]. The operation is computationally efficient, fast and differentiable, which allows backpropagation during training. This layer allows the CNN to learn feature extractors that minimize the inner product of two corresponding points.

We train our models with stereo image pairs from the KITTI dataset [5], where the true displacement of a sparse number of pixels is known. We randomly extract small patches from the left and the right image. This allows to sample diverse training batches while being memory efficient. We treat each disparity value as a mutually exclusive classification problem. The values outputted from the correlation step are used to compute a softmax loss. All parameters are learned with stochastic gradient descent and gradients are backpropagated using the standard Adam optimization [6].

The proposed CNN was trained for 75K iterations with an initial learning rate of $1e-3$. We sampled batches by randomly extracting $32 \times 28 \times 28$ patches from the left image and $32 \times 28 \times 156$ patches from the right one. The CNN model was implemented in Tensorflow [7] and run on a NVIDIA Titax-X GPU.

The final disparity map computed by the CNN can be used with standard stereo point triangulation to project the 2D images to a 3D space.

RESULTS

As a preliminary study, we validate our method using a PVA-C colon phantom manufactured from a 3D model

of a human colon. Data was acquired using a stereo camera from a *da Vinci Surgical System*. The camera was calibrated and stereo image pairs were rectified before being processed by our CNN.

An example of a 3D reconstruction using the disparity map computed with our Siamese architecture is presented in Figure 2.

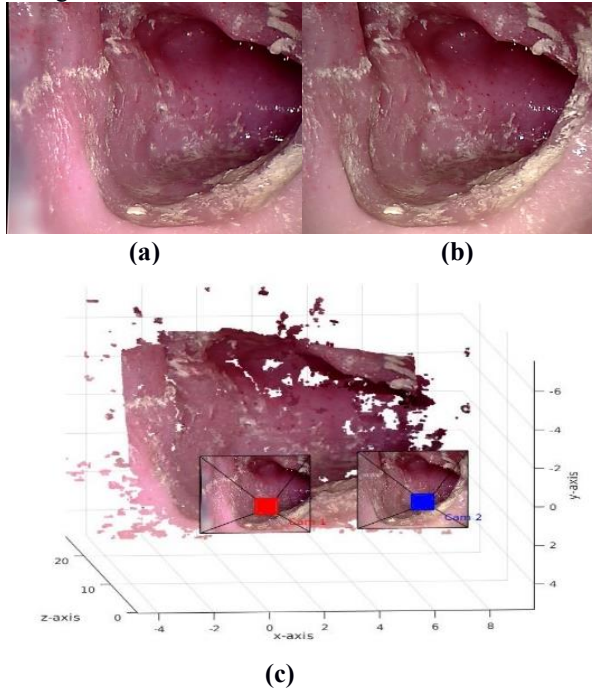


Figure 2 - (a) left and (b) right stereo image. (c) Example of 3D reconstruction of a stereo image pair using a disparity map computed by our CNN.

CONCLUSION AND DISCUSSION

Acquiring ground truth for stereo reconstruction of our colon phantom is complicated by spatial restrictions. Because of this, we limit our analysis to a qualitative evaluation.

Figure 2 shows that the 3D reconstruction faithfully reflects the original phantom environment. The tubular structure is maintained and the shape of the visible folds is also present. Considering that every single pixel is matched individually, without any type of spatial regularization or post-processing, a very dense and cohesive point cloud was obtained. This shows how powerful our Siamese architecture is for the image matching task. This is even more impressive considering that the model was trained to match natural outdoor street view images.

Despite the positive result, a significant amount of points are incorrectly reconstructed. Again, because no spatial consistency is guaranteed, pixels that are mismatched create a series of isolated points in the 3D space. Moreover, because the CNN outputs a dense disparity map, occluded pixels are also reconstructed. This creates gaps in the colon surface and a miss-reconstructed “cloud” of points corresponding to occluded pixels. One example of this is the occluded area from the fold in the right top corner.

Standard post-processing pipelines that minimize spatial irregularities can still be applied to our method in order to minimize the reconstruction error. Furthermore, our model can also be expanded to allow spatial regularization to be learned from data, following the same principle suggested by Kendall et al. [8].

In our future work, we intend to develop an unsupervised training method that would allow matching by learning environment specific features, independently of the existence of ground truth, one of the main limitations in clinical applications.

REFERENCES

- [1] Torre, L. A., Bray, F., Siegel, R. L., Ferlay, J., Lortet Tieulent, J., & Jemal, A. (2015). Global cancer statistics, 2012. CA: a cancer journal for clinicians, 65(2), 87-108.
- [2] Jure Zbontar and Yann LeCun. Stereo matching by training a convolutional neural network to compare image patches. *Journal of Machine Learning Research*, 17(1-32) 2016.
- [3] Wenjie Luo, Alexander G Schwing, and Raquel Urtasun. Efficient deep learning for stereo matching. In *Proceedings of the IEEE Conference on Computer Vision and Pattern Recognition*, pages 5695–5703, 2016.
- [4] Haesol Park and Kyoung Mu Lee. Look wider to match image patches with convolutional neural networks. *IEEE Signal Processing Letters*, 2016.
- [5] Moritz Menze and Andreas Geiger. Object scene flow for autonomous vehicles. In *Conference on Computer Vision and Pattern Recognition (CVPR)*, 2015.
- [6] Diederik P. Kingma and Jimmy Ba. Adam: A method for stochastic optimization. *CoRR*, abs/1412.6980, 2016. URL: <http://arxiv.org/abs/1412.6980>.
- [7] Martín Abadi, Ashish Agarwal, et al. TensorFlow: Large-scale machine learning on heterogeneous systems, 2015. URL <http://tensorflow.org/>. Software available from tensorflow.org.
- [8] Alex Kendall, Hayk Martirosyan, Saumitro Dasgupta, Peter Henry, Ryan Kennedy, Abraham Bachrach, and Adam Bry. End-to-end learning of geometry and context for deep stereo regression. *arXiv preprint arXiv:1703.04309*, 2017.

Multi-region segmentation of IVUS images for endovascular procedures

Tom Eelbode, Phuong Toan Tran, Jos Vander Sloten, Emmanuel Vander Poorten

Department of Mechanical Engineering, KU Leuven

tom.eelbode@gmail.com

INTRODUCTION

Typical endovascular procedures consist in percutaneously inserting a catheter into a blood vessel and steering the catheter to the region of interest. An accurate localization of the catheter with respect to the vessel is essential to successfully guide the catheter. X-ray imaging is traditionally used for visualization despite the exposure to ionising radiation and the low visibility of soft tissues. The latter requires intermittent injection of a nephrotoxic contrast agent [2], lengthens the procedure time and can potentially cause haemorrhagic events due to a puncture of the vessel wall [4].

Actuation and sensing units embedded in robotic catheters have the potential to help the surgeon to safely steer the catheter through the vasculature. Intravascular ultrasound (IVUS) is of particular interest, as it offers a detailed live view of the blood vessels from the inside. Placed at the catheter tip, an IVUS probe generates a radial ultrasound image that can be segmented to recognise the lumen, the adventitia and risk-prone regions, such as calcifications or bifurcations. The automated online segmentation of these regions can then be used to safely steer the catheter – either manually or robotically. This work investigates and improves upon three segmentation methods of IVUS images, and compares their performance and their potential for improving catheter steering.

METHODS

Three different methods are here investigated for the segmentation of the vessel lumen, adventitia and calcifications. The first method is mainly based on wavelet denoising, adaptive thresholding and propagation of a gradient vector flow snake (GVFS). Although originally devised for IVUS images generated in simplified mock-ups [4], wavelet denoising allows extending its use to real IVUS images. The method is however only suitable for segmenting the lumen contour.

The second method consists in denoising the IVUS image using wavelets, enhancing the image contrast and propagating a morphological snake (MS) to segment the lumen and the adventitia [3]. The temporal continuity and coherence of sequential frames is used to effectively improve the convergence speed of the morphological snake between frames.

The third method uses a support vector machine (SVM) to classify image pixels into lumen, adventitia or calcifications [5]. Four features are used here for the classification: the wavelet denoised image, the maximum intensity average, the inverse maximum intensity average and the distance to the catheter.

DATASETS AND MEASURES

Two different datasets are used to evaluate the three methods. Dataset A is extracted from a standardised and publicly available database [1]. It contains IVUS images with labels for the lumen and the adventitia, but not for calcifications. To compensate for the lack of calcification labels, dataset B was gathered from the University Hospital Leuven database. IVUS images of dataset B were manually labelled with the lumen, adventitia and calcifications. The evaluation of the lumen and adventitia segmentation follows the standardised framework based on the Jaccard measure (JM), the percentage of area difference (PAD) and the Hausdorff distance (HD) [1]. The JM is a number between 0 and 1 quantifying how much the area of the ground-truth overlaps with the segmented region (with 1 for a full overlap). The PAD is the difference between the area enclosed by the ground-truth contour and the segmented one. It is normalised relative to the ground-truth area. The closer this measure is to 0, the less area difference. Finally, the Hausdorff distance measures how far two subsets of a metric space are separated from each other. It is the longest of all Euclidean distances from a point in one subset to the closest point in the other subset.

RESULTS

The general performance of the three methods over both datasets is reported in Table 1. Examples of segmentation results are displayed in Figures 1 and 2. The methods were implemented in C++ and executed on an Intel Core i7-3610QM CPU (2.3 GHz) in a single thread. When comparing computation times (Table 1), only the GVFS method can process IVUS images acquired at 30 fps, which is the typical acquisition rate for, e.g., the Volcano IVUS system (Koninklijke Philips N.V., Amsterdam, The Netherlands).

When looking at the segmentation of the lumen boundary, the GVFS method has the best overall performance,

closely followed by the MS method. The SVM method has a significantly lower performance for the three measures. When looking at the detection of the adventitia border, the SVM method performs the best, while the MS method has a lower performance. The latter is to be expected because the border of the adventitia appears less clearly than the lumen, which can prevent the snake to evolve further than the lumen border. The GVFS method is not applied for the adventitia, as it was not devised for it.

Table 1: Median and interquartile range of the three measures and computation time for each segmentation method over the two datasets. An empty cell indicates that this method was not applied.

Region	Dataset	Measure	GVFS	MS	SVM
Lumen	A	JM	0.86 ± 0.07	0.82 ± 0.10	0.68 ± 0.16
		PAD	0.09 ± 0.06	0.13 ± 0.12	0.24 ± 0.25
		HD	2.44 ± 1.85	3.16 ± 2.45	2.81 ± 0.57
Lumen	B	JM	0.47 ± 0.21		0.52 ± 0.22
		PAD	0.48 ± 0.69		0.39 ± 0.49
		HD	7.65 ± 4.46		6.35 ± 3.75
Adventitia	A	JM		0.60 ± 0.18	0.71 ± 0.12
		PAD		0.39 ± 0.19	0.25 ± 0.36
		HD		6.80 ± 3.30	5.04 ± 1.99
Adventitia	B	JM			0.63 ± 0.15
		PAD			0.47 ± 0.51
		HD			6.18 ± 2.35
Computation time [ms]			26.65 ± 1.10	80.58 ± 30.90	137.30 ± 12.80

From the images in which no calcification is present (i.e. the ground-truth segmentation for this region was empty), the SVM method mistakenly indicates that there is some calcification in 87% of the cases. In the case that there is calcification present in the image, the SVM correctly recognises these areas in 72% of the cases. Some examples of segmentation for the SVM method are shown in Figure 2.

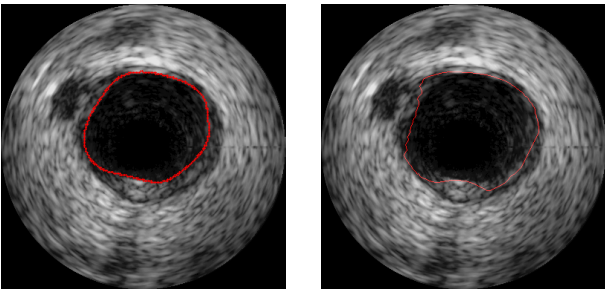


Figure 1: Segmentation of the lumen (red). Left: GVFS method. Right: MS method.

CONCLUSION AND DISCUSSION

This paper investigates three different methods for the segmentation of the lumen, adventitia and calcifications. Depending on the region of interest, one or the other method may be preferred. The GVFS better segments the vessel lumen, while the SVM is capable of additionally detecting the adventitia and calcifications. However, as it is capable of segmenting all three regions, the SVM method may have the most potential, despite its

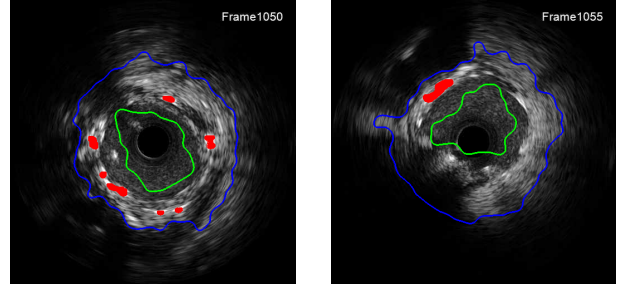


Figure 2: SVM-based segmentation (green: lumen, blue: adventitia, red: calcifications)

lower accuracy for lumen detection and the large over-classification of calcifications. Over-classification of calcifications could be addressed with a feature set that is more adequate for segmenting these specific regions. To increase the accuracy of the lumen segmentation, the GFVS or MS output could be used as an additional feature for the SVM classification, yielding a hybrid method. Computation time of the SVM could be improved with massive parallelisation. The extra information generated by an automated online segmentation of IVUS images has then the potential to help steering robotic catheters in a safer way, ultimately leading to safer and shorter endovascular procedures.

REFERENCES

- [1] S. Balocco, C. Gatta, F. Ciompi, A. Wahle, P. Radeva, S. Carlier, G. Unal, E. Sanidas, J. Mauri, X. Carillo, et al. Standardized evaluation methodology and reference database for evaluating ivus image segmentation. *Computerized Medical Imaging and Graphics*, 38(2):70–90, 2014.
- [2] C. Briguori, D. Tavano, and A. Colombo. Contrast agent-associated nephrotoxicity. *Progress in cardiovascular diseases*, 45(6):493–503, 2003.
- [3] M. Mrabti and H. Ali. Intravascular ultrasound image segmentation using morphological snakes. *IJ Image, Graphics and Signal Processing*, 5.
- [4] C. Shi, S. Giannarou, S.-L. Lee, and G.-Z. Yang. Simultaneous catheter and environment modeling for trans-catheter aortic valve implantation. In *2014 IEEE/RSJ International Conference on Intelligent Robots and Systems*, pages 2024–2029. IEEE, 2014.
- [5] L. L. Vercio, J. I. Orlando, M. del Fresno, and I. Larrabide. Assessment of image features for vessel wall segmentation in intravascular ultrasound images. *International journal of computer assisted radiology and surgery*, pages 1–11, 2016.

Deeply Learned 2D Tool Pose Estimation for Robot-to-Camera Registration

K.K. Maninis¹, A. Chhatkuli¹, J. Pont-Tuset¹, S. Hecker¹, T. Probst¹, M. Ourak², E. Vander Poorten², L. Van Gool^{1,2}

¹Computer Vision Lab, ETH Zürich

²KU Leuven

kmaninis@vision.ee.ethz.ch

INTRODUCTION

Robot-assisted eye surgery is the central topic of the EU funded project EurEyeCase. Major objectives of the project comprise the development of methodologies to perform two surgical procedures that cannot be easily carried out by human surgeons, namely retinal vein cannulation and retinal membrane peeling. In the proposed assistive system, visual guidance is provided from a camera mounted on the microscope. In order to guide the robot using visual cues, it is necessary to register the camera coordinates to the robot coordinates.

To this end, we propose a framework that estimates the position and the pose of the tool to register the two different coordinate systems. Using recent advances in convolutional neural networks (CNNs), we present a comparative study among different intuitive architectural designs, and suggest a methodology to register the coordinates by detecting pre-defined keypoints. Results suggest that tool pose estimation can be highly accurate, running in real-time on a GPU.

MOTIVATION

Visual guidance of a robot from visual cues of a camera requires accurate calibration between the camera and the robot. In the case of retinal surgery, results obtained by post-processing of the imaging system such as segmentation of the veins, and marking of no-go areas, may be used as a feedback to the robot, and thus to the surgeon [1]. To achieve registration of the 3D coordinates of the robot to the 2D coordinates of the camera, one needs to work on the projection equation of a pinhole camera:

$$p = KR^T(P - C) \quad (1)$$

which models the projection of a 3D point $P = \{X, Y, Z\}$ into a pixel $p = \{x, y\}$ of the image, through the camera. K is the intrinsic matrix of the camera. The unknowns of Eq. 1 are the 3D rotation matrix R (3 DoF - Euler angles), and the 3D translation matrix C (3 DoF). To solve this system of 6 unknowns in total, we need 3 pairs of $\{p_i, P_i\}$ correspondences, each of which contributes 2 linearly independent equations. This is in fact a well-studied problem, the solution of which can be obtained through the P3P algorithm [2], once the correspondences are established. This requires the detection of the predefined locations of the tool in each image and its 2D pose.

Recent advances in computer vision employ CNNs to detect keypoints in images for a variety of tasks, the most representative of which is human pose estimation

[3, 4]. We adapt such deep learning techniques to establish the correspondences between the robot and the camera, by detecting pre-defined keypoints on the surgical instrument, which is attached to the robot. The advantages of using the surgical instrument is two-fold: (a) The 3D location of the keypoints can be retrieved by the kinematics of the robot (b) during normal use of the instrument, the corresponding 2D locations are always observable by the camera.

DATA GATHERING AND LABELING

To train supervised deep learning algorithms we need to manually annotate our dataset. We selected frames from 8 video sequences acquired by the microscope. The labeled database consists of 400 annotated frames, each annotated with 3 distinguishable keypoints of the tool. The instrument is a grasper designed for membrane peeling. The tooltips and the junction (grasper joints) are selected as the keypoints. We use 6 of the video sequences to train the CNN models, and the remaining 2 to validate the results. Extensive data augmentation was used to prevent overfitting. All architectures are trained from scratch, with randomly initialized weights.

ARCHITECTURAL DESIGNS

There have been numerous different CNN designs proposed in the literature for various tasks. We examine them separately to select the one most suited for the task. In Figure 1, a combination of such architectures is illustrated.

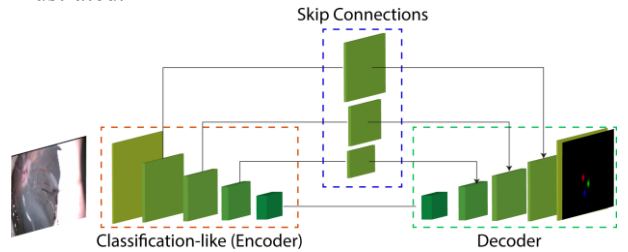


Figure 1: Different architectural designs for Convolutional Neural Networks.

Classification-like: The classification-like architecture was originally used for large scale image recognition, and consists of successive steps of convolutions, ReLU non-linearities, and max-pooling layers. The pooling layers are used to downsample, and produce invariant, semantically rich features in the deeper layers of the CNNs. The downside of such architectures is that they cannot be directly used for tasks that require spatially variant output, like pose estimation, or segmentation. The reason is that it is difficult to recover from the

heavy downsampling, which results in coarse, blobby results (as shown in Figure 2).

Encoder-Decoder: To overcome the effects of downsampling, the encoder-decoder network consists of layers that learn how to gradually upsample the result. In fact, the decoder is added to the head of a classification-like architecture, performing the opposite procedure. The encoder-decoder architecture is able to recover from the coarse scales of the deeper layers.

Skip-Connections: The basic features in the shallow layers of a CNN have proven to be very helpful for many tasks that need detailed output. Skip connections provide a combination of low-level and semantically rich features, usually by concatenation or summation.

Residual blocks: Changing the simple convolutional block to the residual block, proposed in [5], provides a considerable improvement to the results. The idea behind this architecture is that the output G of a layer can be modelled as the sum of its input and a residual, as $G(x) = x + res(x)$. This way, the network only needs to learn the residual, instead of the entire transformation. Indeed, the residual blocks can be trained faster than the simple convolutional ones.

Stacked models: The authors of [3] and [4] proposed an architecture which consists of repetitive downsampling and upsampling phases. This design, referred to as the Stacked Hourglass, takes advantage of successive coarse and fine features, and has been proven very successful in human pose estimation. We observe that these networks lead to the best results in our task.

All architectures were implemented using the PyTorch framework. Training each architecture takes roughly 1 hour, while the inference time is always faster than 30 Hz on a modern GPU.

RESULTS

We evaluate the performance on the validation videos of the EurEyeCase tool pose dataset. For the quantitative evaluation of our study, we use the PCK metric, which measures the accuracy of localization, for each keypoint. In PCK, a detection is correct if it falls in a neighbourhood around the label. The distances are normalized by the distance d of the tooltip to the joint, in each frame. We present results for PCK@0.1, meaning that results that are mislocalized by more than $0.1d$ are considered as false detections.

Results in Table 1 suggest that the classification-like architecture provides inaccurate results for the task, with large errors in pose estimation. The encoder-decoder architecture works a lot better, and provides more accurate results when enriched with skip connections and residual blocks. Finally, by using a stack of modules we observe a further boost in accuracy, reaching 97.2% for the task. This result proves that tool pose estimation can provide accurate correspondences for the desirable 3D-to-2D registration.

Table 1: Quantitative evaluation of keypoint localization, using the PCK@0.1 measure.

Architecture	Top	Middle	Bottom	Mean
Classification-like	08.8	08.8	03.8	07.1
Encoder-Decoder	57.5	72.5	83.8	71.2
+ Skip connections	86.1	86.1	84.7	85.6
+ Residual Blocks	90.0	90.0	87.5	89.2
+ Stacked Modules	98.6	95.8	97.2	97.2

Qualitative results are illustrated in Figure 2, for the baseline and the improved architecture. The classification-like architecture shown on the left, seems to suffer from downsampling, leading to highly uncertain results. The improved version, which uses all the aforementioned developments leads to much more certain, and accurate localization of the keypoints.

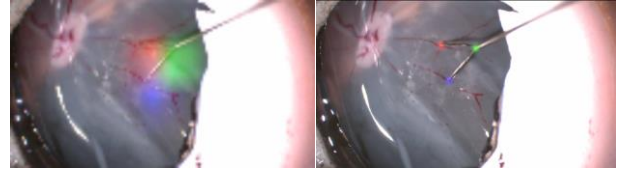


Figure 2: Pose estimation qualitative examples: Left: Classification-like Network, Right: Improved Architecture

CONCLUSIONS AND DISCUSSION

We have presented a study of different CNN architectures to tackle the task of 2D tool pose estimation and localization. Results on our manually annotated dataset show that by using suitable network designs, it is possible to reach almost perfect accuracy for the task. In the future, we would like to reach our end goal of robot-to-camera registration, by using the estimated tool pose.

ACKNOWLEDGEMENTS

This work is funded by the EU H2020 project EurEyeCase – Grant Agreement No 645331.

We thank Georgios Pavlakos and Michal Havlena for all fruitful discussions.

REFERENCES

- [1] K.K. Maninis, J. Pont-Tuset, P. Arbelaez, L. Van Gool. "Deep Retinal Image Understanding", in MICCAI, 2016
- [2] X. Gao, X. Hou, J. Tang, H. Cheng. "Complete Solution Classification for the Perspective-Three-Point Problem". IEEE TPAMI, 2003
- [3] A. Newell, K. Yang, J. Deng. "Stacked Hourglass Networks for Human Pose Estimation", in ECCV, 2016
- [4] G. Pavlakos, X. Zhou, K. G. Derpanis, K. Daniilidis. "Coarse-to-Fine Volumetric Prediction for Single-Image 3D Human Pose" in CVPR, 2017.
- [5] K. He, X. Zhang, S. Ren, J. Sun. "Deep Residual Learning for Image Recognition", in CVPR, 2016

Robotic stabilization of cardiac catheter-tissue contact using endoscopic imaging

B. Rosa^{1,2}, G. Fagogenis¹, M. Mencattelli¹, J. Ha¹, P.E. Dupont¹

¹Cardiac Surgery Department, Boston Children's Hospital, Boston, MA, USA

²ICube, CNRS, University of Strasbourg, Strasbourg, France
b.rosa@unistra.fr

INTRODUCTION

Catheters have been widely adopted as a way of reducing invasiveness of cardiac surgery through beating-heart intracardiac procedures. However, the lack of dexterity for tissue manipulation, combined with an inability to visualize in detail the tissue, have limited the range of procedures.

It was recently shown that cardioscopy can provide high-resolution imaging during tissue contact [1]. Combining this imaging modality with robotic control can provide the needed dexterity to perform complex intracardiac procedures. A fundamental challenge is however to mediate the contact between the robot tip and a moving cardiac tissue to ensure that the interaction forces are not excessive. Previous work has used a combination of ultrasound imaging and force sensors [2]. Alternatively, this paper proposes an image-based contact stabilization algorithm.

Cardioscopic imaging makes use of a chip-on-tip camera and an LED, embedded into a soft optical window. Pressing the tip of the optical window against the tissue displaces the blood at the interface and shows the tissue. Noting that images during contact are significantly different from noncontact images of blood, we propose an image-based contact estimator. A controller is then designed to regulate the contact over a desired fraction of the cardiac cycle, using safe low-bandwidth tip movements. This paper describes the image-based controller together with *in vivo* validation results.

MATERIALS AND METHODS

We propose to use a supervised machine learning algorithm – Bag of Features (BoF) [3] – to estimate the contact state. Given a set of manually labeled images, a set of image descriptors is computed and input to the algorithm together with labels for training. After training, the algorithm outputs the contact state c of a given input image taken at time t :

$$c(t) = \begin{cases} 1, & \text{contact} \\ 0, & \text{no contact} \end{cases} \quad (1)$$

The features are obtained using the FAST feature detector [4] and LUCID descriptor [5] are used. This allows good performance with a low computational burden, allowing the estimation of c at video rate.

Next, let's define the contact ratio r as a fraction of the cardiac cycle during which contact occurs. We propose a controller that will control the position of the robot tip in order to regulate r to a desired value r^d . Noting that the motion of heart structures can be considered to be locally uniaxial, the controller will

operate in the local direction of motion, noted x . r can then be expressed as a function of robot tip position, $x(t)$, and heart position, $x_h(t)$, along the direction of motion. This is illustrated in Fig. 1 for a valve annulus.

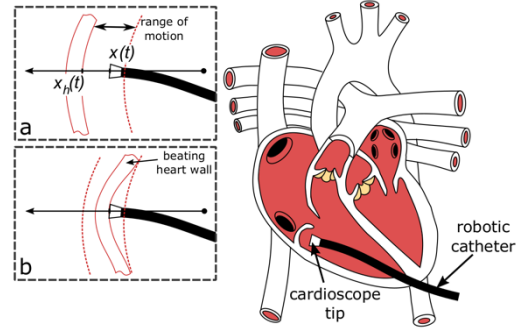


Fig. 1 Transapically-inserted robotic catheter approaching the pulmonary valve annulus to perform intracardiac surgery. (a, b) show the contact between the catheter at position $x(t)$ and the heart for two extremes of the wall movement $x_h(t)$.

Assuming that the measured heart frequency, $1/T_c$, is known and slowly varying, the contact ratio can be estimated as

$$r(t) = \frac{1}{T_c} \int_{t-T_c}^t c(x(u), x_h(u)) du \quad (2)$$

Contact stabilization is then achieved by controlling the position of the robot tip using the following proportional derivative control:

$$\dot{x} = K_p(r^d - r) - K_d \dot{r} \quad (3)$$

Under the assumptions that heart rate remains stable or slowly varying and that the contact ratio does not saturate, $r(t) < 1$, controller stability can be demonstrated using the candidate Lyapunov function:

$$V(r) = \frac{1}{2} (r^d - r)^2 \quad (4)$$

The proposed controller being uniaxial, contact will be stabilized at the robot tip following the main direction of the local heart movement. Orthogonal directions can be controlled by the operator using teleoperation for navigating along the plane of contact, in a shared control scheme.

EXPERIMENTAL VALIDATION

To validate the approach, the contact state estimator was first trained and evaluated. Subsequently, the controller was tuned in bench experiments and tested in an *in vivo* porcine model.

The image-based contact estimator was validated on cardioscopic images taken from six *in vivo* experimental

surgeries, performed using five different cardioscopes (Fig. 2). A total of 1540 images were selected to build a balanced dataset, which was divided into three subsets: 70% for training; 15% for tuning algorithm parameters; and 15% for validation. The trained contact state estimator exhibited an overall accuracy of 95.4% on the test dataset. The average computational time (core i7 CPU) was 2.63msec per image, which is compatible with the video rate of the camera used (48 frames /s).

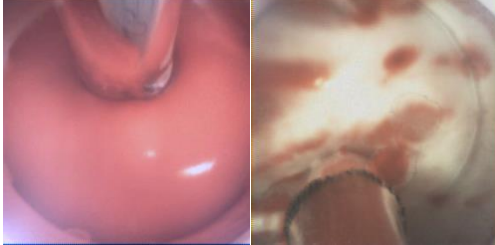


Fig. 2 Sample cardioscopic images. Left: No contact; right: Contact.

A concentric tube robot with a cardioscopic camera at its tip was used for both bench and *in vivo* experiments. In bench experiments, a heart movement of 75 beats-per-minute was simulated using an oscillating target. Starting from a distance of several centimeters, the contact controller was turned on so that the robot approached the target to stabilize at a desired contact ratio of $r^d = 0.5$. The gains of the controller were then tuned at with $K_p = 8$, $K_d = 3$, obtaining an overdamped response.

Finally, the controller was validated in an *in vivo* porcine model (Fig.3). The robot was inserted apically into the heart so that its z-axis would approximately point towards the aortic valve. It was then manually navigated towards the valve, and the controller was activated, regulating the contact ratio to the desired value r^d . The heart rate, $1/T_c$, was obtained in real-time from an electrocardiogram, a device which is always present in the OR during cardiac surgery. Fig.4 depicts the step response of the controller as the robot moves, to set points of $r^d = \{0.3, 0.4, 0.6, 0.7\}$. After an initial transient, the desired contact ratios are achieved and maintained over a period of more than 20 seconds.

DISCUSSION

Force sensing and haptics is often cited by surgeons as a missing element of robotic surgery, generating many research works on the topic. Integrating force sensors in minimally invasive instruments, and developing stable control laws is however still a challenge in many applications. Moreover, high-speed robot movements required to regulate forces on a beating heart wall could prove dangerous in intracardiac surgery if the controller fails.

The proposed technique combining cardioscopy and image-based contact stabilization provides a means for overcoming these challenges that does not rely on force sensing nor on high-bandwidth catheter motion. The method was validated first on the benchtop, and then on an *in vivo* porcine model, showing the potential of the proposed technique in a surgical setting. Further work will go towards the evaluation of this controller in a

shared control teleoperation scheme, where the operator controls the navigation movement in the plane of contact, while the controller regulates the contact ratio in the direction normal to the plane of contact.



Fig. 3. Test set up for *in vivo* evaluation of the proposed controller in the context of paravalvular leak closure.

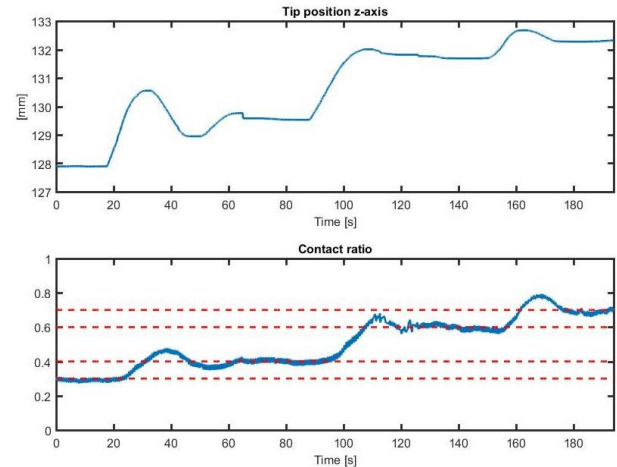


Fig. 4. Step response of contact ratio controller for a sequence of set points (red dotted lines) in an *in vivo* porcine model.

ACKNOWLEDGEMENT

This work was funded by the NIH under grant R01HL124020.

REFERENCES

- [1] A. Ataollahi, I. Berra, N.V. Vasilyev, Z. Machaidze, P. E. Dupont, "Cardioscopic Tool-delivery Instrument for Beating-heart Surgery", *IEEE/ASME Trans. Mechatronics*, vol. 21, no. 1, pp. 584-590, 2016
- [2] S. B. Kesner and R. D. Howe, "Robotic catheter cardiac ablation combining ultrasound guidance and force control," *The International Journal of Robotics Research*, vol. 33, no. 4, pp. 631–644, 2014.
- [3] Fei-Fei, Li, and Pietro Perona. "A bayesian hierarchical model for learning natural scene categories." *Computer Vision and Pattern Recognition, 2005. CVPR 2005. IEEE Computer Society Conference on*. Vol. 2. IEEE, 2005.
- [4] E. Rosten and T. Drummond, "Fusing points and lines for high performance tracking," in *IEEE International Conference on Computer Vision*, vol. 2, October 2005, pp. 1508–1511.
- [5] A. Ziegler, E. Christiansen, D. Kriegman, and S. J. Belongie, "Locally uniform comparison image descriptor," in *Advances in Neural Information Processing Systems*, 2012, pp. 1–9.

Session 6

Sensing and Classification

Task Classification of Robotic Surgical Reconstructive Procedures using Force Measurements

M. Selvaggio, G.A. Fontanelli, F. Ficuciello, L. Villani, and B. Siciliano

Department of Information Technology and Electrical Engineering, Università degli Studi di Napoli Federico II

INTRODUCTION

The development of surgical tasks and skills level classification methods and its combination with adaptive assistance strategies is a very promising approach in robotic surgery. In order to employ adaptive and time-varying shared control methods, such as virtual fixtures [1], task classification constitutes an essential step. It allows to assess surgeon skills and intentions in both training and real interventions. Our objective is to develop a reliable method for the automatic classification of surgical tasks. This procedure is often challenging if it relies only on kinematic information. Vision sensors might be employed but they usually require fine parameters tuning and a huge programming effort. Hence, we propose to adopt the interaction force measurement in the learning process. In this paper, a force-based unsupervised segmentation approach of reconstructive surgical gestures is presented. In the past, similar approaches have been investigated: Zappella et al. have proposed several methods for automatic surgical gesture classification using video and kinematic data [2]; Pierre et al. have developed a human collaborative framework for bimanual surgical tasks based on learned model where they combine active constraints and learning from demonstration [3]; in the work of Despinoy et al. the operating gesture workflow has been taken into account, in order to provide more intuitive training as well as more accurate solutions for procedural knowledge assessment [4]; in the work of Perez-Del-Pulgar et al. the authors address the problem of learning from demonstration trajectories that depend on contact forces instead of depending solely on time [5]. In our work, we use force and kinematic data to train a Gaussian Mixture Model (GMM) in order to cluster subtasks during a robotic surgical reconstructive procedure. Comparing our approach with the manual annotations of the surgical gestures, an average matching score of 88.32% is observed for the fully automated gesture recognition process.

MATERIALS AND METHODS

Our experimental setup is composed by the da Vinci Research Kit commanded in teleoperation mode via open controllers¹. The user teleoperates the Patient Side Manipulators (PSMs) using the Master Tool Manipulators (MTMs) by observing the scene through the endoscopic stereo camera. The complete robot dynamical model has been previously identified in order to estimate external

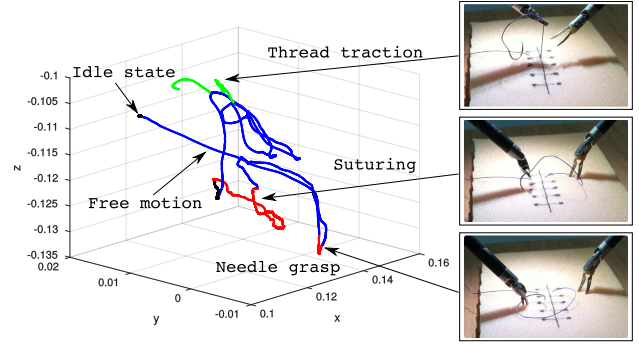


Fig. 1. Example of task classification during a robotic surgical reconstructive procedure. The graph on the left depicts the Patient Side Manipulator tool tip Cartesian trajectory segmented using our approach. The pictures on the right represent some relevant suturing states.

forces from motor current measurements [6]. This method has been used in combination with a recently developed force sensor integrated into the robot trocar [7] that is able to measure the interaction forces (components orthogonal to the instrument's axis) between the tool tip and the environment. The adopted force sensor guarantees a resolution of 0.01 N and a range of measurement of $[-10, 10]$ N that are suitable for measuring interaction forces between the surgical instrument and soft tissues throughout most of robot-aided surgical interventions. This is also the case of in-vivo suturing procedures where the forces can be of very low intensity ($\|f\| \leq 1$ N) during the interaction with the tissues but also $\|f\| \geq 5$ N, in some cases, when the thread traction is executed. During our experiments the PSMs Cartesian state (positions and velocities) and the measured forces are collected at a sampling rate of 200 Hz. In addition, an external Kinect2 RGB camera is used to collect videos of the training and test procedures which are lately exploited to verify the accuracy of our method. ROS is employed to collect all the data in a synchronized way. During the demonstration phase we obtain a sequence of n elements of sensory information $\hat{x}_n = (x_1, x_2, \dots, x_n)$. At each time step we encode a tuple $x_i = (p_i, v_i, f_i)$ with p_i being the Cartesian position of the manipulator, v_i its velocity and f_i the force exerted at the tool tip. These data are classified in an unsupervised way using GMM and Expectation-Maximization (EM) approach (see Fig. 1). A GMM is parametrized by two types of values: the mixture component weights and the component means and variances/covariances. For a multivariate GMM with K components, the k^{th} component has a mean μ_k and covariance matrix Σ_k . Given a tuple x the probability that

¹<https://github.com/jhu-dvrk>

this belongs to an encoded GMM is:

$$P(x) = \sum_{k=1}^K \phi_k \mathcal{N}(x | \mu_k, \Sigma_k) \quad (1)$$

where \mathcal{N} denotes the classical multivariate normal distribution and the sum of ϕ_k is unitary:

$$\mathcal{N}(x | \mu_k, \Sigma_k) = \frac{\exp\left(-\frac{1}{2} (x - \mu_k)^T \Sigma_k^{-1} (x - \mu_k)\right)}{\sqrt{(2\pi)^K |\Sigma_k|}} \quad (2)$$

$$\sum_{k=1}^K \phi_k = 1 \quad (3)$$

The log-likelihood function of a GMM can be written as follows:

$$L(\hat{x}_n) = \sum_{i=1}^n \log(P(x_i)) \quad (4)$$

The learning objective is to find a set of GMM parameters that maximizes Eq. (4). To this end, the EM algorithm iteratively maximizes the likelihood of a statistical model given the training sequence \hat{x}_n and a predefined number of Gaussians. In this work, we have chosen this value to be $K=4$ in order to identify four states of a surgical reconstructive procedure. This value has been established in a heuristic way by observing several surgical reconstructive interventions performed by expert surgeons. We have used 30 suturing procedures as training set and evaluated the unsupervised classification procedure using 2 sequences. Both the training and the test data have been *offline* processed using the Statistical and Machine Learning Toolbox in MATLAB.

RESULTS

In order to validate our clustering procedure we trained the GMM and performed the evaluation using test set data. Demonstration and test phases consisted of suturing procedures conducted on a sponge phantom intended to act as dummy tissue. The result of a classification test is shown in Fig. 2. Here, only the time history of the measured force norm is reported, since it represents the most significant quantity for this evaluation. For the sake of clarity, only PSM1 data and states are shown but same results hold for PSM2. The four states we aimed at identifying were: *idle*, *interaction*, *free motion* and *thread traction*. To give an insightful explanation of the graph, the teleoperated robot is, at the beginning, in the *idle* configuration, then starts to move to perform its first action, *i.e.* needle grasping. The *interaction* state identified between 75 and 80 s is due to the contact occurred with the tissue while grasping the needle. Then, the operator moves and the next contact is detected while the needle is passing the phantom between 82 and 92 s. Successively, a new *idle* state is identified while the needle is regasped by the PSM2. A *free motion* state is identified during the process of thread scrolling performed in alternation with the PSM2. Finally, the *thread traction* state concludes the suturing procedure. Our method allows to classify

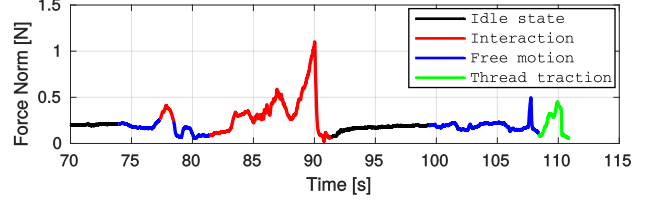


Fig. 2. Force norm variation during a reconstructive procedure used as test set. Different states are classified and shown using different colors.

the correct sequence of states with 88.32% of accuracy during the fully automated gesture recognition process. This result has been calculated by comparing the obtained results to manually annotated data. The annotation phase have exploited the above mentioned recorded videos.

CONCLUSIONS AND DISCUSSION

This paper demonstrates that is feasible to use interaction force information to reliably classify the states of a robotic surgical reconstructive procedure. A GMM has been trained using a set of demonstrations performed by expert surgeons and has been used to cluster test sets. The presented method allows the fully automated gesture recognition with an accuracy of 88.32% with respect to manual annotations of the surgical gestures. These results are encouraging in sight of the development of adaptive assistance strategies for robotic aided surgical interventions. However, some limitations of the method have been identified. Indeed, the use of position information does not allow spatial generalization. Moreover, with the adoption of GMM and force measurements, it is difficult to distinguish between different contact states, *e.g.* needle grasping and suturing. As future works, further investigations on the use of solely differential quantities (velocities), and on the exploitation of tasks sequence information are needed.

REFERENCES

- [1] M. Selvaggio, G. Notomista, F. Chen, B. Gao, F. Trapani, and D. Caldwell, "Enhancing bilateral teleoperation using camera-based online virtual fixtures generation," in *IEEE/RSJ International Conference on Intelligent Robots and Systems*, Oct 2016, pp. 1483–1488.
- [2] L. Zappella, B. Béjar, G. Hager, and R. Vidal, "Surgical gesture classification from video and kinematic data," *Medical Image Analysis*, vol. 17, no. 7, pp. 732 – 745, 2013.
- [3] P. Berthet-Rayne, M. Power, H. King, and G. Z. Yang, "Hubot: A three state human-robot collaborative framework for bimanual surgical tasks based on learned models," in *IEEE International Conference on Robotics and Automation*, May 2016, pp. 715–722.
- [4] F. Despinoy, D. Bouget, G. Forestier, C. Penet, N. Zemit, P. Poignet, and P. Jannin, "Unsupervised trajectory segmentation for surgical gesture recognition in robotic training," *IEEE Transactions on Biomedical Engineering*, vol. 63, no. 6, pp. 1280–1291, 2016.
- [5] C. J. Perez-Del-Pulgar, J. Smisek, V. F. Munoz, and A. Schiele, "Using learning from demonstration to generate real-time guidance for haptic shared control," in *IEEE International Conference on Systems, Man, and Cybernetics*, Oct 2016, pp. 3205–3210.
- [6] G. A. Fontanelli, F. Ficuciello, L. Villani, and B. Siciliano, "Modelling and identification of the da Vinci research kit robotic arms," in *2017 IEEE/RSJ International Conference on Intelligent Robots and Systems*.
- [7] G. A. Fontanelli, L. Buonocore, F. Ficuciello, L. Villani, and B. Siciliano, "A novel force sensing integrated into the trocar for minimally invasive robotic surgery," in *2017 IEEE/RSJ International Conference on Intelligent Robots and Systems*.

Confidence-based abdominal tissue classification in laparoscopy

S. Moccia^{1,2,3}, S. J. Wirkert³, H. G. Kenngott⁴, A. S. Vemuri³, M. Apitz⁴, B. F. B. Mayer⁴, E. De Momi¹, L. S. Mattos², L. Maier-Hein³

¹*Department of Electronics, Information and Bioengineering, Politecnico di Milano, Milano, Italy*

²*Department of Advanced Robotics, Istituto Italiano di Tecnologia, Genoa, Italy*

³*Department of Computer Assisted Medical Intervention, DKFZ, Heidelberg, Germany*

⁴*Department for General, Visceral, and Transplantation Surgery, Heidelberg University Hospital, Heidelberg, Germany*

sara.moccia@iit.it

INTRODUCTION

Surgical data science (SDS) [1] is an emerging research field that aims at improving healthcare through the analysis of clinical data. One of the major SDS challenges is the detection and localization of tissues in the field of view (FOV) of the camera. Indeed, despite the topic of organ classification has already been investigated in the literature, the translation of the proposed methodologies to the clinical practice is still hampered by their low robustness.

In this paper, we aim at addressing this issue in the specific context of abdominal tissue classification. The contribution of this paper is two-fold: (1) we propose an approach to anatomical tissue classification, which features a measure of confidence to estimate its own level of performance; (2) with a comprehensive in vivo analysis conducted with 7 pigs, we evaluate the performance of our method when applied to both conventional RGB imaging and laparoscopic multispectral imaging (MI). This is the first time that in vivo laparoscopic MI data are exploited to abdominal tissue classification. Further, this is the first attempt of including classification confidence estimation in this specific context. The detailed description of the proposed methodology can be found in [2].

MATERIALS AND METHODS

In this section, we present the proposed approach to anatomical structure classification and the validation protocol designed to evaluate it.

Anatomical structure classification

Laparoscopic images are acquired using a custom-build laparoscope. The imaging system includes a Richard Wolf laparoscope (Knittlingen, Germany) and a 5-MP Pixelteq Spectrocam (Largo, FL, USA). The laparoscope acquires multispectral images in 8 light bands, with wavelengths centered at 470, 480, 511, 560, 580, 600, 660 and 700 nm. The full-width at half-maximum (FWHM) is 20 nm for all light channels except for the 480 nm band, for which FWHM is 25 nm. Since the laparoscope does not provide RGB images directly, the 470, 560 and 700 nm bands are elected as RGB bands. To obtain the reflectance image (R) from the multispectral image (I), the dark reference image (D) is subtracted from I. The result is then divided by W-D, where W is the white reference image. D and W are respectively acquired with the camera shutter closed and with a white reference board in the FOV. Anisotropic diffusion filtering is applied on R to lower the noise level while preserving sharp edges in the image. In this paper, we extract features from superpixels (Spx), using all pixels in a Spx. Spx are better suited than regular grid because they are built to adhere to boundaries in the image. This is useful when dealing with multiple organs in the same image. Linear spectral clustering [3] is applied to the RGB image to obtain the Spx segmentation. The Spx segmentation mask is then used for the other channels. To characterize abdominal tissues, we exploit both texture-based and reflectance-based features. The texture information is encoded in the normalized

histogram of uniform rotation-invariant local binary pattern (H_{LBP}). The average reflectance value inside a Spx is used as reflectance feature (AS). Feature classification is performed with support vector machines (SVM) with the radial basis function and one-against-one scheme. The SVM hyperparameter (γ and C) are retrieved with grid-search and cross-validation on the training set. To evaluate the classification confidence, we estimate the dispersion of class probabilities using Gini's coefficient (GC). Such probabilities are computed by training the parameter of a sigmoid function to map the SVM output to probabilities. Spx for which GC is lower than a threshold (τ) are considered non-confident and excluded.

Validation protocol

We used 7 pigs to evaluate the proposed approach. We used 3 pigs for training (29 images) and 4 for testing (28 images). We considered 6 abdominal tissues: liver, spleen, abdominal wall, diaphragm, intestine, and gallbladder. Our dataset included different challenges, such as large variety of illumination and endoscope pose, organ movement, and the presence of multiple organs in one image. The Spx segmentation was achieved imposing an average Spx size of 150^2 pixels and a compactness factor of 0.1. The H_{LBP} was computed using the following combination of radius and distance: (1, 8), (2, 16) and, (3, 24). The SVM hyperparameter grid search space was $[10^8, 10^1]$ and $[10^1, 10^{10}]$ for γ and C , respectively, with 10 values spaced evenly on the \log_{10} scale. To evaluate the performance of our algorithm, we computed the classification accuracy ($\mathbf{Acc}_{class} = \{Acc_{class_j}\}_{j=[1, J=6]}$), where J is the number of considered abdominal tissues. Acc_{Spx} is defined as:

$$Acc_{class_j} = \frac{TP_j}{TP_j + FN_j}$$

where TP_j and FN_j are the number of true positive and false negative of the j^{th} class, respectively. The gold-standard classification was obtained by labeling each superpixel under the supervision of two expert surgeons.

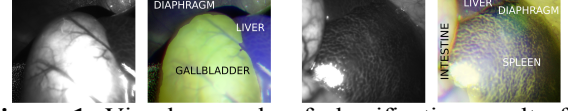


Figure 1. Visual example of classification results for two multispectral images. MI channel (left) and classification results (right).

To assess whether the confidence inclusion influences the classification performance, we computed \mathbf{Acc}_{class} , for different thresholding values on the GC ($\tau \in [0.6:0.1:0.9]$). We used the Wilcoxon signed-rank test (significance level = 0.05) to assess if there were significant differences between RGB and MI, both with and without the confidence inclusion.

RESULTS

When considering the classification performance without including the confidence measure, the median value (inter-quartile range) of \mathbf{Acc}_{class} was 81% (20%) for RGB and 90% (6%) for MI (p-value < 0.05). When including the confidence measure, the median \mathbf{Acc}_{class} monotonically increased to 93% for RGB and 99% for MI and $\tau = 0.9$ (p-value < 0.05). Visual samples of classification results are given in Fig. 1.

CONCLUSION AND DISCUSSION

With our in vivo validation protocol, we showed that: (1) MI data are more suitable for anatomical structure classification than conventional RGB data, and (2) including a classification confidence measure increases the classification performance. A major strength of this method is its high accuracy, which could be a valuable tool for SDS applications in laparoscopy.

REFERENCES

- [1] Maier-Hein L, et al. "Surgical Data Science: Enabling Next-Generation Surgery," *arXiv preprint*, arXiv, 2017.
- [2] Moccia, S, et al. "Uncertainty-Aware Organ Classification for Surgical Data Science Applications in Laparoscopy." *arXiv preprint arXiv:1706.07002* (2017).
- [3] Li, Z, et al. "Superpixel segmentation using linear spectral clustering," *Proceedings of the IEEE Conference on Computer Vision and Pattern Recognition*, 2015.

A Novel Force Sensor Integrated into the da Vinci Trocar for Minimally Invasive Robotic Surgery

G. A. Fontanelli, F. Ficuciello, L. Villani, and B. Siciliano

Department of Information Technology and Electrical Engineering, Università degli Studi di Napoli Federico II

INTRODUCTION

Minimally invasive robotic surgery (MIRS) has revolutionized surgical and therapeutic procedures by changing their effect on patients and significantly reducing collateral damages. On the other hand, the loss of tactile sensation can potentially lead to tissues damage and bad execution of particular surgical tasks, such as suturing and operational decisions that would require feeling the tissue deformation. One of the most challenging problem regards the force sensing in the surgical scenario. On this purpose many prototypes of sensorized surgical instruments have been developed by integrating force sensors in the instrument shaft or wrist, or even in the gripper fingers and clamp faces. For instance, in [1] a prototype of 6-axis FBG-based force sensor located between the wrist and the gripper of the surgical instrument is developed; in [2] a solution that uses FBG sensors integrated in the instrument shaft to measure the forces on the orthogonal plane of the surgical instruments is presented; on the other hand solutions for sensing the forces directly on the surgical gripper are evaluated in [3] and [4], using capacitive and piezoelectric effect. All the above-mentioned works have in common the fact that they require the modification of the instrument structure to integrate the force sensor. This entails higher costs, problems related to the tendon-driven actuation, greater likelihood of instrument breakage, the need of sensorize properly instruments with different characteristics. In this work, a new solution for a force sensor collocated at the end-tip of the trocar is evaluated. With respect to the state of the art, this solution allows measuring the interaction forces between the surgical instrument and the environment without any changes to the instrument structure and with full adaptability to different robot platforms and surgical tools. The sensor would be capable of measuring the forces in the orthogonal plane of the surgical instruments along the axis x_S and y_S in Fig. 1. As a matter of fact, the concerned two components are difficult to be reconstructed using the robot dynamical model. On the other hand, the force exerted along the axis of the instrument shaft is easier to be reconstructed due to the prismatic joint actuation.

MATERIALS AND METHODS

The innovation of the proposed approach consists on conceiving the structure, hosting the sensor element, to be allocated at the end-tip of the trocar. This permits the indirect measurement of the interaction forces between the instrument end-effector and the patient body by means of

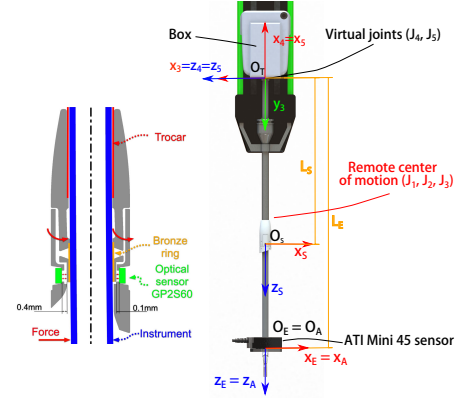


Fig. 1. The Da Vinci PSM arm front view and the sensor static characterization setup.

non-allocated forces generated by the displacement of the instrument shaft with respect to the fixed trocar pipe. Our first prototype is designed to guarantees a resolution of 0.1 N in a range of $[-10, 10]$ N that are common values in robotic surgical procedure.

Working principle

A detailed explanation of the inherent operating principle follows. A little gap between the instrument shaft and the trocar exists to guarantee the reciprocal sliding. When the forces are exerted on the instruments end-effector, the component acting in the plane orthogonal to the instrument axis causes a dis-alignment between the instrument and the trocar axes (Fig. 1). This leads to contacts between the trocar, where it is placed the sensor, and the instrument. In those contact points the forces are discharged causing deformation of elastic frames that compose the sensor. The main idea is to measure the dis-alignment between the instrument shaft and the fixed trocar using four proximity optical sensors mounted in appropriate way. This solution have some advantages with respect to the state of the art: (i) the measure is not influenced by the tendon driven mechanism, as happens for the sensors solutions located in the instrument shaft or wrist; (ii) the connection cables and the data acquisition system are fixed and far away from the surgical site; (iii) the sensor (structure and acquisition system) is cheap and could be disposable.

Mathematical model

In this section a brief description of the sensor model is reported, for the sake of brevity, only the static model is considered. The dynamical model of the instrument

shaft must be taken into account to reduce the effects of its dynamics on the measure. However, we found experimentally that the dynamic effects of the robot motion on the sensor measurements are negligible when instruments with low mass and inertia are used. For further information refer to [5]. In order to estimate the forces on the robot end-effector the prismatic joint position must be explicitly considered. The force on the sensor is related to the force on the instrument end-effector by means of simple geometrical consideration. In particular, we consider two virtual joints in the O_T point, J_4 and J_5 represented in Fig. 1, where the instrument shaft is connected to the instrument's box that slides in the prismatic joint guide. We consider the tube as rigid, thus the static model can be obtained simply considering a frame fixed to the box and centered in O_T . The two jacobian matrices $J_S(q) \in \mathbb{R}^{2 \times 2}$ and $J_E \in \mathbb{R}^{3 \times 2}$ in (1) map, on the virtual joints, the forces acting on the sensor and on the end-effector.

$$J_S(q) = \text{diag}(L_S, L_S) \quad J_E = \begin{bmatrix} \text{diag}(L_E, L_E) \\ \mathbf{0} \end{bmatrix} \quad (1)$$

where $L_S = (0.43 - q_3)$, $L_E = 0.389$ and q_3 is the position of the robot prismatic joint.

For the static equilibrium of the forces, results that

$$\begin{cases} \tau_G = J_E^T f_E \\ \tau_G = J_S^T(q) f_S \end{cases} \implies f_E = (J_E^T)^\dagger J_S^T(q) f_S \quad (2)$$

where $\tau_G \in \mathbb{R}^2$ is the torque vector of the two virtual joints, $f_S \in \mathbb{R}^2$ and $f_E \in \mathbb{R}^3$ represent the two vectors of the forces in the sensor frame and in the end-effector frame, respectively.

RESULTS

The validation of the sensor performances is obtained by two experiment: (i) comparison between our solution and a commercial torque-force sensor (ATI Mini45); (ii) estimation of the interaction forces between the needle and the tissues during a complete suturing procedure. In both the experiment the da Vinci research kit in telemanipulation mode was used to control the instruments in real-time. More in detail, in the first experiment the ATI sensor was fixed in correspondence to the end effector frame of the surgical instrument (see Fig. 1); a force to the ATI sensor was applied while the surgical instrument was in motion along the J_3 axis with the linear law reported in Fig. 2 bottom. The force measured by the ATI sensor, the force measured by the trocar sensor projected in the end-effector frame using the equation 2, and the relative error have been reported in Fig. 2. The results show that the sensor has a good response close to that of the commercial sensor ATI mini 45 with an error less then 12% for both the axis. In the second experiment the high resolution of the proposed sensing system was proved during a complete suturing procedure. In Fig. 3 is possible to evaluate the ability of the sensor to sense forces with very low intensity (less then 0.5 N) during the interaction between the suturing needle and the tissues.

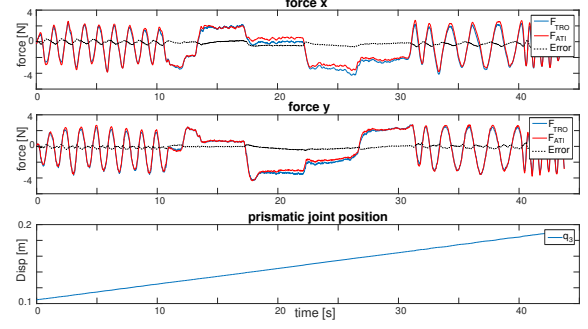


Fig. 2. Comparison between the force measured by a commercial ATI Mini 45 force/torque sensor and by the proposed solution while the instrument is in motion along the PSM prismatic joint J_3

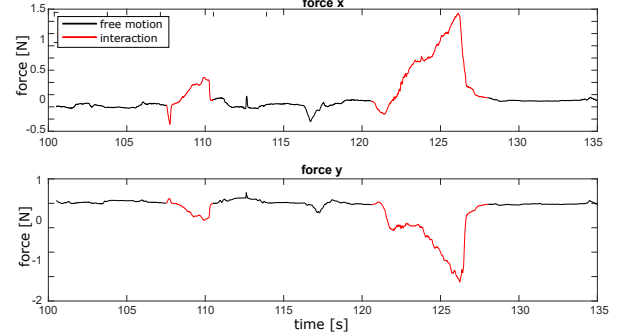


Fig. 3. Needle-tissues interaction force estimation during a suturing procedure (in red is highlighted the interaction between the needle and the tissue).

CONCLUSION AND DISCUSSION

In this work a new concept of force sensing for MIRS is evaluated. The proposed solution differs from the force sensors presented in the literature since does not require the modification of the surgical instruments, but exploits the possibility of placing the force sensor on the trocar. This opens the way for new disposable, low cost and simple force sensors that allowing the haptic feedback on different set-up even on clinical robotic surgical systems currently used in operating rooms. The prototype presented in the paper is printed using 3D printing technology only for proof of concept. In future works a prototype suitable to be used in a real surgical scenario will be developed.

REFERENCES

- [1] R. Haslinger, P. Leyendecker, and U. Seibold, "A fiberoptic force-torque-sensor for minimally invasive robotic surgery," in *IEEE International Conference on Robotics and Automation*, 2013.
- [2] R. Xu, A. Escoto, K. Shahzada, C. Ward, and R. Patel, "A method for installing FBG sensors inside surgical robotic instruments," in *The Hamlyn Symposium on Medical Robotics*, 2016, pp. 22–23.
- [3] U. Kim, D. H. Lee, H. Moon, J. C. Koo, and H. R. Choi, "Design and realization of grasper-integrated force sensor for minimally invasive robotic surgery," *IEEE International Conference on Intelligent Robots and Systems*, pp. 4321–4326, 2014.
- [4] M. O. Culjat, C.-H. King, M. L. Franco, C. E. Lewis, J. W. Bisley, E. P. Dutson, and W. S. Grundfest, "A tactile feedback system for robotic surgery," *International Conference of the IEEE Engineering in Medicine and Biology Society*, pp. 1930–1934, 2008.
- [5] G. A. Fontanelli, L. Buonocore, F. Ficuciello, L. Villani, and B. Siciliano, "A novel force sensing integrated into the trocar for minimally invasive robotic surgery," in *2017 IEEE/RSJ International Conference on Intelligent Robots and Systems*.

Contact force sensor for flexible manipulators for MIS (minimally invasive surgery)

Pawel Gawenda¹, Yohan Noh^{1, 2}, Jan Fras³, Sangjin Han⁴, Shuangyi Wang¹,
Richard Housden¹, Kaspar Althoefer³, Kawal Rhode¹

¹Department of Biomedical Engineering, King's College London, UK

²Department of Informatics, King's College London, UK

³Faculty of Engineering Science, Queen Mary University of London, UK

⁴Department of Electrical and Computer Engineering, Texas A & M University, USA

(Corresponding author: yohan.noh@kcl.ac.uk)

INTRODUCTION

In a master-slave robot-assisted surgery system, it is of critical value to recognise surgical conditions through sensing elements, since surgeons operate surgical instruments that are inside the body by remote control. A force sensor, one of the sensing elements, assists to feel the sense of telepresence [1-2]. With a 'good' force sensor, surgical manipulators are able to generate the path planning to minimise tissue damage [3]. We propose a design method for a contact force sensor for flexible surgical manipulators using an optoelectronic sensing element (light intensity based sensor). The design approach is oriented toward low-cost, miniaturised-size, low-level electrical noise, and simple fabrication by 3D-printing. We explain the sensing principle, describe the design methodology, and present preliminary experiment results.

MATERIALS AND METHODS

1) Sensing principle

External force at the flexure is computed using sensing elements in two steps. The sensing elements attached on the flexure measure deformation, or deflection, when external force presents. The external force is then estimated using the measurement values from the sensors. Three optoelectronic sensors were chosen as the sensing elements.

An optoelectronic sensor (NJL5901R-2, 1.0mm x 1.4

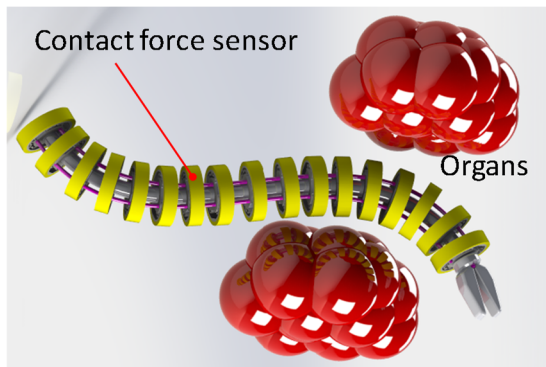


Figure 1. Contact force sensors with a flexible manipulator for MIS (Minimally Invasive Surgery) designed by Solidworks

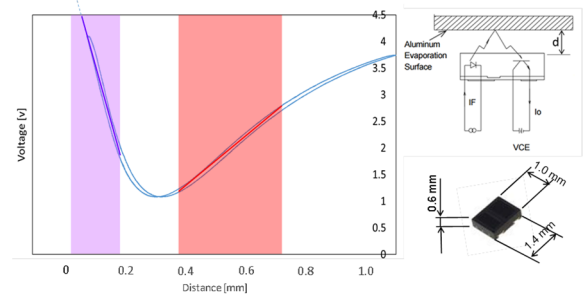


Figure 2. Characteristic of optoelectronic sensor NJL5901R-2 (New Japan Radio Co., Ltd, Japan) from experiments

mm x 0.6mm, New Japan Radio Co., Ltd) consists of an LED (light source) and a photo transistor (converting light intensity into electrical current.) Figure 2 shows the characteristic curve between the output voltage of the sensor and the reflector (mirror) distance, denoted as d . It is easy to see that we have two 'linear' sensing ranges that are highlighted in purple and red. Since the sensor reacts more sensitively in the purple range than in the red range, we choose to fabricate the sensing element which measures distances less than 0.2 mm.

2) Contact force sensor

A contact force sensor consists of a PCB, reflectors, optoelectronic sensors (NJL5901R-2), resistors (for LED and photo transistor), and a sensor mechanical structure [4-5]. The structure is fabricated using a Visijet EX200 via a Projet HD 3000 3D production system as shown in Figures 1 and 3. The outer diameter and height are chosen to be 15 mm and 3.5 mm, respectively, in order to be passed through the MIS trocars. We note that the diameter is not as small as the trocars commonly used in surgical environments which is from 6 mm to 10 mm.

In Figure 3 (top), the mechanical structure of the contact force sensor is designed based on a double S-shape beam, and measures three distances d_1 , d_2 , and d_3 . F_x and F_y are computed by the distances as verified in the FEA (Finite Element Analysis) simulation. The estimation statistics are 3.0% maximum error and less than 1.5% crosstalk. Figure 3 (bottom) shows the

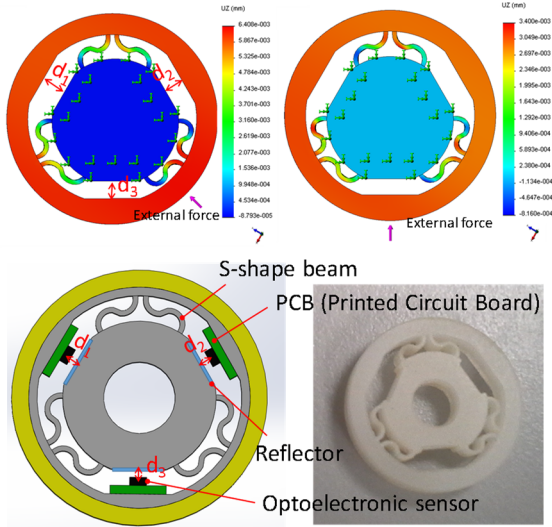


Figure. 3. Measuring three distances whilst external force is applied in FMA Simulation (Solidworks Simulation) and measuring three distances on the sensor structure using three optoelectronic sensors.

geometrical configuration of the optoelectronic sensors and reflectors.

EXPERIMENT AND RESULTS

We carried out an experiment for the relationship between voltages and physical contact force in two steps: 1) obtaining the voltage data of each optoelectronic sensor and 2) calculating the calibration matrix. In Figure 4 (left) a commercial force sensor in the x-z stage is fixed on the linear guide. The fabricated contact force sensor is mounted on the mounting base. The sensor is rotated and fixed at different angles (in increments of 22.5 degrees) as shown in Figure 4 (right). The linear guide moves along the y-axis to load and unload external force at each angle.

Table 1 shows the actual external forces F_x and F_y and the errors from the computed values at different angles. When comparing the amount of RMS error with the actual force applied, our sensor structure showed good performance for all angles except 67.5° and 112.5°. We provide remarks on these cases in the next section.

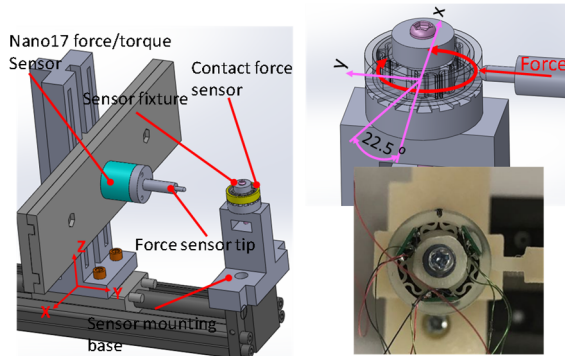


Figure. 4. Calibration device (designed by Solidworks) and a prototype of the contact force sensor.

TABLE I. Sensor Error Property

FORCE DIRECTION	MAX F_x [N]	MAX F_y [N]	F_x RMS ERROR [N]	F_y RMS ERROR [N]
0°	2.58	0	0.2005	0.0193
22.5°	2.031	0.8412	0.1803	0.0603
45°	1.585	1.585	0.139	0.1046
67.5°	0.8975	2.167	0.3136	0.1511
90°	0	2.439	0.0628	0.1674
112.5°	0.951	2.296	0.2019	0.1735
135°	1.536	1.536	0.083	0.1213
157.5°	2.125	0.8804	0.1534	0.1314
FORCE DIRECTION	MAX F_x [N]	MAX F_y [N]	F_x RMS ERROR [N]	F_y RMS ERROR [N]
180°	2.652	0	0.2341	0.1562
202.5°	2.299	0.9521	0.2287	0.111
225°	1.798	1.798	0.1578	0.179
247.5°	0.83	2.004	0.0762	0.178
270°	0	2.145	0.0525	0.153
292.5°	0.8789	2.122	0.0853	0.1371
315°	1.611	1.611	0.0976	0.0929
337.5°	2.058	0.8523	0.1566	0.0486

CONCLUDING REMARKS

The contact force sensor based on the double S-shape beam estimated the force for most of the directions. However, it has distinct errors in a couple of angles for the following reasons: 1) hysteresis in the material properties of 23.19%, 2) the soldering and wiring attached on the PCB which may constrain the behavior of the sensor structure when the external force exists at certain angles.

The contact force sensor presented here is a prototype designed to pass through MIS trocars. However, its diameter, 15 mm, is not small enough compared with the legacy ones. As future work, a film circuit and a sensor structure printed by a 3D metal printer can be considered in order to improve the overall size of the contact force sensor as well as to reduce hysteresis.

REFERENCES

- [1] R. Haslinger, U. Seibold, et al., "A fiberoptic force-torque-sensor for minimally invasive robotic surgery," IEEE International Conference on Robotics and Automation (ICRA), pp. 4390-4395, 2013.
- [2] S. Sunshine, JT. Handa et al., "A force-sensing microsurgical instrument that detects forces below human tactile sensation," *Retina*, 33(1), 2013.
- [3] H. Xie, Y. Noh, K. Althoefer, et al., "A Fiber-Optics based Body Contact Sensor for a Flexible Manipulator," *IEEE Sensors Journal*, 15(6), 7010881, pp. 3543-3550, 2015.
- [4] A. Cirillo, S. Pirozzi, et al., "An artificial skin based on optoelectronic technology," *Sensors and Actuators A* 212, pp. 110-122, 2014.
- [5] Y. Noh, A. Takanishi, et al., "Development of the Airway Management Training System WKA-1 designed to embed arrays of Sensors into a Conventional Mannequin," *IEEE/RSJ International Conference on Intelligent Robots and System*, pp.1296-1301, 2007.

Development of a new bio-impedance sensor to detect retinal vessel punctures for retinal vein occlusion treatment

L. Schoevaerds, L. Esteveny, A. Gijbels, J. Smits, M. Ourak, G. Borghesan, D. Reynaerts, E. Vander Poorten

Dept. of Mechanical Engineering, KU Leuven
laurent.schoevaerds@kuleuven.be

INTRODUCTION

Retinal vein occlusion is a blockage of a retinal vessel by a clot, preventing a proper circulation of oxygenated blood through the eye. This disease is estimated to affect up to 16.4 million persons worldwide [1]. A curative treatment is still under research. A promising approach, known as retinal vein cannulation, consists of dissolving the clot by injecting a thrombolytic agent directly inside the affected vessel during a few minutes [2]. However, such gesture is complex to perform and presents a great risk for complications due to a combination of limited depth perception, the fragility of the vessels (size from 50 to 400 μm , puncture force below 20 mN) and the disturbance caused by physiological hand tremor (typical RMS amplitude around 180 μm).

Robotic assistance techniques that can stabilize the tool and downscale the surgeon's force or motion have been under study quite some time now. Recently, a first in-human robot-assisted cannulation has been successfully performed [3]. However, whereas the robotic assistance already helps in conducting a controlled puncture, determining the exact instant that puncture takes place remains difficult. By introducing sensorised instruments this part could be simplified and double puncture prevented more easily [4].

In this paper, a new sensitive instrument based on bio-impedance measurement is proposed. Its limited cost and simplicity make it a very promising tool. Bio-impedance sensors have been developed earlier for minimally invasive surgery. Since each tissue layer has a specific impedance, the entry into a new layer could be detected as a change in impedance. Bio-impedance instruments are generally composed of two conductive parts insulated from each other. The biological tissue ensures typically the closure of the electrical path at the instrument tip. Several successful demonstrations of this measurement principle have been reported e.g. in animal, to detect prostate cancer [5], access to the renal collecting system [6] or vessel puncture [7] or in human, to detect the spinal fluid [8].

In the following we introduce a new bio-impedance sensor that was developed to detect the puncture of retinal vessels. A prototype sensor has been integrated into a cannulation needle and measurements have been done showing impedance variations while cannulating retinal vessels of *ex-vivo* pig eyes.

MATERIALS AND METHODS

Instrument

A cannulation needle that has been previously validated in animal trials formed the basis of this work [9]. The needle design has been reconsidered to establish a well

determined electrical path back and forth along the needle axis, basically turning the instrument into a sensor. The principle of this sensor is depicted in **Figure 1**. The instrument tip is composed of a 30 μm glass micropipette with an electrically conductive layer deposited over the glass until the very tip.

Saline solution, which typically already fills the eye globe and replaces the vitreous humour after a vitrectomy, is used here to flush the needle too. Hence, through this electrolyte an electrical path is established through the solution in the needle with the solution in eye globe in contact with the outer coating at the needle tip. Upon an external contact, e.g. in the case of a puncture, this path becomes blocked preventing the ion flow at the needle tip resulting in a measurable change in impedance.

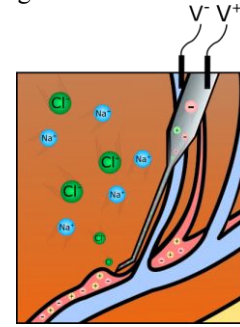


Figure 1. Principle of the bio-impedance sensor

Electrical model

Assuming the impedance from the probe is low enough to be negligible, the electrical path can be schematized as in **Figure 2a** or **Figure 2b**. R_{tip} and C_{dl} represent respectively the resistance from the saline solution and the equivalent double layer capacitance due to ion accumulation at the probe surface when a potential is applied. Their equivalent is the impedance Z_{tip} , which is disturbed by any event occurring at the needle tip. On the other side, C_{ins} (which impedance equivalent is Z_{ins}) is the capacitance from the glass insulating the inner electrical path (lumen of the needle) from the conductive coating. One can easily derive the impedance of the model and compute the sensitivity of phase and magnitude of the total impedance, namely the partial derivatives relatively to R_{tip} and C_{tip} (four equations).

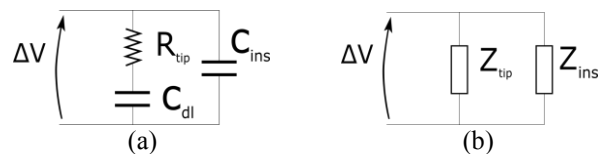


Figure 2. (a) Electrical and (b) simplified electrical scheme of the bio-impedance sensor.

The parameters R_{tip} , C_{dl} and C_{ins} of this model were assessed by sweeping the excitation voltage over a

frequency range from 1 to 100 kHz. For measurement purpose and from the conducted sensitivity analysis an optimal voltage excitation frequency of 6 kHz was found.

RESULTS

In order to prove the feasibility of impedance-based puncture detection methods, experiments on *ex-vivo* pig eyes were conducted. The instrument was introduced in a comanipulation robot that was developed for vitreoretinal surgery [10]. The pig eyes were cut open such that the retinal vessels were easily accessible and exposed in open sky. The vitreous humour was removed and a small volume of saline solution was poured to cover the retinal surface. The instrument tip was therefore surrounded by a solution of Na^+ and Cl^- ions and also the instrument itself was filled with it. Note that the electrical composition of saline solution is very close to that of some thrombolytic agents which could then probably replace the saline solution in the instrument.

The impedance was measured as cannulation attempts were made. It is assumed that the bio-impedance is impacted in two possible ways by a puncture event. First, the impedance will change due to the change of environment, as the electrical path is closed by saline solution or by blood in the vessel. Second, the brief occlusion of the lumen tip while puncturing the vessel wall is expected to also disturb the impedance. While the sensitivity of the sensor mainly affects the first aspect, the second part depends on many factors: the thickness of the blood vessel wall, the pressure in the blood vessel and the puncture speed. Rather than absolute values we therefore expect that impedance variations may more reliably characterize a successful puncture.

To prove the proposed concept, a user was asked to first perform successful punctures of vessels, validated by visual inspection through the microscope binoculars and then, to perform double punctures. A typical example of each case is depicted in **Figure 3** and **Figure 4** where noticeable peaks represent the puncture and the double puncture performed. By multiplying impedance magnitude derivative with impedance phase derivative, clear peaks can be seen to mark the respective puncture events. The data was acquired with the AD5933 device from Analog Devices at a voltage excitation frequency of 6 kHz, with a sampling frequency of 83 Hz. The double puncture shows two peaks, respectively the upper vessel wall puncture and the lower vessel wall puncture. Besides, the experiments showed a negligible difference in terms of impedance between the blood and the saline solution. Therefore, the peak is mainly due to the punctuality of the puncture event.

One can notice the difference of magnitude between the puncture and the double puncture peaks, which might be caused by a pressure drop inside the retinal vessel as the blood gets flushed away. However, the signal-noise ratio is still high enough to detect the puncture events.

CONCLUSION AND DISCUSSION

This work introduced an innovative bio-impedance sensor integrated in a cannulation needle. As far as we are aware, this is the first time this technology has been implemented in an eye surgical context. Through *ex-vivo*

experiments the proposed bio-impedance sensor was shown to have good potential to serve as a low-cost means to detect retinal vessel punctures.

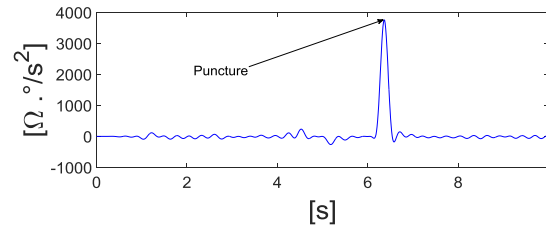


Figure 3. Multiplication of the impedance magnitude derivative by the impedance phase derivative ($\Omega \cdot ^\circ/\text{s}^2$) as a function of the time (s). Detection of a puncture inside a retinal blood vessel.

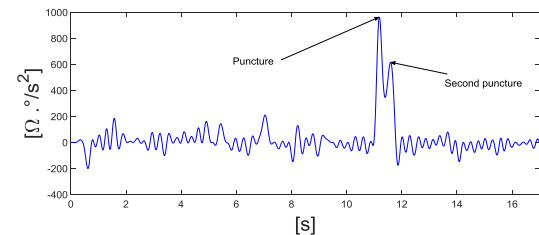


Figure 4. Multiplication of the impedance magnitude derivative by the impedance phase derivative ($\Omega \cdot ^\circ/\text{s}^2$) as a function of the time (s). Detection of a double puncture inside a retinal blood vessel.

ACKNOWLEDGMENTS

Research funded by a C3-fund (3E160419) from KU Leuven.

REFERENCES

- [1] S. Rogers, R. McIntosh, N. Cheung, L. Lim, J. Wang, P. Mitchell, J. Kowalski, H. Nguyen, T. Wong and International Eye Disease Consortium, "The prevalence of retinal vein occlusion: pooled data from population studies from the united states, europe, asia, and australia," *Ophthalmology*, vol. 140, no. 2, pp. 313-319, 2010.
- [2] K. Van Overdam, T. Missotten and L. Spielberg, "Updated cannulation technique for tissue plasminogen activator injection into peripapillary retinal vein for central retinal vein occlusion," *Acta Ophthalmologica*, vol. 93, pp. 739-744, 2015.
- [3] <https://medicalxpress.com/news/2017-01-surgical-eye-robot-precision-patient.html>, 2017.
- [4] A. Gijbels, E. Vander Poorten, P. Stalmans and D. Reynaerts, "Development and experimental validation of a force sensing needle for robotically assisted retinal vein cannulations," in *IEEE ICRA*, 2015.
- [5] B. Lee, W. Roberts, D. Smith, H. Ko, J. Epstein, K. Lecksell, A. Partin and P. Walsh, "Bioimpedance: Novel use of a minimally invasive technique for cancer localization in the intact prostate," *The Journal of Urology*, vol. 162, pp. 1546-1547, 1999.
- [6] D. Hernandez, V. Sinkov, W. Roberts, M. Allaf, A. Patriciu, T. Jarrett, L. Kavoussi and D. Stoianovici, "Measurement of bio-impedance with a smart needle to confirm percutaneous kidney access," *Journal of Urology*, vol. 166, pp. 1520-1523, 2001.
- [7] H. Saito, K. Mitsubayashi and T. Togawa, "Detection of needle puncture to blood vessel by using electric conductivity of blood for automatic blood sampling," *Sensors and Actuators A: Physical*, vol. 125, no. 2, pp. 446-450, 2006.
- [8] S. Halonen, K. Annala, J. Kari, S. Jokinen, A. Lumme, K. Kronström and A. Yli-Hankala, "Detection of spine structures with bioimpedance probe (bip) needle in clinical lumbar punctures," 2016.
- [9] K. Willekens, A. Gijbels, L. Schoevaerdts, L. Esteveny, T. Janssens, B. Jonckx, J. H. M. Feyen, C. Meers, D. Reynaerts, E. Vander Poorten and P. Stalmans, "Robot-assisted retinal vein cannulation in an in vivo porcine retinal vein occlusion model," *Acta Ophthalmologica*, 13 January 2017.
- [10] A. Gijbels, E. Vander Poorten, B. Gorissen, A. Devreker, P. Stalmans and D. Reynaerts, "Experimental Validation of a Robotic Comanipulation and Telemanipulation System for Retinal Surgery," in *IEEE International Conference on Biomedical Robotics and Biomechanics (BioRob)*, São Paulo, Brazil, 12-15 August 2014.

Combined Force and Distance Sensing for Robot-Assisted Vitreo-Retinal Surgery

J. Smits^{1*}, M. Ourak^{1*}, A. Gijbels¹, G. Borghesan¹, L. Esteveny¹, L. Schoevaerds¹, K. Willekens², P. Stalmans², E. Lankenau³, H. Schulz-Hildebrandt⁴, G. Hüttmann⁴, D. Reynaerts¹, E. B. Vander Poorten¹

¹Department of Mechanical Engineering, University of Leuven,

²Department of Ophthalmology, University Hospitals Leuven, ³OptoMedical Technologies GmbH,

⁴Medical Laser Center Lübeck GmbH,

Jonas.smits@kuleuven.be

INTRODUCTION

Vitreo-retinal (VR) surgery is a branch within ophthalmologic microsurgery that encompasses a range of demanding tasks at the posterior side of the eye. Depending on the procedure, a number of incisions are created in the sclera and equipped with sealed trocars, through which the required instruments are inserted. During the procedure, the surgeon looks through a stereoscopic microscope located directly above the patient's eye. Often, additional wide-angled lenses are placed above the patient's eye lens, to enlarge the field of view of the surgeon. The workspace is illuminated by means of a handheld light probe, or a pair of light fibers commonly referred to as "chandeliers". Despite this enhanced visualization of the surgical workspace, physiological hand tremor, limited depth perception and lack of tactile or force feedback contribute to the surgical risk and limit the performance of VR surgery.

Commercially available vitreoretinal instruments do not provide any feedback to the surgeon. Smart sensing instruments acquiring important intraoperative information such as the proximity of the retina and tool interaction forces could help reduce surgical risks and improve surgical outcomes.

Intraoperative Optical Coherence Tomography (iOCT) is an optical imaging technology that can be integrated within the surgical microscope [1]. It offers high resolution images of the eye's anatomy. In the posterior eye segment it has been mainly used to detect the different retinal layers. When used in combination with a light fiber integrated in a VR instrument, OCT can be used to extract the distance between the instrument and the retina [2]. Several prototypes of sensor-integrated vitreoretinal instruments have been reported in the past [3], [4]. However to the knowledge of the authors, no OCT integrated distance sensing microneedle or combined force-sensing and distance sensing instrument has been reported.

This abstract reports on a first proof of concept of a combined force and distance sensing microneedle for vitreo-retinal surgery. An OCT A-scan probe was aligned and mechanically fixed to a previously developed force sensing cannulation microneedle (**Figure 1**). This combination of sensors was used together with a previously developed robotic surgical assistive system to perform a series of retinal vein cannulations on ex-vivo enucleated porcine eyes.

MATERIALS AND METHODS

A previously developed stainless-steel force-sensing microneedle was used, consisting of a force-sensitive shaft based on FBG gratings [5]. The microneedle has an 80 μ m outer diameter tip, which is 30 degrees angulated with respect to the instrument shaft. Axial tip forces are determined by taking advantage of the angulation and measuring radial forces on the force-sensitive shaft. For a similar needle, accuracy and precision were found to be 0.2 mN at a sample rate of 10Hz for forces up to 15 mN [5].

A long range optical distance sensor providing OCT A-scan data was made by the Medical Laser Center Lübeck GmbH and connected via a switch to an iOCT scanner by (OptoMedical Technologies) mounted on a Haag-Streit stereoscopic surgical microscope. OCT A-scan data is collected at a sample rate of 200 Hz. The measurement range of 3,9mm combined with a 1024 pixel CCD sensor

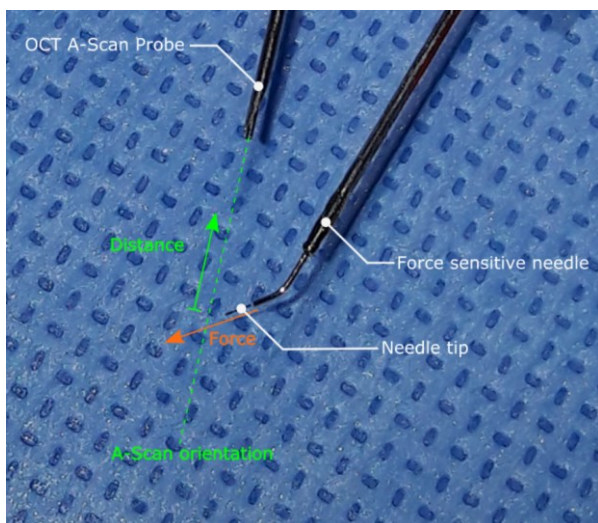


Figure 1. Annotated close-up of sensor combination, positive measuring directions indicated

(*) Both authors equally contributed to this work.

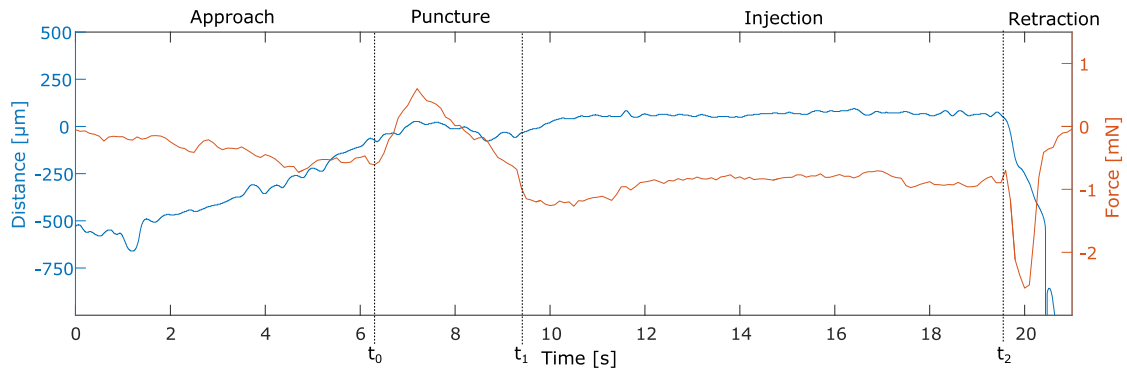


Figure 2. Registered distance (blue, left vertical axis) and force (orange, right vertical axis) data of a retinal vein cannulation on an ex-vivo porcine enucleated eye.

provides a resolution of 3,8 μm . The samples undergo noise reduction, median filtering, and a threshold binary conversion, after which the distance value is extracted by means of first feature recognition. A 3D-printed connector piece was used to align and fixate the force-sensing needle with the distance sensing OCT A-scan probe. The probe is aligned with the instrument axis at an angle of 15° , at a distance of 9 mm from the needle tip (**Figure 1**). Needle tip distance calibration and time synchronization is performed by means of a manually actuated micrometer precision translation stage (Newport, M-423). The needle tip is approached by a non-reflective surface oriented perpendicular to the A-scan direction. A series of steps of 10 μm are applied, with a steady period of 5 seconds. The distance at which forces are registered for the first time is then set as the needle tip reference. After distance calibration, time synchronization is established by matching the derivative sign change of both distance and force signals. A previously developed robotic surgical assistive system was used to perform retinal vein cannulations on ex-vivo enucleated porcine eyes [6]. A total of 7 retinal vein cannulations were performed on 3 eyes by one user. Veins were injected with demineralized water for a period of 10s to confirm correct puncture.

RESULTS

Figure 2 depicts the measured distance and force data during one of the performed cannulations. The sequence can be categorized in four periods. Firstly, the user approaches the targeted vessel. The distance between the retinal surface and the needle tip gradually decreases while forces remain around zero. A low negative force slope can be noticed. It is hypothesized that this is due to a viscous counteracting force caused by remaining vitreous on top of the retina. Secondly, a high positive rise in force level indicates a vessel puncture, at which time measured distance values start to stabilize. After puncturing, a positive distance value can be observed of approximately 65 μm , indicating that the needle tip is underneath the first observed layer. Thirdly, during the injection period both force and distance values remain stable. Finally, after the injection period, the needle is retracted. A steep rise and fall in force levels is observed,

in combination with an increasing distance between retinal surface and needle tip.

CONCLUSION AND DISCUSSION

A first report on the ongoing development of a novel combined force and distance sensing needle is presented. Hereby it is shown that by combining force and distance data by means of respectively FBG and OCT technology, relevant distance and force data can be acquired on ex-vivo enucleated porcine eyes. Future work includes the development of a robust real-time distance sensing algorithm, the design of a novel instrument that allows for both sensing technologies to be used with single port access, and the usage of such an instrument towards safer vitreo-retinal interventions.

ACKNOWLEDGMENTS

Research funded by The EU Framework Programme for Research and Innovation - Horizon 2020 - Grant Agreement No 645331 and an SB Fellowship of the Research Foundation – Flanders (1S41517N).

REFERENCES

- [1] E. M. Lankenau, M. Krug, S. Oelckers, N. Schrage, T. Just, and G. Hüttmann, "iOCT with surgical microscopes: a new imaging during microsurgery," *Adv. Opt. Technol.*, vol. 2, no. 3, pp. 233–239, Jan. 2013.
- [2] G. Borghesan, D. Bouget, E. Lankenau, R. Neffin, and P. Koch, "Single Fiber OCT-based Retina Detection for Robot-assisted Retinal Vein Cannulation."
- [3] M. Balicki, J. Han, and I. Iordachita, "Single Fiber Optical Coherence Tomography Microsurgical Instruments for Computer and Robot-Assisted Retinal Surgery," *Med. Image Comput. Comput. Interv. – MICCAI 2009*, pp. 108–115, 2009.
- [4] B. Gonenc, P. Gehlbach, J. Handa, R. H. Taylor, and I. Iordachita, "Motorized Force-Sensing Micro-Forceps with Tremor Cancelling and Controlled Micro-Vibrations for Easier Membrane Peeling*," pp. 1–22, 2014.
- [5] A. Gijbels, E. B. Vander Poorten, P. Stalmans, and D. Reynaerts, "Development and Experimental Validation of a Force Sensing Needle for Robotically Assisted Retinal Vein Cannulations," *Robot. Autom.*, pp. 2270–2276, 2015.
- [6] A. Gijbels, K. Willekens, L. Esteveny, P. Stalmans, D. Reynaerts, and E. B. Vander Poorten, "Towards a clinically applicable robotic assistance system for retinal vein cannulation," 2016.

Poster Session 1

Augmented Reality Visualization Based On 3D Ultrasonography

Jun Shen^{1,2}, Nabil Zemiti¹, Oscar Caravaca¹, Antoine Simon²,
Jean-Louis Dillenseger², Philippe Poignet¹

¹LIRMM, UMR5506, CNRS/University of Montpellier

²Inserm, U1099; University of Rennes 1, LTSI
jun.shen@etudiant.univ-rennes1.fr

INTRODUCTION

Two main limitations in minimally invasive robotic surgery (MIRS) are the restricted field of view of the workspace and the lack of tactile and force feedback during the intervention. To compensate these limitations and provide complementary information, some MIRS bring ultrasonography (US) into the operating room to image the surgical area in real-time (e.g. [1] used US in transoral robotic resection of oropharyngeal tumors). This information can then be brought into the surgeon view by mean of augmented reality (AR) techniques to guide his/her gesture [2].

In this paper, we propose a simplified and easy to set up US-based AR guidance system. For this, we developed a new joint localization/calibration framework for the three-dimensional (3D) US probe based on an own-designed calibration phantom. This framework associated to stereoscopic camera allowed us to display the information from the US data to video-see-through display device (such as head-mounted display or a console viewer as in the da Vinci Surgical System). The usability of the whole system has been proved in a needle insertion experiment.

SYSTEM OVERVIEW

The objective was to display and overlay the preoperative information (e.g. a 3D model of the target as in Fig.1) to the stereo camera view. In the intraoperative stage, the target was localized by a calibrated 3D US device, as shown in Fig.1. Since the US probe was calibrated with an attached position sensor (an active marker s), the spatial position and orientation of the US data were known in the coordinate system of the position sensor s , and so in the world coordinate system of the tracking system w . Meanwhile, the stereo camera c was also calibrated and localized according to w . This allowed us to register the preoperative information to the camera view. The two key points of this system were the US calibration/localization, and the camera-tracking system calibration.

ULTRASOUND CALIBRATION

The objective of the calibration procedure was to determine a rigid transformation sT_i (Fig.1) between the position sensor attached on the probe and the US data.

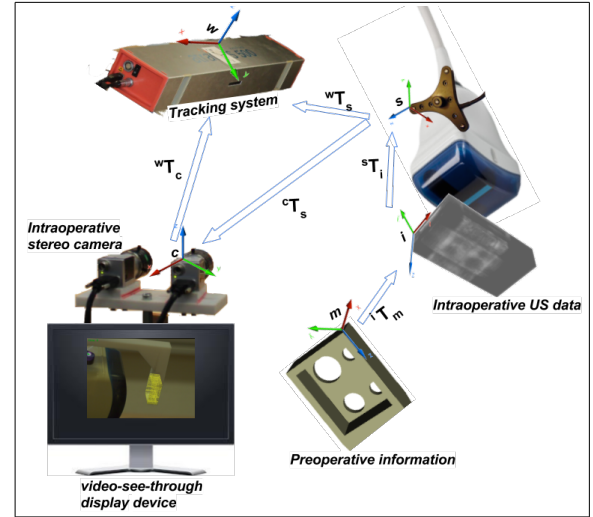


Figure. 1. System overview of the augmented reality setup based on calibrated ultrasonography.

The proposed calibration approach was based on an own-designed phantom with known geometrical properties, as depicted in Fig.2a. Compared to many conventional phantom-based methods using two references (one for the probe and the other one for the phantom) [3][4], there was only one reference s used in our design (Fig.2b). It greatly simplified the calibration procedure and highly improved the accuracy, because sT_i can be estimated by only a registration between the phantom in the acquired 3D US data and the phantom mesh model.

The setup of Fig.2b was placed into a water tank for US scanning, and the acquired data shown in Fig.3 was segmented. We generated a mesh model from the segmentation, and registered it to the model in Fig.2a with surface ICP registration method in 3D Slicer[5].

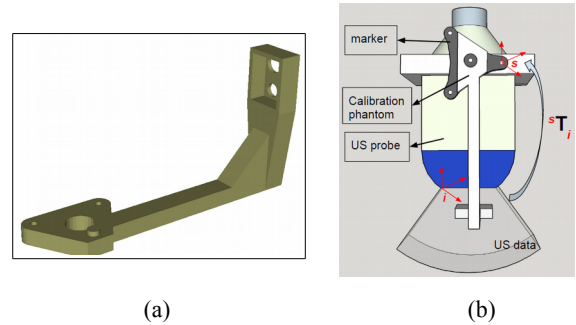


Figure. 2. (a) calibration phantom mesh model; (b) calibration design: the phantom, the marker and the US probe were fixed together.

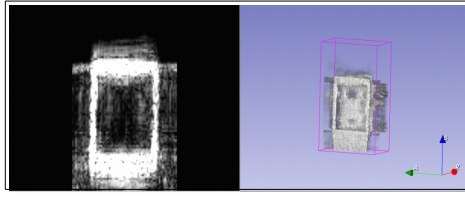


Figure 3. Acquired 3D US data

CAMERA – TRACKING SYSTEM CALIBRATION

A stereo camera was used for the 3D view, and it was calibrated by the classic chessboard-based method[6] with OpenCV[7]. Camera – tracking system calibration meant to determine the camera view in the world coordinate system w in Fig.1. For this, we used the marker s as common information between the camera and the world coordinate system w . The calibration problem can simply be solved by locating (currently manually) the position of the 4 LEDs of s in the stereo camera view.

For the moment, this calibration is only valid when the tracking system and the camera are in a fixed pose. Hereby, we will attach a marker on the camera for tracking its movement in the future work.

RESULT AND CONCLUSION

Calibration setup: we used the tracking system Atracsys easyTrack 500 (0.1mm RMS at 1 meter distance) with the Atracsys active marker (0.04mm RMS calibration error). The calibration phantom was printed by Stratasys Fortus 400mc 3D Printer with resolution 0.178mm. OpenCV estimated the calibration error of the stereo camera to be 0.28mm RMS. In order to estimate the influence of the human interaction for the camera tracking system calibration, we asked 10 people for manually locating the 4 LEDs in the camera view. Compared to the real LEDs position, the highest error in the manually location estimation was 0.275mm. The accuracy of the 3D US probe calibration was estimated by the fiducial registration error (FRE) between the mesh model segmented from US data and the designed phantom model. In our experiment, the FRE was 0.86mm. We also estimated the error between the calibration phantom in the stereo camera view and its mesh model by comparing 4 pairs of vertices. The resulting RMS error was 1.971mm.

Needle insertion experiment: we used our guidance system to help to insert some needles into 11 holes of 1.5mmØ in a plastic plane embedded in opaque gel (Fig.4a). The 3D model of the plastic plane was used as preoperative information which simulated the preoperative MRI/CT information in the real surgery scenario. In the intraoperative stage, we set the 3D US probe on the gel to image the plastic plane. This allowed us to locate the plastic plane and project its 3D model on the camera view (Fig.4b). The user inserted the needles according to the augmented information in the camera view. We performed first a set of 7 manual

insertion experiments, and succeeded in 67 times out of 77 holes. Then, we simulated a robotic surgery scenario

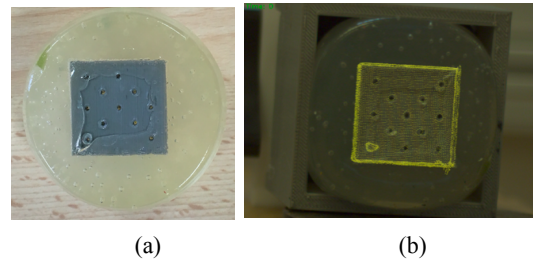


Figure 4. (a) target: a plastic plane with 11 holes embedded in gel; (b) augmented 3D mesh model of the plastic plane in the camera view.

with the Raven II Surgical Robot holding the needles for insertion without force feedback. After several times practicing, the operator was able to insert the needles into most of the 11 holes by controlling the robotic arms.

In conclusion, we presented an US-based AR guidance system with high accuracy in the design and each calibration step. The needle insertion experiment shown the feasibility of the application in MIRS scenarii.

ACKNOWLEDGMENT

This work was supported in part by the French ANR within the investissements d'Avenir Program Labex CAMI, ANR-11-LABX0004 and the Region Bretagne.

REFERENCES

- [1] Clayburgh, Daniel R., et al. "Intraoperative Ultrasonography During Transoral Robotic Surgery." *Annals of Otology, Rhinology & Laryngology* 125.1 (2016): 37-42.
- [2] Sauer, Frank, et al. "Augmented reality visualization of ultrasound images: system description, calibration, and features." *Augmented Reality, 2001. Proceedings. IEEE and ACM International Symposium on. IEEE, 2001.*
- [3] Lange, Thomas, et al. "Automatic calibration of 3D ultrasound probes." *Bildverarbeitung für die Medizin 2011. Springer Berlin Heidelberg, 2011.* 169-173.
- [4] Lasso, Andras, et al. "PLUS: open-source toolkit for ultrasound-guided intervention systems." *IEEE Transactions on Biomedical Engineering* 61.10 (2014): 2527-2537.
- [5] Fedorov, Andriy, et al. "3D Slicer as an image computing platform for the Quantitative Imaging Network." *Magnetic resonance imaging* 30.9 (2012): 1323-1341.
- [6] Zhang, Zhengyou. "A flexible new technique for camera calibration." *IEEE Transactions on pattern analysis and machine intelligence* 22.11 (2000): 1330-1334.
- [7] Bradski, Gary, and Adrian Kaehler. *Learning OpenCV: Computer vision with the OpenCV library.* "O'Reilly Media, Inc.", 2008.

Automatic Technical Surgical Skill Scoring from Motion Data

C. Julliard¹, F. Despinoy², N.Zemiti¹, P. Jannin², P.Poignet¹

¹ LIRMM - UMR 5506, Université de Montpellier

² LTSI - UMR 1099, Université de Rennes 1
chantal.julliard@lirmm.fr

ABSTRACT

Robotic minimally invasive surgery requires well-trained psychomotor skills. In order to facilitate automatic and quantitative assessment of surgical training, we present in this paper the study of relationships between quantitative metrics computed from robotic kinematic data and OSATS evaluation using machine learning. Results show the performance of the trainee can be converted into a global OSATS level with an accuracy of 91.7%.

INTRODUCTION

Surgical training in minimally-invasive surgery is crucial for ensuring quality of the surgical outcome. Various surgical training programs have been developed from basic tutorials for surgical psychomotor skills to whole simulated interventions. Due to its specific human-machine interface, acquiring manual skills with a daVinci System is even more challenging. A lot of research was also conducted for standardising assessment to make surgical performances comparable and less subjective. According scores such as OSATS and GOALS are often used in research and allow complementing metrics-based assessment with a more qualitative feedback.

However, these scores need to be filled in by human observers that are domain experts. Automatic skill assessment has the potential of quantitative, objective, standardised and affordable assessment. In this direction, recently, motion data analysis was studied for automatic skill classification and gesture recognition [1]. Thereby, motion data was converted into metrics and classified into three competence levels by different statistic approaches.

The idea of this paper is shown in Figure 1 and starts with taking the trajectories of the trainee's trial. Those are used for metrics computation, which allow after machine learning, an automatic translation into an additional qualitative assessment. More recently, relationships between quantitative metrics and qualitative assessment with OSATS overall score were studied by Kowalewski [2] by a Spearman's Correlation. Another unpublished work from Wolf outlined relationships between the GOALS scores and quantitative metrics [3].

In this paper we further studied such relationships between OSATS scores and metrics by relying on a

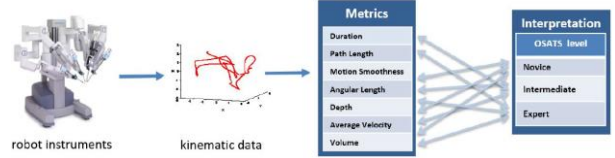


Figure. 1. Workflow towards evaluation learning

data-driven mapping approach using a supervised learning approach.

MATERIALS AND METHODS

We propose a qualitative-quantitative mapping by analysing relationships between the qualitative OSATS evaluation and the quantitative motion data of the robot by applying a classification learning approach.

This method was tested on a reference data set: the JHU-ISI Gesture and Skill Assessment Working Set (JIGSAWS) [4].

Training Data Set

The JIGSAWS data set provides kinematic and video data as well as a surgical activity annotation and a surgical skill annotation using a modified Global Rating Score (GRS) of the OSATS. Additionally, the competence level of the subjects is classified according to their robotic surgical experience varying from novice with an experience less than 10 hours, up to experts with more than 100 hours of robotic surgical experience. Kinematic data of the patient-side manipulators includes gripper angle, tool tip's positions as well as linear and angular velocities.

Kinematic metrics

From the trajectories we computed 43 metrics such as duration, path length, average linear velocity, average acceleration, average jerk, bi-manual dexterity, motion smoothness, depth, idle time, relative phase, response orientation, economy of volume and working volume of the instrument's positions. For each metric, we determined whether or not it was applicable to the right, the left and a combination of the two instrument sides as well as different ways to compute it.

Table 1: Confusion Matrix of the robot experience hours

	true N	true I	true E	precision
pred. N	16	2	0	88.9%
pred. I	0	8	0	100.0%
pred. E	0	0	10	100.0%
recall	100.0%	80.0%	100.0%	95.0%

OSATS Evaluation

For the categorization of the trainee's OSATS level the cut-offs of Vedula are used [5]. According to this work, the overall GRS score is handled as expert (E) when the score is higher than 22, as novice (N) for scores lower than 14. A score between 14 and 22 is considered as intermediate (I).

In addition, for each OSATS categories "Respect for Tissue", "Suture and Needle Handling", "Time and Motion", "Flow of Operation" and "Overall Performance" an evaluation is expressed on a Lickert Scale with a grade between 1 (beginner's performance) to 5 (expert's performance). A detailed description of the semantic scale for each category and their grades can be found in [4].

Training and Testing

An Artificial Neural Network was used to predict the OSATS scores from the calculated metrics (one hidden layer and 24 nodes is set up with 500 training cycles, a learning rate of 0.3 and a momentum of 0.2). A 2-fold cross-validation was used and the Spearman's rho was determined. First, the global OSATS level as response output was selected and the calculated metrics as input attributes, then the different OSATS categories with their grades from 1 to 5 were used as response.

RESULTS

The confusion matrices are shown in Tables 1, 2 and 3, horizontally the predicted levels/grades (labelled as pred.) and vertically the actual levels/grades (labelled as true). After the categorization into the OSATS level, none of the participants is labelled as expert, see Table 2. This is also supported by the OSATS grades in Table 3 as nobody reaches a perfect performance grade of 5. The Spearman's rho between the OSATS level classification and the metrics is excellent. The classification of the OSATS level, in Table 2, is below the accuracy the competency levels regarding the robotic experience hours, in Table 1. For the OSATS category, an example is shown in Table 3, the accuracy considerably lies under the level classification.

CONCLUSION AND DISCUSSION

We demonstrated in this paper the existence of a qualitative-quantitative mapping between the metrics and OSATS levels by using a machine learning approach.

Table 2: Confusion Matrix of the OSATS level

	true N	true I	true E	precision
pred. N	17	2	0	89.5%
pred. I	1	16	0	94.1%
pred. E	0	0	0	0.00%
recall	94.4%	88.9%	0.00%	91.7%

Table 3: Confusion Matrix of OSATS "Flow of Operation"

	true 1	true 2	true 3	true 4	true 5	precision
pred.1	3	1	0	0	0	75.0%
pred.2	2	8	2	0	0	66.7%
pred.3	0	1	10	5	0	62.5%
pred.4	0	1	2	1	0	25.0%
pred.5	0	0	0	0	0	0.0%
recall	60.0%	72.8%	71.4%	16.3%	0.0%	61.0%

The results are a first step towards automatic assessment of surgical training. Our results for the Spearman's rho of the classification on the OSATS level are in line with the findings from Kowalewski [2]. We additionally studied the OSATS levels and categories by using all metrics and trials for the learning and testing part. The classification in the OSATS levels with an accuracy of 91.0% has already the advantage of being less subjective than the expert, but more expressive than a simple level classification. However, the classification in the OSATS categories needs further analysis. Despite the low accuracy of 61.0% in the "Flow of Operation" category, the predicted grades are quasi diagonal and revolve around the correct classification. Therefore, a study of single metrics and their relationships to the OSATS categories and grades is needed.

REFERENCES

- [1] Despinoy, F. et al. "Unsupervised Trajectory Segmentation for Surgical Gesture Recognition in Robotic Training". IEEE Transactions on Biomedical Engineering; 2016; 63(6):1280-91.
- [2] Kowalewski, K.-F. et al. "Development and validation of a sensor- and expert model-based training system for laparoscopic surgery: the iSurgeon". Surgical Endoscopy; 2016; 31(5):2155-2165.
- [3] Wolf, R. "Quantification de la qualité d'un geste chirurgical à partir de connaissances a priori". Université de Grenoble; 2014; HAL Id: tel-00965163.
- [4] Gao, Y. et al. "The JHU-ISI gesture and skill assessment data set (JIGSAW): A surgical activity working set for human motion modeling". Medical Image Computing and Computer-Assisted Intervention (MICCAI); 2014.
- [5] Vedula, S. et al. "Analysis of the Structure of Surgical Activity for a Suturing and Knot-Tying Task." PLoS ONE; 2016; 11(3): e0149174.

Foot pedal interface for intra-operative annotation of surgical phases and skill in robotic surgery

D. Dall'Alba¹, D. Naftalovich², G. De Rossi¹, J. W. Burdick², P. Fiorini¹

¹ *University of Verona, Department of Computer Science, Verona, Italy,*

² *California Institute of Technology, Mechanical and Civil Engineering, Pasadena, USA
diego.dallalba@univr.it*

INTRODUCTION

Life long learning is a fundamental aspect of professional growth in medicine, in particular when novel technologies, such as medical robots, require new manual and intellectual skills to exploit their capabilities. Due to the long and challenging training in surgery, there is a strong interest for accurate and continual evaluation of surgical skill and training outcomes [1].

Surgical trainee evaluation often occurs from direct observation by attending surgeons who oversee the trainees in a residency program. As this can be a slow, laborious, and subjective process, there has been work on structured and objective assessment of surgical skills, particularly technical surgical skills. The use of specific criteria for an evaluating observer to consider when assessing trainee's technical surgical skill is considered to make the assessment process more objective, valid, and reliable [2]. The Objective Structured Assessment of Technical Skills (OSATS) or Global Operative Assessment of Laparoscopic Skills (GOALS) rubrics are validated tools that provides such scoring guidelines. These rubrics have been extended to surgical robotics, and have been used as Structured Assessment of Robotic Microsurgical Skills (SARMS) and as Global Evaluative Assessment of Robotic Skills (GEARS) [3]. Despite the training protocol and rubric used, surgical training benefits most from feedback that points out specific opportunities for improvement. It is a key factor to support expert user in the effective assessment of different users and/or the trainee in the self-assessment of his/her skills. The ability for a surgical trainee to track errors and receive feedback about performance quality is important, both by self feedback or mentor oversight. Additionally, a surgical trainee's ability to self evaluate is also important and is a skill that must be acquired. Therefore, a user interface to enable intra-operative self-assessment annotation by an operating subject is a very useful addition to improve the training process. In this work, we are presenting a foot pedal interface supplement for intra-operative annotation in a robotic-assisted setting.

The da Vinci Surgical system provides improved comfort for the operating surgeon via its master console and includes an arm rest bar that the surgeon leans on while in a seated position. This ensures the surgeon's feet as being relatively not weight bearing and contributes to foot pedals being an effective potential

mode of the proposed user interface. Indeed, the da Vinci system uses a foot pedal platform for controlling some of its core native features.

The proposed approach of a surgeon annotating information intra-operatively in a robotic-assisted setting, such as using supplemental foot pedals, enables him or her to mark informative content into the existing stream of robot operative data, which can include camera view of the surgical site and other information such as kinematic data from robotic manipulator [4].

The proposed intra-operative annotation approach can be used for at least two purposes: 1) for marking self-assessed skill related information, and 2) for annotating information about the surgical process, such as transitions between various phases of the procedure. The latter is particularly useful in research settings as it can increase efficiency by eliminating or reducing the need for retroactive annotation efforts. This paper describes these intra-operative annotation applications of a proposed foot pedal supplement interface for use in the da Vinci system. We have applied the proposed system for marking phases and skills information in datasets obtained during training procedure in robotic assisted micro-anastomosis exercises performed on Da Vinci Research Kit (DVRK) [4, 5]. The proposed setup has also been found to have utility as an interface for improved control of camera motions [6].



Figure 1 Photo of the supplement foot pedals tray and original DVRK foot pedals platform. The additional tray replicating the same pedals configuration used in recent da Vinci surgical system.

MATERIALS AND METHODS

Starting from the motivations and requirements described in the previous section, we decided to use a standard foot pedal replicating the same configuration available in the recent da Vinci surgical system, visible in Figure 1. This choice has been motivated by the fact that most of the medical trainers, even with small experience on the surgical robot, are used to this layout and no extra effort is required despite from learning the mapping between pedals and functions. The foot pedals used in this work has been designed by BBZ srl (Verona, Italy) and it is part of Acteon, their robotic surgical simulator. The hardware configuration is based on 7 mechanical pedals connected to a microcontroller, which communicate with the computer through Universal Serial Bus (USB) interface. We mapped the foot pedals used for controlling energy activation of the electrified tools for marking different procedure's phases, while the other pedals are used for annotating different type of errors, following SARMS guidelines [3]. A complete scheme representing the mapping between pedals and different annotation functions are represented in Figure 2. Since we have tested the proposed system in anastomosis training exercise, we configured specific skill assessment and segmentation functions, corresponding to the main steps of surgical suturing: grabbing, treating, pulling and knotting. We also used an unused pedal from the DVRK tray for additional annotations, i.e. errors related to robotic skills. Anyway, the mapping between pedals and functions could be easily configured in the software component that we have designed and integrated in the Robot Operating System (ROS) to ease the acquisition and integration of annotation data in the video and kinematic data acquired with DVRK [5]. The proposed foot pedals device is also compatible with different operating system and software implementation, since it emulates a standard keyboard, with configurable foot pedals mapping to specific keyboard key press event.

RESULTS

We have tested the proposed annotation device during the execution of 22 consecutive trials of an end-to-end microvascular anastomosis, performed on the non-animal Konnyaku/Shirataki phantom laboratory model which is composed of a hollowed small Japanese noodle (2.5 mm) [4]. Operative data includes stereoscopic video and kinematic data composed of joint angles and joint velocities of all the robotics manipulators, along with some additional data. Data capture was performed using ROS interface to the DVRK, and includes annotation acquired with the proposed foot pedal interface relatives to different type of error and the segmentation of difference procedure's steps. The subject performing the procedure has provided positive feedback, and the introduction of the annotation did not change significantly the completion time of the single exercise trials. The same foot pedal interface has been used for improved intra-operative endoscope motion control in our DVRK setup, as detailed described in [6].

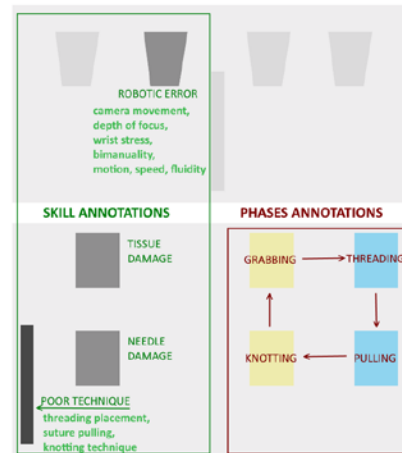


Figure 2. Schematic representation of the mapping between foot pedals and functions: foot pedals on the left are dedicated to skill assessment (green), while pedals on the right are used for surgical phases annotations (red).

CONCLUSION AND DISCUSSION

In this work, we have presented a foot pedal interface suitable for intra-operative annotations. The main goal of the proposed system is to keep the evaluator focused on the task, the trainee in case of self-assessment of surgical skills. This characteristic will enable the evaluator to introduce annotation with a minimum amount of time overload.

We demonstrated the feasibility of using the system for self-annotation of 22 training trials of a complex robotic assisted micro-anastomosis procedure performed on DVRK, including in the resulting dataset both task segmentation and skill annotation information. The same approach could be easily extended to training performed on virtual simulators or with the clinical surgical system. The interface could be used when the evaluation is performed by external expert user, even if the ergonomic of the foot pedal interface needs to be evaluated. Future works will focus in redesign of the foot pedal interface to improve the ergonomics and usability and extending the system evaluation with more complete user-test and considering different procedures.

REFERENCES

- [1] J.A. Martin, G. Regehr, R. Reznick, H. Macrae, J. Murnaghan, C. Hutchison, M. Brown, *British Journal of Surgery* 84(2), 273 (1997)
- [2] K. Moorthy, *BMJ* 327(7422), 1032 (2003). DOI 10.1136/bmj.327.7422.1032.
- [3] T. Alrasheed, J. Selber, *Seminars in Plastic Surgery* 28(01), 005 (2014). DOI 10.1055/s-0034-1368161.
- [4] D. Naftalovich, D. Dall'Alba, G. De Rossi, P. Fiorini, J.W. Burdick. *Computer Assisted Radiology and Surgery (CARS)*, June 20-24, 2017.
- [5] P. Kazanzides, Z. Chen, Z. Deguet, G.S. Fischer, R.H. Taylor, S.P. DiMaio. In *Proc. Of the IEEE Intl. Conf. on Robotics & Automation (ICRA)*, pages 6434-6439, 2014.
- [6] D. Naftalovich, D. Dall'Alba, G. De Rossi, P. Fiorini, J.W. Burdick, *Under revision CRAS 2017*.

System Identification and Feed-Forward Control of a Magnetic Laser Scanner

Alperen Acemoglu¹, Daniele Pucci², Leonardo S. Mattos¹

¹Department of Advanced Robotics, and ²iCub Facility Department

Istituto Italiano di Tecnologia, Genova, Italy

INTRODUCTION

Laser-based microsurgeries have recently been used in different medical operations such as transoral microsurgery, fetal surgery and refractive eye surgery. Good post-operative functions, low morbidity and minimal peripheral tissue injury are the main strengths of laser-based microsurgery over conventional operation techniques [1, 2]. The main technologies allowing these advantages are: free-beam lasers and flexible fiber laser ablation systems. In free-beam systems, tissue is ablated from large distances (often about 400-500 mm) whereas fiber-based systems ablate only when in close proximity to the surgical site. Consequently, the former requires direct line of sight and very high laser control performance, while the latter can operate in difficult to reach parts of the anatomy. On the other hand, laser ablation quality is significantly superior with free-beam lasers for two reasons: availability of laser focusing optics and a scanning system [3]. Neither of these are currently available for fiber-based lasers.

Developing a compact fiber-based laser ablation system capable of scanning and laser focusing can potentially couple the benefits of free-beam and fiber-based surgical laser systems, enabling high-quality ablations from a small and flexible structure. This is the aim of our research, which has produced a magnetic laser scanner prototype for endoscopic non-contact tissue ablations [4]. In this paper, we present the modeling of the dynamics of this system. The system parameters are identified and an inverse model is used to perform feed-forward control of the device. Control validation is performed through trajectory scanning trials, demonstrating excellent results in terms of scanning frequency and trajectory tracking errors.

MATERIALS AND METHODS

The laser scanning system has four electromagnetic coils around a cylindrical tool. Identical coil pairs are placed perpendicular to each other in y- and z- axis. An optical fiber is placed as a cantilever beam in the center of the cylindrical tool. A permanent magnet is attached to the optical fiber. The actuation mechanism is based on interaction between the electromagnetic field created by the coils and the permanent magnet. Since magnetic field variations in the workspace are relatively small, the magnetic force acting on the permanent magnet can be neglected. Thus the fiber beam bending is primarily dependent on the magnetic torque. For actuating the two degrees of freedom, the magnetic torques T_y and T_z act

on the permanent magnet and the bending of the optical fiber beam is achieved on the y- and z- axis (Fig. 1). To focus the laser light we use two plano-convex lenses: the first lens collimates the laser beam and the second focuses it on the target plane (in this case at 30 mm distance, which was the defined working distance). The laser spot position on the target changes according to the bending of the fiber. For two degrees of magnetic actuation, we have a two dimensional position control.

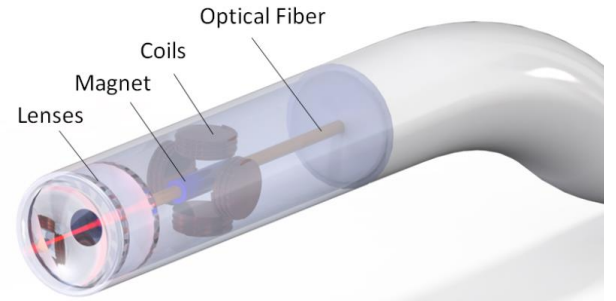


Figure 1. Conceptual design of the magnetic laser scanner.

SYSTEM IDENTIFICATION

Observing the system's step response and frequency response, it is seen that the system can be modeled as a second order system. Thus, the governing equation for the dynamic model for a single degree of freedom is written as

$$\ddot{d} = A\dot{d} + Bd + Cu, \quad (1)$$

where A , B and C are three scalars, u is the current input, d is the measured position, \dot{d} is the velocity and \ddot{d} is the acceleration. Considering the availability of a set of experimental data, (1) can be written as

$$\ddot{\mathbf{d}} = A\dot{\mathbf{d}} + B\mathbf{d} + C\mathbf{u}. \quad (2)$$

$$\ddot{\mathbf{d}} = \mathbf{P}\mathbf{M}, \quad (3)$$

where $\mathbf{P} = [A, B, C]$ is the coefficient matrix and $\mathbf{M} = [\dot{d}; d; u]^T$ is the measurement matrix. Estimating the coefficients matrix is an optimization problem, solved by minimizing the error between the estimated and the actual response of the system.

Here, the experimental dataset included laser spot positions, \mathbf{d} , extracted from the recorded videos with a laser spot detection algorithm, and the corresponding

current values recorded during the experiment, u , \dot{d} and \ddot{d} are derived from the position measurements.

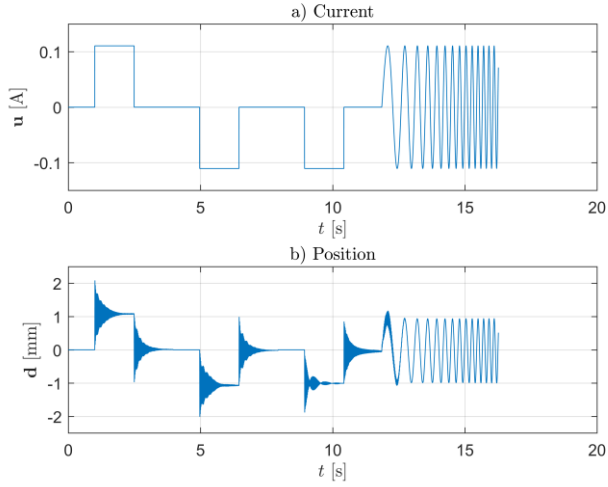


Figure. 2. Calibration data set for system identification a) current input and b) position response.

Calibration experiments are composed with step responses and chirp signal. The experiments that are used for the system identification are presented in Fig 2 and \mathbf{P} coefficient matrix is calculated with least square method. After estimating the coefficients of the system, inverse of the model is used to perform feed-forward control (Fig 3). Then desired trajectories are compared with the actual ones.

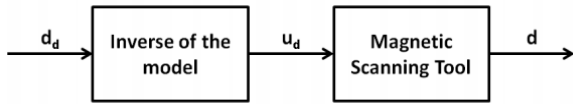


Figure. 3. Block diagram of the feed-forward controller.

RESULTS

For validation of the estimated model and control method, we perform experiments with different desired trajectories. Fig 4 presents the actual and the desired trajectories for sinusoidal and triangular input signals.

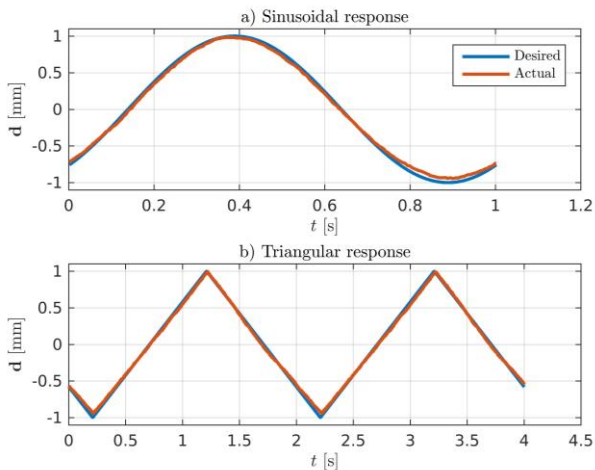


Figure. 4. Validation experiments with sinusoidal and triangular responses.

Calculated RMSE values for sinusoidal and triangular responses are 38 and 28 μm , respectively. Maximum errors are not more than 80 μm in both cases.

CONCLUSION AND DISCUSSION

In this paper, we have presented the modeling, design and validation of a single-axis feed-forward controller for a magnetically actuated endoscopic laser scanner. Modeling was performed based on experimental data. Estimation of the laser spot position in laser-based operations in narrow workspaces is crucial for the miniaturization of the surgical tool. Considering such workspaces, placing additional sensors for laser position observation is not desired. At the same time, visual-servoing of the laser spot is highly challenging considering the stringent requirements in terms of speed and robustness of the image processing algorithms. Thus, model-based control of the magnetic laser scanner seems to be an optimal solution to achieve fast and precise laser control without the need for additional sensors. The results demonstrated that the approach is valid and robust. It allows stable scanning with frequencies up to 35 Hz and the execution of the desired laser trajectories with precision in the order of 40 μm .

At this point, our ongoing efforts are focused on extending the research presented here to perform 2D position control. Once that is done, we will focus on validating the hypothesis of this work through real tissue ablation trials.

REFERENCES

- [1] Solares, C. Arturo, and Marshall Strome. "Transoral robot assisted co2 laser supraglottic laryngectomy: Experimental and clinical data." *The Laryngoscope* 117.5 (2007): 817-820.
- [2] Desai, S. C., Sung, C. K., Jang, D. W., and Genden, E. M. (2008). "Transoral robotic surgery using a carbon dioxide flexible laser for tumors of the upper aerodigestive tract." *The Laryngoscope*, 118(12), 2187-2189.
- [3] Remacle, M., Lawson, G., Nollevaux, M. C., & Delos, M. (2008). Current state of scanning micromanipulator applications with the carbon dioxide laser. *Annals of Otolaryngology, Rhinology & Laryngology*, 117(4), 239-244.
- [4] Acemoglu, A. and Mattos, L.S. "Magnetic Laser Scanner for Endoscopic Microsurgery" In *Robotics and Automation, 2017. Proceedings 2017 ICRA. IEEE International Conference on.* IEEE.

Objectively Assessing Performance in Transoesophageal Echocardiography from Image Comparison and Alignment

E.B. Mazomenos^{1*}, F. Vasconcelos¹, J. Smelt², M. Jahangiri², B. Martin³, A. Smith³, S. Wright² and D. Stoyanov¹

¹ Centre for Medical Image Computing, University College London, London, U.K.

² St Georges University Hospitals, NHS Foundation Trust, London, U.K.

³ St Bartholomews Hospital, NHS Foundation Trust, London, U.K.

INTRODUCTION

Transoesophageal echocardiography (TEE) is a valuable diagnostic procedure. In TEE the heart is imaged with an ultrasound (US) transducer, attached to a flexible endoscope (probe), inserted in the oesophagus. TEE requires refined psychomotor skills and high-level of hand-eye coordination. Methods for objectively assessing competency can have a significant impact in the training process of new TEE interventionalists by providing a platform for developing the necessary skills more effectively. Proper image acquisition is essential for diagnosis and a strategy to objectively characterise the quality of TEE views based on image similarity and alignment features is proposed in this work.

Previous studies exclusively focus on the kinematic analysis of the US probe [1, 2, 3, 4]. Here, our hypothesis is that the image content and structure will differ between practitioners of different experience, due to improper position and orientation of the probe. To evaluate this we used a set of gold standard views, representing nominal US images and performed a comparative investigation with test images from a diverse cohort. We focused on two aspects; first representing the content and structural differences of the images (test vs gold standard) using image similarity features and secondly representing the spatial displacement by aligning the test images to the gold ones. A high degree of similarity and a low amount of motion is expected for properly acquired images. We anticipate the opposite as the images differ. Statistical analysis on the extracted parameters reveals significant differences and trends between the two experience groups that can be exploited for performance evaluation.

MATERIALS AND METHODS

Experiments took place with the HeartWorks TEE simulation (Inventive Medical, Ltd, London, U.K.) platform, illustrated in Figure. 1. Nineteen volunteers took part, divided into two experience groups. The experts group (n=6) comprised of anaesthetists with more than 500 TEE exams. Novices (n=13) were trainees (cardiac and thoracic) in the early years of residency. The study consisted of a simulated TEE exam in which every participant had to capture 10 (a subset of the 20 recommended views by the American Society of Echocardiography and the Society of Cardiovascular Anesthesiologists [5]) US views, depicted in Figure 2. The gold standard images were obtained from a different consultant anaesthetist performing the exact same test.

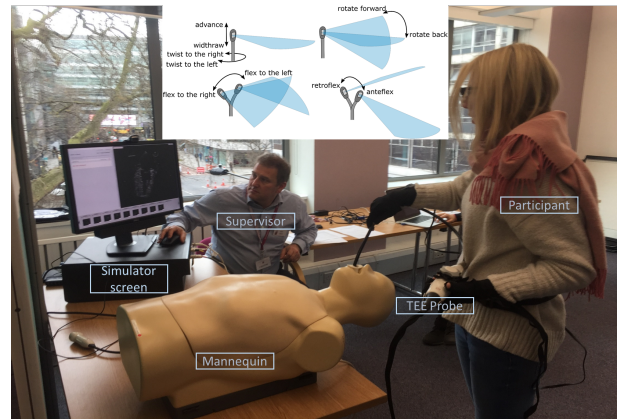


Figure. 1. The experimental setup with a volunteer operating the HeartWorks simulator. Inset the TEE probe movements.

High-resolution images from the 10 views were captured for analysis. The initial stage of the processing pipeline, shown in Figure. 3, consists of conditioning (opening and Otsu thresholding) to enhance the US image and eliminate specular highlights. Gaussian filtering is applied to smooth sharp edges, facilitating the segmentation process. The Chan-Vese active contour segmentation is used to delineate the heart structure in the US images. To compare images in terms of their content and structure similarity, we employed three metrics; (a) the structural similarity index (SSI) [6]; (b) the mutual information value (MI) [7], and (c) the normalised cross-correlation (NXCORR), calculated from the segmented contours.

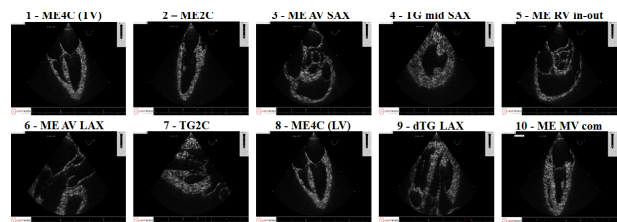


Figure. 2. The 10 US views in our tests: 1: Mid-Esophageal 4-Chamber (centred at tricuspid valve), 2: Mid-Esophageal 2-Chamber, 3: Mid-Esophageal Aortic Valve Short-Axis, 4: Transgastric Mid-Short-Axis, 5: Mid-Esophageal Right Ventricle inflow-outflow, 6: Mid-Esophageal Aortic Valve Long-Axis, 7: Transgastric 2-Chamber, 8: Mid-Esophageal 4-Chamber (centred at left ventricle), 9: Deep Transgastric Long-Axis, 10: Mid-Esophageal Mitral Commissural.

To assess differences in the way the operators positioned and oriented the US plane, segmented contours were aligned with the Lucas-Kanade algorithm,

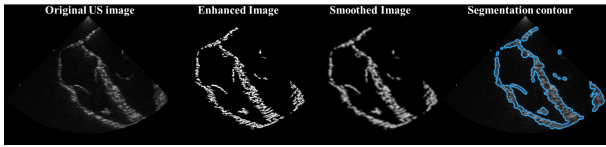


Figure 3. First stage of the processing pipeline resulting in the segmentation contour of the heart's structure in the US image.

as illustrated in Figure 4. We extracted the translation and angle of rotation from the resultant alignment matrix.

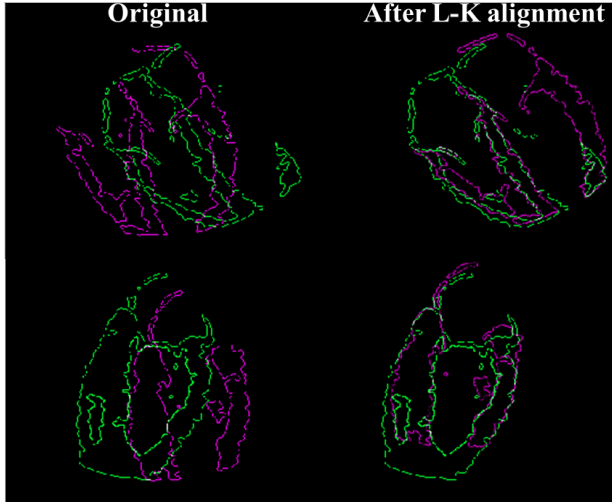


Figure 4. Examples of the Lucas-Kanade (L-K) alignment.

RESULTS

The nonparametric Mann-Whitney *U*-test was used for statistical analysis with the differences considered significant for *p*-value 0.05. The median values with novices listed first, and *p*-values (in parentheses, in red colour for *p*<0.05) are given in Table. 1 and Table 2 for the similarity and alignment (translation and absolute rotation angle) parameters respectively.

Table 1. Median and *p*-values for the similarity metrics

US View	Structural similarity	Mutual information	Cross correlation
1	0.77 vs 0.79 (0.10)	0.0002 vs 0.0006 (0.0066)	0.06 vs 0.07 (0.28)
2	0.82 vs 0.82 (0.6388)	0.0009 vs 0.0008 (0.4155)	0.07 vs 0.09 (0.41)
3	0.83 vs 0.82 (0.0365)	0.0005 vs 0.0005 (0.4670)	0.08 vs 0.09 (0.89)
4	0.89 vs 0.89 (0.9661)	0.0007 vs 0.001 (0.1061)	0.1 vs 0.1 (0.76)
5	0.82 vs 0.83 (0.2441)	0.0004 vs 0.0008 (0.2100)	0.08 vs 0.1 (0.04)
6	0.78 vs 0.77 (0.467)	0.0002 vs 0.0005 (0.2100)	0.06 vs 0.08 (0.01)
7	0.77 vs 0.80 (0.7654)	0.0006 vs 0.0006 (0.6388)	0.07 vs 0.07 (1)
8	0.77 vs 0.83 (0.0092)	0.0002 vs 0.0007 (0.0365)	0.06 vs 0.08 (0.08)
9	0.73 vs 0.74 (0.6388)	0.0004 vs 0.0006 (0.5789)	0.05 vs 0.06 (0.02)
10	0.80 vs 0.80 (0.3607)	0.0006 vs 0.0006 (0.3170)	0.07 vs 0.07 (0.6264)

Table 2. Median and *p*-values for translation and rotation.

US View	Translation (px)	Rotation(°)
1	37.3 vs 27.9 (0.467)	7.51 vs 4.64 (0.8314)
2	14.1 vs 9.4 (0.3229)	4 vs 1.33 (0.0365)
3	35.5 vs 27.5 (0.5789)	5 vs 11 (0.9661)
4	45.5 vs 29.9 (0.8983)	11.2 vs 7.8 (0.8314)
5	56.7 vs 14.4 (0.0047)	5.4 vs 3 (0.21)
6	37.1 vs 19.4 (0.0715)	11.4 vs 3.2 (0.022)
7	30.3 vs 34.5 (0.8314)	6.9 vs 6.4 (1)
8	24.3 vs 33.7 (0.4155)	7 vs 4.3 (0.3676)
9	41.7 vs 22.5 (0.467)	10.7 vs 4 (0.791)
10	28.3 vs 58.1 (0.2768)	3.8 vs 10.4 (0.3607)

CONCLUSION AND DISCUSSION

Significant differences were found in 6 out of the 10 views for the similarity parameters. In the majority of views, the expert group yields a higher median MI and NXCORR value, which shows that the images obtained by experts are structurally more similar to the gold standard than the ones from novices. The values of translation and rotation were smaller in the expert images indicating that experts placed the US transducer closer to the nominal position and with the appropriate scanning orientation. In conclusion, this initial investigation reveals that image similarity and spatial alignment analysis has good potential for developing automated techniques to objectively assess the quality of images and overall performance in TEE. Future work will focus on employing active learning strategies with feature selection for developing models to characterize operational performance in TEE from obtained US images.

REFERENCES

- [1] B.Sohmer et al. "Transesophageal echocardiography simulation is an effective tool in teaching psychomotor skills to novice echocardiographers". *Can J Anaesth*, 61(3), 235-241 (2014).
- [2] R. Matyal et. al., "Manual Skill Acquisition During Transesophageal Echocardiography Simulator Training of Cardiology Fellows" A Kinematic Assessment", *J. Cardiothorac. Vasc. Anesth.* 29(6), 1504-1510 (2015).
- [3] E.B. Mazomenos et. al. "Motion-based technical skills assessment in transoesophageal echocardiography". In *MIAR*, pp. 96-103 (2016).
- [4] J.D. Mitchell et. al. "Novel, multimodal approach for basic transesophageal echocardiographic teaching", *J. Cardiothorac. Vasc. Anesth.* 28(3), 800-809 (2014).
- [5] R.T. Hahn et al. "Guidelines for performing a comprehensive transesophageal echocardiographic examination: recommendations from the American Society of Echocardiography and the Society of Cardiovascular Anesthesiologists". *J. Am. Soc. Echocardiogr*, 26(9), 921-964 (2013).
- [6] Z. Wang et. al. "Image quality assessment: from error visibility to structural similarity", *IEEE Trans. Image Process.* 13(4), 600-612 (2004).
- [7] F. Maes et. al. "Multimodality image registration by maximization of mutual information", *IEEE Trans. Med. Imaging* 16(2), 187-198 (1997).

Robot-Assisted Bone Cement Injection

N. Lepoutre¹, L. Meylheuc¹, G. I. Bara¹, L. Barbé¹ and B. Bayle¹

¹ICube – University of Strasbourg – UMR 7357 CNRS – INSA Strasbourg
nlepoutre@unistra.fr

INTRODUCTION

Percutaneous vertebroplasty is a minimally invasive intervention that involves injecting bone cement, under fluoroscopic guidance, into a damaged vertebral body [1]. This intervention is beneficial since one can observe a sustainable stabilization of the vertebra, an early raising up of the patient and a very immediate improvement in pain. However, some drawbacks related to the cement polymerization must be considered. At the beginning of the injection, the bone cement viscosity is very low, which introduces a high risk of leakage outside the vertebra and serious complications. During the injection, the polymerization reaction progresses and the cement hardens, leaving a short working phase. Furthermore, the operator is permanently exposed to unhealthy X-rays. Among a large number of patents [2] and commercialized systems [3], authors claim a temperature and/or a viscosity measurement but none of them combines a solution for a reduction of cement leakage risk by controlling its viscosity, and a radiation protection while preserving the practitioner's tactile perception. The present abstract focuses on a teleoperated injection device with haptic feedback. It features a fine control of the cement injection together with the radioprotection of the medical staff, a reduction of the leakage risks and an extended injection phase.

S-TRONIC ROBOT

Specifications

The aim of our S-Tronic project is to help radiologists meet the two most important requirements of the vertebroplasty procedure: filling the vertebral body conveniently and preventing cement leakages while removing the practitioner from the X-ray area. To that purpose, a robotic device has been developed allowing the remote supervision of the cement injection and the avoidance of the cement leakage through a fine-tuned viscosity control. However, the bone cement that undergoes an exothermic polymerization reaction during its injection has a highly complex behavior. According to a preliminary rheological study [4], a temperature control is the most appropriate choice to perform the viscosity control. Then, besides the visual control of the cement delivery via real time fluoroscopic images, the curing state of the cement can be rendered by force feedback on a remote console. The system presented in this section combines these features.

Design of a temperature control system

A specific Peltier-based heat exchanger has been designed in order to perform, later on, an efficient bone

cement viscosity control. The injected material flows through a cylindrical channel machined into a mass of copper. Its important thermal diffusivity ensures a uniform temperature around the flowing bone cement. On each face of this block, a Peltier module, a heat sink and a fan are positioned in a cascade arrangement (see Fig. 1). Copper heat sinks and fans are introduced in order

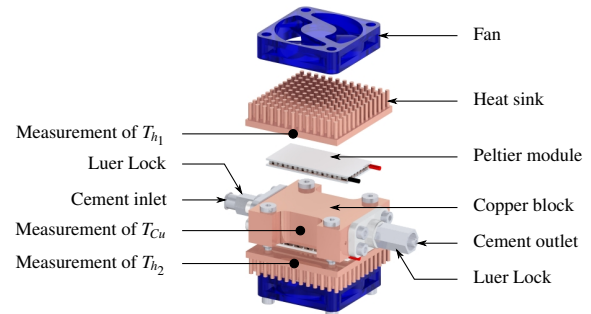


Figure 1 – CAD view of the thermal exchanger block.

to maximize the thermal efficiency by lowering the temperature difference between the hot and cold side of each Peltier module. Based on the modeling and identification of this exchanger [5], our original control approach consists in a switching strategy between two different controllers, one for the heating phase and another for the cooling phase.

Robotic injection device

The injection device is based on a syringe pusher (Fig. 2). The carriage in translation imposes the speed of the pis-

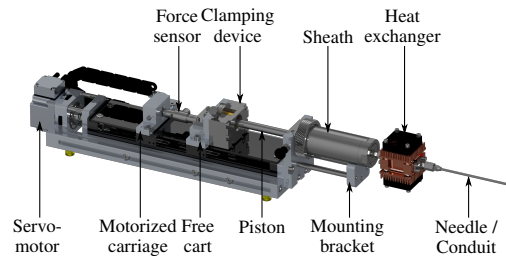


Figure 2 – CAD view of the injection device.

ton in order to push the cement from the syringe into the treated vertebra through a needle. At the end of the guide, a mounting bracket allows to easily plug and remove the sheath holding the syringe filled beforehand with bone cement. In order to compute online the bone cement viscosity, an adapted instrumentation has been included to

the injection device. A linear position sensor has been mounted on the carriage while the force sensor in the transmission provides the measurement of the injection force. Finally, at the outlet of the syringe, the heat exchanger and a conduit are connected one after another.

Teleoperated cement injection

A haptic interface has been designed in order to allow the remote control of the injection and to render a force feedback representing the cement hardening to the practitioner. It is built around a cable-driven pulley-capstan transmission. A rate control strategy has been preferred, which means that the position of the master interface is interpreted as a velocity command by the slave system.

RESULTS AND DISCUSSION

The system presented in the previous section has been implemented to inject bone cement. Several experiments have been completed with an experienced practitioner in the Interventional Radiology room at the University Hospital of Strasbourg. Each trial began by reaching a homogeneous bone cement after hand-mixing an amount of powder, based on PMMA, and liquid MMA. Once obtained, the cement was poured into the syringe that was itself inserted into the sheath. The latter, on which the heat exchanger and a needle were plugged, was placed on the slave device. While the temperature of the cement was fixed at 24 °C thanks to the thermal exchanger, the injection of cement was carried out into a L5-phantom vertebra, either hollow (experience 1) or with a cancellous insert (experience 2). This foam simulates the bone tissue inside a human vertebral body, which renders the cement spread more complex. The operator controls the cement injection through the handle of the master system while visualizing the images of the X-ray imaging device (Fig. 3). Along with the design of the robot-assisted

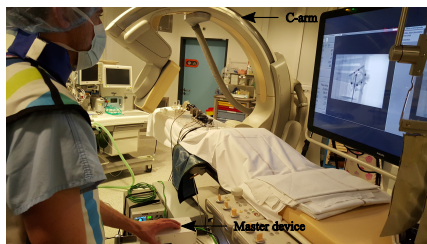


Figure 3 – Experiments led by an experienced practitioner.

bone cement injection, a method allowing to compute online the bone cement viscosity has been developed. Our approach is based on the principle of mass conservation coupled to the resolution of the Navier-Stokes equation and the adapted instrumentation that has been included to the injection device. It also assumes that the bone cement flows out of the needle at atmospheric pressure. Fig. 4 gathers a reference curve for percutaneous vertebroplasty acquired on a rotational rheometer and the curves of the online viscosity computation for both experiments. During these experiments, viscosity values that have been reached are consistent with the practitioner's habits. A comparison of the first experiment results with a rheological model, identified offline but out of the scope of this

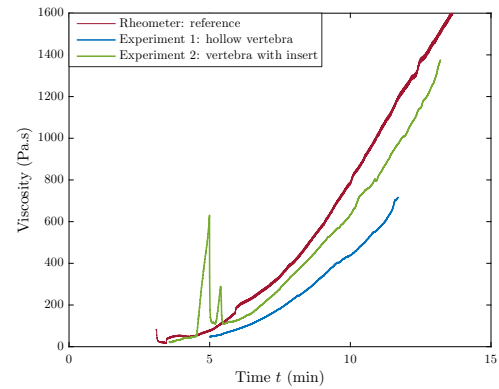


Figure 4 – Computation of the bone cement viscosity.

abstract, proves the ability to compute the viscosity online. For the second experiment, one can notice two sharp peaks because of the establishment of a plug at the end of the needle, which is a common phenomenon during actual vertebroplasty procedures. Moreover, the distortion between both experiments questions the assumption of the bone cement outlet at atmospheric pressure.

CONCLUSION

Percutaneous vertebroplasty procedures are expanding worldwide in spite of the complex behavior of the injected orthopedic bone cement that may cause severe complications in case of cement leakage. In this paper, we described the design of an injection device for vertebroplasty procedures using a rate control scheme, which is adapted to the very slow injection flow rates. Moreover, the conducted experiments feature the ability of computing the bone cement viscosity online while setting the bone cement temperature. Prospects include an improved control of the cement viscosity due to an adapted temperature closed-loop control and the design of a second temperature control system that is deported from the patient in order to meet the standard requirements of an operating room.

REFERENCES

- [1] A. Gangi, T. Sabharwal, F. G. Irani, X. Buy, J. P. Morales, and A. Adam, "Quality assurance guidelines for percutaneous vertebroplasty," *Cardiovascular and Interventional Radiology*, vol. 29, pp. 173–178, April 2006.
- [2] M. Loeffel, I. Pappas, and L. Nolte, "Injection Device With Haptic Feedback," US20090216191 A1, Aug. 2009.
- [3] Merit Medical Systems, "StabiliT[®], Vertebral Augmentation System." <https://www.merit.com/interventional-oncology-spine/vertebral-compression-fracture/vcf/stabiliit-vertebral-augmentation-system/>, 2017.
- [4] N. Lepoutre, G. I. Bara, L. Meylheuc, and B. Bayle, "Phase space identification method for modeling the viscosity of bone cement," in *European Control Conf.*, June 2016.
- [5] N. Lepoutre, G. I. Bara, L. Meylheuc, F. Schmitt, L. Barbé, and B. Bayle, "Design and control of a thermal device for bone cement injection," in *6th IEEE Intern. Conf. on Biomedical Robotics and Biomechatronics*, June 2016.

Tactile robotic endoscopic capsule for safe closed-loop force control

D. Camboni*, R. Calì*, J. Ortega Alcaide, C. M. Oddo, M. C. Carrozza, A. Menciassi, G. Ciuti, P. Dario

The Biorobotics Institute, Sant'Anna School of Advanced Studies, Pisa, Italy.

domenico.camboni@santannapisa.it

*These authors equally contributed to the work

INTRODUCTION

Magnetically-driven capsules represent one of the most promising technologies in the field of active capsule endoscopy [1]. This technology aims at going beyond the major drawbacks of traditional endoscopes, *i.e.*, the invasiveness and discomfort caused by hand-guided control, which can lead to conventional scope looping and therefore pain and potential tissue damage or, in the worst case, perforation (*e.g.*, 0.1–0.3 % for diagnostic procedures in the colonic district) [2]. However, magnetically-driven systems require a precise localization system for implementing a closed-loop control for robot-assisted navigation [3].

In this paper, the authors present an endoscopic capsule equipped with a dense array of MEMS tactile sensors [4], preliminarily used as a force sensor module for enhancing closed-loop control. This system can allow improved magnetic link control, serving as a redundant system beside magnetic localization techniques, and it can avoid exceeding the upper limit of magnetic attraction forces for safe tissue interaction [5].

MATERIALS AND METHODS

The system is composed of: *i*) a capsule of 33 mm (l), 26 mm (w), 17 mm (h), with a soft circular dome of 7 mm diameter made of Dragon Skin® 10 (Figure 1c), covering a 2x2 array of MEMS tactile sensors (each sensor consisting of 4 piezo-resistive channels at the roots of a cross-shaped structure, with a central pillar - Figure 1d) and a permanent magnet (N50 NdFeB: 12 mm x 8 mm x 8 mm); *ii*) a robotic platform consisting in a 6-DOFs anthropomorphic manipulator (Comau Racer 5-0.80, Comau, Grugliasco, Italy), with a permanent magnet mounted on its end-effector (cylindrical-shape N52 NdFeB: length 80 mm, diameter 90 mm); and *iii*) a control and processing unit which receives the tactile sensors output and updates the robot trajectory accordingly (Figure 1b). In the present study a selection of four piezo-resistive channels of the capsule has been used, for the sake of data order reduction (Figure 1d).

The capsule is inserted in a rigid plastic tube (5.5 cm in diameter and 37 cm in length) and is moved by the robotic manipulator till the end of the tube with a predetermined constant speed of 25 mm/s, by means of the established magnetic interaction link. The z distance is automatically adjusted during locomotion in order to maintain a constant contact force between the capsule and the tube wall. A series of four tests has been performed setting the tube at four different angles with

respect to the x - y horizontal plane, *i.e.*, 0°, 8°, 14° and 23°.

The experiment starts with the magnetic end-effector over but distant from the capsule, which is not in contact with the tube wall. The magnet at the end-effector of the robotic arm is moved towards the capsule (varying z) to establish the magnetic link. The capsule is considered in contact when at least one sensor of the array overcomes 0.25 N of estimated contact force. All the reference values have been selected after a preliminary experimental pilot test. Once the capsule is in contact with the tube it starts moving at constant speed. The capsule stops moving only if the contact condition is lost; in this case only z is varied in order to re-establish a magnetic link with the capsule. The trajectory of the robot is adjusted by a proportional control (with K_p 0.25) based on the norm of the used four channels of the array, with a desired target force of 1.1 N, selected after a pilot test. This value is compatible with the maximum force the large bowel can sustain, which is 13.5 N [5].

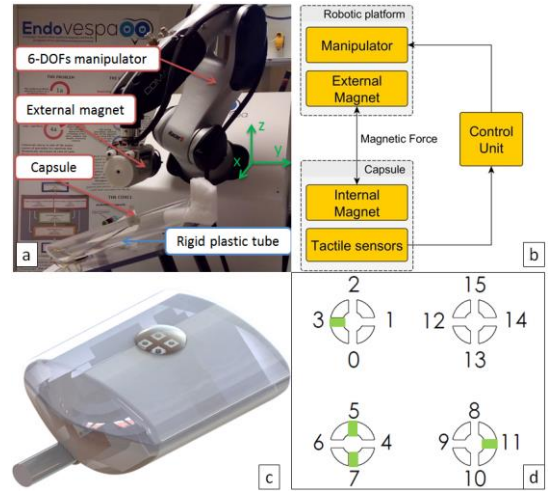


Figure 1 a) Robotic test bench, b) block diagram of the system, c) capsule rendering and d) sensors map showing the 4 channels in use.

When the capsule reaches the end of the tube it goes back to the initial position. The forward/backward path is performed three times per configuration.

RESULTS

Table 1 summarizes the data obtained from the experiments. The results show that the norm of the force sensors is well maintained at the target force in all the configurations tested, with small variations during each single trial. The manipulator's Cartesian coordinates have been used for a control calculation of the angle

trajectory, in order to assess the effectivity of the system to follow the path. The angle mean value gives a good estimation of the actual tube inclination, meaning that the manipulator accurately maintains a constant distance with the capsule in order to guarantee the desired contact force. The significant value of standard deviation is given by the continuous adjustment caused by small variations of contact conditions and non-smooth sliding of the capsule, caused by stick and slip, on the tube wall. The high frequency angle adjustment explains the high values of standard deviation but it also points out the responsive reaction of the control system. The results have been averaged on the three trials performed per each configuration.

Angle test		Angle trajectory		Angle adj.	Force readout	
		Mean [deg]	Std [deg]	Mean [Hz]	Mean [N]	Std [N]
0°	frw	0.5	3.1	5.4	1.1	0.04
	bck	0.6	4.2	2.1	1.1	0.06
8°	frw	7.8	8.2	3.6	1.14	0.07
	bck	9.2	5.8	3.4	1.07	0.03
14°	frw	15.0	5.1	9.3	1.16	0.04
	bck	15.9	2.8	10.3	1.03	0.03
23°	frw	22.6	3.5	10.8	1.19	0.06
	bck	25.1	4.9	7.9	1.01	0.08

Table 1 Angle trajectory estimated from the robot output, angle adjustment frequency and norm of the force sensed by the used four sensors of the array. Frw: forward; bck: backward.

Figure 2 shows the movement of the robot along the z axis and the norm of the sensor output while sliding in the tube. During the first tract the robot approaches the tube in order to establish a magnetic link with the capsule, thus stopping the vertical descent at the contact condition at the imposed force. Then the movement starts and the capsule goes up until the end of the tube and then returns to the initial position. The sensor output slightly oscillates around the force threshold value, while sliding. It is worth noting that, as expected, the force sensor readout is always higher than the target value while ascending and lower while descending. This is because, *e.g.*, while ascending the robot attempts a horizontal movement causing a force increase until the control reacts and corrects the trajectory. A fast variation in the force readout happens when the robot changes direction in order to come back to the beginning of the tube.

DISCUSSION AND CONCLUSION

This work presents a novel device based on an array of MEMS tactile sensors for controlling forces and then pressure applied on the wall of a rigid plastic tube, which represents a simplified endoscopic scenario, with a straight path and without obstacles. These preliminary

tests are meant to assess the system capabilities for improving closed-loop maneuverability and implementing safety measures. It is worth noting that the device is robust enough to work properly with a subset of channels among the 16 available. The system will be tested in a more realistic environment resembling compliance and obstacles of a real intestinal tract. Extensive tests will also be performed in combination with the capsule localization strategy that is under development by the authors. These experiments also represent a first assessment of the capabilities of such a system, which can be developed to work also as a tactile probe for remote palpation in endoscopic procedures, providing the physician with a new tool for diagnosis, beside the established vision-based techniques.

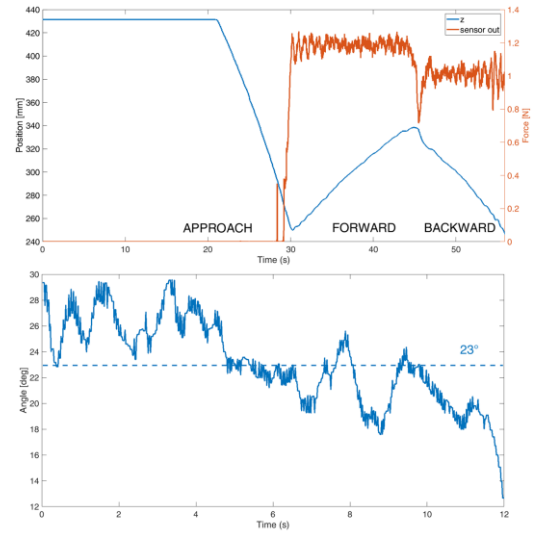


Figure 2 z movement of the manipulator and norm of the force sensors during the 23° inclination test and angle variation during forward movement.

ACKNOWLEDGMENTS

The work described in this paper was supported by the European Commission within the framework of EndoVESPA European project - H2020-ICT-24-2015 (GA: 688592). The authors thank all the collaborators of the EndoVESPA EU project (www.endovespa.eu).

REFERENCES

- [1] L. Liu, *et al.*, "A review of locomotion systems for capsule endoscopy," *IEEE Rev. Biomed. Eng.*, vol. 8, pp. 138-151, 2015.
- [2] G. Ciuti, *et al.*, "Frontiers of robotic endoscopic capsules: a review," *JMBR*, vol. 11, pp. 1-18, 2016.
- [3] H. Mateen, *et al.*, "Localization of Wireless Capsule Endoscope: A Systematic Review," *IEEE Sensors J.*, vol. 17, pp. 1197-1206, Mar 1 2017.
- [4] C. M. Oddo, *et al.*, "A Biomimetic MEMS-based Tactile Sensor Array with Fingerprints integrated in a Robotic Fingertip for Artificial Roughness Encoding," *Robio 2009*, vol. 1-4, pp. 894-900, 2009.
- [5] E. A. M. Heijnsdijk, *et al.*, "Inter- and intraindividual variabilities of perforation forces of human and pig bowel tissue," *SURG ENDOSC*, vol. 17, pp. 1923-1926, 2003.

Precise estimation of the Position of Continuum Instruments in Robotic Endoscopic Surgery using LWR

P. Cabras¹, F. Nageotte¹, P. Zanne¹, C. Doignon¹

¹*ICube laboratory, University of Strasbourg, CNRS, France (Nageotte@unistra.fr)*

INTRODUCTION*

Flexible systems with continuum bendable sections are of high interest for minimally invasive procedures. They are used in several teleoperated robotic systems [1]. However, it is desirable to improve the accuracy of position control of continuum sections for realizing automatic movements or providing assistance.

In the scope of endoscope-like systems it seems essential to use external feedback to obtain sufficient accuracy, because the shape of the flexible shaft is usually not known and mechanical features, such as friction, are subject to change during use.

An appealing approach for measuring bendable instrument positions is to use the endoscopic images because it avoids integrating additional sensors, such as Fiber-Bragg Grating or EM sensors. Commonly, a single endoscopic camera is available. Models are therefore needed for inferring 3D information from 2D images [2]. Correct geometric parameterizations must be provided as shown in [3], [4], which requires modeling uncertain motions and using subtle regularization techniques [4]. These difficulties advocate for finding alternative approaches.

MATERIALS AND METHODS

We propose to investigate the use of learning-based approaches, which are of interest for the mentioned problem, because (1) they do not require explicit models and (2) they can implicitly incorporate complex behaviors, which would be difficult to describe, such as non-uniform bending curvature, or which are specific to a given instrument. Nevertheless, learning-based methods usually require large amounts of data, whereas the application requires simple and fast training stages.

In the context of position estimation of continuum robotic sections instruments from endoscopic images, the objective is to learn the function relating an n dimensional input vector $x = (x_1, \dots, x_n)$ composed by some descriptors of the 2D image of the instrument with the 3D position of its tip (TCP) $y = (X, Y, Z)$. Our point of view is that the training stage must be performed for each particular instrument before its use. This approach would allow to learn the specific behavior arising from unavoidable manufacturing variability (especially large for miniature instruments) or from wears for reusable instruments. This could also be applied for rapidly

prototyped instruments specifically designed for a given task. As a consequence, the method should include a very simple, fast and automatic training stage. For demonstrating the potential of such methods, we consider the robotic system STRAS described in [1], which has instruments with a single bendable section (3DOFs). We are interested in recovering the 3D position of the tip of the instrument.

A. Input visual information

The input data must contain the information on the instrument position, while being easily and automatically segmented from endoscopic images. We propose to use the centroids of five colored markers attached to the continuum bendable part of the instruments. Such markers can be robustly extracted from in vivo images ([4]) and their coordinates provide an input set of dimensionality 10.

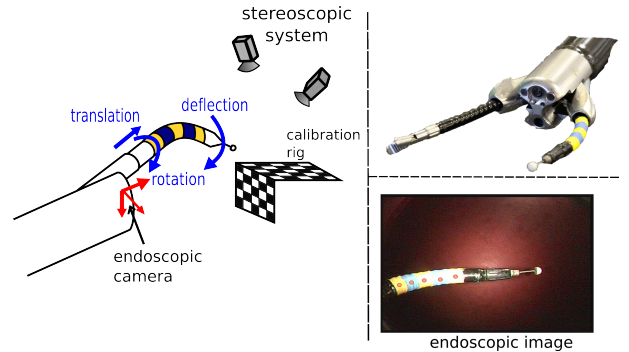


Fig. 1 Setup of the learning-based approach for bendable instrument position measurement. The instruments of STRAS (top right) have 3 Degrees of Freedom. They are marked with 5 colour strips. During training, the instrument position is measured by a stereoscopic system (left) and centroids are automatically extracted from endoscopic images (bottom right)

B. Creation of the training set

The training set must provide values of the 3D position of the TCP, expressed in the endoscopic camera frame. We have opted for vision-based measurements provided by a calibrated external stereoscopic system (see Fig. 1) (accuracy of the setup: 0.45mm RMS). This allows measuring the position of the instrument without contact and without attaching sensors to it.

For good training, the workspace of the instrument should be regularly and finely sampled. However, the training step should be performed quickly, typically in less than 5 minutes. This directly limits the sampling of the workspace. As a simple solution we rely on a subdivision of the workspace at the proximal side (the 3 DOFs of the instruments), fixed to $[7 \times 7 \times 7]$ samples. The input information is obtained using the same

* This work was partly funded by the French program "Investissement d'Avenir" run by the 'Agence Nationale pour la Recherche' under grant reference 'Infrastructure d'avenir en Biologie Santé - ANR-11-INBS-0006'

segmentation algorithm that will be used subsequently for the position estimation.

C. Locally Weighted Regression

The use of a network of Radial Basis Functions (RBF) was proposed in [3]. However, the maximal errors encountered at some positions was largely superior to 5mm, the limit usually provided as a guideline by surgeons for minimally invasive surgery. A possible reason might be the large number of (hyper)-parameters to be tuned for RBF, which becomes an issue with a small training set.

Therefore, as an alternative and simpler approach, we propose to use Locally Weighted Regression (LWR), with the objective to decrease the maximum estimation errors. LWR [5] consists in computing a weighted linear regression on the points of the training set x_m around the query point x_q . This comes to minimize

$$\chi^2 = \frac{1}{2} \sum_{m=1}^M w_m(x_q) \|y_m - \gamma^T x_m\|^2 \quad \text{over the regression coefficients } \gamma, \text{ with weights coding the distance between the query point and the training points: } w_m(x_q) = \exp\left(-\frac{1}{2}(x_m - x_q)^T D (x_m - x_q)\right).$$

D defines the neighborhood used as support for the regression. The minimization can be solved in closed-form, but for avoiding singularities in the computation, input data should be pre-processed in order to remove information redundancy. In the case of instruments with 3DOFs and with the chosen image features, it appears that 99% of the variance of the visual information is explained by the 3 first components of a PCA. Therefore, only these components are used in the LWR.

D. Parameters tuning

Tuning parameter D from a small training set might lead to over-fitting. Therefore, we propose to rely on simulation, with the purpose of observing the general behavior of LWR in function of D for representative datasets. Therefore the ingredients of the simulation are the model of the endoscopic system and of the instrument (as given by the CAD), the workspace to span and typical noise expected onto the input data of the training set.

Considering $D = \frac{Q}{div}$ where Q is the total variance of the training set, we performed a grid search on div (see Fig. 2) which was consequently fixed to $div = 3$ in order to minimize the maximum estimation error in the workspace.

RESULTS

We have performed tests on a laboratory setup with the STRAS robotic system [1]. The training set with a subdivision of $[7 \times 7 \times 7]$ is created in less than 3 minutes (172s, 0.5s/sample). The segmentation method described in [4] is applied for extracting the 5 centroids of the markers (Fig. 1).

The RBF method [3], an advanced model-based approach [4] and LWR are applied on a testing set composed of 237 images. For quantitative assessment,

the ground truth for the 3D position of the TCP is obtained using the external stereoscopic cameras. Results are presented as sorted errors for all tested positions on Fig. 2.

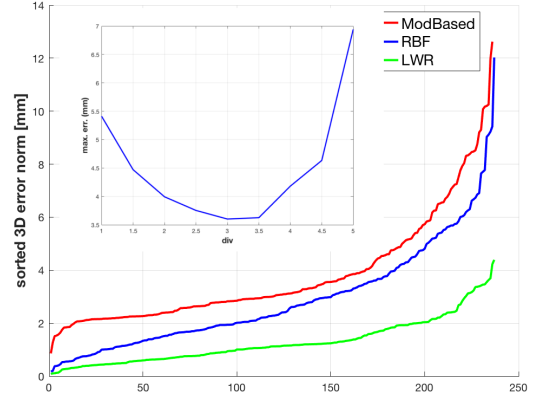


Fig. 2. The norms of the 3D estimation errors obtained on the testing set with an adaptive model, with RBF and with LWR all presented in sorted order. The inlay shows the evolution of the maximum error in function of div obtained in simulation.

CONCLUSION AND DISCUSSION

LWR allows to simply and precisely capture the image-to-TCP relationship of 3 DOFs bending instruments with only a small training set. The maximum error is reduced to only 4.2 mm. Moreover 93% of the estimates are below 3mm, which is the length of the instrument effector. Model-based techniques do not allow to reach the same accuracy, showing that the model was not trustful, but still sufficient for the aim of tuning the parameter of the LWR. Estimation accuracies are now compatible with automatic control aspects. Dynamic effects should however be investigated for on-the-fly position estimation. In addition, an integrated system should be designed in order to allow easy and intuitive training set generation.

REFERENCES

- [1] A. De Donno, et al., "Introducing STRAS: A new flexible robotic system for minimally invasive surgery," in 2013 IEEE ICRA, 2013, pp. 1213–1220.
- [2] R. Reilink et al., "3d position estimation of flexible instruments: marker-less and marker-based methods," IJCARS, vol. 8, no. 3, pp. 407–417, May 2013.
- [3] P. Cabras et al., "Comparison of methods for estimating the position of actuated instruments in flexible endoscopic surgery," in 2014 IEEE/RSJ IROS, Sept 2014, pp. 3522–3528.
- [4] P. Cabras, et al., "An adaptive and fully automatic method for estimating the 3d position of bendable instruments using endoscopic images," IJMRCAS, April 2017, .
- [5] C. G. Atkeson, A. W. Moore, and S. Schaal, "Locally Weighted Learning," in Lazy Learning, D. W. Aha, Ed. Springer, 1997, pp. 11–73,

Probabilistic Principal Component Analysis and Particle Filtering for real-time retina detection from a single-fiber OCT.

G. Borghesan*, M. Ourak*, E. Lankenau†, R. Neffin†, P. Koch‡, H. Schulz-Hildebrandt‡, K. Willekens§, P. Stalmans§, D. Reynaerts*, E. Vander Poorten*

*Dept. of Mechanical Engineering, KU Leuven, †OptoMedical Technologies GmbH, Lübeck, Germany

‡Medical Laser Center Lübeck, Lübeck, Germany, §Dept. of Ophthalmology, University of Leuven
gianni.borghesan@kuleuven.be

Abstract—Vitreoretinal surgery concerns a set of particularly demanding micro-surgical interventions that take place at the back of the eye. Examples of such procedures are retinal vein cannulation (where the surgeon aims to insert a needle in a vein of the size of human hairs) and epiretinal membrane peeling (where a detached membrane must be removed from the retina). As severe retinal damage can be caused by undesired collisions, good instrument to retina distance perception would be very useful. We propose to use an OCT-fiber instrumented tool, and purposefully designed algorithms to interpret the measurements and extract a reliable real-time distance estimate. This abstract describes the progress that was made and includes a test conducted with a robotic platform on a synthetic eye mockup.

I. INTRODUCTION

Vitreoretinal (VR) surgery is currently performed in a fully manual manner. Upon start of the procedure the surgeon carefully puts up to four trocars into place at 3 to 4 mm from the corneal limbus, the border between the cornea and the sclera. Through these trocars thin instruments and illumination are inserted to operate on the interior part of the eye. The micro-surgeon observes the retina and relative instrument motion via a stereo-microscope positioned above the patient's eye. Depth perception is achieved by means of stereo vision, by observing the shadows that are cast by lateral illumination, by checking whether an instrument is in focus, or by indentation of the tissue (*e.g.* in the case of cannulation). These methods require significant expertise to be used effectively, given the small size of the structures the micro-surgeon is to deal with: for *epiretinal membrane peeling* (ERM-peeling) a membrane up to about $60\ \mu\text{m}$ is to be peeled off; for ILM peeling the *internal limiting membrane* is only about $4\ \mu\text{m}$ thick. Veins that are to be cannulated to treat *retinal vein occlusion* have diameters in the order of $100\ \mu\text{m}$ - it is clear that inaccurate depth perception and depth control can cause serious complications [1], [2]. Research has been conducted to improve depth perception through adoption of alternative sensing techniques. OCT and force sensing are some of the more mature techniques that have been investigated in the past.

II. GOALS AND RELATED WORK

In this work we build further upon our earlier work [3] and on work of others such as [4] and [5], where OCT images have been employed in a number of algorithms targeting automatic

segmentation of retinal layers, or to identify markers that predict certain diseases. Most of prior works rely on 2D or 3D OCT images, referred to as B- and C-scans respectively. Conversely, in [3], following the earlier work by Balicki *et al.*, [6], we employ OCT data that is acquired via an optical fibre incorporated directly inside the surgical instrument. This gives a one-dimensional depth scan also known as A-scan. Balicki *et al.* studied the use of A-scans with an OCT probe mounted on a micro-surgical pick; our work is mainly investigating its use for vein cannulation, more concretely we aim to the development of algorithms for robust distance estimation. Compared to [3], we evaluate and expand the earlier algorithm by introducing the use of a Particle Filter to overcome the problem of initialization that flaws Extended and Unscented Kalman Filters. In addition, we moved towards a more realistic setting by employing a robotic setup and the retina phantom shown in fig. 1, rather than relying on OCT B-scans captured through the microscope lenses, and interpret them as A-scans. We keep the retina modeling method that employs *probabilistic principal component analysis* (PPCA, [7]) to characterize a number of *latent* variables, as detailed in [3].

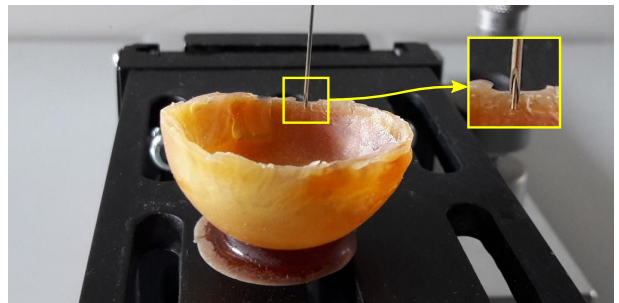


Fig. 1. Experimental setup showing the instrument (zoom in on fiber lens inside the needle) and the retina phantom (from *OptoMedical Technologies*).

III. MATERIALS

The setup is composed of: *i*) a 3DoF stage upon which *ii*) the OCT-Probe enabled instrument is mounted, *iii*) an OCT camera, *iv*) a synthetic eye mock-up. The instrument holds a fiber (assembled by *Medical Laser Center Lübeck GmbH*). The fiber is connected to an OCT camera by *OptoMedical Technologies GmbH* (OPM) which has been modified to be

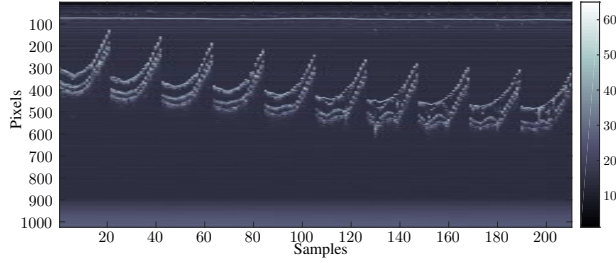


Fig. 2. Learning data set of 10 slices (0.4 mm spacing) of 21 points each (0.4 mm apart); the reflection of the fiber tip are visible at pixel ≈ 80 .

used with the above mentioned fiber. The Eye mock-up, provided by OPM, a multi-layered phantom of human retina, including structures that resembles veins. A close up of the needle, fiber, and phantom is shown in fig. 1.

IV. METHODS

The proposed procedure consists of a learning phase and a run-time identification phase (using a single line, as produced by an OCT fiber probe). Both phases are summarised next.

a) Learning phase: In order to build a base for the *PPCA*, we register scans in discrete points (each point is observed for 2 seconds, and an average is kept). Figure 2 shows the learning data set. *PPCA* needs a normalised training set (i.e. each pixel must represent the same information). To achieve this, we extract in a semi-automatic way some landmarks around important features. The data set is then re-sampled in such a way that these landmarks appear in the same area. *PPCA* defines the signal in function of the mean and modes. In such way, an approximated A-scan can be described in function of x :

$$x = [P \quad \Delta P \quad M1 \quad M2 \quad M3 \quad \dots]$$

where P is the starting pixel where the mode is applied, ΔP is the number of pixels that is considered as window for the model, and M_i are the latent variables associated with the modes.

b) Tracking: Particle filtering is used to track the contour of the retina. Preliminary experiments have been carried out by scanning the synthetic eye with a movement parallel to the retina, building something analogous to a B-scan. Data is currently saved and processed offline with MATLAB (The MathWorks Inc.). A particle filter with state x and 200 particles is used. The first three modes are employed to reconstruct the measured signal. Figure 3 shows how the filter tackles a horizontal sweep, in which the fiber is moved of 8 mm in ≈ 8 s. In fig. 3 are reported: *i)* the time evolution of the estimated state (first 5 subplots), *ii)* the A-scans captured by the fiber superimposed with the time evolution of P (yellow), $P + \Delta P$ (green), and the estimated location of retina layers (red), and *iii)* the y position of the probe.

V. CONCLUSIONS

This abstract reported on the combination of local OCT sensing, retina modeling based on *PPCA*, and particle filtering.

It was shown how this can be used to track in real-time the retinal layers with robot-assisted interventions in mind.

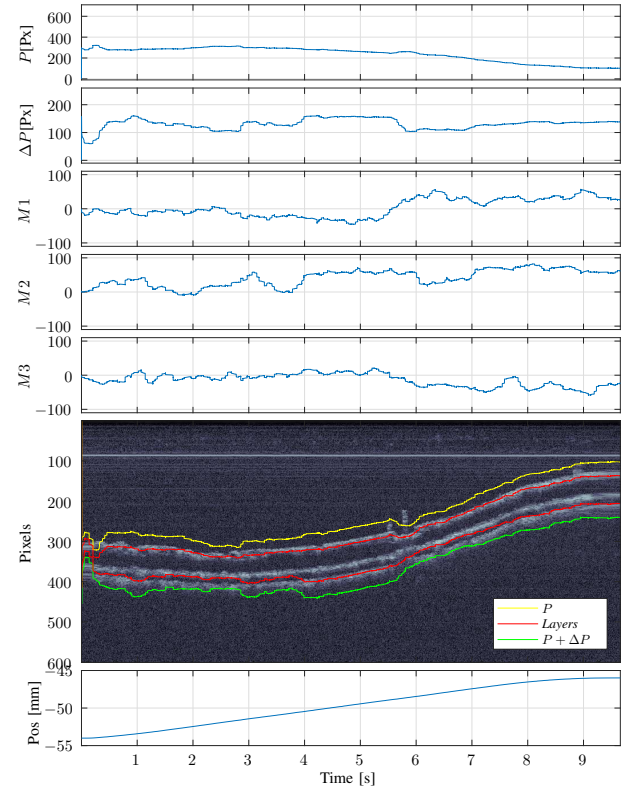


Fig. 3. Data from experiments; first five sub-plots show the time evolution of the estimated state, the sixth sub-plot shows the A-scan (Vs. time), and the layer estimation result, the last one the robot position. The constant peak around pixel 80 is the reflection of the lens at the tip of the instrument.

ACKNOWLEDGMENT

Research funded by The EU Framework Programme for Research and Innovation - H2020 - GA No 645331.

REFERENCES

- [1] Sjaarda *et al.*, "Distribution of iatrogenic retinal breaks in macular hole surgery," *Ophthalmology*, vol. 102, no. 9, pp. 1387–1392, 1995.
- [2] Nakata *et al.*, "Sub-retinal hemorrhage during internal limiting membrane peeling for a macular hole," *Graefe's Archive for Clinical and Experimental Ophthalmology*, vol. 241, no. 7, pp. 582–584, 2003. [Online]. Available: <http://dx.doi.org/10.1007/s00417-003-0676-y>
- [3] Borghesan *et al.*, "Single fiber oct-based retina detection for robot-assisted retinal vein cannulation," in *CRAS-2016*, 2016.
- [4] Lu *et al.*, "Automated layer segmentation of optical coherence tomography images," *IEEE Transactions on Biomedical Engineering*, vol. 57, no. 10, pp. 2605–2608, Oct 2010.
- [5] Kafieh *et al.*, "A review of algorithms for segmentation of optical coherence tomography from retina," *J Med Signals Sens*, vol. 3, no. 1, pp. 45–60, 2013.
- [6] Balicki *et al.*, "Single fiber optical coherence tomography microsurgical instruments for computer and robot-assisted retinal surgery," in *Medical Image Computing and Computer-Assisted Intervention–MICCAI 2009*. Springer, 2009, pp. 108–115.
- [7] Tipping and Bishop, "Probabilistic principal component analysis," *Journal of the Royal Statistical Society, Series B*, vol. 61, pp. 611–622, 1999.

A Framework for Assisted Tele-operation with Augmented Reality

N. Enayati¹, A. Mariani¹, E. Pellegrini¹, T. Chupin¹, G. Ferrigno¹, E. De Momi¹

¹Politecnico di Milano,

nima.enayati@polimi.it

INTRODUCTION

This extended abstract introduces a software framework that equips a teleoperation setup with basic 3-dimensional (3D) Augmented Reality (AR) and haptic guidance capabilities. The design goal of this software framework is to facilitate rapid prototyping of AR interactive tasks for research studies in fields such as surgical training and human-robot interaction. The software is developed and tested on a da Vinci research kit, which comprises two slave arms with laparoscopic tools, two master manipulators and an endoscopic camera manipulator.

AR combines 3D computer-generated objects superimposed onto real images and video in real time, which creates a unique channel of interaction with virtual objects and data. In surgical and robot-assisted surgical fields, the implementation of AR and its advantages has been well discussed in the literature [1] [2]. While there remain many challenges to tackle, especially in tracking and 3D reconstruction of deformable organs, several research groups have expanded effort on developing AR platforms for surgical robotics research. For instance, in [2] the feasibility of an AR interface was demonstrated in a palpation and surface tracing tasks performed with artificial tissue. In a previous work, we introduced a framework for tracking and visual augmentation of blood vessels [3]. Here we introduce a framework with intricate 3D graphics, simulated physics and assistive force/torque capabilities. Such a framework can be used

in research studies that demand task performance measurements that would be otherwise difficult to acquire with interaction with real objects. The study of motor learning for surgical training is an example, where using AR can allow reproducing common surgical robotic exercises with the real robot (compared to completely simulated environments in Virtual Reality (VR) training) and at the same time provide real-time measurements of the interactions with the virtual objects for performance metrics analysis.

MATERIALS AND METHODS

We present in this section an overview of the Assisted Teleoperation with Augmented Reality (ATAR) software framework. Fig. 1 shows the general structure of the ATAR framework. A basic “task class” structure is extended into study-specific child classes, which are further extended to encode implemented graphics, dynamics and task logic. Each task class (Labeled in Fig. 1 as loaded task) provides a method that runs at 1 KHz in a dedicated thread and generates the desired pose of the defined tools according to the task’s design. These desired poses are communicated through Robot Operating System (ROS) messaging to a separate executable that generates guidance wrenches in form of guidance active constraints [6] for each manipulator. Four methods of wrench generation is provided that include the common elastic method and non-energy-storing ones [7].

The 3D graphics are produced using the Visualization Toolkit (VTK) and OpenGL libraries. Two virtual

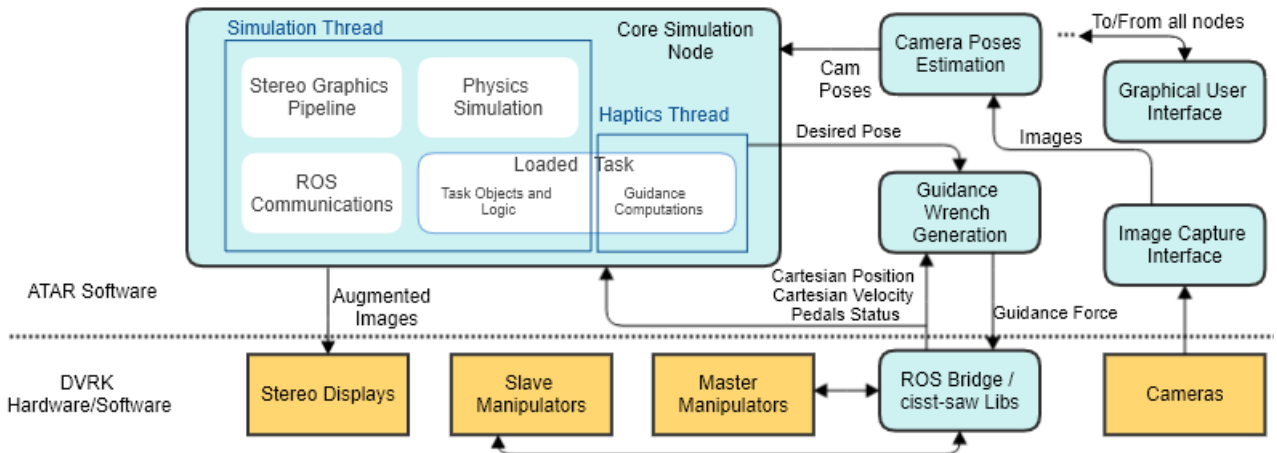


Figure. 1. The complete Software/Hardware architecture of the developed setup. Blue boxes represent software executables and yellow ones represent hardware components. The white components in the core simulation node represent the principal classes. The task class is dynamically loaded from the available tasks by the user through the graphical user interface. Once a task is loaded, a haptic thread is started that calculates the desired poses of the tools according to the definition provided by the task. These poses are used to generate the guidance wrench.

cameras are configured with the intrinsic parameters of the endoscopic cameras (estimated based on the common pinhole camera model) to produce correct overlaying of the virtual data on the real images. The images augmented with the rendered graphics are sent to the DVRK stereo displays through two output ports of a GeForce GTX 980 Ti GPU (Nvidia Corp.) with a refresh rate equal to that of the captured endoscopic images (25 Hz).

The Bullet physics library [4] was deployed to perform the dynamic simulation of 3D virtual objects. The robotic tools are simulated as kinematic objects and their pose is constrained to that of the real tools calculated through forward kinematics. To ensure real-time interactivity with realistic collision detection, mesh objects are approximated through convex hull decomposition [5]. A 3D mesh is decomposed into a minimal number of clusters, which are computed to have a concavity lower than a user defined threshold.

The ability of quantifying and manipulating spatial information to relate sets of data (registration) is fundamental to AR. The challenges of accurate registration in the operating room has been discussed since more than two decades ago [1]. Robotic systems partly simplify the hurdles of registration as they can provide the pose of the tools and cameras through joint position measurements and direct kinematics. The chain of tools and camera geometrical transformation must be registered to a “world frame” through measuring a set of fiducials. We performed this registration by measuring a set of points on a checkerboard augmented with fiducial visual markers (that allowed for partial occlusion of the board) with each tool and perform a least-squares estimation of the transformation between the set of points measured in the tool coordinate frame and the known world coordinate frame. The camera coordinate frame was registered to that of the world frame through online extrinsic calibration of the camera.

RESULTS

The developed framework has been tested and is currently being used for studying motor learning in surgical training and human-robot collaborative methods. An example of a task developed using the ATAR framework is shown in Fig. 2. The task is a replica of the steady-hand game where the subject is guided with forces/torques applied through the master manipulators to keep the rings at the ideal pose where the surface of the ring is as far as possible from the tube’s surface. The ideal pose of rings are calculated by estimating the tangent to the cylindrical tube through measuring the closest points on the mesh tube to a set of points on the ring object. The graphics and physics simulations run at the exact frequency of the captured images and the haptic thread meets the desired 1 KHz frequency that is essential for generating stable haptic cues.

CONCLUSION AND DISCUSSION

This extended abstract introduced a software

framework for generating AR and haptic assistance for tele-operation research studies. The framework can currently be used for rigid body augmented reality interactions. Future works include integration of deformable mesh simulation, image feature tracking and approximate real-time 3D model reconstruction that can increase the possible applications of such a framework to include further surgery related tasks and studies. This work received funding from the European Union’s Horizon 2020 research and innovation program under grant agreement No. H2020-ICT-26-2016-1-732515 (SMARTsurg project).

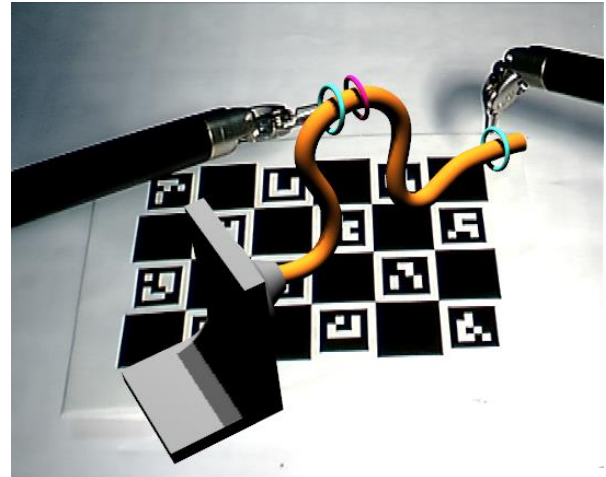


Figure. 2. An example of a task developed with the ATAR framework. The task shown is a classic steady-hand game in which the subject is asked to use the real DVRK surgical tools to move two rings along a tube (all virtual objects) towards a destination (the magenta ring), while preventing the rings from touching the tube surface.

REFERENCES

- [1] S. Lavallée, P. Cinquin, R. Szeliski, O. Peria, A. Hamadeh, G. Champeboux, and J. Troccaz, “Building a hybrid patient’s model for augmented reality in surgery: A registration problem,” *Comput. Biol. Med.*, vol. 25, no. 2, pp. 149–164, 1995.
- [2] T. Yamamoto, N. Abolhassani, S. Jung, A. M. Okamura, and T. N. Judkins, “Augmented reality and haptic interfaces for robot-assisted surgery,” *Int. J. Med. Robot. Comput. Assist. Surg.*, vol. 8, no. November 2011, pp. 45–56, 2012.
- [3] V. Penza, E. De Momi, N. Enayati, T. Chupin, J. Ortiz, and L. S. Mattos, “EnViSoRS: Enhanced Vision System for Robotic Surgery. A User-Defined Safety Volume Tracking to Minimize the Risk of Intraoperative Bleeding,” *Front. Robot. AI*, vol. 4, pp. 1–15, May 2017.
- [4] E. Coumans, “Bullet physics library,” *Open source bulletphysics.org*, 2013.
- [5] K. Mamou and F. Ghorbel, “A simple and efficient approach for 3D mesh approximate convex decomposition,” in *2009 16th IEEE International Conference on Image Processing (ICIP)*, 2009, pp. 3501–3504.
- [6] N. Enayati, E. De Momi, and G. Ferrigno, “Haptics in Robot-Assisted Surgery: Challenges and Benefits,” *IEEE Rev. Biomed. Eng.*, vol. 9, pp. 49–65, 2016.
- [7] N. Enayati, E. C. Alves Costa, G. Ferrigno, and E. De Momi, “A Dynamic Non-Energy-Storing Guidance Constraint with Motion Redirection for Robot-Assisted Surgery,” in *IEEE/RSJ International Conference on Intelligent Robots and Systems, IROS*, 2016.

Poster Session 2

Breast Tissue Parameter Estimation Using Finite Element Analysis

F. Visentin, B.M. Maris, P. Fiorini

*Department of Computer Science, University of Verona, Italy
francesco.visentin@univr.it*

INTRODUCTION

Prediction of the mechanical behaviour of a soft biological tissue is of great interest in different medical fields. In fact, knowing how the tissue reacts under gravity, or to the surgeon's actions can provide important information for surgical planning, or for the development of semi-autonomous robotic surgery tasks.

The patient specific model is extracted from radiological images such as MRI or CT. However, according to the clinical settings, different postural configurations might be required. As a consequence, it is necessary to acquire novel sets of data that reflects the different postural configuration. This approach can be very onerous both in terms of time and money. For this reasons, a different method should be used: predict a new view by biomechanical models.

In the last years, the modelling of human soft tissues had an important progress [1], especially in modelling the human breast [2]. With the use of MRI or CT scanners and Finite Element (FE) numerical tools, it is possible to create patient specific models that can be used to predict large deformations of the soft tissue. This approach can also be employed to simulate the mechanical behaviour of the breast during a mammography examination.

One of the main problems of this approach is the correct estimation of the properties of the tissue. In this work, we have designed an iterative approach to determine the Young's modulus of the breast tissue. The value is then used to derive an "at rest" model that allows to obtain any other view or to simulate the effect of external forces such as surgeon's manipulations. We validate the method by comparing the results with other acquisitions of the breast as a ground truth.

MATERIALS AND METHODS

To estimate the properties of the isotropic material used to simulate the breast tissue, we simulate the change of posture from prone to supine by using FE analysis. In order to do this, we assume that the body is subjected only to the force of gravity that acts along a single direction (for the prone case along the negative direction of the y-axis). With this assumption, by simply inverting the direction of the force of gravity (from -y to +y), and by doubling its magnitude (from 9.8N to 19.6N), it is possible to simulate the change of configuration from prone into supine.

As initial case study, we employed a multimodality breast phantom CIRS 0731 (CIRS Inc.) that accurately mimics the heterogeneous appearance of the breast tissue under different imaging scanners—such as

ultrasound, mammography, MRI, and CT—but not its Young's modulus. However, the later is not a limitation since the proposed method can be easily applied to the human breast case without any constraint.

To evaluate the method, a CT scanner acquired high-resolution 3D data. The acquisitions were performed by positioning the phantom in four different configurations: prone, supine, lateral, and vertical. The single acquisitions were aligned rigidly in a common reference system by using markers visible in the CT data. To generate the volume mesh of the breast phantom, we segmented the external surface of the phantom from the CT images by using an automatic algorithm based on region growing and threshold. Smoothing and decimation processes were employed to improve the quality of the surface reconstruction. The volume mesh was then processed to generate a refined mesh to be used in FE analysis. For simplicity, the FE model is considered to be homogeneous and no internal parts have been added to it.

The so created meshes were then used to simulate biomechanical deformation using a FE analysis software (FEBio [3]). The breast tissue is modelled as a neo-Hookean material which Young's modulus (E) is estimated by iteratively comparing the current deformation with a reference mesh. At each step, the value of E is estimated using the Newton's method applied on the parameter value and its goodness. The goodness of the parameter was evaluated by measuring the error over a control set of points. These are selected along the deformation axis, and within the volume located around the nipple region.

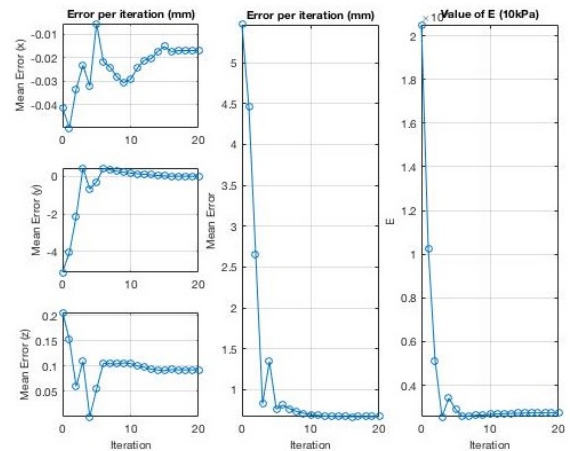


Figure. 1. Error and value of the parameter E w.r.t. each iteration step of the proposed method. (Left) error computed along the single component, (centre) total error, and (right) E value.

When pre procedure ends, i.e. when the method achieves a pre-defined error or reached a maximum number of iterations, the estimated E parameter is returned with its associated error. By using this value, it is possible to derive an “at rest” breast model by simply applying the same deformation with half of the magnitude (9.8N). To validate the derived value, we then deform the “at rest” model in order to simulate a different view. In this study we used as validation data measurements acquired in a vertical configuration where the force of gravity was acting only along the negative direction of the z -axis, and lateral configuration where the force of gravity was acting only along the negative direction of the x -axis. The “at rest” model was then deformed accordingly: 9.8N along $-z$, and 9.8N along $-x$. As in the previous case, the error was computed w.r.t. the same control set of points.

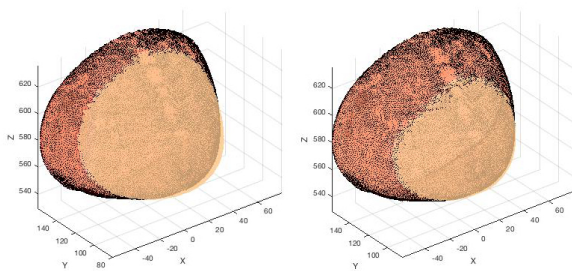


Figure 2. Overlay of the prone and supine meshes before (left) and after (right) the parameter estimation. Initial error is around 5.40mm, while the final error is around 0.65mm.

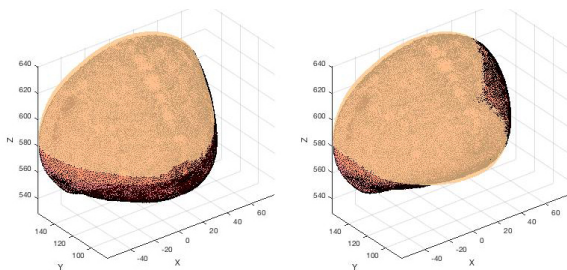


Figure 3. Overlay of the “at rest” and vertical meshes before (left) and after (right) the simulation. Initial error is around 4.13mm, while final error is around 2.17mm.

RESULTS

All the computations have been performed on a single core of a 2.6Ghz i7 machine with 16GB of RAM. Each model was composed by around 34000 nodes forming 123000 4-node tetrahedron elements. From the computation point of view, the time required for each simulation differs according to the stiffness of the material. Stiffer materials take shorter computation time (~15s), while softer material requires longer time (~45s). In total, the parameter estimation required around 13min.

Figure 1 shows the errors—w.r.t. the control set—at each iteration and the changes of the value of E . As the graphs suggest, the method terminated after 20 iterations without reaching the required value (0.5mm). In fact, the simulation with the best value of E (2.85kPa,

found at step 19) matches the control set with an error of 0.65mm, which is an acceptable value. In Figure 2 the overlay of the prone and supine meshes is shown before (left) and after (right) the parameter estimation. Darker regions represent full matching, while lighter ones only partial matching. The results suggest that the global error decreased. Results for the ground truth acquisition are shown in Figure 3. Here, the “at rest” model is compared with the vertical mesh. As in the previous case, the global error is reduced but result larger than 2mm. A similar trend can be observed also in the lateral case where the error decreases from 4.06mm to 2.63mm. This can be caused by error in the simulations, or in the image registration, or misalignment during the acquisition. However, the results are still acceptable.

CONCLUSION AND DISCUSSION

In this study, we proposed a FE modelling framework for the estimation of the material properties of a breast phantom by registering its surface in different positions under the action of the force of gravity. The model presented here will be a raw initialization of a finer model that will include materials with much different stiffness properties, such as breast tumours, therefore the parameters we have estimated by using the load of the gravity force serve only for the modelling of the average properties of the breast tissue considered as an isotropic material. This is not a limitation since several studies show that the elastic properties of the skin and the fat tissue that constitute more than 90% of the breast volume are similar. There is also the fact that stiff materials inside the breast (such as tumours) constitutes very small volumes compared to the whole breast, therefore they do not affect the global deformation.

As future works, we plan to investigate more complete models that consider also internal structures and the extension to clinical data.

FUNDING

This project has received funding from the European Union’s Horizon 2020 research and innovation programme under grant agreement No.688188 as part of the MURAB project.

REFERENCES

- [1] Carter T.J., Sermesant M., Cash D.M., Barratt D.C., Tanner C., Hawkes D.J., “Application of soft tissue modelling to image-guided surgery.” *Med. Eng. Phys.*, 2005, 27 (10) 893 – 909.
- [2] Han L., Hipwell J.H., Tanner C., Taylor Z., Mertzaniidou T., Cardoso J., Ourselin S., and Hawkes D.J., “Development of patient-specific biomechanical models for predicting large breast deformation,” *Physics in Medicine and Biology*, 2012, 57 (2) 455.
- [3] Maas S.A. et al. “FEBio: Finite Elements for Biomechanics.” *Journal of Biomechanical Engineering*, 134.1 (2012): 11005–NaN. *PMC*.

Foot pedal interface supplement for intra-operative camera control during microsurgery using the da Vinci Research Kit

D. Naftalovich¹, D. Dall'Alba², G. De Rossi², P. Fiorini², J. W. Burdick¹

¹ *California Institute of Technology, Mechanical and Civil Engineering, Pasadena, USA,*

² *University of Verona, Department of Computer Science, Verona, Italy*
nafty@caltech.edu

INTRODUCTION

Teleoperated surgical robots improve the surgeon's abilities through their physical mechanisms and digital control. The da Vinci Surgical System provides a control interface for the surgeon through free-moving 7-degrees-of-freedom (DOFs) hand interfaces and additional foot pedal buttons. The hand interfaces control motion of the tool arms in the Patient-Side Manipulator, and of the camera arm when in the camera motion mode, and the foot pedals toggle the camera and workspace clutch modes as well as control optical focus, electrocautery activation, and other features like third arm toggling on some models. Supplemental foot pedal buttons are proposed for enabling additional control features during surgical robot use, particularly for camera motion control during microsurgery.

In a recent experiment of performing microscopic surgery using the da Vinci Research Kit (DVRK)[1, 2] the existing control interfaces of the DVRK were found to be unideal for microsurgery and the proposed supplemental foot pedal tray system was implemented. The motivations of the addition were two fold: 1) to enable advanced control of camera motion and optical magnification to support activities of microscopic surgery using the surgical robot, and 2) to enable effective integrated intra-operative annotation markings by the operating surgeon. The present paper discusses the first of these topics.

Microscopic surgery is performed on small anatomical structures such as approximately 1-2.5 mm diameter blood vessels, nerves, and lymphatic vessels [3]. Traditionally (i.e., non-robotically) it is performed with optical magnification assistance using an operative microscope with foot pedal control for focusing, magnification, and visual field positioning. Surgical actions are performed with specialized microsurgical tools that have fine and delicate tips. While there is direct perceptory assistance by light passing through optical magnification between the surgical field and the surgeon's eyes, there is no direct actuation assistance or scaling since the tools are controlled directly by the surgeon's finger's, much like regular surgical tools but smaller. However, other peripheral methods are used to

assist microsurgical actions and tool motions, which seek to be very precise and steady, in order to eliminate tremor and provide fine dexterous control. These include distal anchoring at wrists and even finger tips, careful handling of the tools, and explicit attention to comfort and ergonomics. There is great importance for maintaining comfortable posture during microsurgery, as a strained posture results in increased tremor and degraded tool control and precision. Even motion factors like breathing and twitching due to lack of rest or substance use (e.g. coffee) can be considered by a careful microsurgeon.

Traditional microsurgery is performed in an overall static posture with anchored wrists [3]. Positioning of the surgical field in the microscope's visual field is controlled with a footpedal joystick. Image magnification and focusing is controlled via foot pedal buttons. In the da Vinci Surgical System video images are captured from an endoscopic camera and magnification of the images is achieved through motion of the camera towards and away from the surgical field, rather than via optical lensing. Motion of the camera is achieved via gross hand motions in the master console workspace, while holding the camera motion mode foot pedal button pressed. Focusing is achieved via optical lensing controlled by foot pedal buttons, like in the traditional case.

Due to the high importance of still posture during microsurgery, especially at the wrist, and due to the critical importance of intra-operative image magnification control there is conflict in the design of the da Vinci Surgical System and DVRK when used for microsurgery due to the use of hand motions for controlling camera motion and image magnification (via endoscopic camera motion). To address this challenge, the proposed foot pedal interface was implemented and its use enabled retention of hand and wrist position while moving the surgical field in the view and controlling image magnification. The experience emulates traditional microsurgical image control in a closer fashion and allowed the operating surgeon to maintain proper stationary microsurgical technique while achieving critical control of image magnification and positioning.



Figure 1. Photo of the foot pedals tray (B.B.Z. s.r.l.)

MATERIALS AND METHODS

A foot pedal pad was connected to the da Vinci Research Kit (DVRK) via a universal serial bus (USB) interface and integrated into the Robotic Operating System (ROS) recording of the operative robotic data. The hardware is shown in Figure 1 and the foot pedals buttons' functionalities and layout are shown in the schematic of Figure 2. The four right buttons were used to control movement of the camera tip in discrete small jumps in the four planar directions along the image plane. The two grouped left pedals were used to move the camera in and out of the image plane in small discrete steps, thus achieving an effect of image magnification. The left vertical button was used as a mode toggle button to switch the foot pedal setup into an annotation mode that enabled ROS-integrated timestamp signals along different channels in order to annotate surgical phase and skill related events intra-operatively by the operating surgeon.

CONCLUSION AND DISCUSSION

A hardware tray of seven foot pedal buttons was added to supplement the foot pedal interface of the da Vinci Research Kit in order to provide improved intra-operative control of camera motion. This control assistance was particularly useful for performing microsurgery using the DVRK platform. Although imposing some additional work and attention onto the user, the use of the additional intra-operative foot pedals was found to be feasible. Foot pedal control of camera motion enabled retaining the wrist and forearm in constant posture on the da Vinci's arm rest bar which is of particular importance in microsurgery in order to maintain reliable and comfortable anchored posture that enables finest tool control and minimal tremor. Camera motion foot control also enabled convenient image magnification control, with the same beneficial non-intrusion on hand positioning. Additional benefits were enabled by the foot pedal platform such as enabled intra-operative annotations of surgical phase and skill information.

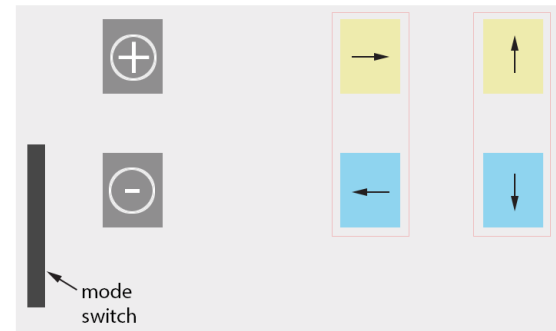


Figure 2 Schematic of the foot pedal buttons layout and camera motion control functionalities

REFERENCES

- [1] D. Naftalovich, D. Dall'Alba, G. De Rossi, P. Fiorini, J.W. Burdick. *Robotic-assisted microsurgical anastomosis training with motion capture using the DVRK: The Caltech-Verona Dataset*. Computer Assisted Radiology and Surgery (CARS), June 20-24, 2017, Barcelona, Spain.
- [2] P. Kazanzides, Z. Chen, Z. Deguet, G.S. Fischer, R.H. Taylor, S.P. DiMaio. *An open-source research kit for the da Vinci® Surgical System*. In Proc. Of the IEEE Intl. Conf. on Robotics & Automation (ICRA), pages 6434-6439, 2014.
- [3] S. Lee. *Manual of Microsurgery*. CRC Press, 1985.
- [4] K. Moorthy. *Objective assessment of technical skills in surgery*. BMJ 327(7422), 1032 (2003). DOI 10.1136/bmj.327.7422.1032.
- [5] T. Alrasheed, J. Selber. *Robotic Microsurgical Training and Evaluation*. Seminars in Plastic Surgery 28(01), 005 (2014). DOI 10.1055/s-0034-1368161.
- [6] C.E. Reiley, H.C. Lin, D.D. Yuh, G.D. Hager. *Review of methods for objective surgical skill evaluation*. Surgical Endoscopy 25(2), 356 (2010). DOI 10.1007/s00464-010-1190-z.
- [7] Y. Sharma, T. Plotz, N. Hammerld, S. Mellor, R. McNaney, P. Olivier, S. Deshmukh, A. McCaskie, I. Essa. *Automated surgical OSATS prediction from videos*. in 2014 IEEE 11th International Symposium on Biomedical Imaging, 2014. DOI 10.1109/isbi.2014.6867908.
- [8] J.D. Mason, J. Ansell, N. Warren, J. Torkington. *Is motion analysis a valid tool for assessing laparoscopic skill?* Surgical Endoscopy 27(5), 1468 (2012). DOI 10.1007/s00464-012-2631-7.
- [9] V. Datta, A. Chang, S. Mackay, A. Darzi. *Motion Analysis in the Assessment of Surgical Skill*. The American Journal of Surgery 184(1), 70 (2002). DOI 10.1016/s0002-9610(02)00891-7.

A multidisciplinary medical-engineering teamwork for high fidelity simulation in Neonatology

M. Del Pistoia¹, M. Ciantelli², R.T. Scaramuzzo², C. Tuoni², Davide Panizza², I. Baldoli³, S. Tognarelli³, C. Laschi³, F. Vangi³, E. Sigali², P. Ghirri¹, A. Menciasci³, A. Cuttano²

¹*Università di Pisa, Pisa, Italy*

²*Centro di Formazione e Simulazione Neonatale “NINA”, UO Neonatologia, Azienda Ospedaliera Universitaria Pisana, Pisa, Italy,*

³*The BioRobotics Institute, Scuola Superiore Sant’Anna, Pisa, Italy,*

martadelpistoia@gmail.com

INTRODUCTION

In the last few years, the “NINA” Centre of Education and Simulation for Neonatal Resuscitation, located in the Neonatal Intensive Care Unit (NICU) at Pisa University Hospital, started a collaboration with engineers of the BioRobotics Institute of Scuola Superiore Sant’Anna, Pisa. This teamwork began with the design and implementation of a pulmonary simulator (MEchatronic RESpiratory System SIMulator for Neonatal Applications - MERESSINA) and has continued with implementation of other devices. The last project was the technical realization of a real scale model of a sensorized neonatal head, for intubation training. Simulation-based training is increasingly emerging in NICUs since high-fidelity simulation has been confirmed as an effective instructional strategy to develop clinicians’ skills needed for patient care. Mannequin-based simulators help learners to work in real-life scenarios, promoting team-working, crisis management and resolution.

MATERIALS AND METHODS

The MERESSINA project arose from the need to develop a high-fidelity simulator of neonatal airways and lungs both for staff training and mechanical ventilator testing. It was developed to reproduce different clinical conditions and to simulate different scenarios. The simulator is formed of two main units: the first one consists of electronic components connected to a personal computer used for controlling the mechanical unit of the system. The software was designed to allow the operator to set all the functional parameters of a specific respiratory pattern and to simulate specific critical situations (e.g. apnea) through a user-friendly interface. The mechanical components include 5 proper chambers arranged to reproduce anatomical distribution: 3 lobes on the right and 2 on the left. Each compartment was characterized by its own compliance; right and left respiratory branches were subjected to an independent and adjustable resistance level. The 5 compartments had variable volume and were linked by a circuit of plastic tubes with a diameter of 4mm, which allows connection

of the simulator to mechanical ventilators commonly used in NICUs. In particular, we tested BEAR CUB[®]750PSV Infant Ventilator, Leoni Plus and Babylog 8000 Plus. Plastic airway tree was sized to reproduce upper respiratory tract of infants (total volume of 6mL and airway resistance at rest of approximately 60cmH₂O/L/s29). The 5 chambers were 50mL glass syringes arranged to reproduce lobes distribution and partially modified to allow direct and robust connection to airway tree (Figure 1). Each plunger was mounted and built in with the rod of a DC linear motor (QUICKSHAFT[®]Linear DC-Servomotors LM2070-080-01) that can be driven through a dedicated software interface (LabVIEW software). An analog pressure sensor MS147105GT was fixed on each plunger to detect pressure profiles during each respiratory cycle. Pressure signals are acquired by traditional data acquisition hardware (i.e. DAQ system NI USB-6218) with a sampling frequency of 1 kHz and treated with LabVIEW software for amplification and filtering.

Additionally, to this first prototype, we are now also investigating state-of-the-art on microsystems and smart materials technologies to select the most suitable solution for replicating the anatomo-physiological behavior of human respiratory system but guaranteeing a miniaturized structure. Smart materials and novel physical processes are being analyzed to design a miniaturized system prototype able to show desired performances by exploiting intrinsic characteristics of materials. A variable stiffness system could be obtained by using electroactive polymers or actuators based on granular jamming. This improvement allows us to interact with a realistic scenario rather than with a computerized software. Simultaneously we are beginning development of a reliable neonatal skill trainer able to provide clinicians with real-time information about intubation in terms of force peak value, force distribution and timing. This work is based on integration of different sensing elements (FSR[®]400short) into a commercial Laerdal[®]Neonatal Intubation Trainer. Each force sensor has been integrated in well-defined points, recognized as anatomical area mainly subjected to injuries during intubation (gingival arches, epiglottis and

tongue). Powering and data acquisition from sensor were managed with an Arduino Mega board. Calibration range was chosen considering maximum intubation force on adults as reported in literature. A friendly GUI was developed using MATLAB® (Figure 2). GUI was designed and implemented to acquire and record force data generated during the simulated intubation procedure and to provide full dataset required for debriefing phase after performance. Over threshold events are counted and signaled with a real-time warning sound useful in learning phases. The software is also provided with a timer that points out performance durations longer than 30s and records total session duration. The first prototype was in fact developed fixing sensing elements on phantom surface, but repeated stress on sensor surface reduced their sensitivity. Through the use of dedicated materials, for the new prototype we are investigating to embed sensors inside the simulator material. The developed system is a useful tool to train intubations, but is also useful to improve the procedure for expert clinicians, reducing the risk of in vivo damage.

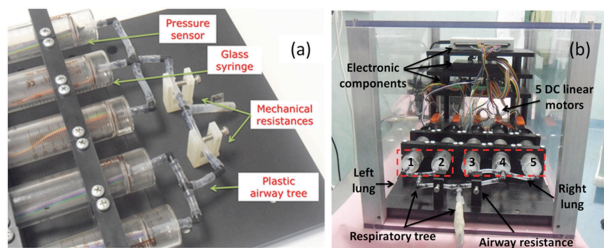


Figure 1. Images of simulator: (a) plastic tubes simulating airway tree and (b) whole system included in a plastic case.

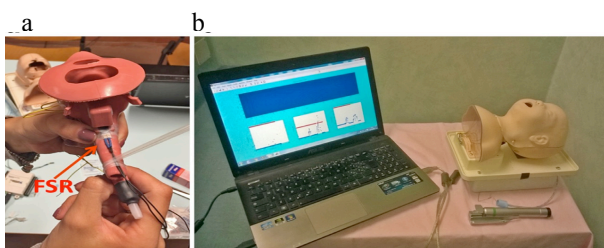


Figure 2. Integration phases of instrumented mannequin: (a) the FSR force sensor fixed on epiglottis, by exploiting external surface of airway structure; (b) the instrumented Laerdal® Neonatal Intubation Trainer connected to a laptop.

RESULTS

The base of this collaboration is to exploit knowledge and expertise of each group for a multidisciplinary collaboration able to assure new robotic systems ready for clinical application. Assessment of educational usefulness of these projects was tested at the NINA Center. For MERESSINA, we organized training sessions with some residents of anesthesiology, who weren't experienced in mechanical ventilation yet. The device was used to show how ventilator respond under specific conditions and to test different ventilation modalities. During simulated sessions, trainer defined possible clinical scenarios, and residents were asked to set ventilation parameters; they were helped by software (i.e. LEDs and warning messages) in choosing optimal

combination. Overall usefulness of simulator was satisfactory: considering lack of clinical experience, training sessions were accomplished with promising results. On the other hand, assessment of the sensorized neonatal intubation trainer was performed by 9 experts selected within the NINA Center who were asked to practice 3 intubations apiece. Median and maximum forces, over threshold events and execution time were measured for each trainee. Data analysis revealed epiglottis as the point mainly stressed. The debriefing phase was used to enhance clinicians' awareness of applied force and gestures performed, confirming this study as a starting point to achieve and optimize neonatal intubation skills.

CONCLUSION AND DISCUSSION

Deliberate practice using simulation has been shown to improve performance in many areas of neonatal intensive care. Realistic and reliable devices are essential for simulation training and their creation is now possible thanks to advances in biomedical engineering.

An ideal simulation system should have anatomical resemblance to involve operators during training. Use of simulation-based training is becoming source of experimental learning in medical education. It provides safe and effective procedures for practice and acquisition of clinical skills needed for patient care. This education is aimed to improve abilities of medical professional to ensure patient safety.

Biomedical engineering, characterized by integration of information technology, electronics, mechanics, chemistry and material science, has a leading role in emerging field of medical education and training, as it can strongly contribute to design and development of innovative technological devices able to simplify and improve clinical learning activities. Close collaboration between medical staff and bioengineers represents a key factor to develop devices replicating physiological systems, in terms of architecture and active behavior.

REFERENCES

- [1] Cuttano A, Scaramuzzo RT, Gentile M, Ciantelli M, Sigali E, Boldrini A. "Education in neonatology by simulation: between reality and declaration of intent." *J Matern Fetal Neonatal Med.* 2011 Oct;24 Suppl 1:97-8.
- [2] Baldoli I, Cuttano A, Scaramuzzo RT, Tognarelli S, Ciantelli M, Cecchi F, Gentile M, Sigali E, Laschi C, Ghirri P, Menciassi A, Dario P, Boldrini A. "A novel simulator for mechanical ventilation in newborns: MEchatronic RESpiratory System Simulator for Neonatal Applications." *Proc IMechE Part H: J Engineering in Medicine* 2015, Vol. 229(8) 581–591.
- [3] Tognarelli S, Baldoli I, Scaramuzzo RT, Ciantelli M, Cecchi F, Gentile M, Laschi C, Sigali E, Menciassi A, Cuttano A. "Development and validation of a sensorized neonatal intubation skill trainer for simulation based education enhancement". *Int J Med Res Health Sci.* 2014;3(4):833-839.

A Shape Similarity Metric for Brain Fibers Classification

M. De Piccoli¹, P. Fiorini¹

¹ *Altair Robotics Lab, Department of Computer Science, University of Verona,
michela.deplicoli@univr.it*

INTRODUCTION

Diffusion Imaging (DI) is a structural Magnetic Resonance Imaging (MRI) technique, which provides a non-invasive way to explore organization and integrity of the white matter structures in the human brain [1]. From DI data, the white matter fiber tract can be reconstructed using a class of techniques called tractography. DI is widely used to probe the three-dimensional structure of brain fibers. In order to make fiber-based analysis more practical, the fiber set needs to be preprocessed to eliminate redundancies. To simplify the visualization and analysis of white matter fiber tracts obtained from DI data, it is often necessary to group them into larger clusters or bundles [2]. In order to perform clustering, first a mathematical definition of fiber similarity (or, more commonly, fiber distance) must be specified. Then, pairwise fiber distance is calculated and used as input to a clustering algorithm [3]. The most common metrics used for distance only captures the local relationship between streamlines but not the global structure of the fiber. The global structure refers to the fiber variability shape. Together, local and global information, define a good metrics of similarity [4]. We propose a new method to classify fibers with respect to a novel shape criterion. The proposed method considers the concept of fiber correlation as a similarity indicator.

MATERIALS AND METHODS

As dataset we have considered a Fornix bundle [5]; it is composed by 3831 streamlines Figure 1.

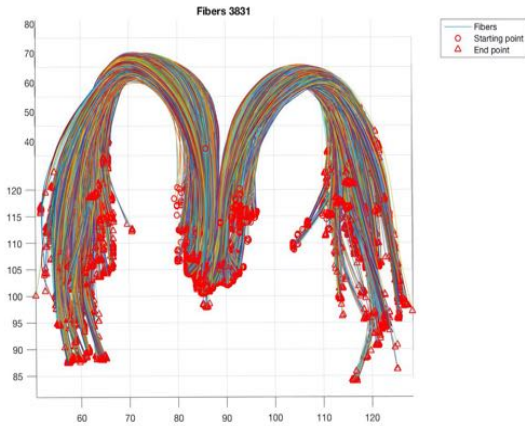


Figure. 1. Fornix Bundle Dataset

Fornix consists of two long distant legs (left and right) and a thicker upper part, Body of Fornix. We show the steps for Shape Similarity Metric:

1. We considered the first fiber as a fiber of reference. Each streamlines in the bundle is compared with streamline of reference, black line in Figure 3.
2. For each point of the streamlines we have calculated the Frenet Frame. Through the Frenet Frame we have information describing the geometry of the fibers.
3. To analyze the shape of fibers, we introduce two parameters that describe a geometric similarity, computed for each pair of fibers and for each points:
 - we denote with symbol D (*Difference*), the Euclidean distance between points. This is the Real component of our method
 - we denote with symbol AS (*Angular Shape*), the value obtained by comparing the angle between tangents. This is the Imaginary component of our method
4. We represented the fibers as complex form De^{iAS} , as a result of the previous point, and we computed correlation function between pair of fibers
5. We considered the maximum value of the correlation function. The maximum correlation value corresponds to the point where the fibers have a similar distance value and a similar angle value
 - we estimated the correlation index
6. We extracted the fibers with different range of values corresponding to correlation index

RESULTS

Below we report the results of the similarity metric.

Applying the method explained in the previous section we plotted (Figure 2 and Figure 3) in the complex plane, a description of how, with respect to correlation values, fibers are placed in space.

Each blue circle contains information about the concept of distance and angle. In red circle we have the information extracted by correlation index.

In Figure 2, the values in red correspond to values where the fibers have high correlation index respect to the streamline of reference; otherwise, in Figure 3 we have the fibers with low correlation index (respect to the streamline of reference).

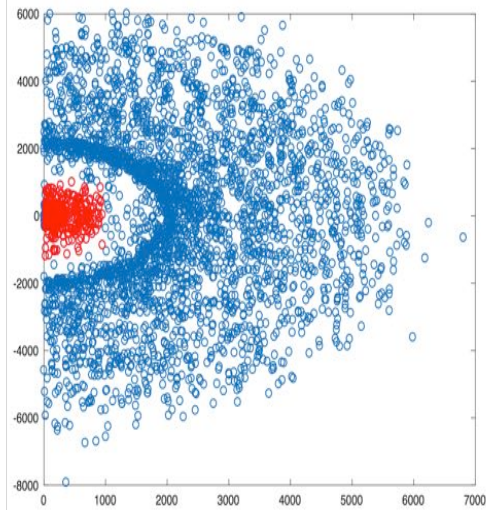


Figure. 2. Highlighted the range where the fibers have a high correlation value. The set of values plotted (red and blu) are the information about the Real and Imaginary part

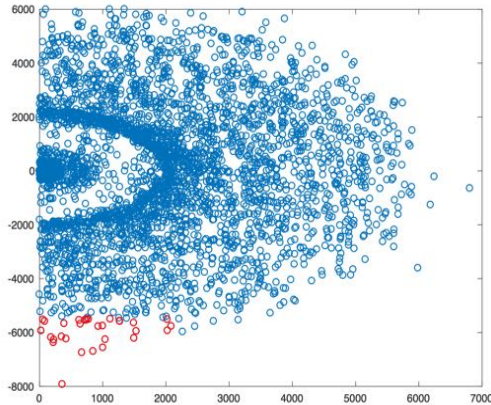


Figure. 3. Highlighted the range where the fibers have a low correlation value. The set of values plotted (red and blu) are the information about the Real and Imaginary part

In Figure 4 and Figure 5, we have the fibers extracted by our method. The fibers extracted are those represented by red circles.

Respect to the black fiber, that is the fiber of reference, the initial dataset is subdivided with respect to the similarity criterion.

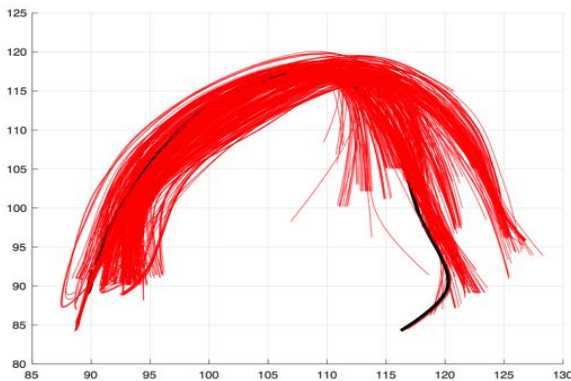


Figure. 4. Selected fibers respect to high correlation index (values in red color Figure 2). In black color, we have the reference fiber used for comparison with other fibers.

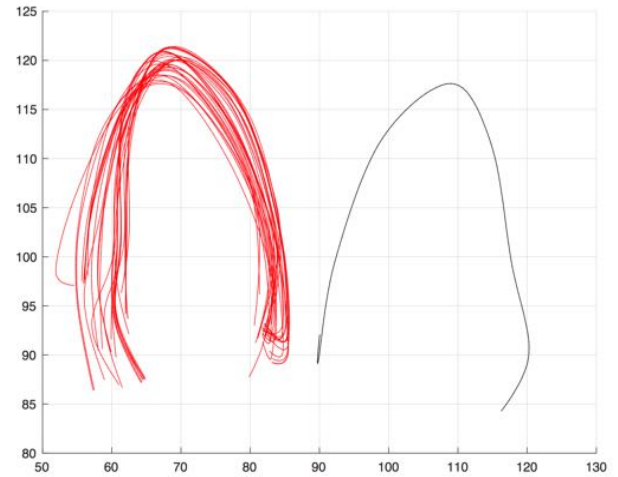


Figure. 5. Selected fibers respect to low correlation index (values in red color Figure 3). In black color, we have the reference fiber used for comparison with other fibers.

If we considered the dataset in Figure 1, we can distinguish the fibers, which, compared to the black fiber, are in the right side Figure 4 respect to initial dataset or in left side Figure 5 of the reference beam. This is a good result for fiber identification.

DISCUSSION

In this paper we presented a new criterion for classifying fibers. The method has been applied to Fornix datasets. We introduce a new concept of similarity between fibers, computed for each pair of fibers and for each point. Using this new shape similarity metric, we have information on how two fibers are oriented with respect to each other; indeed, calculating the angle for each pair of points of two different fibers, we can estimate how much the fibers are comparable in shape. The criterion used to classify fibers is based on the correlation concept. The results confirm a good fiber classification. In future we want to consider another dataset and we want to compare our metric with others and validate the clustering results by means of a ground-truth.

REFERENCES

- [1] S.Mori, Introduction to Diffusion Tensor Imaging. Elsevier Science, May 2007.
- [2] I. Corouge, G. Gerig, and S. Gouttard, "Towards a shape model of white matter fiber bundles using diffusion tensor mri", in ISBI, 2004.
- [3] S. T. Mai, S. Goebel, and C. Plant, "A Similarity Model and Segmentation Algorithm for White Matter Fiber Tracts", in ICDM, 2012.
- [4] Z. Ding, J. C. Gore, and A. W. Anderson, "Classification and quantification of neuronal fiber pathways using diffusion tensor MRI", Magnetic Resonance in Medicine. 2003.
- [5] M. Catani, R. J. Howard, S. Pajevic and D. K. Jones, "Virtual in Vivo Interactive Dissection of White Matter Fasciculi in the Human Brain", NeuroImage 17, 77-94 (2002). diffusion tensor MRI", Magnetic Resonance in Medicine. 2003.

Soft-magnetic retractor for Minimally Invasive Surgery

A. Cavallo¹, M. Brancadoro¹, S. Tognarelli¹, A. Menciasci¹

¹The BioRobotics Institute, Scuola Superiore Sant'Anna, Pisa

selene.tognarelli@santannapisa.it

INTRODUCTION

In the last decades, traditional surgery has significantly changed towards minimally invasive regime. Minimally Invasive Surgery (MIS) is recognised as the most suitable approach for the vast majority of clinical interventions, especially for abdominal surgery. Despite the well-known benefits for the patient, from a medical viewpoint MIS requires high skills. Tissue manipulation and retraction remain the most challenge tasks [1]. Several commercial retractors have been already included in clinical practice but they are rigid, frequently invasive and not easy to use. To overcome these limitations, the use of magnets has been intensively investigated in literature [2, 3]. However, magnetic devices suffer from i) annoying magnetic interferences with traditional laparoscopic instruments and ii) tissue invasiveness due to clips or clamps teeth anchored on the retracted tissue. Aim of this work is to investigate an innovative solution for abdominal tissues retraction that results simple, reliable, easy to use, safe and compatible with all MIS procedures. The main objective of this work is to overcome the limits of the magnetic anchoring devices by proposing a novel retraction system with variable stiffness equipped with ferromagnetic elements. By taking into consideration the anatomical constraints and the medical requirements, the ideal retractor is flexible enough to enable easy insertion into the abdominal cavity without damaging surrounding tissues but, at the same time, it is properly stiff for applying the required retraction forces. The physical principle that can be exploited to implement all these features in only one system is jamming [4]: a physical process in which materials consisting of numerous smaller pieces, such as grains (i.e. granular jamming) or sheets (i.e. layer jamming), change from a flexible to a rigid state, if vacuum is applied on the volume. Following the active interest around soft robotics, authors proposed a soft-ferromagnetic cylindrical retractor by exploiting their previous experiences in both magnetic surgical robotics systems [5] and soft robotics [6].

MATERIALS AND METHODS

The proposed soft-ferromagnetic retractor is composed of two main units (Figure1): the extracorporeal unit, namely two permanent magnets and the intra-abdominal unit represented by the soft-ferromagnetic retractor. The soft-ferromagnetic retractor shows a cylindrical shape for optimizing insertion port constraints and tissue-retractor contact. It is realized putting together i) a soft central part filled of granular material with variable stiffness, ii) two rigid ferromagnetic components (i.e. pure iron cylinders)

located at the far ends of the device. Iron allows us to solve the important problems of magnetic interferences, guaranteeing a stable magnetic anchoring on the abdominal wall. On the other hand, the soft part of the system ensures a safety interaction with tissues. In the rigid state, the retractor can move and hold the tissues without additional clamps or sutures and it is more stable than a soft system in case of bumps during surgery.

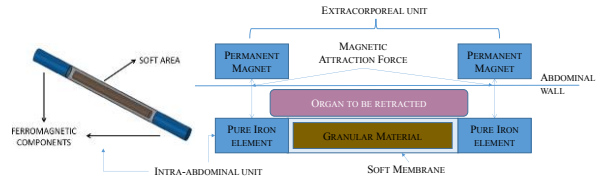


Figure 1. Schematic representation of the retraction system

To the best of authors' knowledge, in abdominal surgery, liver, stomach and intestine are the organs mainly involved in retraction tasks. Considering the different anatomical features of those organs, we proposed here a common system design to be properly modified in dimensions for making it compliant with the technical requirements (e.g. organs weight, and retraction forces). Regarding the extracorporeal unit, no specific anatomic constraints have to be considered, however the permanent magnets dimensions have to be optimized for avoiding interferences with surgical instruments. On the contrary, the intra-abdominal unit was designed by taking into account the typical laparoscopic trocar diameter (i.e. 12mm) as the main mechanical constraint for covering all MIS techniques. Additionally, the length of the soft part relies on organ dimensions and shape; magnetic attraction force has to be, at least, equal to the required force to retract the organ (Table 1).

Organ	Required Retraction Force	Soft Part Length
Liver	6.63N	180mm
Stomach	1N	90mm
Intestine	5N	80mm

Table 1. Data used as reference for system design.

Moreover, the soft component design requires a deeply investigation of the physical principle of granular jamming. Specific analyses have been performed for defining: i) soft bags number filled with granular matter, ii) soft material for bag membrane and iii) granular matters. In order to define the suitable dimensions of iron elements for assuring a safe retraction, a proper magnetic analysis was performed by using COMSOL Multiphysics language (COMSOL, Palo Alto, USA).

RESULTS

The retractor was realized based on the previous dimensioning. The external unit is composed of two axially magnetized N52 NdFeB permanent magnets

(50.8mm in diameter, 25.4mm in height). The intra-abdominal unit of the system was specifically designed for each organ. Each retractor has a cylindrical shape (11mm in diameter) and the soft central part is equipped with only one chamber that showed the higher stiffness variation. The dimensions of the soft central part of the retractors are reported in Table 2.

Organ	Soft membrane dimensions [mm]	Granular jamming bag dimensions [mm]
Liver	H=190, R=5.5	H=180, R=4
Stomach	H=110, R=5.5	H=100, R=4
Intestine	H=90, R=5.5	H=80, R=4

Table 2. Operative dimensions of the soft part of each retractor (H=height; R=radius).

The soft membrane is realised in Ecoflex-0030 (Smooth-On, Inc.), a biocompatible silicone certificated for medical devices, and it is completely filled with ground coffee. Ecoflex-0030 was chosen as the most appropriate soft material for membrane because it shows good handling and adaptability. The soft bag was filled with ground coffee as a trade-off between stiffness variation and replicability of the results; high repeatability is one of the most important requirements for clinical acceptability. Finally, a small flexible tube (2mm in diameter) has been integrated in the soft area for vacuum management. The using of iron elements instead of NdFeB permanent magnets for solving the problem of magnetic interferences entails a significant reduction in the attraction forces. Validated FEM analyses have been carried out for identifying the best iron dimensions for each retraction procedure. Attraction forces between the external permanent magnet and the intra-abdominal iron cylinder have been calculated by changing both abdominal wall thickness (from 20mm to 40mm for selecting the most suitable abdominal wall thickness [7]) and cylindrical height (10mm in diameter).

Taking into account all these data, the design of the final retractors (Figure2) has been carried out (Table 3); they can be used in patients with abdominal wall thickness up to 30mm. Iron elements are attached to each end of the soft area by using Smooth-Sill 950 (Smooth-On, Inc.) silicone that totally covers the extremities of every ferromagnetic sample guaranteeing a unique structure.

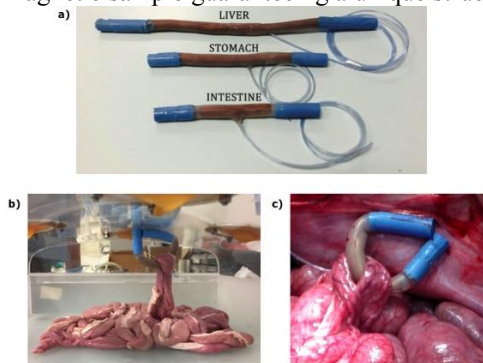


Figure 2. a. Retractor final prototypes; b. ex-vivo and c. in-vivo tests of the intestine retractor.

Organ	Iron Element Height	Guaranteed Forces	Soft Part Length	Total Length
Liver	40mm	7.1N	190mm	290mm
Stomach	10mm	1.5N	110mm	150mm
Intestine	30mm	5.4N	90mm	170mm

Table 3. Final retractors prototypes design features.

The system assessment was carried out by means of ex-vivo and in-vivo experiments with the final aim to establish the right design of each retractors component and to demonstrate the advantages of using a soft system. The ex-vivo validation (Figure2b) allows to simulate the traditional retraction task: the ex-vivo tissue has been fixed into the laparoscopic simulator as into the abdomen and after the retraction task was executed. All prototypes showed good performances; the soft component and the iron elements have the right dimensions in each prototype. Finally, an additional in-vivo test (Figure2c) in laparotomic regime was performed in a domestic pig model reaching good results and showing promising applications.

CONCLUSION AND DISCUSSION

An innovative soft-ferromagnetic system for specific organ retraction, i.e. liver, stomach and intestine was designed, realized and preliminary validated both in ex-vivo and in-vivo tests. We proposed here the idea to join together the ferromagnetic principle with stiffness variation induced by granular jamming phenomena for solving the main drawbacks of the retraction devices reported in literature. The ferromagnetic link assures stable tissue retraction but solving magnetic interference problems and granular jamming varies retractor stiffness for different surgical applications. The soft component is in contact with the retracted tissue guaranteeing a non-invasive retraction for healthy and pathologic tissue. The retractor can be inserted and extracted from the abdomen using an existing access port and it can be positioned with traditional laparoscopic tools. After retractor positioning, it is necessary to place the external magnets on the abdominal wall and to active the vacuum: the retractor is anchored at the abdominal wall and the organ is maintained in the retracted position. Good results have been obtained, showing promising applications.

REFERENCES

- [1] Steele PR, et al. "Current and future practices in surgical retraction." *Surgeon*, 2013; 11(6):330-7.
- [2] Choi YH, et al. "Laparoendoscopic single-site simple nephrectomy using a magnetic anchoring system in a porcine model." *Investig Clin Urol*. 2016; 57(3):208-14.
- [3] Padilla BE, et al. "The use of magnets with single-site umbilical laparoscopic surgery." *Semin Pediatr Surg*. 2011; 20(4):224-31.
- [4] Liu AJ, et al. "Nonlinear dynamics: Jamming is not just cool any more." *Nature* 1998; 396(6706):21-22.
- [5] Brancadoro M, et al., "A novel magnetic-driven tissue retraction device for minimally invasive surgery" *MITAT* 2017; 26(1):7-14.
- [6] Cianchetti M, et al. "Soft Robotics Technologies to Address Shortcomings in Today's Minimally Invasive Surgery: The STIFF-FLOP Approach." *Soft Robotics*. 2014;1(2):122-31.
- [7] Best SL, et al. "Maximizing coupling strength of magnetically anchored surgical instruments: how thick can we go?" *Surg Endosc*. 2011;25(1):153-9.

Simultaneous hand-eye registration and instrument tracking initialization for continuum robots

B. Rosa

Icube, University of Strasbourg, CNRS, France

INTRODUCTION

Continuum robots have been developed for minimally invasive surgery, and offer unparalleled access to deep anatomy compared to conventional rigid tools [1]. However, several difficulties remain. One of them is the ability to precisely control the tip of a flexible continuum robot with the accuracy required for surgery. While concentric tube robots, for instance, are one of the most promising technologies, modeling errors remain in the millimeters, which could be problematic when finer movements are required, often during the most critical parts of the surgery.

Using vision to track surgical instruments has been proposed as a way of solving this problem [2]. Tracking the instrument in the camera frame could for instance allow precise tip control using visual servoing. However, while many approaches allow instrument tracking without using specific markers, they often require training on manually-labeled datasets.

Alternatively, this paper proposes to use the model of the continuum robot (possibly including errors) in an iterative optimization scheme, which simultaneously registers the eye-hand transformation and initializes the tracking system. The output of the algorithm is a registration between the camera and the robot frame, as well as a trained classifier which can serve as an initialization for 2D/3D tracking of the robot [3]. Details of the algorithm are presented below, as well as preliminary simulation results.

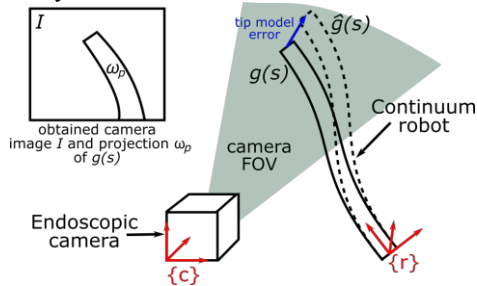


Figure. 1. Continuum robot inserted in working channel of an endoscope and visualized by the endoscopic camera

MATERIALS AND METHODS

Let's consider the situation from Fig. 1: a continuum robot is inserted through an endoscope and in the field of vision (FOV) of an endoscopic camera. The shape of the robot is noted $g(s)$, and its estimation (using a mechanical model, for instance) is noted $\hat{g}(s)$. The camera frame is noted $\{c\}$ and the robot base frame is noted $\{r\}$. In this work, the camera is considered as calibrated and images rectified, with a projection

matrix K_c . Considering a transformation T from the robot frame to the camera frame, one can express the projection of the robot shape on the image I as:

$$K_c T g(s) \quad (1)$$

s being the curvilinear abscissa parameterizing the robot shape. If one takes a random transformation T and projects the estimated robot shape $\hat{g}(s)$ onto the image using (1), one will obtain a projected shape of the robot on the image, which defines an area $\omega_p \subset I$. The corresponding pixels in I can then be used as a foreground model in a supervised machine learning algorithm, to train a classifier which tracks the continuum robot in the surgical images. In this work, we use a random forests model. Random forests is a supervised machine learning algorithm which trains many weak classifiers and averages the response to form the output [4]. It has been shown in [3] to be very efficient for instrument tracking in minimally invasive surgery, using a combination of pixel features from the opponents and HSV color spaces. One particularity of this algorithm is that it uses bootstrap aggregating during training, which allows computing an out-of-bag error, giving an estimate of the potential prediction error just after training the model, without requiring a separate validation dataset [4].

Let's now consider the situation for which the transformation T is wrongly calibrated, i.e. T is different from the actual robot-to-camera transformation T_r^c . In this case, the projection ω_p of $g(s)$ on I will not be aligned with the robot shape as it appears on the image. As such, the classifier will have mixed background and foreground data points in its input which, after training, will make the out of bag error e increase. Conversely, one can reasonably infer that the out-of-bag error will be minimal when the transformation T is aligned with T_r^c . This, of course, assumes that the selected features (in our case Hue, Saturation, and Opponent 1 and Opponent 2 values for each pixel) allow discriminating between background and foreground.

Given this hypothesis this paper proposes an iterative optimization algorithm, which will search the rigid transformation space $SE3$ in order to find the transformation \hat{T} which minimizes the error e . Similarly to [5], I propose to use a stochastic branch-and-bound algorithm to explore the search space in order to avoid getting trapped in possible local minima of the cost function. This algorithm recursively constructs and updates a binary tree by dividing the search space and evaluating the cost function at a randomly sampled point within the search space of the newly created leaves. In order to speed up the search, large costs are assigned to transformations T resulting in a projected

shape out of the image (i.e. $\omega_p = \emptyset$). For other transformations, the cost function is the out-of-bag error e of a random forest model, which is trained using the endoscopic image and the current projected robot shape ω_p on the image. After convergence, the algorithm returns the registered transformation \hat{T} , as well the final trained random forests model.

RESULTS

The proposed algorithm was implemented in python, using OpenCV for the image processing routines and scikit-learn for its random forests implementation [4]. Validation was performed in simulation, using VTK for rendering the robot shape projected on a virtual camera, and a surgical background image (600x600 pixels). The number of iterations in the stochastic branch-and-bound algorithm was set to 100. Optionally, speckle noise of intensity $\alpha \in [0,0.01]$ was added to the generated endoscopic images to evaluate robustness of the algorithm to image noise. The robot shape $g(s)$ was generated using a torsionally-compliant three-tubes concentric tube robot (CTR) kinematic model [6] and randomly generated joint values. To simulate robot modeling error $\hat{g}(s)$ was obtained by adding a tip error vector of random direction (see Fig.1). The norm of the tip error was drawn from a Normal distribution of mean 0 and of standard deviation $\sigma \in [0,5 \text{ mm}]$. This tip error was then propagated towards the base of the robot.

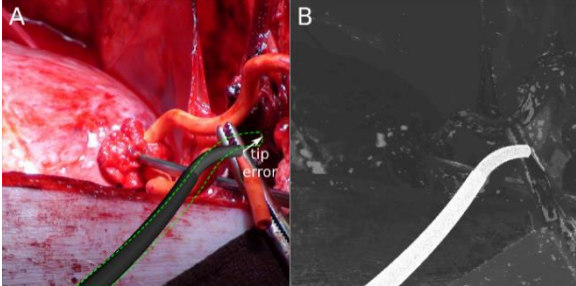


Figure. 2. Example of optimization results with $\alpha=3$ and $\sigma=0.01$. A: simulated endoscopic image with the projection of the estimated robot shape $\hat{g}(s)$ using equation (1) and $T = \hat{T}$ (green dotted line); B: foreground probability as output by the final random forests model.

Fig. 2 shows a typical registration result with $\alpha=3$ and $\sigma=0.01$. Note that \hat{T} is correctly estimated, but the modeling error (white arrow at the tip) prevents a perfect alignment (Fig.2A). The obtained random forests model is however good enough to allow easy segmentation of the robot outline, despite the presence of surgical tools in the background image (Fig. 2B). Fig.3 shows the dependency of the results to speckle noise and modeling errors. One can see that the final out-of-bag error e is only marginally dependent on noise and modeling errors. The transformation registration error $e_t = \|I - T_c^r \hat{T}^{-1}\|$ increases with α or σ . A two-way ANOVA with 500 optimization results as samples shows that, as expected, the tip model error parameter σ has a statistically significant influence on e_t ($p < 0.01$). However, neither the noise level α ($p=0.32$) nor its

interaction with σ have a statistically significant effect ($p=0.91$). The average processing time is $24.5 \pm 5.81 \text{ s}$, which could be improved by implementing the algorithm in C++ using parallel processing.

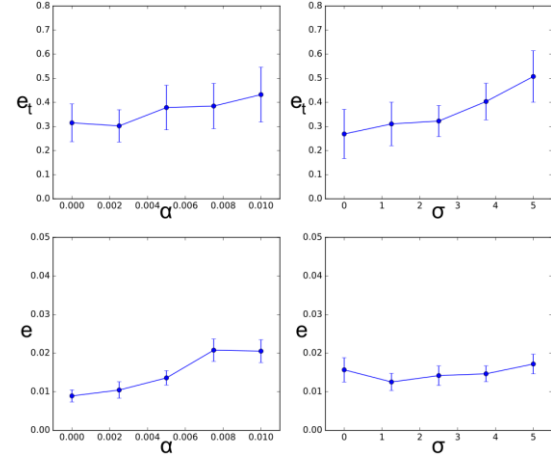


Figure. 3. Errors for varying levels of noise and tip error. Dots and bars present the mean and 95% confidence interval over 20 optimization runs with random robot shapes.

CONCLUSION AND DISCUSSION

This paper presents an optimization algorithm allowing to simultaneously register an estimated robot shape with a camera (eye-hand calibration) and train a classification model in order to perform endoscopic 2D/3D tracking. It is particularly well-suited for continuum robots such as CTRs, for which an approximate shape estimation is obtained from the joint values. The algorithm output can subsequently be used for initializing a more complex tracking technique, such as one described in [2, 3]. The proposed algorithm was validated in a simulation framework. Those preliminary results show a good robustness to noise and robot modelling error. Further work will go towards validation in a clinically-realistic setup.

REFERENCES

- [1] J. Burgner-Kahrs *et al*, 2015. Continuum robots for medical applications: A survey. *IEEE Trans. Robotics*, 31(6), 1261-1280.
- [2] D. Bouget *et al*, 2017. Vision-based and markerless surgical tool detection and tracking: a review of the literature. *Med. Image Analysis*, 35, 633-654.
- [3] M. Allan *et al*, 2013. Toward detection and localization of instruments in minimally invasive surgery. *IEEE Trans. Biomed. Eng.*, 60(4), 1050-1058.
- [4] G. Louppe, 2014. Understanding random forests: From theory to practice. PhD dissertation, Université de Liège.
- [5] C. Gruijthuijsen *et al*, 2016. An Automatic Registration Method for Radiation-Free Catheter Navigation Guidance. *J. Med. Rob. Res.*, 1(03), 1640009.
- [6] Dupont *et al*, 2010. Design and control of concentric tube robots, *IEEE Trans. Rob.*, 26(2), 209-225.

Toward Global Calibration of a Robot-Assisted Vitreo-Retinal Surgery based on OCT C-Scan Image Registration

M. Ourak¹, G. Borghesan¹, L. Esteveny¹, S. Hecker², T. Probst², A. Chhatkuli², K. K. Maninis², E. Lankenau³, H. Schulz-Hildebrandt⁴, D. Reynaerts¹, E. B. Vander Poorten¹

¹Department of Mechanical Engineering, University of Leuven,

²ETH Zurich, ³Optomedical Technologies GmbH, ⁴Medical Laser Center Lübeck GmbH,

mouloud.ourak@kuleuven.be

INTRODUCTION

Vitreo-retinal (VR) surgery, a sub-specialty of ophthalmology, refers to surgical interventions to treat eye problems affecting the retina, macula, and vitreous fluid. VR surgery is performed to treat retinal detachment, macular holes, epiretinal membranes and complications related to diabetic retinopathy. The procedure is based on advanced instrumentation and wound-construction techniques to minimize the risk towards the patient. Over times visualization during vitrectomy surgery has significantly improved with a better imaging system and improved lighting [1]. Nevertheless, VR surgery remains technically challenging requiring high levels of manual dexterity, precision and repeatability.

In order to reduce physiological hand tremor, to provide fine motion control and consequently enhance microsurgical accuracy several assistive robotic systems have been developed in the past [2]. Robots can potentially scale down surgeon hand motion and filter tremor. In order to enhance patient safety it could be also beneficial to offer additional information regarding the working environment to the robotic system. For example it might be useful to track the robot's tool tip over time to intervene before damage occurs, or to label certain anatomic areas and provide feedback when in the vicinity of those areas. Nowadays, such feedback would typically be generated from image sensors. Different modalities are available. In VR surgery one commonly uses white light stereo microscope and optical coherence tomography (OCT) systems. In order to use this information for assistive control, it is necessary to register this with respect to the robot frame. The literature describes a number of methods that solve the registration problem between a robot and white light camera [3]. This quality of the registration is limited by the precision and robustness of the camera calibration and its resolution.

In this paper, we propose to use the OCT image modality to register images to the robot. Indeed, methods for C-scan registration are already performed [4]. However, this related to the same probe acquisition. While, we use two acquisition modes that are available in our platform: the C-scan grabbed by an iOCT (Intraoperative Optical Coherence Tomography) system that is incorporated in the employed stereo microscope

system (Haagstreit Surgical GmbH) and A-scan data that is measured by an OCT fiber probe that is embedded in an instrument held by the robot, and that is stacked as a second C-scan.

By registering the two C-scans, the iOCT data can be registered with respect to the robot frame. As far as the authors are aware of this is the first time a point cloud registration approach was used to register iOCT data to a surgical robot.

MATERIALS AND METHODS

An OCT-fiber probe made by the Medical Laser Center Lübeck GmbH and connected to an iOCT scanner of OptoMedical Technologies is used for getting the A-scan data during the different experiments (Fig 1). The fiber probe grabs only A-scan data with a rate of 200 Hz. The OCT system is a spectral domain OCT with a depth range of 3.9 mm. The iOCT scanner is mounted on a Haag-Streit Surgical stereo microscope. It shares the same optical path with the white light stereo-microscope camera. The iOCT scanner uses two inner mirrors to scan the sample surface. It offers the possibility to grab A-scan, B-scan and C-scan images. The C-scan data from the microscope are collected as raw data at a sample rate of 90 second for each 400 x 400 x 1024 pixels.

A checkerboard pattern from Applied Image mounted in a specific configuration (i.e., translation and rotation) is used as test sample. This pattern is chosen because it offers the possibility to easily match corresponding features. Moreover, the geometric information from the pattern is known, which simplifies the evaluation of the registration quality.

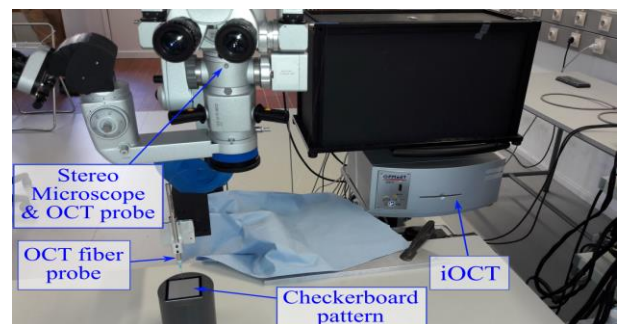


Figure 1. Experimental setup used for registration.

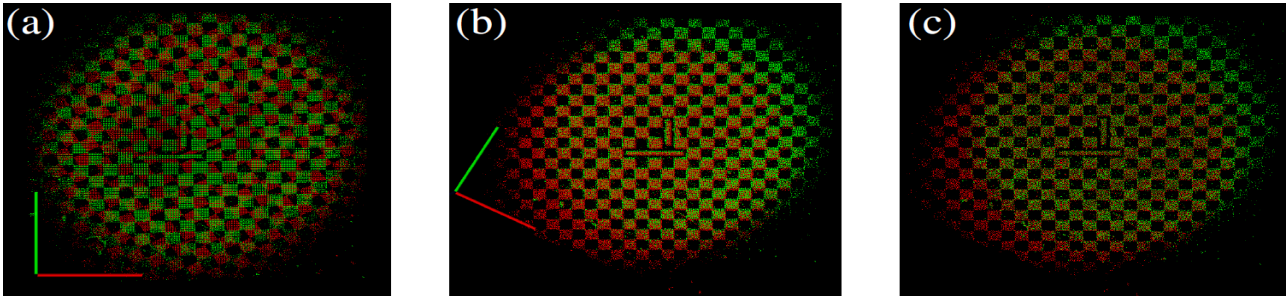


Figure 2. Image snapshot acquired during the registration process of two point clouds: (a) the initial point cloud configuration, (b) the first coarse registration, (c) finer point cloud registration.

In order to achieve the registration and the estimation of the geometric transformations between the point clouds, we propose an approach based on a point cloud library (PCL) [5], following three steps:

1. Data processing

This step is used to build the C-scan from the different A-scans grabbed by the scanning fiber probe. Based on the known robot position when scans were taken the data is expressed in the robot reference frame. Moreover, the data from the probe is processed to extract relevant features (i.e., the checkerboard pattern point cloud clear as possible).

2. Coarse manual registration

Coarse manual positioning step is achieved using the two point clouds. This step is conducted manually by the user with his mouse. In this step, the operator coarsely positions the source point cloud relatively to the target. In this case, the transformation between the two points cloud is estimated from the applied motion.

3. ICP registration

This last step uses the algorithm of iterative closest point (ICP) [6] as it is, to achieve the finer registration. This allows improving the matching quality between the two point clouds obtained in previous step.

Once executed, the transformation matrix between both point clouds is obtained. Finally, this transformation is used to express the position of the stereo-microscope with respect to the robot coordinate frame.

RESULTS

A first experimental test is initiated with the aim of validating the proposed registration method applied in the C-scan data. For this purpose, two OCT C-scan grabbed with the same stereo microscope probe of the checkerboard are used with two different geometric configurations (i.e., two different translations and rotations).

Figure 2 shows some snapshots acquired during the procedure. The coarse manual registration leads to matching quality displayed in the Fig 2(b), while Fig 2(c) depicts the final matching after ICP registration. Finally, it can be underlined from this first test the possible use of checkerboard C-scan data information for image registration.

CONCLUSION AND DISCUSSION

In this paper a novel approach was introduced to register an iOCT to a robot coordinate frame by means of an OCT-fiber instrument mounted on the robot. The feasibility of this approach was demonstrated by a first experiment using a checkerboard pattern in the same C-scan probe data. This test showed already nice overlapping volumes. As the stereo-camera and the OCT-camera share the same optical path, the registration of the stereo-camera to the robot coordinate frame comes for free.

Further work will be conducted in order to use the data coming from the two probes (i.e., microscope probe and fiber probe) as it is stated in the introduction. Then, a series of test will be achieved to estimate the quantitative measures of the precision and repeatability of the proposed approach.

ACKNOWLEDGMENTS

This work is conducted with a financial support from The EU *Framework Programme for Research and Innovation* - H 2020 - Grant Agreement No 645331.

REFERENCES

- [1] Williamson, Thomas H. "Introduction to Vitreoretinal Surgery." *Springer Berlin Heidelberg*, pp 21-60, 2013;
- [2] Molaei, Amir, et al. "Toward the art of robotic-assisted vitreoretinal surgery." *Journal of ophthalmic & vision research*, 2017;
- [3] Dornaika, Fadi, and Radu Horaud. "Simultaneous robot-world and hand-eye calibration." *IEEE transactions on Robotics and Automation*, pp. 617-622, 1998;
- [4] Wang Xin, et al. "An iterative closest point approach for the registration of volumetric human retina image data obtained by optical coherence tomography." *Multimedia Tools and Applications*, pp. 6843—6857, 2017;
- [5] Rusu, Radu Bogdan, and Steve Cousins. "3d is here: Point cloud library (pcl)." *IEEE The International Conference on Robotics and Automation*, pp. 1-4, 2011;
- [6] Segal, Aleksandr, Dirk Haehnel, and Sebastian Thrun. "Generalized-ICP." *Robotics: Science and Systems*. Vol. 2., No. 4. 2009.

Robot Assisted Needle Control and Visualisation

G Dwyer¹, John Byard¹, Francisco Vasconcelos¹, Tom Vercauteren², S Ourselin²,
D Stoyanov¹

¹*Surgical Robot Vision Group, Centre for Medical Image Computing, University College London,*

²*Translational Imaging Group, Centre for Medical Image Computing, University College London*
george.dwyer.14@ucl.ac.uk

INTRODUCTION

Percutaneous interventions offer several advantages over open or laparoscopic interventions, access ports and often sutures are not needed due to the size of the tool, reducing the scar size and improving on the cosmetic outcome of the procedure. However, these procedures often use Ultrasound (US) for the visualisation of the tool requiring the clinician to simultaneously manipulate the US probe and the tool.

Percutaneous procedures often aim to keep the needle axis in-plane to the US image, with the clinician manually controlling both the US transducer and the needle. There have been efforts to assist the procedures by tracking the needle using a range of sensor and sensor-less approaches. 3D US transducers allow a robust sensor-less approach, however the field of view and framerate of these are limited and they are generally not common in practice. Electro-magnetic (EM) sensors allow tracking of the instrumentation out of the US plane but is adversely affected through the presence of external magnetic fields with in the environment [1]. This approach has been integrated into a commercial system, with pre-calibrated transducers (SonixGPS, BK Ultrasound, USA). Echogenic needles can be used to increase the visibility of the needles in-plane, however this offers no out of plane tracking [2]. A recent approach uses a fibre-optic hydrophone and a custom-made transducer to increase the visibility of the needle in plane, but the transducer also had two unfocused arrays to track the needle out of plane [3].

This paper presents the use of two compliant serial robotic arms to control both the percutaneous instrument and US transducer for visualization. The two manipulators are calibrated within the same coordinate system allowing the transducer to follow the needle in plane through the kinematics of the manipulators.

MATERIALS AND METHODS

Needle Calibration

The needle is mounted to the KUKA LBR iiwa 7 R800 using a custom made mount, 3D printed using PLA on an Ultimaker 2 (Ultimaker B.V, NLD). The mount follows a design often used by milling machines, employing a collet to ensure a precise and repeatable mount in

addition to being concentric with the flange and 7th joint axis. The transform between the needle tip and flange is determined through a pivot tip calibration to determine the offset from the flange of the manipulator to the tip of the needle. The orientation of the tip is set as the same as the flange orientation. The pivot calibration requires the robot to be moved to multiple positions while the position of the needle tip is maintained. The flange poses are then fitted to a sphere where the center of the sphere is the tip of the tool [4].

US Calibration

Hand-eye calibration between the robot and US probe attached to its end effector is obtained by scanning a known, static object whose coordinates are known in the robot base frame. In the case of an already calibrated needle, its tip is carefully aligned with the US scanning plane, producing a 2D point feature in the US image. This gives us a correspondence between a 2D point in the US reference frame and a 3D point (stylus tip) that is known in the robot base. After several acquisitions with the probe and the stylus in different poses, the full transformation between the US image reference frame and the robot base can be estimated from the geometric registration between 2D and 3D points [5].

Robot Calibration

The bases of both robots are calibrated through a rigid fixation to an optical table. The base link of the iiwa is centered on the mounting plate and rigidly fixed to the



Figure. 1. CAD model of the two robots with the mounts for the needle and US transducer and shown with the US image overlaid.

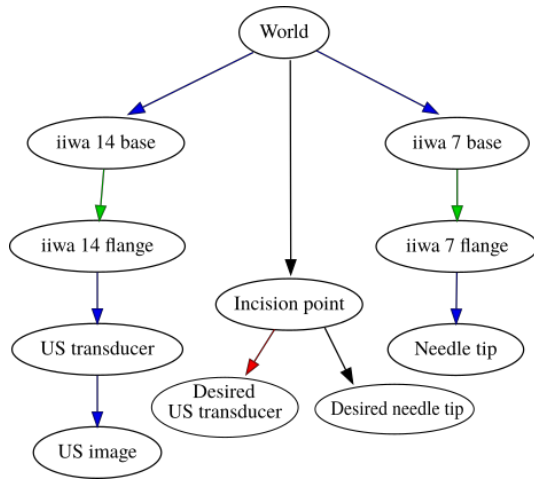


Figure. 2. Tree diagram of the transformations within the system, where the blue arrows indicate transforms determined through calibration, green through sensors (robot encoders), black are user defined and red are derived automatically.

optical table allowing the transform between the two base links to be determined from the geometry of the mounts and optical table.

Control

Once inserted, the needle is constrained at the incision point to 4 degrees of freedom (DOF), similar to laparoscopic surgery. This allows the needle to be rotated on each axis about the incision point and inserted along the instrument. The US transducer can be manipulated in 6 DOF, these are constrained through the relative position of the needle determined from the forward kinematics of the robotic manipulators. Currently the transducer is constrained to a plane placed at the incision point of the needle removing two rotational and one translational DOF due to the use of a linear probe. Leaving rotation along the Z axis (aligned with the depth of the US image) and translation of the X axis (across the image) and Y axis (out of plane). The translation of the transducer (x and y) is directly taken from the kinematic position of the needle within the same parent frame. While the orientation (γ) is determined from the current position of the needle in reference to the entry point.

Implementation

The main control is implemented in the Robotic Operating System (ROS). The robotic manipulators used are the LBR iiwa (KUKA GmbH, DE). Communication with the manipulators is through the iiwa stack [6], which establishes a ROS node on the robot controller using ROS-java.

The transformations between the robotic manipulators and attached tools are handled using the TF2 library in ROS, with the transform tree shown in Figure 2. The US system used is the Sonix MDP system with the L14 – 5 Transducer (BK Ultrasound, USA).

RESULTS

The pivot calibration was undertaken on the needle mount with an attached needle of unknown length and 2.45mm diameter. Four poses were used to determine the transform between the flange and the needle tip. The acquired translation was -0.1, -1.39, 269.04 on the X, Y and Z axis respectively but with a reprojection error of 1.84mm

CONCLUSION AND DISCUSSION

This paper presents the system design for an image guidance platform for assisted needle insertions. The use of robotic manipulators is currently applied to determining the transforms between the needle and US transducer and having the US transducer maintain sight of the needle just through the kinematics allowing the clinician to focus on the procedure. Current calibration techniques provide results with errors over a 1mm, such as the tool calibration of 1.84mm, however for percutaneous procedures where the tool diameter is generally less than 3mm, higher accuracy is required. Future work will focus on combining image based tracking from the US with the kinematic position to maintain sight of the needle and allowing the US transducer to move across unknown and deformable surfaces.

REFERENCES

- [1] A. M. Franz, K. März, J. Hummel, W. Birkfellner, R. Bendl, S. Delorme, H.-P. Schlemmer, H.-P. Meinzer, and L. Maier-Hein, "Electromagnetic tracking for US-guided interventions: standardized assessment of a new compact field generator," *Int. J. Comput. Assist. Radiol. Surg.*, vol. 7, no. 6, pp. 813–818, 2012.
- [2] S. Hebard and G. Hocking, "Echogenic technology can improve needle visibility during ultrasound-guided regional anesthesia," *Reg. Anesth. Pain Med.*, vol. 36, no. 2, pp. 185–9.
- [3] W. Xia, S. J. West, M. C. Finlay, J. Mari, A. L. David, and A. E. Desjardins, "Looking beyond the imaging plane: 3D needle tracking with a linear array ultrasound probe," no. August 2016, pp. 1–9, 2017.
- [4] Z. Yaniv, "Which pivot calibration?," 2015, p. 941527.
- [5] L. Mercier, T. Lango, F. Lindseth, and D. L. Collins, "A review of calibration techniques for freehand 3-D ultrasound systems," *Ultrasound Med. Biol.*, vol. 31, no. 4, pp. 449–471, 2005.
- [6] C. Hennesperger, B. Fuerst, S. Virga, O. Zettinig, B. Frisch, T. Neff, and N. Navab, "Towards MRI-Based Autonomous Robotic US Acquisitions: A First Feasibility Study," *IEEE Trans. Med. Imaging*, vol. 36, no. 2, pp. 538–548, Feb. 2017.

Towards the use of a robotic 3-D trans-esophageal ultrasound system for monitoring cardiac interventions: study of the workflow

Shuangyi Wang¹, Areeb Zar¹, Ruchi Gandecha¹, Davinder Singh²,
James Housden¹, Kawal Rhode¹

¹*Division of Imaging Science & Biomedical Engineering, King's College London, UK*

²*Xtronics Ltd., Gravesend, UK*
shuangyi.wang@kcl.ac.uk

INTRODUCTION

In recent years, the use of 3-D trans-esophageal echocardiography (TEE) for monitoring cardiac interventions has gained wider acceptance among cardiologists, such as in the transseptal puncture, the mitral valve repair, and the closure of paravalvular leaks procedures as reviewed in [1]. Despite the advancement in imaging mode, TEE is still a manually controlled approach. This is tedious and harmful for the duration of the longer interventional procedures, especially when used in conjunction with X-ray [2]. Heavy protective clothing and standing for long periods of time can lead to several occupational diseases. Motivated by these reasons, we designed an add-on robotic system which allows remote control of a commercial TEE probe [3]. Our previous study has demonstrated an automatic acquisition workflow to place the probe based on tracking and feedback [4]. Complementary to the works on automation, this paper focuses on using the robot with the priority on the operator's decision. A more manually-based robotic workflow without additional computing and sensing during the procedure is described. Based on this workflow, phantom and simulation experiments were performed to evaluate its feasibility and performance. The overall aim of this study is to illustrate an easy-to-perform approach for the robotic TEE to be used clinically and to understand its impacts in terms of probe positioning errors.

MATERIALS AND METHODS

The developed add-on TEE robot (Fig. 1a) holds the probe handle and manipulates four degrees of freedom (DOFs) that are available in manual handling of the probe. The mechanism's translational axis is designed allowing for both robotic and manual control. In the view-planning platform designed for pre-planning the 3-D TEE view (Fig. 1b), an automatically segmented 3-D heart model from a pre-scanned MR image, a manually segmented esophagus centre line, and the model of the TEE probe head can be loaded and viewed intuitively. The kinematics of the probe is modelled [3] and the corresponding virtual 2-D centre slice and the cone-sized 3-D volume FOV are displayed based on the given probe parameters. In the platform, a number of markers representing the target structures required to be monitored are defined from the pre-scanned MR image and used to decide the necessary monitoring range of a

view. As the operator virtually moves the probe, two quantitative parameters are calculated in real-time to assist the operator to decide the probe location. The first parameter (P_1) indicates the percentage of the defined markers which are located within the FOV and the second parameter (P_2) indicates the distance from the mass centroid of the defined markers to the centre of the 3-D ultrasound FOV.

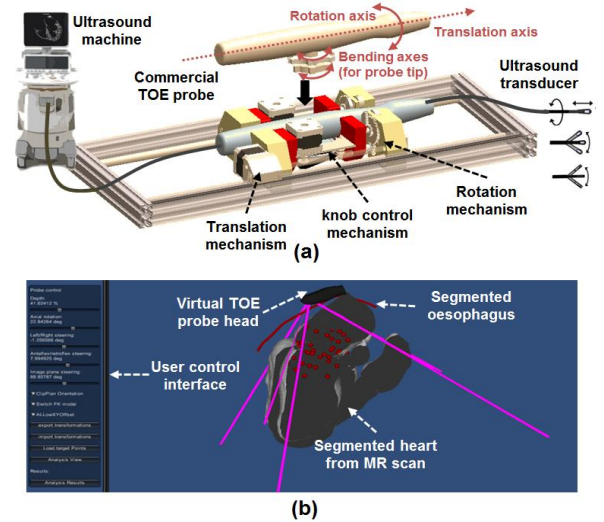


Figure. 1. Overview of (a) the robotic 3-D TEE system and (b) the ultrasound view-planning platform.

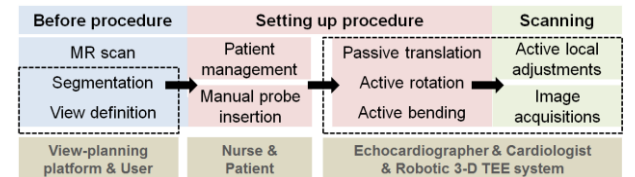


Figure. 2. Overview of the proposed robotic workflow. The dotted boxes summarize the work covered in this study.

For the proposed workflow, the targeted views would be pre-planned using the proposed platform with the probe movement parameters recorded. The centre simulated slices of the planned 3-D views would also be recorded from the platform. During the procedure, the probe would be attached to the robot manually. Based on the depth scales marked on the original probe, the operator would manually insert the probe into the oral cavity using the passive translation feature of the robot to the approximate distance as pre-planned. The active axes

for rotation and bending of the probe driven by the robot would be utilized by the operator controlling from a PC based on the pre-planned angles and visual feedback comparing the ultrasound images (centre slices) to the pre-planned views. After setting up a view, the robot would be controlled remotely by the operator for any local adjustments using the active rotation and bending control axes. The workflow is summarized in Fig. 2.

To simulate the proposed workflow, an experiment using a custom-made heart-esophagus phantom was performed (Fig. 3). The phantom was MR scanned and six custom views were defined. These views were acquired following the proposed workflow. To assess the performance of the acquisition, the acquired ultrasound images were registered to the pre-scanned MR images. This calculates the probe poses which can be compared with the pre-planned desired poses using the root sum square (RSS) error for the translation and orientation components decomposed from the transformation matrices. As the custom-made phantom has a different anatomical relationship to the real heart, an analysis using a real patient's heart-esophagus data was performed. Three different views and the corresponding desired probe poses were defined. For each view, 100,000 simulated probe locations within a similar range of the amount of error found in the phantom experiment from the desired probe location were generated. The corresponding P_1 and P_2 for each location were calculated and the average values of three views given the same position and orientation errors were analyzed.

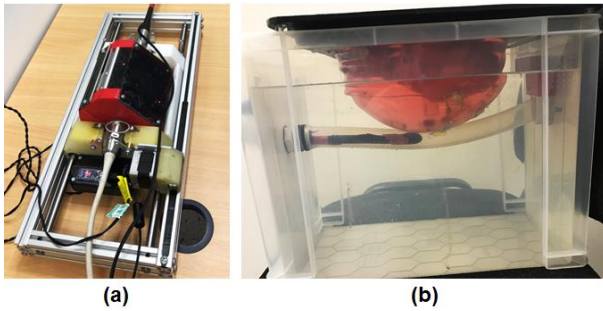


Figure 3. Phantom experimental setup with (a) the TEE robot and (b) a custom heart-esophagus phantom.

RESULTS

The correct working of the 3-D pre-planning method in the software platform for manual selection of probe location has been verified. With P_1 at 100%, targeted structures are located within the TEE FOV. With P_2 as close to 0 as possible, targeted structures are located at the centre of the 3-D TEE FOV. For the probe positioning when setting up the views manually, the mean position and orientation errors were found to be $13.0 \pm 4.5\text{mm}$ and $7.5 \pm 4.5^\circ$ respectively. For the simulation study using the real patient data with the probe positioning error found in the phantom experiment, effects of the errors on the assessment parameters P_1 and P_2 are shown in Fig. 4.

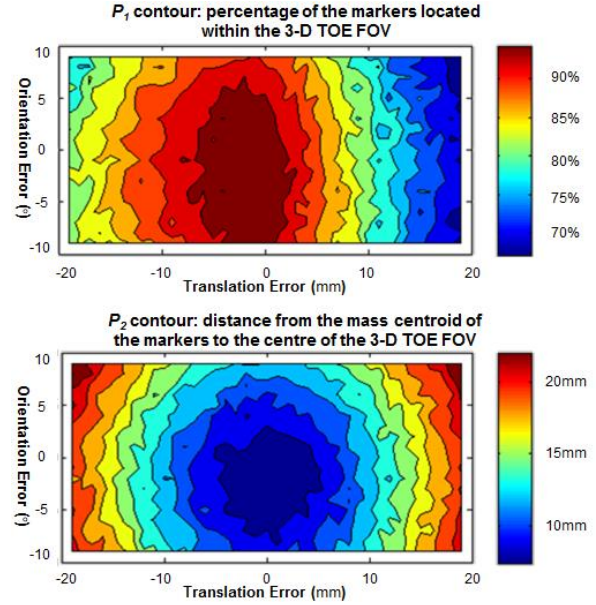


Figure 4. Contour plots showing the effects of the probe positioning errors on the ultrasound image space.

CONCLUSION AND DISCUSSION

Robotic 3-D TEE during cardiac procedures has a clear advantage in terms of radiation safety and occupational disease protection as the operator no longer needs to manually hold the probe for long periods of time. This paper demonstrates a easy-to-perform workflow for clinical use of the robot in terms of planning and setting up views. A phantom study has been performed and the probe positioning errors were quantified. As indicated in Fig. 4, we found that more than 80% of the targeting markers are still within the FOV with the amount of mean positioning errors. Furthermore, the targeting structures are still close enough to the centre of the FOV compared with the range of heart motion in 1 cm order of magnitude. To summarise, this study demonstrates a possible roadmap to implement the TEE robot in clinical use and our future work will aim at cadaver and a first-in-man study to promote this technique.

REFERENCES

- [1] Faletra, FF., Pedrazzini, G., Pasotti, E., Muzzarelli, S., Dequarti, MC., Murzilli, R., Schlossbauer, SA., Slater, IP., and Moccetti, T. "3D TEE during catheter-based interventions." *JACC Cardiovasc Imaging*; 2014; 7(3):292-308.
- [2] Goldstein, JA., Balter, S., Cowley, M., Hodgson, J., and Klein, LW. "Occupational hazards of interventional cardiologists: prevalence of orthopedic health problems in contemporary practice." *Catheter Cardiovasc Interv*; 2004; 63(4):407-11.
- [3] Wang, S., Housden, J., Singh, D., Althoefer, K., and Rhode, K. "Design, testing and modelling of a novel robotic system for trans-oesophageal ultrasound." *Int J Med Robot*; 2016; 12(3):342-54.
- [4] Wang, S., Singh, D., Johnson, D., Althoefer, K., Rhode, K., and Housden, J. "Robotic ultrasound: view planning, tracking, and automatic acquisition of trans-esophageal echocardiography." *IEEE Robot Autom Mag*; 2016; 23(4):118-127.

Rendering Flexible Endoscopy Manageable through In-Hand Automation

T.Vandebroek^{1*}, M.Ourak^{1*}, C.Gruijthuijsen¹, L.Esteveny¹, A.Javaux¹, C.Pimsamut¹, D.Reynaerts¹, S.Ourselin³, D.Stoyanov³, T.Vercauteren³, J.Deprest², E.Vander Poorten¹

¹Department of Mechanical Engineering, University of Leuven, ²University Hospitals Leuven, ³Centre for Medical Imaging Computing, University College London,
Tom.Vandebroek@kuleuven.be

INTRODUCTION

Twin-to-twin Transfusion Syndrome (TTTS) is a condition that affects up to 9% of all monochorionic diamniotic twin pregnancies [1]. TTTS is caused by unbalanced placental vascular anastomoses between the monochorionic twins. If left untreated perinatal mortality rate exceeds 90% [2]. Surgical treatment by laser ablation has an excellent outcome, but induces in about 30% of the cases iatrogenic (i.e. caused by the surgery itself) preterm prelabor rupture of membranes.[3]. Petersen *et al.* concluded that the diameter of the instruments (typically between 2.3 and 4.0mm) may affect the likelihood for preterm birth [4]. Stresses applied upon the uterine and fetal membranes are also being investigated as possible causes for preterm membrane rupture [5].

Identifying and ablating submillimeter diameter anastomoses absorbs full surgeon attention. Additional to typical MIS drawbacks, visualization quality, even compared to usual laparoscopy, is very poor: Illumination is low, the field of view is extremely narrow and amniotic fluid may blur the image. Despite the previous, the surgeon is to avoid contact with the placenta and preferably maintain a distance of 10 mm during ablation [6]; while the distance from insertion to placenta may be as large as 300 mm. For ideal control over the ablation a laser pose perpendicular to the placental surface is maintained. So far only (semi-)rigid fetoscopes have been used for this treatment. When the placenta is in an anterior position, straight instruments cannot reach perpendicularity to the placental surface, possibly leading to overly large forces applied on the membranes when trying to reach difficult poses.

Compared to rigid instruments, flexible instruments possess additional degrees of freedom (DoFs) that in theory make possible to achieve adequate alignment. In practice, no flexible instruments are available for this procedure. Moreover surgeons used to rigid or semi-rigid instruments indicate that they would quickly lose the sense of orientation when asked to work with flexible instruments. Aside from lengthy learning curves, safety issues might arise when additionally asking the surgeon to control the adjustable DoFs.

MATERIALS AND METHODS

To meet the conflicting requirements in terms of usability and dexterity a setup offering 'in-hand automation' is proposed. The flexible instrument allows

achieving the same surgical tasks while theoretically reducing stress on the uterine wall. The automation avoids increasing the already saturated mental load of the surgeon.

Applied on a commercial ureteroscope (Flex-Xc, Karl Storz, Tübingen) this add-on turns the ureteroscope into either button-based or an intelligent single-handedly manipulated fetoscope; the latter aligning the tip automatically perpendicular to the placental surface as described in C. Gruijthuisen *et al.*[7]. From the user's viewpoint the scope can be operated as a traditional rigid or semi-rigid scope. In the following the requirements and mechanical design of the add-on are summarized briefly. A basic verification of the performance is included next.

Requirements for in-hand automated fetoscope

The Flex-Xc was chosen as a basic endoscopic platform to implement the working principle. Being a robust (commercial and medical-grade) scope with a small outer diameter (2.4 mm) and spacious working channel (1 mm) it has a chip-on-tip sensor and illumination system. The distal tip can be oriented +/- 180 degrees by pushing and pulling a lever at the ureteroscope handle. For fetal surgery, amongst other problems, the usability of the distal bending DoF is rather problematic. It requires the operator to use both hands to orient the scope's body and control the distal tip. An add-on to empower in-hand automation should meet the following main requirements:

- | | |
|--|---|
| R1: compatible with and respecting integrity of Flex-Xc | R5: isotropic mass/inertia for balanced manipulation |
| R2: enabling intuitive single-hand operation | R6: compact, allowing strong & comfortable grip |
| R3: cause no interference in gross scope motion | R7: precise control over distal DoFs |
| R4: lightweight | R8: modularity, easy (dis-)assembly |

State-of-the-art

Earlier works such as by Fang *et al.* [8] or Ruiter *et al.* [9] augmented flexible scopes by attaching motors and couplings or by transferring actuation via Bowden cables. In many cases full robotic actuation of all motion DoFs is elaborated using teleoperation. These methods violate one or more requirements (**R3**, **R4**, **R5** and **R6**).

* The first and second author equally contributed to this work.

This work explores a co-manipulation or handheld configuration where the surgeon stays near the patient. The envisioned system is minimalistic; the surgeon remains responsible for the main fetoscope motions, whereas the distal motion is overtaken by the robotic system. A configuration that can be installed easily (**R1**, **R8**) and whereby the adjustments made, minimally affect the original gross motion (**R3**, **R4**, **R5** and **R6**) could maximally tap onto surgeon's expertise and skill in controlling the gross motion (as if controlling a rigid, semi-rigid scope), and would probably be fairly easy accepted by clinicians provided it offers precise and intuitive control over distal DoFs (**R2** and **R7**).

Fluidically actuated flexible endoscope

Figure 1 provides an overview of the envisioned active flexible endoscope. The distal DoF is pneumatically actuated. The setup consists of a frontal part (two halves are screwed against each other) and a single rear part slid over the native scope handle between which a pair of artificial muscles are suspended. The muscles are operating on one side against a spring and can accurately rock the handle back and forth. A cover to shield the muscles and to allow for comfortable grasping of the instrument is not shown here. A potentiometer (blue) allows for accurate position control. A pair of buttons (red) is ergonomically placed on top of the frontal connector allowing the user to single-handedly steer the endoscope and the distal tip. All components apart from the artificial muscles are 3D-printed leading to a minimal increase of scope volume and mass. Furthermore, the added mass/inertia is evenly distributed allowing similar handling as before. The pneumatic supply lines are extremely small, flexible and can be routed alongside the camera cable so that their presence is not noticeable.

RESULTS

A first version of the said scope was built. The mass of the add-on including cabling was about 40g whereas the scope weighs 640g. **Figure 2** shows the relation between the pressure applied at each muscle and the resulting deflection.

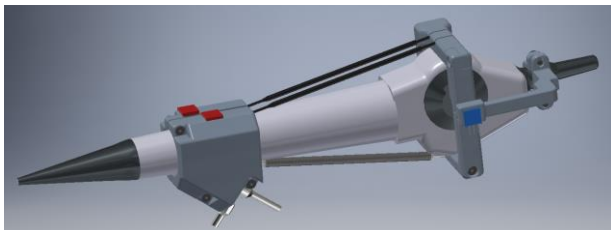


Figure 1. Fluidically actuated automated in-hand scope.

As the employed return spring was rather stiff it limits the total angulation to 45 degrees for a pressure variation between 3 to 5 bars. By optimizing the spring stiffness and the McKibben muscles diameters, the operation range can be enhanced to $\pm 90^\circ$ at the expense of having to design new custom muscles.

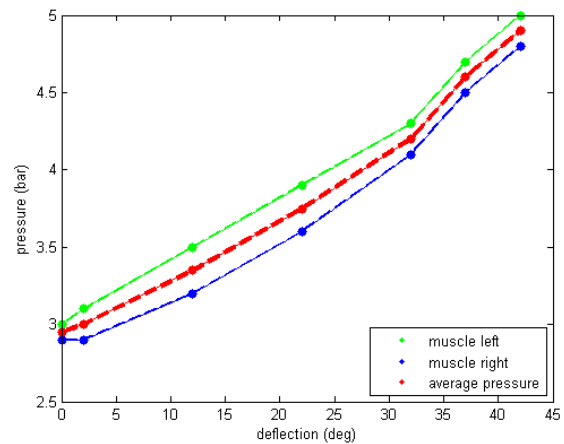


Figure 2 – Deflection of flexible actuated scope as function of the pressure in both muscles.

CONCLUSION

A modular, compact and lightweight add-on is proposed to allow single-handed operation of a flexible scope. Through a simple button push the distal tip of the flexible endoscope can be bent precisely over a 45 degrees range. Further optimization of components is expected to offer a broader operating range and automatic tip orientation will be included thanks to a sensor measuring the surroundings of the endoscope tip [7].

ACKNOWLEDGMENTS

This work was supported through an Innovative Engineering for Health award by Wellcome Trust [WT101957]; Engineering and Physical Sciences Research Council (EPSRC) [NS/A000027/1] and through PRESlice (C22/16/015), an internal KU Leuven grant focusing on ENT-surgery.

REFERENCES

- [1] L. Lewi, J. Jani, *et al.*, "The natural history of monochorionic twin gestations," in *Am J Obstet Gynecol*, vol. 199, 2008, pp. 514–521.
- [2] R. Robyr, *et al.*, "Prevalence and management of late fetal complications following successful selective laser coagulation of chorionic plate anastomoses in twin-to-twin transfusion syndrome," *Am. journal of obstetrics and gynecology*, vol. 194, no. 3, pp. 796–803, 2006.
- [3] V. Beck, *et al.*, "Preterm prelabor rupture of membranes and fetal survival after minimally invasive fetal surgery: a systematic review of the literature," *Fetal diagn. and therapy*, vol. 31, no. 1, pp. 1–9, 2012.
- [4] S. G. Petersen, *et al.*, "The impact of entry technique and access diameter on prelabor rupture of membranes following primary fetoscopic laser treatment for twin-twin transfusion syndrome," *Fetal diagnosis and therapy*, vol. 40, no. 2, pp. 100–109, 2016.
- [5] M. Perrini, "Towards prevention of the premature rupture of fetal membranes: mechanical characterization and repair strategies," Ph.D. dissertation, ETH Zurich, Faculty of Science., 2014.
- [6] J. Deprest, G. Barki, *et al.*, Eds., *Endoscopy in Fetal Medicine*, 3rd edition. EndoPress, 2015.
- [7] C. Gruijthuisen, *et al.*, "Haptic Guidance Schemes for Robot-assisted Minimal Invasive Fetal Surgery." *Proceedings of the 6th Joint Workshop on New Technologies for Computer/Robot Assisted Surgery. Joint Workshop on New Technologies for Computer/Robot Assisted Surgery*. Pisa, September 2016, 83–84.
- [8] C. Fang *et al.*, "A motorized hand-held flexible rhino endoscope in ent diagnoses and its clinical experiences," *BioRob*, pp. 853–858, 2012.
- [9] J. Ruiter, E. Rozeboom, M. van der Voort, M. Bonnema, and I. Broeders, "Design and evaluation of robotic steering of a flexible endoscope," *BioRob*, pp. 761–767, 2012.

Towards automatic needle grasping for robotic surgical suturing

Claudia D'Ettorre^{1,2}, Mirek Janatka², Francisco Vasconcelos², Elena De Momi¹, Danail Stoyanov²

¹*Department of Electronics, Information and Bioengineering, Politecnico di Milano, Milan, Italy,*

²*Centre for Medical Image Computing, University College London, London, U.K.
claudiadettorre@mail.polimi.it*

INTRODUCTION

In robotic minimally invasive surgery (RMIS), the surgeon tele-manipulates the surgical tools. Although RMIS is more ergonomic for the surgeon, complex or dexterous surgical tasks are still demanding to perform [1]. In particular, suturing requires considerable training to manipulate the needle and thread skillfully [2].

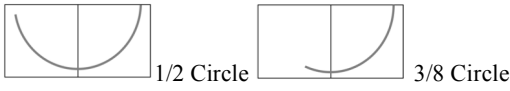


Fig 1. Above, 1/2 or 3/8 circular crested needles used for surgical suturing. Below, the three phases description: first the right-hand tool grasps the needle after 2/3 of his length (starting from the tip), then it passes the needle to the left-hand tool that usually approaches around 1/3 of the length. The last step is the final approach of the needle from the right-hand tool that need to grasp the needle in the proper final position.

As a process, suturing requires a starting procedure, pre-suturing, that can be summarized in three phases, as shown in Fig 1. This allows the surgeon to position the needle as perpendicularly as possible to the suturing surface [3]. Subsequently the needle path required for a suture can be obtained through path planning, for example by minimizing the interaction forces between the tissue and the needle [4]. Multiple sutures can be performed through the use of suture needle angular position as a metric and optimization based on sequential convex programming used to estimate the reorientation phase [5]. However, the pre-suturing phase is needed to initialize this process and the aim of this paper is to evaluate the accuracy of driving the Patient Side Manipulator (PSM) of the da Vinci Research Kit (dVRK) platform [6]. The study is preliminary and focuses on the 2D planar case with planned future developments towards a 3D system to achieve the complete automatic process for the pre-suturing needle grasping task.

MATERIALS AND METHODS

The experimental procedure is performed through a da Vinci Classic Surgical System equipped with the dVRK [6]. For controlling the PSM motion, we built upon a previously developed Matlab-ROS interface [7].

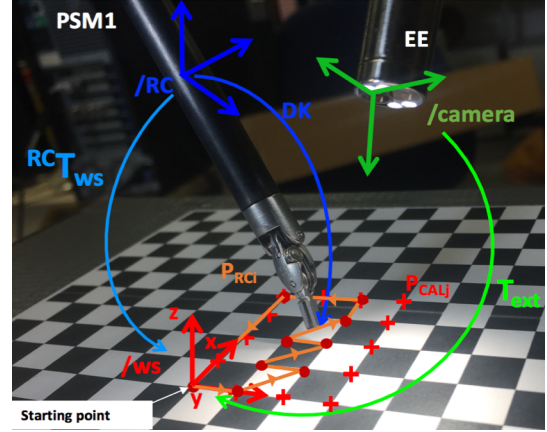


Fig 2. Set-up: PSM1, Endoscope (EE), Large Needle Driver (LND), a grasper with 10 mm fingers. Chessboard used: 6cmx8cm with a chess dimension of 1cm. Reference Frame system used: remote center of PSM (/RC), Left Camera (/camera), Workspace (/ws). Matrix involved: Direct Kinematic of the PSM (DK), Horn's Methods estimation matrix (${}^{RC}T_{ws}$), camera calibration (T_{ext}).

Calibration - To determine the transformation ${}^{RC}T_{ws}$ between the work space (/ws) reference frame and the remote center of the PSM reference frame (/RC), a calibration between the 14 red crossed points (P_{CALJ_ws}), Fig.2, and the same points acquired in tele-operation (P_{CALJ_PSM}) with the PSM arm, was performed using classical absolute orientation [8].

The transformation T_{ext} , between the endoscope and the workspace was estimated, through the Matlab Calibration toolbox [9], to obtain direct measurements of the tool pose. Only the left camera from the stereolaparoscope was used.

Automation - The motion of the Large Needle Driver (LND) instrument held by the PSM is generated with respect to the remote center of the PSM. To evaluate the accuracy of the LND's automatic movements, a general randomized trajectory path, represented in orange in Fig.2, was generated (P_{RCI}) in the /ws.

Analysis - To evaluate the tool tip's coordinate position in the /ws from the camera's image, a clicking interface through which the operator interacts directly with the scene was created to assist with selecting points of interest (P_{camera}). Once the coordinates of the tool tip have been selected into the camera reference frame system, and given that T_{ext} is known, it is possible to infer these in the workspace reference system (P_{map}), K contains the intrinsic camera parameters [10].

$$P_{map} = T_{ext} * \begin{bmatrix} K^{-1} * P_{cam} \\ 1 \end{bmatrix}$$

The entire experimental procedure was repeated 4 times to verify the repeatability.

Error evaluation

$$E = \frac{\sqrt{\sum_{i=1}^n \|P_{CAL_PSM}^{fit} - P_{CAL_PSM}\|^2}}{n}$$

where:

$$P_{CAL_PSM}^{fit} = T_{ws}^{RC} * P_{CAL_ws}$$

$$P_{CAL_PSM} = \sum_{j=1}^m P_{CALj_PSM} / m$$

j represents the number of acquisitions of P_{CAL} , in this case was up to five different times, and n represents the 14 points acquired during the calibration procedure.

RESULTS

By applying the transformation ${}^{RC}T_{ws}$ to the P_{RCi} points it is possible to visually identify the presence of an error in the estimation of ${}^{RC}T_{ws}$. At present, there is limited precision in the overlap of the blue dots with blue stars as highlighted (red circle) in Fig 3.

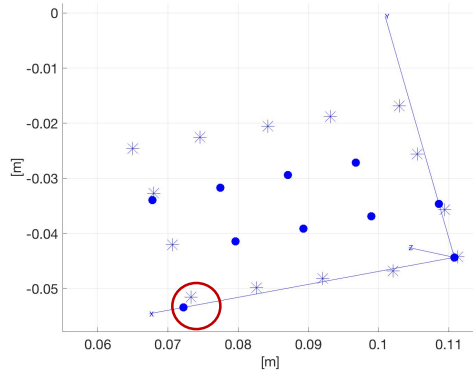


Fig 3. Stars represent the calibration grid corners (P_{CALj}), while solid dots represent the tool trajectory points (P_{RCi}).

After averaging the coordinates of two acquisition of P_{CAL} cloud ($j=2$) the average error E reaches a minimum value of 0.44 mm.

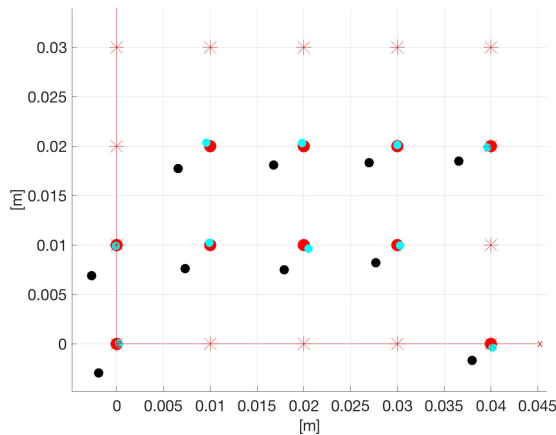


Fig 4. The black solid dots are obtained by mapping the coordinate of the tip in the camera frame into the /ws (P_{map}), in red P_{RCi} ones and the cyan's are the black ones after compensating the offset (P_{end}).

The overall accuracy of the PSM motion was evaluated as the mean Euclidean distance among P_{map} and P_{RCi} ,

$$acc = \sqrt{\sum_{i=1}^n (P_{map}(i) - P_{RC}(i))^2} / n$$

reaching a value of 3.5mm with standard deviation of 0.4mm.

The presence of a common offset was detected and evaluated defining the transformation matrix (${}^{ws}T_{map}$), through the absolute orientation algorithm. By applying that transformation to P_{map} , it is possible to obtain a closer overlapping of the points (Fig 4) represented by the cyan points (P_{end}).

CONCLUSION AND DISCUSSION

There is a systematic offset is due to the kinematics of the PSM, which do not take into account the particular tool that is in use and requires compensation. In our work using the LDN, which has 10 mm tips, an error of 3.16 mm is generated due to this offset. The offset is projected into the calibration plane with respect to the orientation angle of the LDN during motion. By applying the compensation defined by ${}^{ws}T_{map}$, the error decreases up to 0.34 ± 0.2 mm. Further improvements could be made to both the calibration matrix estimation and to the manual tip coordinate detection.

With the current results, we believe that the LDN tool is able to properly grasp the needle, even though the accuracy is approximately equal to the diameter of the needle. The opening range of LND fingers is 30 degrees which ensures grasping. The next step of our work will be to develop the methods for passing of the needle between the two tools in order to measure the accuracy in the 3D motions. Future developments of a 3D system will allow achieving a complete automatic process for the pre-suturing needle grasping task.

REFERENCES

- [1] S. A. Darzi and Y. Munz, "The impact of minimally invasive surgical techniques," in *Annu Rev Med.*, vol. 55, 2004, pp. 223–237.
- [2] A. P. Stegemann, K. Ahmed *et al.*, "Fundamental skills of robotic surgery: a multi-institutional randomized controlled trial for validation of a simulation-based curriculum," *Urology*, 2013.
- [3] N. Semer, "Practical plastic surgery for nonsurgeons" (second ed.), Authors Choice Press, Lincoln, NE, USA (2007)
- [4] Jackson, R.; Cavusoglu, M. "Needle path planning for autonomous robotic surgical suturing". ICRA, 2013.
- [5] Siddarth S., Animesh G., et al. "Automating Multi-Throw Multilateral Surgical Suturing with a Mechanical Needle Guide and Sequential Convex Optimization". ICRA, 2016.
- [6] P. Kazanzides, Z. Chen, *et al.* An "Open-Source Research Kit for the da Vinci Surgical System". ICRA, 2014.
- [7] Z. Chen, A. Deguet *et al.* "Interfacing the da Vinci Research Kit (dVRK) with the Robot Operating System (ROS)"
- [8] Berthold K.P. Horn, "Closed-form solution of absolute orientation using unit quaternions". Received August 6, 1986; accepted November 25, 1986
- [9] Fetić *et al.* "The procedure of a camera calibration using Camera Calibration Toolbox for MATLAB." *MIPRO, 2012 Proceedings of the 35th International Convention*. IEEE, 2012.
- [10] Hartley *et al.* "Multiple view geometry in computer vision". Cambridge university press, 2003.

Modular tactile sensing array for localising a tumor for palpation instruments

Yuen Ting Creamy Lam¹, Yohan Noh^{1,2}, Shan Luo³, Sangjin Han⁴, Matthew Howard², Kawal Rhode¹

¹Department of Biomedical Engineering, King's College London, UK

²Department of Informatics, King's College London, UK

³Department of Civil Engineering, University of Leeds, UK

⁴Department of Electrical and Computer Engineering, Texas A & M University, USA

(Corresponding author: yohan.noh@kcl.ac.uk)

INTRODUCTION

In surgical operations, the use of sensing elements during interactions with surgical instruments helps in identifying medical conditions and making diagnoses. For instance, a palpation instrument aims at localising a tumor in the soft tissue of a human body during surgery. The palpation device embedding force or tactile sensing array can visualise a force map which facilitates the identification [1]. There are various sensing approaches for the map visualization such as: 1) fibre optics; 2) capacitive sensor; 3) optoelectronics; 4) polyvinylidene fluoride (PVDF) films; and 5) piezoresistive materials [1-5]. We propose a low cost tactile sensing array module using optoelectronic sensors. The concept of the tactile sensing array aims at robustness, higher resolution for smaller forces, low level electrical noise, and simple fabrication by 3D-printing. This paper describes the sensing principle and the module based-fabrication, and presents preliminary experiment results.

MATERIALS AND METHODS

1) Sensing principle

In order to measure external force it is necessary to know the amount of deformation or deflection of the mechanical structure. Conversely, if sensing elements measure the deformation or deflection, then the external force can be estimated. Thus, an optoelectronic sensor is adapted to measure an amount of deflection.

An optoelectronic sensor (NJL5902R-2, 1.5 mm x 2.0 mm x 0.5 mm) consists of an LED and a photo

transistor as shown in Figure 1 (right). Figure 1 (left) shows its characteristic curve with respect to the relative current versus the reflector (mirror) distance d . The curve shows two distinctive 'linear' ranges which are highlighted in purple and red, respectively. The sensing range highlighted in red has already been investigated in several other studies, as seen in [3-4] and the references therein. It can be seen that the response of the voltage against the distance variation is more sensitive in the purple range than the red. However there are relatively fewer studies on the purple range. As the purpose of using electrical sensor in general is to be able to use the smaller distance variation to give significant output, we decide to use the purple range as our operation domain for the voltage and distance values while working on the tactile sensing array and investigate its performance.

2) Modular tactile sensing array

A modular tactile sensing array consists of an analog-digital-converter (ADC), a flat flexible cable (FFC), an FFC socket, a sensor base, a sensor mechanical structure, optoelectronic sensors, and reflectors on a PCB. The PCB is fabricated by V-One (Voltera Inc., Canada). Each optoelectronic sensor, NJL5902R-2, is connected with two resistors: R1 is for the LED and R2 for the photo transistor. The ADC is MCP3208 (Microchip Technology, United States). The FFC socket is 08FMN-SMT-A-TF (J.S.T. Mfg. Co., Japan.) The sensor base and sensor mechanical flexure is comprised of four simply supported beams which are fabricated by the Projet HD 3000 3-D production system with Visijet EX200. Figure 2 shows the sensor base and mechanical flexure designed using Solidworks. Figure 3 shows the

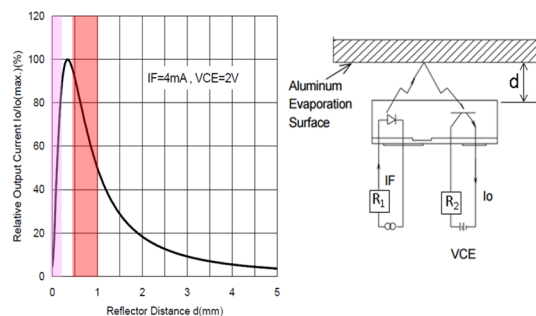


Figure 1. Characteristic curve of optoelectronic sensor NJL5902R-2 (left) (datasheet, New Japan Radio Co., Ltd, Japan) and a circuit for an optoelectronic sensor (right).

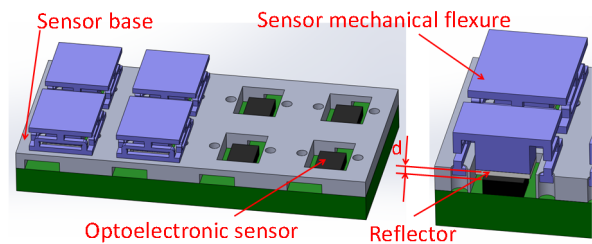


Figure 2. Sensor base and flexure for the tactile sensing array: overall view of the array (left) and magnified view of the array showing reflector (right.)

actual device of the array. In Fig. 3, (a) is the front view and shows the optoelectronic sensors with two resistors, (b) shows the ADC, FFC and FFC socket in the back view, (c) is the final structure attached with sensor base and mechanical flexure designed in Fig. 2.

The size of the array is less than 10 mm x 20 mm so that it passes through conventional trocars for MIS (minimally invasive surgery.) The ADC and FFC are located at the back side of the array such that the electric noise from the array and wire movement are separated from the digital data transmission to the micro-controller-units. Note that the FFC is adopted for the sake of easy assembly and disassembly of the array.

EXPERIMENT AND RESULTS

Two resistor values were calculated as suggested in the sensor datasheet and so R1 is 1.2K Ohm; R2 10K Ohm.

A set of experiments was carried out to obtain the characteristic curve between the output voltage of the optoelectronic sensor and the reflector distance as shown in Fig. 4 (left). The curve shows the two highlighted linear ranges: from 0 to 0.15mm (purple colour) and from 0.5 to 1.0 mm (red colour) where the voltage varied from 3.2 V to 4.7 V as shown in Fig. 5 (left).

A set of sensor calibrations was conducted to find the relationship between the voltage in the purple range and the physical force (obtained by ATI Nano 17, ATI Industrial Automation, USA) as shown in Fig. 4 (right.) Here, the tactile sensing array in Fig. 3 was mounted on the experiment device. The result shows that each tactile sensor had force measurements ranging from 0 N to 0.85 N with respect to the voltage variation from 3.5 V to 4.5 V. The error was mainly caused by hysteresis, around 30 %, and the curve fitting error was around 23 % for both loading and unloading cases in Fig. 5 (right).

CONCLUSION AND DISCUSSION

In the chain of relationship: voltage to distances to physical force, the length of the meaningful voltage range was about 1 V. This could be further improved by optimising four parameters: the two resistors, the reflectance of the reflector, and its surface shape using

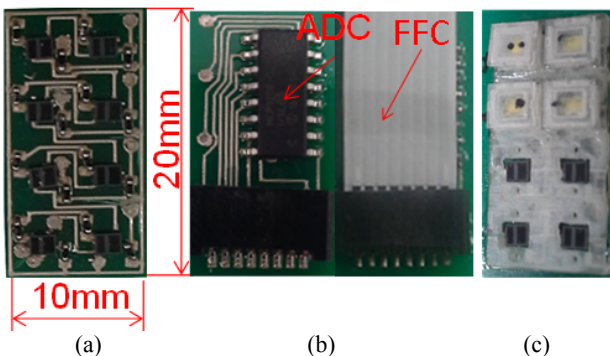


Figure 3. Tactile sensing array integrated with an ADC and an FFC socket: (a) front view without sensing base and flexure; (b) back view with an FFC and an FFC socket; (c) front view with sensing base and flexure attached.

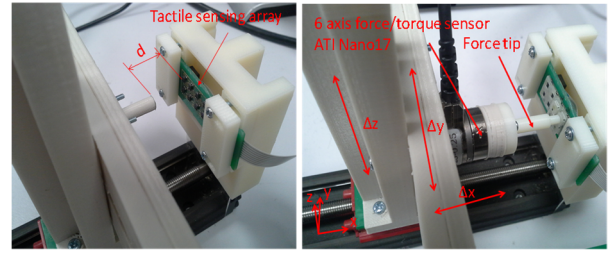


Figure 4. Device setup for experiment of an optoelectronic sensor (left) and a tactile sensor (right.)

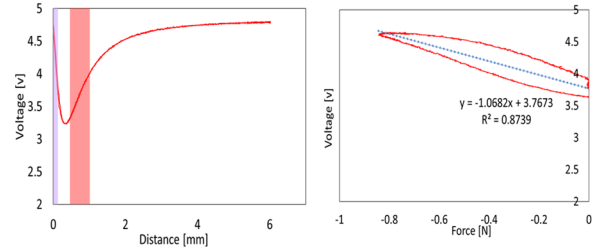


Figure 5. Characteristic curves for an optoelectronic sensor (left) and a tactile sensor (right.)

light intensity model.

The mechanical sensor flexure had large hysteresis. Different material and sensing structure could be used to reduce hysteresis, and we will also conduct experiments again to investigate what really caused large hysteresis.

The electric circuit of the tactile sensing array, a prototype, was designed to pass through the 10 mm to 12 mm trocars. This size can be further reduced by using a smaller optoelectronic sensor (NJL5901R-2, 1.0 mm x 1.4 mm x 0.6 mm) with which the prototype could be 6 mm x 12 mm. This sensor has higher sensing resolution and so the combination could result in better force resolution.

REFERENCES

- [1] M. Li, K. Althoefer, et al., "Intra-operative Tumor Localization in Robot-assisted Minimally Invasive Surgery: A Review," Proceedings of the Institution of Mechanical Engineers, Part H: Journal of Engineering in Medicine, vol. 228, issue 5, 2014
- [2] S. Najarian, J. Dargahi, V. Mirjalili, "Detecting embedded objects using haptics with applications in artificial palpation of tumors," Sensors and Materials 18(4), pp. 215-229, 2006.
- [3] A. Cirillo, S. Pirozzi, et al., "An artificial skin based on optoelectronic technology," Sensors and Actuators A 212, pp. 110-122, 2014.
- [4] Y. Noh, A. Takanishi, et al., "Development of the Airway Management Training System WKA-1 designed to embed arrays of Sensors into a Conventional Mannequin," IEEE/RSJ International Conference on Intelligent Robots and System, pp.1296-1301, 2007.
- [5] A. S. Naidu, R. V. Patel, et al., "A Breakthrough in Tumor Localization: Combining Tactile Sensing and Ultrasound to Improve Tumor Localization in Robotics-Assisted Minimally Invasive Surgery," IEEE Robotics & Automation Magazine, 24(2), pp. 54 - 62, 2017.

CRAS 2017

7th Joint Joint Workshop on New Technologies
for Computer/Robot Assisted Surgery



September 14-15, 2017 - Montpellier, France

Best paper Award

L. Schoevaerds, L. Esteveny, A. Gijbels, J. Smits, M. Ourak, G. Borghesan, D. Reynaerts and E. Vander Poorten

Development of a new bio-impedance sensor to detect retinal vessel punctures for retinal vein occlusion treatment

Best paper Award- Finalists

L. Zorn, F. Nageotte, P. Zanne and M. de Mathelin

STRAS: A Robotic Platform for Intraluminal Surgery Successfully Tested In-vivo

M. Chauhan, N. Deshpande and L. Mattos

Design of a Robotic Microsurgical Forceps for Transoral Laser Microsurgery

G. A. Fontanelli, F. Ficuciello, L. Villani and B. Siciliano

A Novel Force Sensor Integrated into the da Vinci Trocar for Minimally Invasive Robotic Surgery

